

Characterizing the Constitutive Behaviour and Austenite Decomposition of an 1,800 MPa Press

Hardenable Boron Steel

by

Stan Lu

A thesis

presented to the University of Waterloo

in fulfilment of the

thesis requirement for the degree of

Master of Applied Science

in

Mechanical and Mechatronics Engineering

Waterloo, Ontario, Canada, 2024

© Stan Lu 2024

## **Author's Declaration**

I hereby declare that I am the sole author of this thesis. This is a true copy of the thesis, including any required final revisions, as accepted by my examiners.

I understand that my thesis may be made electronically available to the public.

## Abstract

The mechanical behaviour of a new 1,800 MPa strength grade of Al-Si coated, 37MnB5 press-hardenable steel, designated PHS 1800, was investigated under hot stamping conditions. Prior to mechanical testing, a novel heat treatment technique was developed to pre-alloy the Al-Si coating thereby preventing it from melting during austenitization. The alloy was held at 700°C for 7 – 10 minutes and then quenched to room temperature. This heat treatment technique prevented loss of DIC speckle patterns due to melting of the coating, thereby enabling digital image correlation (DIC) strain measurements of the test specimen at elevated temperatures, and was not observed to affect the constitutive behaviour of the material prior to necking.

For constitutive testing, the pre-alloyed material was austenitized and then immediately deformed at strain rates varying between 0.01 and 1s<sup>-1</sup> and temperatures between 500°C and 900°C. The experimental tensile test results were processed to obtain the material flow curves, such that the data could be used for finite element simulation of hot stamping processes. An identical series of experiments was also performed on the widely studied 1,500 MPa 22MnB5 hot stamping grade (designated PHS 1500) in order to validate the testing methods and to provide a baseline for assessment of the new PHS 1800 grade. The PHS 1500 results from the current research were compared to several results published in the literature and were found to be in good agreement, indicating the pre-alloying heat treatment and DIC techniques utilized in the current work were valid for the constitutive testing of PHS.

Compared to PHS 1500, this new grade of PHS 1800 demonstrated approximately 20% higher flow stress at any given strain level, at the same temperature and strain rate test conditions. This relationship also holds true for both materials after quenching to a fully martensitic state, where the ultimate tensile strength of PHS 1800 is approximately 2,000 MPa and 25% higher than the tensile strength of PHS 1500. For the elevated temperature tensile tests, PHS 1800 exhibited similar strain rate and temperature sensitivities as PHS 1500, wherein higher strain rates or lower temperatures resulted in higher flow stresses. PHS 1800

also experienced necking at up to 31% lower strains than PHS 1500, with the strain to necking varying depending on the test conditions.

A modified Norton-Hoff constitutive model, with a second-order polynomial equation to describe the variation in the strain hardening coefficient and strain rate coefficient with respect to temperature, was fit to the experimental results for both PHS 1500 and PHS 1800. An excellent fit (R-squared value of 0.971) was achieved overall at all temperatures and strain rates. A finite element model of the elevated temperature tensile test was created to evaluate the accuracy of the fit curves, and less than 12% error was observed in the predicted load versus displacement response.

In addition to the mechanical behaviour of the material, the austenite decomposition characteristics of PHS 1800 were also investigated via constant cooling rate experiments. The effect of deformation on the austenite decomposition was investigated at three strain levels (0%, 10%, 20%), for three different cooling rates (5°C/s, 10°C/s, 50°C/s). It was found that higher cooling rates resulted in greater martensite phase fractions and higher microhardness values. Specimens cooled at 5°C/s and 10°C/s resulted in complex microstructures including ferrite, bainite, and martensite, while the 50°C/s specimens were fully martensitic. The range of hardness results (with no induced deformation) varied between 430HV to 570HV. When deformation was applied to PHS 1800 in its austenitic state, the fraction of ferrite and bainite phases increased substantially after quenching, resulting in a hardness as low as 320HV, a drop of up to 26%. For the specimens cooled at 50°C/s, induced deformation had no effect on the phase fraction or hardness values.

Finally, the hardness and phase composition results of the constant cooling rate experiments were utilized to update an existing LS-DYNA PHS material model to enable the prediction of accurate phase change and hardness values for PHS 1800. The updated material model was capable of predicting the final hardness of PHS 1800 to less than 2% error at zero applied deformation, and to less than 14% error for the deformed specimens. The accuracy of the phase fraction predictions varied drastically, ranging from 8% to 56% difference compared to the experimental measurements, depending upon how the material parameters were calibrated.

## Acknowledgements

I would like to thank my research supervisor, Professor Michael Worswick, for not only providing me the opportunity to be involved in such a unique and interesting project, but also for the opportunity to conduct cutting edge research in such a well-organized and well-funded lab. I would like to thank Ryan George, Eckhard Budziarek, Jose Imbert, and Tom Gawel for helping me overcome all the operational hurdles I encountered when using the lab equipment. Thanks go to Mark Whitney, whose generous assistance with the Gleeble enabled me to complete my experiments at a much faster pace than otherwise possible. I would also like to thank Sante DiCecco, who helped me get a running start on my research by providing me direction and for assisting me with much of my initial experiments.

Thank you to all the other MME staff that have helped me progress my research. These include all the staff at the Engineering Machine Shop for all the components and specimens machined for me, as well as all the IT staff that have solved my numerous technical issues.

I would also like to thank all my colleagues in EC4 and the University of Waterloo in general for the friendship, advice, and inspiration throughout my research. You know who you are. Thank you to all my friends for your readily available support and advice.

I would like to thank my parents and my sister for your patience, and endless support these past couple of years.

Lastly, I would like to express my gratitude to the sponsors of this project: Ford Motor Company, Magna International, Promatek Research Centre, the Natural Sciences and Engineering Research Council of Canada (NSERC), Ontario Centres of Excellence (OCE) and the Ontario Advanced Manufacturing Consortium.

# Table of Contents

Author’s Declaration .....	ii
Abstract .....	iii
Acknowledgements .....	v
List of Figures .....	x
List of Tables .....	xx
1. Introduction .....	1
1.1. Hot Stamping Processes .....	4
1.2. Hot Stamping Materials.....	6
1.3. Experimental Techniques for Constitutive Testing .....	10
1.3.1. Elevated Temperature Constitutive Testing.....	13
1.3.2. Digital Strain Measurement Techniques.....	19
1.3.3. High Temperature Digital Image Correlation .....	24
1.4. Numerical Modelling.....	30
1.4.1. Hardening Models.....	31
1.4.2. Austenite Decomposition Modelling .....	39
1.5. Scope of Work.....	47
2. Experimental Procedure .....	49
2.1. Studied Materials.....	49
2.2. Experimental Equipment.....	50
2.2.1. Electric Furnace .....	50
2.2.2. Hydraulic Press .....	50
2.2.3. Gleeble 3500 .....	51
2.2.4. MTS Universal Test System .....	55
2.2.5. Optical Strain Measurement (Digital Image Correlation) Equipment .....	56

2.2.6.	Metallography and Metallography Equipment .....	58
2.2.7.	Microhardness Tester .....	59
2.3.	Surface Alloying Experiments.....	59
2.4.	Room Temperature Tensile Tests.....	63
2.5.	Elevated Temperature Tensile Tests.....	64
2.5.1.	General Considerations .....	64
2.5.2.	Specimen Design.....	65
2.5.3.	Surface Alloying Comparison.....	68
2.5.4.	Test Program .....	69
2.5.5.	Results Post Processing.....	72
2.5.6.	Thermal Characterization.....	79
2.6.	Phase Transformation Experiments.....	80
3.	Experimental Results.....	84
3.1.	PHS 1500 and PHS 1800 Post-Quench Tensile Test Results.....	84
3.2.	Surface Alloying Results.....	85
3.2.1.	As-Received Coating Micrographs and Measurements .....	85
3.2.2.	Selected Heating Profile and Surface Alloying Results.....	87
3.2.3.	Microstructure Comparison After Surface Alloying Treatment .....	90
3.2.4.	Elevated Temperature Surface Alloyed Tensile Test Comparison .....	91
3.3.	PHS 1500 Elevated Temperature Tensile Test Results .....	94
3.3.1.	Results Overview .....	94
3.3.2.	Temperature Effects.....	96
3.3.3.	Strain Rate Effects .....	97
3.3.4.	Comparison To Other Published Data for PHS1500 .....	99
3.4.	PHS 1800 Elevated Temperature Tensile Test Results .....	101
3.4.1.	Results Overview .....	101

3.4.2.	Temperature Effects.....	103
3.4.3.	Strain Rate Effects .....	104
3.5.	Comparison of PHS 1500 and PHS 1800.....	105
3.6.	Elevated Temperature Tensile Test Thermal Characterization .....	106
3.7.	PHS 1800 Phase Transformation Results.....	108
3.7.1.	Temperature History .....	108
3.7.2.	Hardness Results.....	111
3.7.3.	Optical Micrographs and Phase Fractions.....	113
4.	PHS 1800 Constitutive Modelling.....	121
4.1.	Constitutive Model Fitting .....	121
4.2.	Finite Element Model Setup.....	128
4.3.	Finite Element Model Results .....	131
5.	Phase Transformation Modelling .....	136
5.1.	Finite Element Model to Determine Activation Energy.....	136
5.2.	Finite Element Model to Determine Deformation Scale Factors .....	139
5.3.	Activation Energy Calibration Results .....	141
5.3.1.	Calibration to Phase Area Fraction Measurements .....	141
5.3.2.	Calibration to Microhardness Measurements.....	149
5.4.	Summary of Activation Energy Calibration results.....	156
6.	Discussion .....	157
7.	Conclusion.....	161
7.1.	Constitutive Testing and Modelling .....	161
7.2.	Phase Transformation Experiments and Modelling .....	162
8.	Recommendations .....	163
	References .....	165
	Appendix A: Modifications to Gleeble Grips.....	175



Appendix B: Stress-Strain Data Showing Variability in Measurements.....	178
Appendix C: Flow Curve Results in Strain Rate Subplots.....	182
Appendix D: Norton-Hoff (Equations (24) - (26)) Fits for PHS 1500.....	184
Appendix E: LS-DYNA MAT_244 Material Parameters for Baseline Austenite Decomposition Simulations.....	186

## List of Figures

Figure 1: Hot stamped components in the BIW of a modern crossover sport utility vehicle, figure adapted from [7].....	3
Figure 2: Direct hot stamping process, adapted from [9].....	4
Figure 3: Indirect hot stamping process, adapted from [9] .....	5
Figure 4: Schematic engineering stress-strain curve obtained from a uniaxial tensile test, with notable points and deformation stages listed .....	11
Figure 5: Generic temperature-time profile of a representative hot stamping thermal cycle for constitutive testing of PHS materials .....	15
Figure 6: Stress contour of a finite element simulation of a compression test, showing a non-uniform stress field throughout the specimen, from Eriksson et al. [40] .....	16
Figure 7: Use of dilatometer to measure strains from a tensile test, from Li et al. [34] .....	17
Figure 8: Modified Gleeble grips to allow for a more uniform temperature distribution and a rotated specimen orientation that allows for DIC in the Gleeble, from Li et al. [45].....	18
Figure 9: Modified specimen geometry and insulated grip design, and the resultant improved temperature uniformity along the specimen from Ganapathy et al. [44].....	19
Figure 10: Principle of digital image correlation, as shown by tracking pixel groups before and after deformation [52].....	21
Figure 11: Unprocessed images of a specimen with a speckle pattern (left) and the surface principal logarithmic strain results after DIC processing (right).....	22
Figure 12: Schematic basic 3D DIC camera setup, showing how coordinate locations are identified in reference to a known pattern (grid for calibration), from Sutton et al. [49] .....	23

Figure 13: Visual effect of thermal radiation on a speckled specimen when heated from (a) room temperature to (b) approximately 700°C .....	25
Figure 14: Sample images obtained between 600°C-1125°C using a UV bandpass filter, and the corresponding grey value histograms for each image from Berke and Lambros [58] .....	27
Figure 15: Method of debossing the surface to promote better paint adhesion, and subsequent DIC results by Li et al. [45] .....	29
Figure 16: Relationships between the mechanical, thermal, and microstructural aspects of a hot stamping process, from Karbasian and Tekkaya [14] .....	31
Figure 17: Schematic showing the differences between experimental results (black, solid line), a Swift model (red, dashed line) model fit to the experimental data, and a Voce model (orange, dotted line) fit to the experimental data.....	33
Figure 18: The effect of strain rate and temperature on the stress response of 22MnB5 from isothermal compression testing (from [47]) .....	34
Figure 19: The effect of the strain rate on the stress response of 22MnB5 from a tensile test at 700°C (from [42]) .....	34
Figure 20: Work hardening exponent $n$ as a function of temperature difference to the lowest temperature condition, for PHS 1500 (from [42]) .....	35
Figure 21: Strain rate sensitivity parameter as a function of increasing temperature difference to the lowest temperature condition, for PHS 1500 (from [42]) .....	36
Figure 22: Experimental data of PHS 1500 and the fit modified Norton-Hoff equation fit (solid line) (from [42]) .....	37
Figure 23: Comparison of the modified Norton-Hoff (N-H) model and the Molinari-Ravichandran (M-R) model fit to experimental PHS 1500 data at 650°C (from [70]).....	38

Figure 24: Continuous cooling transformation (CCT) diagram for 22MnB5, with various cooling rates shown (from [38]).....	40
Figure 25: Measured and predicted microhardness of a hot-stamped 22MnB5, from Åkerström and Oldenburg [66] .....	43
Figure 26: Continuous cooling transformation (CCT) diagram for 22MnB5, with 40% induced compression strain during cooling, with various cooling rates shown (from [38]) .....	44
Figure 27: Comparison of geometrical deviance of measured results to predicted results based on the Åkerström-based model (MAT_244, left) and the Hippchen et al. updated model (MAT_248, right), taken from Hippchen et al. [78].....	46
Figure 28: 125 ton Macrodyne hydraulic press (left) and Deltech electric furnace (right) oriented for manual specimen transfer.....	50
Figure 29: Gleeble 3500 and associated equipment including the thermocouple spot welder, computer for loading test programs, and the control panel for manual Gleeble control.....	52
Figure 30: Default specimen orientation (left) and the rotated specimen orientation (right) accomplished with nested wedge grips. The right figure hides the right jaw and top outer grip to better reveal the nested grip assembly.....	53
Figure 31: Gleeble chamber interior setup, featuring the nested grips to rotate the specimen orientation, and the air hose for quenching/cooling .....	55
Figure 32: MTS tensile frame and DIC image acquisition setup, MTS 685 hydraulic grip supply partially shown to the left .....	56
Figure 33: Image acquisition setup for the Gleeble, with both cameras facing the specimen from the rear window and two angled overhead blue LED lights directed through the top window.....	57
Figure 34: High temperature aerosol paint speckled pattern at (a) room temperature, and at (b) 930°C ...	60

Figure 35: PHS 1800 flat blanks in the (a) as-received state, (b) after hot stamping .....	61
Figure 36: Temperature recording setup for the electric furnace, showing the modified blank and the thermocouple connection.....	63
Figure 37: The modified half scale JIS #5 (MMJIS) specimen for Gleeble use, with critical dimensions labeled .....	67
Figure 38: Images of a speckled specimen (a) at room temperature (25°C), (b) after the heating stage (930°C), (c) after quenching and during deformation (800°C).....	69
Figure 39: Schematic of the temperature-time tensile test program for elevated temperature testing of PHS 1500 and PHS 1800 .....	71
Figure 40: (a) raw captured image at 800°C and (b) the processed image showing the principal ( $\epsilon_1$ ) strain field.....	74
Figure 41: Constructed cross-section profile using the area reduction method and an example of how strains are applied to the discretized sections, adapted from Omer et al.[89].....	76
Figure 42: Engineering (left) and true (right) stress strain curves as calculated from results of a tensile test, using a virtual extensometer and the area reduction method (ARM) .....	77
Figure 43: Photograph of specimen with multiple thermocouples (with wire insulators) attached for thermal characterization, during the heating stage .....	80
Figure 44: Schematic of the constant cooling rate and induced deformation test program, red lines indicate when deformation took place .....	83
Figure 45: Engineering stress-strain curve of critically quenched (fully martensitic) PHS 1500, at room temperature, from quasi-static ( $0.001 \text{ s}^{-1}$ ) tensile test.....	84
Figure 46: As-received microstructure of PHS 1500 and Al-Si coating viewed with a optical microscope .....	86

Figure 47: As-received microstructure of PHS 1800 and Al-Si coating viewed with an optical microscope .....	87
Figure 48: Selected surface alloying heat treatment cycle for (a) PHS 1500 and (b) PHS 1800.....	88
Figure 49: Effect of surface alloying time on the surface appearance, starting with 30 seconds at 700°C (far left) and increasing to 10 minutes at 700°C (far right).....	89
Figure 50: Physical appearance of PHS 1800 (a) in its as-received state, (b) after surface alloying.....	89
Figure 51: (a) As-received PHS 1800, (b) post surface-alloyed PHS 1800 micrographs at 2000x magnification (F: ferrite, P: pearlite, SP: spheroidized pearlite (dark dots)).....	90
Figure 52: (a) Critically quenched PHS 1800, and surface-alloyed then critically quenched PHS 1800 (b) at 2000x magnification.....	91
Figure 53: Engineering stress-strain curves of as-received and surface alloyed PHS 1500 from isothermal tensile tests at 800°C and 0.5s <sup>-1</sup> , and at 900°C and 1s <sup>-1</sup> .....	92
Figure 54: Engineering stress-strain curves of as-received and surface alloyed PHS 1800 from isothermal tensile tests at 700°C and 1s <sup>-1</sup> , and at 800°C and 0.5s <sup>-1</sup> .....	93
Figure 55: Experimental PHS 1500 flow curves at various temperatures and strain rate conditions after austenitization.....	95
Figure 56: PHS 1500 flow stress values at various strain values and strain rates, versus temperature with error bars showing +/- 1 standard deviation of the flow stress values.....	97
Figure 57: PHS 1500 flow stress values at various strain values and temperatures, versus strain rate with error bars showing +/- 1 standard deviation of the flow stress values.....	98
Figure 58: PHS 1500 flow stress values at various strain values and temperatures, versus strain rate on a log scale with error bars showing +/- 1 standard deviation of the flow stress values .....	99

Figure 59: Experimental PHS 1500 results from this work compared to PHS 1500 flow curves published by Merklein and Lechler [42], Abspoel et al. [43], and Li et al.[45] .....	100
Figure 60: Experimental PHS 1800 flow curves at various temperature and strain rate conditions after austenitization.....	102
Figure 61: PHS 1800 flow stress values at various strain values and strain rates, versus temperature with error bars showing +/- 1 standard deviation of the flow stress values.....	103
Figure 62: PHS 1800 flow stress values at various strain values and temperatures, versus strain rate with error bars showing +/- 1 standard deviation of the flow stress values.....	104
Figure 63: PHS 1800 flow stress values at various strain values and temperatures, versus strain rate on a log scale with error bars showing +/- 1 standard deviation of the flow stress values .....	105
Figure 64: Experimental PHS 1800 (solid lines) and PHS 1500 (dotted lines) flow curves at various temperature and strain rate conditions after austenitization .....	106
Figure 65: Average surface temperature along the length of the tensile specimen, after quenching to various deformation temperatures .....	107
Figure 66: Measured temperature and cooling rate vs time from a 5°C/s cooling rate condition experiment with zero-deformation experiment (left) and a 20% deformation experiment (right).....	109
Figure 67: Measured temperature and cooling rate vs time from a 10°C/s cooling rate condition experiment with zero-deformation experiment (left) and a 20% deformation experiment (right).....	110
Figure 68: Measured temperature and cooling rate vs time from a 50°C/s cooling rate condition experiment with zero-deformation experiment (left) and a 20% deformation experiment (right).....	111
Figure 69: Measured Vickers microhardness of PHS 1800 after quenching to room temperature at various cooling rates and with various levels of applied deformation. Error bars indicate +/- 1 standard deviation of each measurement set.....	112

Figure 70: Optical and SEM micrographs of PHS 1800 after quenching at 50°C/s and with varying levels of applied deformation at 800°C .....	114
Figure 71: Optical and SEM micrographs of PHS 1800 after quenching at 10°C/s and with varying levels of applied deformation at 800°C .....	116
Figure 72: Optical and SEM micrographs of PHS 1800 after quenching at 5°C/s and with varying levels of applied deformation at 800°C.....	118
Figure 73: Comparison of original SEM micrograph and processed image of a PHS 1800 sample cooled at 10°C/s with 10% applied deformation. For the processed image, martensite phases are green, ferrite phases are red, and bainite structures are blue.....	119
Figure 74: Experimental (solid) and fit (dash) flow curves of PHS 1800, fit to the modified Norton-Hoff equation (equation (6))proposed by Merklein and Lechler [42] .....	122
Figure 75: Best fit strain hardening exponent (n) for every PHS 1800 flow curve .....	123
Figure 76: Best fit strain rate sensitivity coefficient (m) for all PHS 1800 flow curves.....	124
Figure 77: Experimental (solid) and fit (dash) flow curves of PHS 1800 fit to the modified second order polynomial Norton-Hoff equation.....	126
Figure 78: Tensile test finite element mesh and mechanical boundary condition setup to validate fit flow curves.....	129
Figure 79: Prescribed temperature boundary conditions to the tensile test finite element model, based on experimentally measured results .....	130
Figure 80: Temperature profile applied to the tensile test finite element model shown in °C, based on experimentally collected surface temperatures for tensile tests conducted at 700°C.....	131
Figure 81: Comparison of principal strain contours generated by digital image correlation (DIC) measurements (top) and FEA predictions (bottom) for the 800°C and 0.1s <sup>-1</sup> test condition.....	132



Figure 82: Comparison of FEA prediction versus the input flow curve for the 800°C and 0.1s <sup>-1</sup> test condition .....	133
Figure 83: Comparison of FEA prediction and experimentally obtained flow curve for the 800°C and 0.1s <sup>-1</sup> test condition .....	133
Figure 84: Comparison of FEA prediction versus the input flow curve for the 700°C and 0.01s <sup>-1</sup> test condition .....	134
Figure 85: Comparison of FEA prediction and experimentally obtained flow curve for the 700°C and 0.01s <sup>-1</sup> test condition .....	135
Figure 86: Single element model of the zero-deformation phase transformation experiments .....	136
Figure 87: Single element model of the induced-deformation phase transformation experiments.....	139
Figure 88: Sampled values of MAT_244 activation energies during the optimization of said parameters when optimized to experimental phase area fractions .....	142
Figure 89: Comparison of measured and FEA predicted phase fractions of PHS 1800 using default and activation energies optimized to measured phase fractions (zero deformation).....	144
Figure 90: Comparison of measured and FEA predicted microhardness values of PHS 1800 using default and activation energies optimized to measured phase fractions .....	145
Figure 91: Comparison of measured and FEA predicted phase fractions of PHS 1800 for the quenched and simultaneously deformed specimens, FEA parameters calibrated to phase fractions .....	147
Figure 92: Comparison of measured and FEA predicted microhardness values of PHS 1800 for the quenched and simultaneously deformed specimens, FEA parameters calibrated to phase fractions .	149
Figure 93: Comparison of measured and FEA predicted phase fractions of PHS 1800 using default and activation energies optimized to measured Vickers microhardness .....	151

Figure 94: Measured and predicted Vickers microhardness values of PHS 1800 after quenching at various cooling rates, using activation energies optimized to microhardness.....	152
Figure 95: Comparison of measured and predicted phase fractions of PHS 1800 for quenched and simultaneous deformation experiments, with FEA parameters calibrated to microhardness .....	154
Figure 96: Measured and predicted Vickers hardness of PHS 1800 after quenching at various cooling rates combined with non-isothermal deformation starting at 800°C.....	155
Figure 97: Drawing for the inner set of grips for rotating the orientation of the tensile specimen .....	175
Figure 98: Drawing for the outer set of grips for rotating the orientation of the tensile specimen .....	176
Figure 99: Assembly drawing of the grips for rotating the orientation of the specimen, the required dowel pin is not shown.....	177
Figure 100: Engineering stress-strain curves of as-received and surface alloyed PHS 1500 from isothermal tensile tests at 800°C and 0.5s <sup>-1</sup> , and at 900°C and 1s <sup>-1</sup> .....	178
Figure 101: Engineering stress-strain curves of as-received and surface alloyed PHS 1800 from isothermal tensile tests at 700°C and 1s <sup>-1</sup> , and at 800°C and 0.5s <sup>-1</sup> .....	179
Figure 102: Experimental PHS 1500 flow curves at with all three repeat test results plotted for a range of conditions .....	180
Figure 103: Experimental PHS 1800 flow curves at with all three repeat test results plotted for a range of conditions .....	181
Figure 104: Experimental PHS 1500 flow curves at various temperatures, plotted together with the same strain rate conditions.....	182
Figure 105: Experimental PHS 1800 flow curves at various temperatures, plotted together with the same strain rate conditions.....	183

Figure 106: Experimental (solid) and fit (dash) flow curves of PHS 1500 fit to the modified second order polynomial Norton-Hoff equation ..... 184

Figure 107: LS-DYNA MAT\_244 material card used for the baseline activation energy simulations. All parameters are default values taken from the LS-DYNA Keyword Manual [75] with the exception of the chemical composition, which was updated to that of the studied PHS 1800 ..... 186

## List of Tables

Table 1: Chemical compositions of PHS 1500 and PHS 1800 studied in this research.....	49
Table 2: Proposed tensile test matrix for both PHS materials .....	72
Table 3: DIC analysis settings used to process speckle pattern images from tensile testing .....	73
Table 4: Mechanical properties of quenched PHS 1500 and PHS 1800 from quasi-static room temperature tensile tests .....	85
Table 5: PHS 1800 coating thickness measurements in various conditions, N = 8 .....	91
Table 6: Average of standard deviation of true stress between all repeats, for every tensile test condition of PHS 1500.....	96
Table 7: Summary of test parameters between the current research and PHS 1500 flow curve results obtained from literature .....	101
Table 8: Average of standard deviation of true stress between all repeats, for every tensile test condition of PHS 1800.....	103
Table 9: Average area fractions and standard deviations for ferrite, bainite, and martensite of PHS 1800 specimens quenched at various cooling rates with varying levels of deformation.....	119
Table 10: Coefficients for the Modified Norton-Hoff equation for PHS 1800, obtained by fitting Equations (24) - (26) to the experimental flow curves.....	127
Table 11: R-Squared of the fit flow curves compared to the experimental flow curves, using the coefficients from Table 10 .....	127
Table 12: Default and optimized activation energies (normalized by the universal gas constant) for MAT_244 for the diffusion reactions of ferrite, pearlite, and bainite after calibration to measured phase fractions .....	143

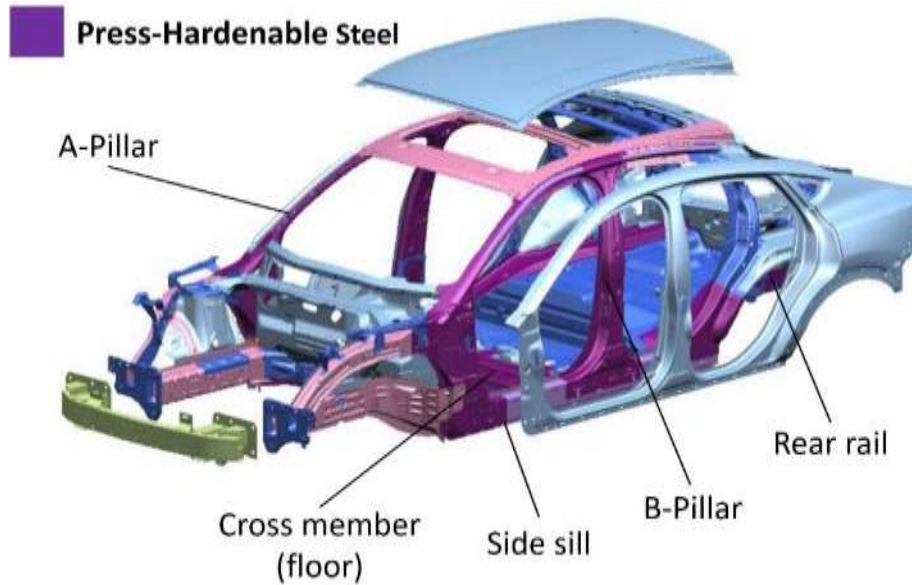
Table 13: Optimized deformation scale factors for PHS 1800 for MAT_244, determined by optimizing to phase fraction measurements.....	146
Table 14: Default and optimized activation energies of PHS 1800 (divided by the universal gas constant) for MAT_244 calibration to measured Vickers microhardness .....	150
Table 15: PHS 1800 deformation scale factors obtained from optimization to hardness measurements .	153
Table 16: Coefficients for the Modified Norton-Hoff equation for PHS 1500, obtained by fitting Equations (24)(6), (25) and (26) to the experimental flow curves .....	185
Table 17: R-Squared of the fit flow curves compared to the experimental PHS 1500 flow curves, using the coefficients from Table 16.....	185

# 1. Introduction

In recent years, new and traditional automakers have been focused on introducing more fuel-efficient (and alternative energy source) vehicles to satisfy government regulations and shifting consumer demands. Government regulations such as the Corporate Average Fuel Economy (CAFE) [1] in the United States and the Motor Vehicle Fuel Consumption Standards Act in Canada [2] were implemented in 1975 and 1982, respectively, to gradually improve the fuel economy of new vehicles. To meet ever increasing fuel economy regulations, automakers must strive to improve all aspects of the vehicle relevant to performance efficiency. Significant contributors to a vehicle's fuel/energy efficiency are the vehicle's aerodynamics, powertrain performance, and overall weight. Another trend to consider is the increasing consumer demand for hybrid, electric, and other alternative energy vehicles [2]. Many government programs have been initiated in recent years to promote this transition to alternative energy vehicles, such as the use of subsidies for new vehicle purchases [3]. Like traditional internal combustion engine vehicles, many of these alternative energy automobiles also directly benefit from improved overall efficiency which could attract customers with lower costs and greater ranges.

Vehicle safety regulations have also continued to intensify in recent years, as seen by the continued increase of new safety requirements by government agencies such as the National Highway Traffic Safety Administration (NHTSA) in the United States. These safety requirements involve the development of new tests, increasing performance associated with existing test requirements, as well as additional safety features such as rear camera systems or automatic emergency braking systems [4]. In terms of crashworthiness, structural components of the vehicle must be continually improved to be stronger and safer. To stand out among the competitive consumer vehicle market, automakers have also increasingly participated in voluntary crash safety assessment standards such as the New Car Assessment Programme (NCAP) [5], that involve a wide variety of collision scenarios that demand further improvements to a vehicle's crashworthiness.

Current automotive trends therefore consist of two main objectives: (i) to develop more fuel efficient vehicles; while (ii) simultaneously increasing crash safety. One of the easiest ways to improve fuel economy is by reducing the overall weight of the vehicle. It has been shown that a 10% decrease in vehicle weight can result in up to a 8% fuel economy improvement [6]. To achieve both objectives simultaneously, automakers must follow a lightweighting strategy that either promotes greater use of lower density materials of comparable strength, or higher strength materials with similar densities, therefore reducing the total amount (mass) of required material. For sheet metal components, this is often referred to as down-gauging, which means reducing the gauge, or thickness, of the sheet material. For certain steel components such as the exterior body panels, lower density alternatives like aluminum have been increasingly used to reduce overall weight [7], [8]. However for most passenger vehicles, the primary body structure, also known as the body-in-white (BIW), offers the greatest opportunity for lightweighting [9]. The BIW contains the occupant safety cell, which is responsible for maintaining the survival space of the occupants during an impact or collision. In the past, the vehicle's BIW consisted primarily of high strength steel, which were low cost, high strength, and highly formable [9]. Nowadays, most new vehicle models have transitioned to the use of ultra high strength press-hardenable steels (PHS) or boron steels for the most safety-critical BIW components such as the A-pillars, B-pillars, roof rails, cross members and side impact members [7], [10]–[13]. Figure 1 (from [7]) depicts the BIW of a crossover sport utility vehicle, with notable PHS components labeled.



*Figure 1: Hot stamped components in the BIW of a modern crossover sport utility vehicle, figure adapted from [7]*

Commercial grades of PHS are carbon-manganese-boron low alloy steels that exhibit ultimate tensile strengths in excess of 1,500 MPa, which is much higher than that of high strength and advanced high strength steels. The commercial use of PHS was started by European automakers in the 1980s [14]. The initial challenges of using PHS were the complex manufacturing requirements and the high costs associated with processing the material [9]. However, as new coating solutions developed and manufacturers became more familiar with the processing parameters, the use of PHS is now widespread among all automakers. In order to achieve the desired high strength while still allowing adequate formability to produce complex geometries, PHS requires a unique processing procedure. Unlike traditional steel sheet materials that are cold formed (formed at room temperatures), PHS is formed by a process generally referred to as hot stamping or press-hardening. In the following review, conventional hot stamping processes are described, followed by an introduction to new or improved grades of PHS. Afterwards, the behaviour of PHS materials, both during and after the hot stamping forming process is discussed. To quantify and evaluate the performance of PHS materials, experimental techniques to determine the behaviour of hot stamped materials are introduced. Finally, numerical models which enable virtual predictions of hot stamping processes and hot stamped components are presented.



## 1.1. Hot Stamping Processes

Hot stamping describes the manufacturing process required to produce an ultra-high strength PHS component from a flat blank. Most commercial PHS arrive at the component manufacturer as ductile, 600 MPa tensile strength material consisting of a mixed pearlite-ferrite microstructure. After shearing the sheet to the desired blank dimension, the blank is heated in a furnace to around 900°C, transforming the as-received pearlite-ferrite microstructure entirely to austenite. The blank is then removed from the oven and immediately placed in a press where it is simultaneously formed and rapidly cooled to obtain the final geometry with a fully martensitic microstructure with strengths exceeding 1,500 MPa. Surface treatment and laser trimming may be performed on the final component as needed; however, those additional operations are not exclusive to hot stamping. Two processes for hot stamping are often cited in literature. Direct hot stamping is the production of a fully-formed component from an austenitized flat blank, where the entire forming process occurs after blank removal from the oven [14]. Figure 2 shows a schematic of a direct hot stamping process from steel coil to final component.

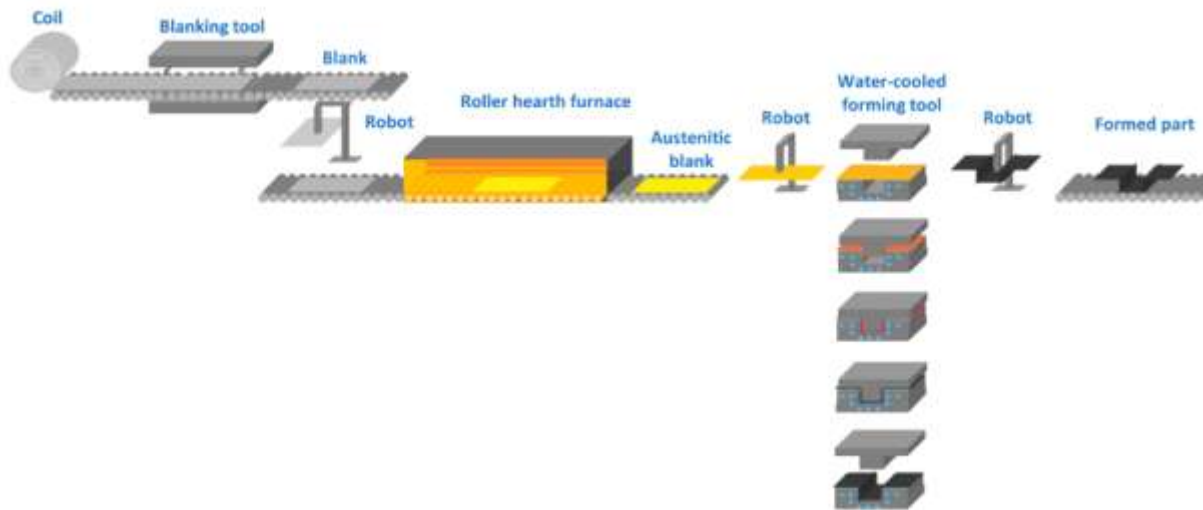


Figure 2: Direct hot stamping process, adapted from [9]

Indirect hot stamping involves a cold forming procedure prior to austenitization that partially or fully forms the final geometry. The pre-formed part then undergoes the standard hot stamping process to arrive at the final shape and/or final strength [14]. Figure 3 shows a schematic of the indirect hot stamping process.

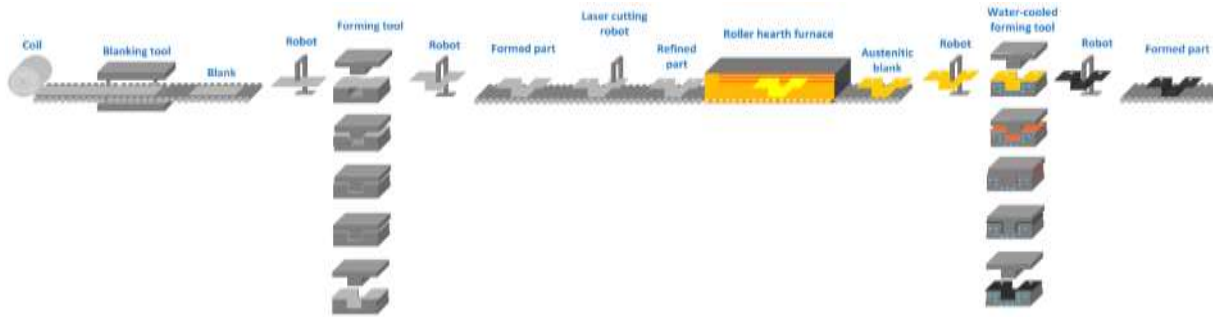


Figure 3: Indirect hot stamping process, adapted from [9]

Other methods exist to process PHS materials, depending on the needs of the specific geometry or other limiting constraints. Hot blow forming is a similar technique to direct hot stamping for producing tubular geometries such as the A-pillar on certain vehicles [12]. Hot blow forming involves pressurizing round tubes that have been austenitized, and then are gas formed to the desired final geometry. The tube is then quenched in combination with liquid as well as the tool surface to achieve a fully martensitic microstructure [15].

For certain components, in specific regions or locations, it may be desirable to achieve greater ductility than what a fully martensitic microstructure would allow. Therefore, as hot stamping technologies matured, various processing techniques were developed to allow for tailoring of material properties. Tailored heating was the one of the first strategies to vary material properties across a singular component. Tailored heating involves selectively heating a part of the blank to the austenite formation temperature ( $A_{c3}$ ), such that when quenched, only the austenitized region of the component is fully-martensitic [16]. The part of the blank that remained below the  $A_{c3}$  temperature therefore remains ductile with the original ferrite-pearlite microstructure. In contrast, tailor quenching involves cooling regions of the part at different cooling rates to achieve a mixed final microstructure [9]. By changing the cooling rate (such as by utilizing heated dies), regions that experienced rapid cooling will be fully martensitic while regions that were cooled at a lower rate might consist of a microstructure containing a mixture of ferrite, pearlite, bainite, or martensite. This mixed-microstructure region would in turn have a mixture of properties that could be optimized to obtain the desired strength, ductility, toughness, *etc.* Another tailoring strategy is the use of tailor-welded blanks, which involve laser welding two (or more) sheets with varying thicknesses or material chemistry prior to

hot stamping [16]. After a standard hot stamping cycle, the different regions of the blank would result in different properties. For example, regions with a higher thickness would be stronger or stiffer than thinner regions, saving manufacturers from needing to otherwise join two separate parts together. Other tailoring techniques include patchwork blanks, which increases blank thickness at desired locations, as well as tempering or tailored tempering strategies to selectively enhance the ductility of the hot stamped components [9].

After hot stamping, parts can be further heat treated such as by tempering at low temperatures to increase the ductility of the component, depending on the specific application. If a component is intended to be painted, then a typical automotive paint baking process may be applied to the PHS part to cure the applied paint. Typical paint baking processes occur between 150-190°C for up to 60 minutes, which results in a bake hardening effect on the PHS [17]. Depending on the strength (and carbon content) of the PHS subjected to paint baking, Järvinen *et al.* [17] have reported that the bake hardening process can decrease tensile strength by up to 160 MPa, while increasing total elongation.

## **1.2. Hot Stamping Materials**

The most common grade of commercial hot stamping material is known generically as “22MnB5”, corresponding to its main chemical constituents of approximately 0.22% Carbon, and 0.005% Boron (weight percentages). Nowadays, the exact chemical composition for 22MnB5 is dependent on the manufacturer, with carbon content varying from 0.20% - 0.28%, boron from 0.001% - 0.005%, and various ranges for other alloying elements [9]. Other notable alloying elements include manganese, silicon, chromium, and titanium. The addition of boron in PHS significantly improves the hardenability of the material by slowing ferrite and pearlite transformation during quenching, which better enable a fully martensite transformation [14]. Delaying formation of ferrite and pearlite crucial for hot stamping since it enables the forming process to occur without compromising the final martensite content. Carbon and manganese also contribute to the hardenability of the material, however the tensile strength is mostly related to the carbon content [9]. 22MnB5 will be referred to as PHS 1500 in this document, a general naming

convention which signifies that it is a press-hardenable steel exhibiting a tensile strength of approximately 1,500 MPa in its fully martensitic state.

Originally, PHS materials were produced without a protective coating. Due to the high temperature nature of the hot stamping process, these uncoated blanks were highly susceptible to oxidation and surface decarburization when heated during austenitization. The issue of surface oxidation made hot stamping relatively cost prohibitive due to the need for descaling (such as sand or shot blasting) after forming. The hard oxide scales also increased die wear (further increasing costs), and also led to unpredictable thermal contact conditions resulting in inconsistent cooling rates and the formation unwanted formation of softer bainite or ferrite phases [9]. In the early 2000s, aluminum-silicon (Al-Si) coated PHS 1500 were commercially introduced to automotive manufacturers [9]. The introduction of these high-temperature resistant coatings eliminated fundamental issues such as oxidation of the blank during heating and the requirement of post-forming descaling operations. The Al-Si coating used for PHS is known as a type 1 coating, which is applied by hot dipping and consists of approximately 89% Aluminum and 11% Silicon (by weight) [18]. Al-Si coatings are typically quantified in terms of total coating weight (for both sides of the blank) per unit surface area 80-150 g/m<sup>2</sup>. A coating weight of 80 g/m<sup>2</sup> corresponds to a thickness of approximately 10-15 μm thick (per side), while a coating weight of 150 g/m<sup>2</sup> typically results in a coating thickness of approximately 20-30 μm [19]. The Al-Si coating is capable of acting as a protective barrier in oxidizing environments up to 1100° C, well beyond the typical hot stamping furnace temperatures of around 900°C. The addition of silicon to the coating is necessary to enhance the ductility which is essential during forming to ensure continued adhesion to the material substrate [18]. After the hot dipping process, the Al-Si coating melts when heated above approximately 600°C before re-solidifying, as Fe from the base steel diffuses into the coating [19]. Multiple layers of different Al-Si-Fe intermetallic compounds are formed due to the diffusion between the coating and substrate [19]. These new Al-Si-Fe intermetallic compounds are what protects the steel substrate for the remainder of the hot stamping process. In addition to the intermetallic layers, a thin protective aluminum oxide layer has also been observed at the surface of the coating [20].

An alternative to Al-Si coating is galvanized PHS, which contains a primarily zinc (Zn) based coating. Unlike the Al-Si coating, the zinc coating acts as the sacrificial anode to the steel (iron) substrate, offering cathodic protection to the steel [16]. Zinc coated high strength steels are commonly used for traditional cold-stamping applications due its superior corrosion resistance [9]. Zinc coatings are also commonly applied via hot dipping (galvanizing), a process in which the steel sheet is moved (dipped) through a molten pot of zinc during the sheet fabrication process. During this galvanizing process, Fe-Zn intermetallic compounds develop between the zinc coating and the steel substrate [9]. The primary issue with zinc coatings for PHS is the relatively low melting point of the zinc, which leads the coating to melt and liquify at the temperatures required to completely austenitize the PHS blank prior to forming. During the forming operation of the PHS, this liquid zinc may leach into microcracks in the steel (which are produced by the deformation of the sheet), resulting in liquid metal induced embrittlement (LMIE) that significantly decreases the ductility of the material during forming [21]. To avoid LMIE, the PHS blank needs to be cooled prior to the stamping operation such that the zinc coating re-solidifies prior to the development of any microcracks, however forming at lower temperatures significantly reduces the formability of the PHS [9]. Alternatively, indirect hot-stamping processes can be employed to minimize the amount of deformation at elevated temperatures when the coating is liquid [21]. The low melting point of the zinc coating is also an issue after the hot stamping process. For chassis applications where a significant amount of welding is required for assembly, the extreme heat of the welding operation(s) would evaporate the zinc coating near the welded areas [9]. Other solutions to LMIE and the low melting point of the zinc coating include adding alloying elements to increase the melting temperature of the coating. Kondratiuk *et al.* [22] applied a Zn-Ni coating to PHS and observed the development of a stronger protective oxide layer and Zn-Ni-Fe intermetallic phases with higher melting points than typical Zn-Fe phases, however the formability of this Zn-Ni coating has yet to be evaluated. Nevertheless, although zinc coatings offer greater corrosion resistance over the lifecycle of a stamped component, Al-Si coatings are the more versatile and more commonly used option for the hot stamping process.

Despite the wide usage and popularity of PHS 1500 materials, many researchers are actively developing new grades of PHS that address existing issues or offer more desirable properties. Kurz *et al.* [23] studied the properties of a modified zinc coated PHS 1500 with added manganese to increase hardenability to enable hot stamping at lower temperatures. Lu *et al.* [24] investigated the properties of an uncoated PHS 1500 with greater additions of chromium and silicon to provide high temperature oxidation resistance without the use of a protective coating. Grades of PHS have also been developed for hot stamped components that may be subjected to high levels of deformation in energy-absorbing applications. Lower strength materials, such as Ductibor 500 developed by ArcelorMittal, offer greatly improved energy absorption performance compared to PHS 1500 even after undergoing a hot stamping process [25]. The high energy absorption performance of Ductibor 500 compared to PHS 1500 is due to the high ductility of the material after hot stamping, which is a result of a final microstructure consisting of a significant fraction of soft ferrite phases combined with a small amount of martensite. This mixed-phase microstructure is achieved by having a lower carbon content and negligible boron, which significantly reduces the hardenability of Ductibor 500, resulting in a high critical cooling rate that is typically not achievable by common die quenching capabilities. Samadian *et al.* [26] demonstrated that the final microstructure of Ductibor 500 remains primarily (>50%) ferrite even after die quenching. A common method of applying Ductibor 500 (or similar ductile press-hardenable steels) is using the material in combination with PHS 1500 (or similar high strength PHS grades) in the form of tailor welded blanks (TWB) [25] [9]. TWBs allow the manufacture of hot stamped components that are highly ductile in desired regions of a component and extremely high strength elsewhere. Applications for TWB components can be currently found in B-pillars or crash rails, where a high-strength main structure is required to prevent unwanted deformation, and a small ductile region is preferred that allows for greater overall energy absorption that would not otherwise be possible with a fully PHS 1500 design. Múnera *et al.* [27] demonstrated the potential of up to 40% in weight savings with no loss of crash performance by substituting traditional lower strength cold-stamped front and rear crash rails with tailor welded PHS 1500 and Ductibor 500 components. Another recent PHS grade is Ductibor 1000® which has a strength in excess of 1,000 MPa. The fracture resistance of this alloy

has been characterized by Samadian *et al.* [28] and application of this grade within a prototype frontal crush tip was demonstrated by Lee *et al.* [29].

Another recent development of hot stamping materials is the development and introduction of PHS 1800, with an ultimate tensile strength of approximately 1800 MPa after quenching. This grade of PHS is clearly desirable as its high strength enables further lightweighting of components. PHS 1800, also designated as 37MnB5 (or 38MnB5 by some researchers), features an increased carbon content of up to 0.38% (by weight) [9]. The additional carbon contributes to an increase in the hardenability and an increase in the tensile strength (and hardness) of the fully martensitic material after hardening. Despite the similar 'B5' naming convention to 22MnB5, 37MnB5 or 38MnB5 typically require much less boron (as well as less manganese) than 22MnB5 to provide adequate hardenability due to the increased carbon content. In order to understand the applicability of these higher strength PHS grades, it is necessary to first determine the constitutive behaviour of the material under hot stamping conditions; such PHS1800 constitutive properties are the primary focus of the current thesis.

### **1.3. Experimental Techniques for Constitutive Testing**

Constitutive testing refers to experimental techniques that determine the stress-strain response of a material as a function of factors such as strain rate and temperature, for example. A constitutive model refers to a mathematical model that captures the response of the material under certain loading and/or deformation conditions. Constitutive models may relate the applied forces (or stress) to the resulting deformation (or strains) and may include other relevant parameters that affect the stress-strain relationship. Typically, constitutive models are only derived after experimentation on the material under specific test conditions.

Many experimental tests have been derived to study the hardening response of steel sheet materials. Possibly the most popular and well-known test is the uniaxial tension (tensile) test. The tensile test is conducted by deforming the specimen uniaxially along the specimen longitudinal axis [30]. By recording the required force to deform the specimen and the amount of deformation, the material's uniaxial

engineering stress-strain curve can be determined. The results from this test are most commonly used to derive the material's elastic modulus, yield strength, ultimate tensile strength, and ductility, just to list a few. Tensile tests with specimens cut in various orientations can also be used to determine anisotropic behaviour of a material. Figure 4 depicts a generic engineering stress-engineering strain curve that can be derived from a uniaxial tensile test. Notable points include the yield point, when plastic deformation begins; the ultimate stress point, which is often indicative as the end of uniform elongation and therefore the end of the uniaxial stress state.

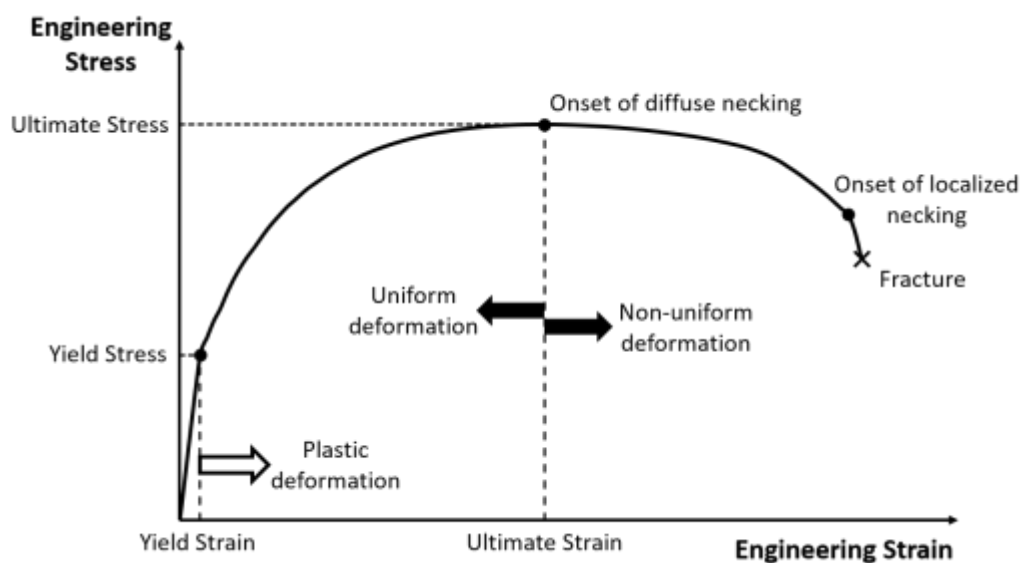


Figure 4: Schematic engineering stress-strain curve obtained from a uniaxial tensile test, with notable points and deformation stages listed

The objective of tensile testing is to obtain the stress-strain curve, also known as the flow curve, of the material under uniaxial tensile conditions. The flow curve in the context of constitutive modelling describes the stress response of the material during plastic deformation, which is relevant for many manufacturing and other high deformation scenarios. For finite element analysis, the material flow curve is a critical input that enables prediction of a component's non-linear behaviour under plastic deformation.

Tensile specimen designs can vary depending on the shape or application of the material. For example, large billets or round extrusions may be best and most easily represented by round axisymmetric specimens whereas sheet or plate materials would be best maintained in its current form as flat specimens. In addition to the specimen design, many test parameters can also be modified based the application of the test. Loading



of the specimen can be force or displacement driven and can be constant or variable (increasing or decreasing). The rate of loading (deformation) can also be varied to better represent the anticipated requirements of the material. For example, quasi-static material properties may be irrelevant to high strain rate loading applications, such as ballistic or vehicle crash situations. Several international and industry-specific standards exist for tensile tests, the use of which varies by industry or geography depending on customer and relevant regulatory requirements. Standards that cover tensile testing of metallic materials include ASTM (formerly American Society for Testing and Materials) E8/E8M, ISO (International Organization for Standardization) 6892-1, JIS (Japanese Industrial Standards) Z 2241, among others.

Many other material characterization tests exist to identify and describe the deformation behaviour of materials. Compression tests have been used extensively for forging applications where compression loading is more relevant to the typical deformation processes than tension [30]. Compression tests have also been used as an alternative to tensile tests to achieve higher strains without necking, or when complexities of tensile testing negatively affect the results [31], [32]. Material characterization tests can also be conducted to target specific manufacturing issues. For sheet metal forming, springback tests are highly relevant to deformed components where significant elastic strain recovery results in springback concerns [30]. In regard to formability, many representative forming, drawing, or stretching experiments can be conducted to determine the forming limits of the material. Experiments such as the Marciniak or Nakajima tests deform sheet specimens under different strain conditions to enable the determination of forming limit curves at different strain states [33]. However, prior to any of these more sophisticated experiments, the fundamental plastic behaviour of the material should be understood via tensile testing.

For hot stamping, the temperature of the material has a significant effect on the material behaviour. For most metals, elevated temperatures typically result in thermal softening, which is seen as reduced flow stresses [34]. Specifically, for PHS, the temperature history after austenitization substantially influences the evolution of the material microstructure. Since different microstructures have different hardening responses, the microstructure composition at any given time will result in a unique mechanical response. In order to capture and quantify these thermal and microstructural effects, material testing of PHS must be

able to accurately represent the thermal history experienced by the material in a typical hot stamping process. It should be noted that standards for elevated temperature testing are not yet well established. Due to the high variability in the type of materials, applications, and testing apparatuses, novel testing techniques are constantly being developed to satisfy new material/process requirements.

### **1.3.1. Elevated Temperature Constitutive Testing**

Several experimental techniques have been established for testing materials at elevated temperature using a range of devices. For tensile tests, the main challenge revolves around achieving and maintaining the desired test temperature in a precise manner. The mechanical needs of the device remain similar to that of standard room temperature tensile tests, with the exception that the test frame must withstand the elevated test temperatures for prolonged periods of time. The thermal needs can typically be achieved by one of three common approaches to heating and maintaining the temperature of tensile specimens, by means of (primarily) convective heating, induction heating, or resistive heating. For (primarily) convective heated specimens, some sort of a heated and insulated environmental chamber (akin to an oven, or furnace) is used to encompass the specimen during testing. The heating source for this setup typically comes from heating elements within the chamber similar to that of a conventional oven, with the mechanism of heat transfer being primarily convection, although radiation and conduction (from the grips) may also contribute. Potential downsides of this approach include relatively slow and inconsistent heating rates, the need for preheating, greater emphasis on operator safety, and the necessity for heat-resistant extensometers and grips. The slow heating rate and lack of precise temperature control also makes this testing approaching incompatible for materials that follow rapidly changing temperature histories (as in hot stamping processes). Additionally, unless the test frame was specially designed for high temperature applications, most tensile frames cannot be easily converted to allow for this setup.

An alternative approach that allows for rapid heating of specimens and precise temperature control is through the use of induction heating [23]. This heating technique is commonly found in industrial heat treating operations, but has also been applied extensively for a variety of research projects, such as formability testing, tribology studies, and phase change experiments [30], [35]–[38]. When coupled with

compressed air or liquid quenching, rapid cooling can be achieved with an induction heating setup. However, induction heating setups are less commonly used for tensile testing and are more commonly seen for dilatometry or phase transformation experiments, as seen in phase change experiments on PHS 1500 conducted by Bariani *et al.* [35], Ghiotti *et al.* [37], and Nikravesh *et al.* [38].

The final commonly used method for rapid heating of specimens is by means of resistive heating. Resistive heating is accomplished by completing an electrical circuit with the specimen as the resistor, and then applying a current through the circuit to generate heat within the specimen. This type of heating is typically only accomplished by specialized devices and only electrically conductive (with electrical resistance) materials can be heated using this method. Like inductive heating, compressed air or liquid quenching can be utilized to achieve rapid cooling rates following heating. The disadvantage of both inductive and resistive heating is that unless perfect insulation is achieved at the grips, only the location with the control thermocouple will be at the target temperature. This non-uniform temperature distribution results since conduction into the unheated grips holding the specimen will draw heat away from the centre of the specimen, resulting in a parabolic temperature distribution along the length of the specimen [39]. Of course, it is possible to heat specimens with any combination of the aforementioned methods, however such an accommodating device would likely be overly sophisticated and expensive due to the redundant features.

The primary requirement for accurate and representative constitutive characterization of PHS is the need to follow a similar thermal history to that of industrial hot stamping processes. As previously mentioned, a PHS blank will typically undergo a heating stage from room temperature to the austenitization temperature. After heating, the blank is held at temperature (also known as the soaking stage) in the furnace as temperatures stabilize and austenite forms and the Al-Si coating alloys with the Fe substrate. Following austenitization, the blank is then removed from the oven and air cooled during transfer, before being simultaneously deformed and quenched in the forming press. Specifically, precise temperature control is needed to control the temperature at which the tensile test is to be conducted, while consistent and rapid cooling is required to simulate the quenching stage after austenitization. Figure 5 shows a generic hot

stamping thermal cycle in the form of a temperature-time plot that needs to be simulated prior to tensile testing.

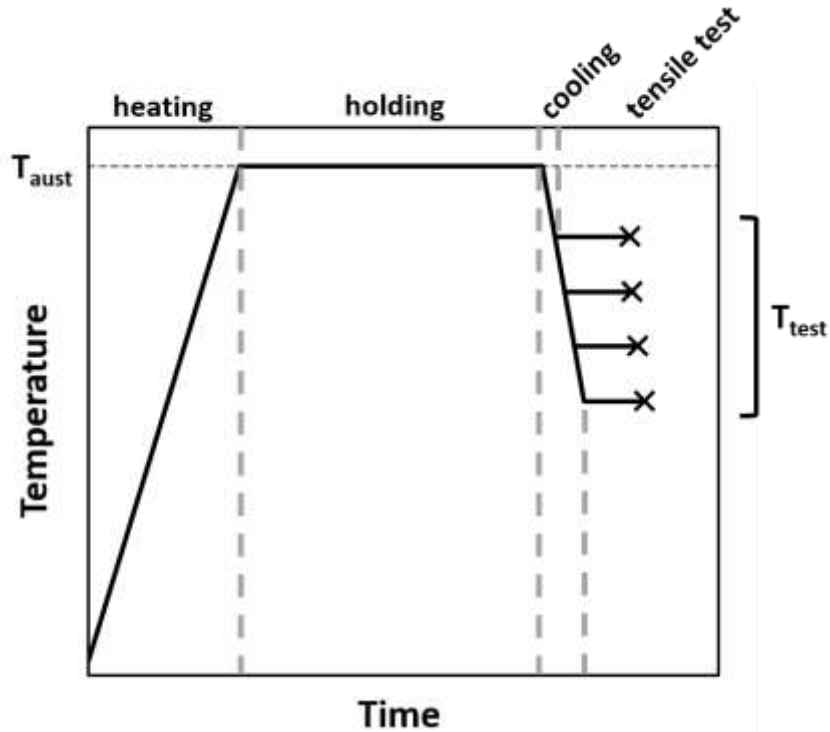


Figure 5: Generic temperature-time profile of a representative hot stamping thermal cycle for constitutive testing of PHS materials

The most common device used for testing of PHS at elevated temperatures is the Gleeble thermo-mechanical simulator (Gleeble) by Dynamic Systems [32], [34], [40]–[45]. The Gleeble is a universal testing device that utilizes resistive heating to rapidly heat specimens and compressed air (or other gases) or water for rapid cooling. The mechanical system allows for deformation rates between 0.001 mm/s – 1000 mm/s within a maximum stroke displacement of 100 mm [46]. The thermal system is capable of precise temperature control and maintaining steady temperatures which is essential to replicate hot stamping thermal histories. The Gleeble system can also achieve rapid cooling rates of up to 80°C/s using compressed air, as seen by cooling rates reported by Merklein and Lechler [42] for air-quenched tensile tests from 900°C. An additional feature of the Gleeble is the environmental chamber that can either provide a vacuum or be filled with inert gas to prevent high temperature oxidation or decarburization [43]. Compression, tension, and dilatometry tests are often performed on the Gleeble. To control and monitor the temperature

of the specimen, a thermocouple must be attached to the specimen prior to testing. Typically, this is accomplished by spot welding a high temperature rated K-type thermocouple to the center of the specimen. The Gleeble is also capable of recording data from additional thermocouples for measuring the temperatures elsewhere on the specimen. It should be noted that materials (such as certain aluminum alloys) with poor weldability may encounter issues with reliably attaching the thermocouple.

Several researchers have utilized Gleeble devices for constitutive testing of PHS 1500. Eriksson *et al.* [40], Naderi *et al.* [47], and Li *et al.* [32] conducted isothermal compression tests on PHS 1500 specimens with a Gleeble device to determine material properties at various temperatures and strain rates. The difficulty of compression tests stems from the fact that numerous sheets must be stacked and adhered together to create stacked compression (round cylindrical) specimens. Additionally, the friction interaction between the specimen and the anvil results in barreling of the specimen, which requires inverse finite element analysis to decouple the friction effects [36]. Figure 6 shows the barreling effect on the stress distribution for cylindrical specimens under compression, due to the impact of friction.

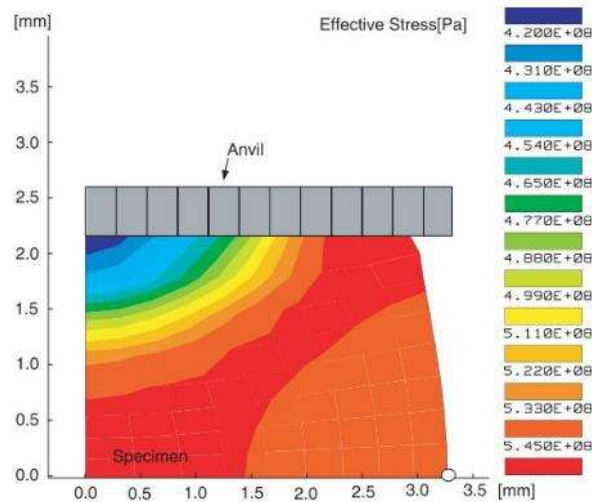


Figure 6: Stress contour of a finite element simulation of a compression test, showing a non-uniform stress field throughout the specimen, from Eriksson *et al.* [40]

Merklein and Lechler [42], and Li *et al.* [32] utilized a Gleeble 1500 to conduct isothermal tensile tests on PHS 1500 at various temperatures and strain rates. Merklein and Lechler [42] also conducted tensile tests in different material directions and showed that the austenitization step eliminated anisotropy within

the material. Li *et al.* [32] obtained flow curves for different phases of PHS 1500 by varying the thermal history prior to tensile testing. For the austenite flow curves, Li *et al.* [32] followed a hot stamping thermal cycle prior to tensile testing, and limited the tests to above 600C to prevent the formation of any ferrite, pearlite, and bainite phases. To determine the flow curves for a mixed ferrite-pearlite microstructure, Li *et al.* [32] heated as-received PHS 1500 to the desired test temperature without austenitization. Merklein and Lechler [42] used an optical measurement technique to calculate strains, however, did not go into detail as to how this was achieved. Li *et al.* [32] utilized the cross-head stroke to determine the deformation strain. Li *et al.* [34] conducted tensile tests on PHS 1500 with a Gleeble 3800. To circumvent the issue of the non-uniform temperature distribution along the gauge length, Li *et al.* [34] utilized a dilatometer placed at the centre of the specimen to measure the width strain during testing instead of using an extensometer to measure longitudinal strains. However, a geometric assumption had to be made for strain corrections when necking took place off-center, away from the dilatometer. Figure 7 shows the measurement setup used by Li *et al.* [34] to only measure the strains at the temperature controlled location on the specimen.

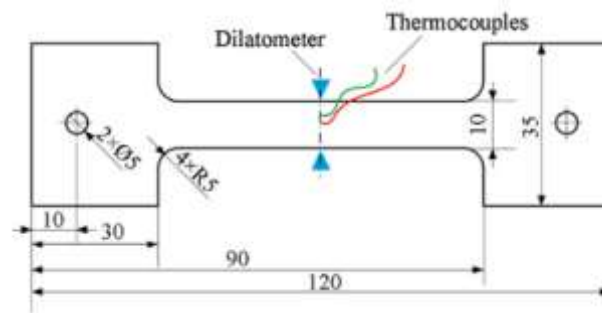


Figure 7: Use of dilatometer to measure strains from a tensile test, from Li *et al.* [34]

Li *et al.* [45] utilized digital image correlation (DIC) to measure deformation during isothermal tensile tests of PHS 1500 using a Gleeble 3500. However, to create the required speckle pattern for DIC analysis, Li *et al.* [45] debossed the surface of the specimen to create micro-cavities for paint to adhere. The debossing procedure was not observed to affect the material behavior, however, the added complexity of such a step remains undesirable. Li *et al.* [45] also devised a modified grip design that rotated the specimen orientation for DIC, and resulted in better thermal insulation (by reducing the conduction contact area) to promote greater temperature uniformity along the specimen.

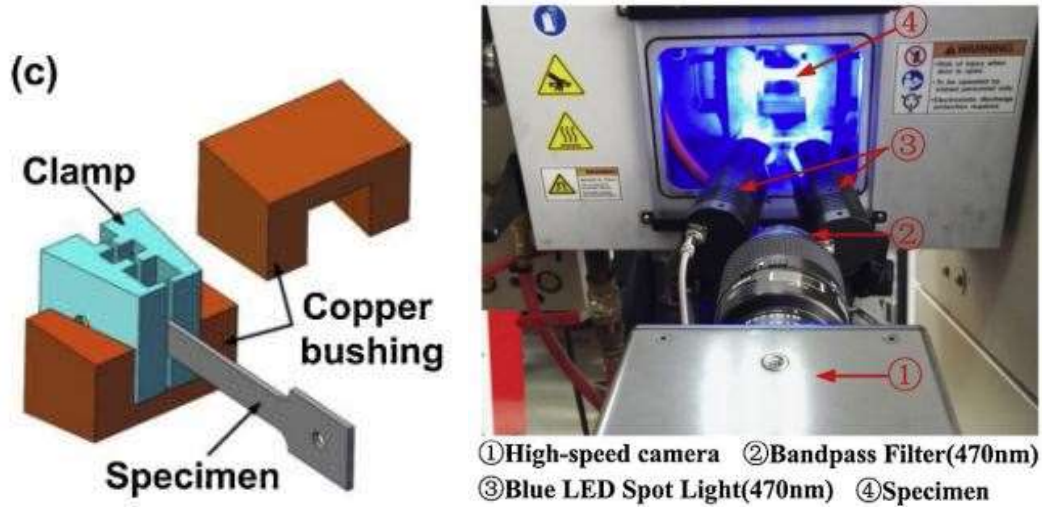


Figure 8: Modified Gleeble grips to allow for a more uniform temperature distribution and a rotated specimen orientation that allows for DIC in the Gleeble, from Li *et al.* [45]

Both Abspoel *et al.* [43] and Ganapathy *et al.* [44] used Gleeble devices to determine the flow curves of a PHS 1500 and modified the specimen geometry to reduce the temperature variation within the gauge length of the specimen during testing. Abspoel *et al.* [43] created a novel specimen design with additional shunts and connecting conductive wires to promote equal current density across the gauge and shoulder of the specimen. Ganapathy *et al.* [44] created a modified grip assembly with enhanced thermal insulation and electrical conduction to reduce thermal variation in the specimen, however encountered clearance issues when installing the complex specimen. Figure 9 shows the modified specimen geometry and insulated grips by Ganapathy *et al.* [44] as well as the improved temperature uniformity of the new specimen and grip design.

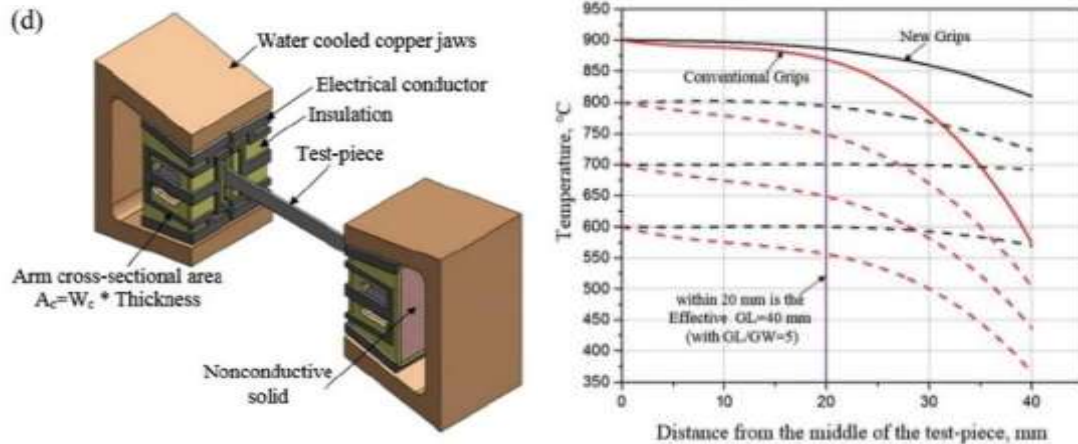


Figure 9: Modified specimen geometry and insulated grip design, and the resultant improved temperature uniformity along the specimen from Ganapathy et al. [44]

Overall, the use of Gleeble devices is highly prevalent when conducting constitutive testing of PHS 1500 during representative hot stamping conditions. A review of results from high temperature testing of PHS 1500 is discussed in Section 1.4.1.

### 1.3.2. Digital Strain Measurement Techniques

Digital image correlation (DIC) is a relatively new deformation measurement technique that is becoming widely used for both research and industry applications. The use of DIC offers many benefits over traditional technologies such as using the crosshead or extensometers to measure specimen displacement/deformation. The first benefit of DIC is that it is a non-contact measurement technique, meaning it does not require the measurement device to physically adhere to or grip the specimen of interest [48]. Secondly, DIC allows for collecting and visualization of full-field deformation data, compared to traditional extensometers which typically only records displacement between two points. Full-field deformation data allows for the computation of full-field (surface) strains experienced by the specimen during loading, enabling the development of advanced analytical techniques and allowing for full-field validation of numerical predictions [49]. For example, for tensile tests, accurate strains can be computed up to the onset of fracture rather than just to the onset of diffuse necking [50]. With the use of DIC, an initial uniform deformation length (typically assumed to be the gauge length) of tensile specimens no longer needs to be assumed, since one can precisely determine the region of uniform deformation at any given



time. Because of these advanced capabilities, many new experimental parameters can now be directly identified, such the local strain fields around geometric changes, local strain rates, local strain paths, instantaneous geometry measurements during testing, *etc.*, DIC is already extensively used in research for various reasons, such as to identify material properties (thermal expansion coefficients and Young's modulus) by Grant *et al.* [51], evaluation of sheet metal formability by Bariani *et al.* [35], strain distributions around notched specimens by Yoneyama *et al.* [52] and constitutive characterization of PHS 1500 by Li *et al.* [45].

The most basic form of DIC is 2D correlation for plane strain measurements (also known as 2D DIC), using images taken from a single camera oriented perpendicular to the surface of interest. This technique allows for non-intrusive, full-field displacement measurements of the surface. However, due to the lack of depth perception only planar displacements and strains can be accurately calculated, resulting in increasing error when out-of-plane motion and deformation occur. A speckle pattern is required on the surface of interest to identify and track deformation of the surface throughout the test. A high contrast pattern is required because the speckling pattern is identified by the DIC algorithm based on the grey level of each individual pixel. To start, a DIC algorithm divides the entire area of interest into numerous pattern subsets, or small regions that contain distinct patterns that are uniquely identifiable based on the grey level distribution within the subset. As the surface of a specimen is deformed or translated, which in turn deforms or translates the speckle pattern, the new location of the subset is matched to the original based a correlation of the grey level of all pixels in the image [49]. Figure 10 shows a visualization of the basic principle of digital image correlation, highlighting the need for a speckle pattern and subset tracking of the speckles.

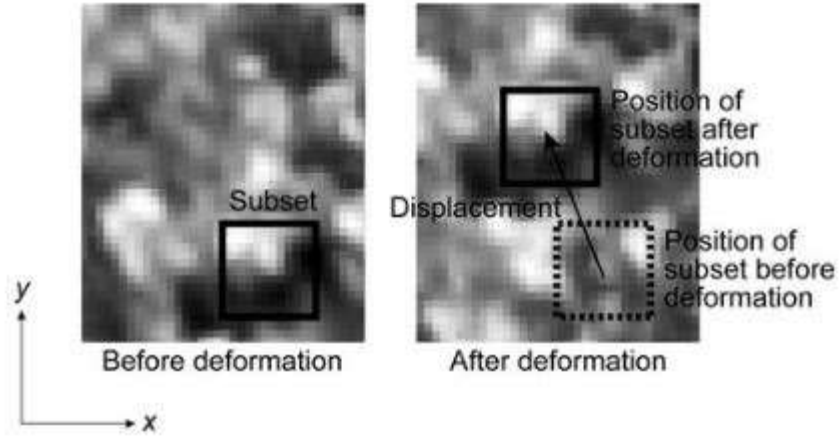


Figure 10: Principle of digital image correlation, as shown by tracking pixel groups before and after deformation [52]

By tracking the positional and shape changes in each subset from its original location and orientation, the deformation of the speckled surface can be identified by iteratively solving for the potential displacements and displacement gradients that would result in the change in the subset [52]. Using the gray level values to represent the speckle pattern, a correlation function that relates the initial and the deformed subset can be defined based on the original location of the subset, as well as the displacement. This correlation function, also known as the correlation coefficient, is shown by Equation (1), where  $F$  is the grey level of a pixel of the initial pattern,  $G$  is the grey level of a pixel in the deformed pattern,  $x$  and  $y$  are the pixel coordinates, and  $\mathbf{u}$  is the displacement gradient vector [52].

$$C(x, y, \mathbf{u}) = \frac{\sum F(x, y)G(x, y, \mathbf{u})}{\sqrt{\sum F(x, y)^2 \sum G(x, y, \mathbf{u})^2}} \quad (1)$$

By maximizing the correlation function with an optimization scheme, the best possible match of an initial subset pattern to the deformed subset pattern is solved, thus identifying the displacements that occurred to the pattern between the two images. Once deformations are computed for each subset within the entire of interest, strains can be derived by differentiating the displacements following using Equations (2) – (4).

$$\varepsilon_x = \frac{\partial u_x}{\partial x} \quad (2)$$

$$\varepsilon_y = \frac{\partial u_y}{\partial y} \quad (3)$$

$$\gamma_{xy} = \frac{\partial u_y}{\partial x} + \frac{\partial u_x}{\partial y} \quad (4)$$

Once the surface strain components are determined, additional post processing calculations may be performed to obtain principal strains, the average strain within a region or strain values along a path. If the time between images is recorded, then the deformation rate or strain rate can also be calculated by accounting for the change strain between each image (time step). Figure 11 below shows a sample test image obtained with a 3D DIC system and the corresponding strain contour results after DIC processing.

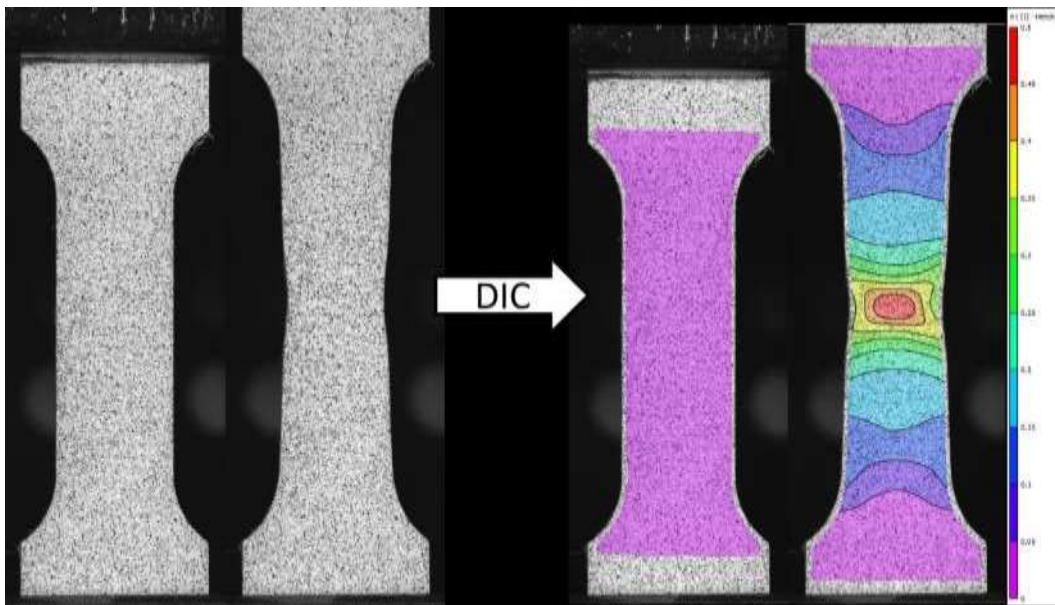


Figure 11: Unprocessed images of a specimen with a speckle pattern (left) and the surface principal logarithmic strain results after DIC processing (right)

Although 2D DIC offers much more insight compared to traditional physical strain measurement devices, its uses are quite limited when test surfaces experience out-of-plane deformation or motion. Even for a simple tensile test, excessive thinning experienced by planar specimens during plastic deformation

could result in large errors when processed by a 2D DIC system. In cases where non-planar deformation occurs, three dimensional (stereoscopic or 3D) DIC analysis has been developed to enable the capture of out-of-plane displacements. By simultaneously capturing two images of the surface of interest from two different perspectives, depth perception of the speckle pattern can be established based on trigonometric relations if the camera locations are known [53]. To allow for the determination of the three-dimensional location of the speckle pattern, the perspectives of both cameras must first be calibrated to a known pattern with fixed distances between select points (also known as a calibration grid or pattern) [54]. Prior to DIC analysis, a set of pictures of the calibration target must be obtained in various orientations from both cameras. The camera setup (distance to target, angle from target, lens length) for both calibration and test images must be identical for the calibration images to remain relevant [54]. Once the calibrated pattern has been linked to the images captured by both cameras, the surface displacements and strains can be obtained in a similar manner to that of 2D DIC analysis, where Equation (1) is expanded to include the z-coordinates (and z-displacements) and must now be solved for both set of images simultaneously. Figure 12 shows a basic schematic for how images from two cameras are correlated to a known grid for a 3D DIC acquisition setup.

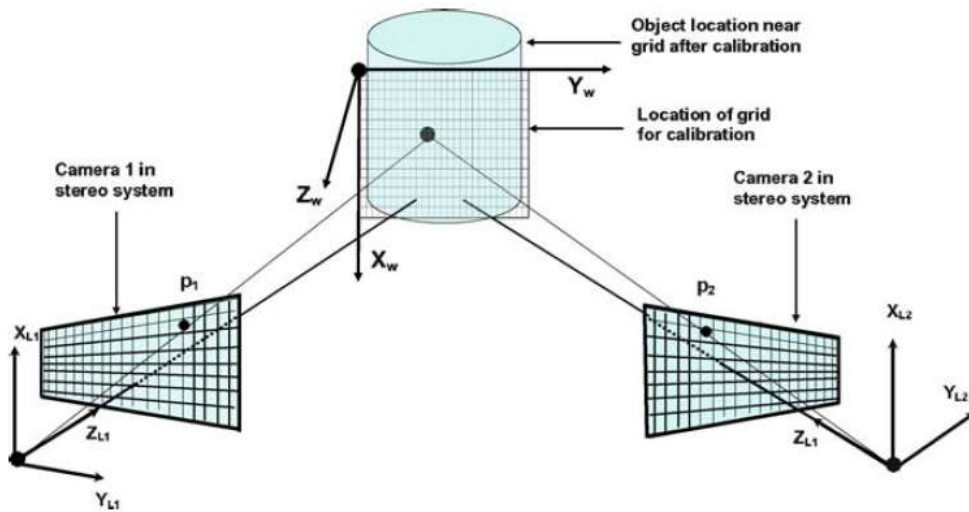


Figure 12: Schematic basic 3D DIC camera setup, showing how coordinate locations are identified in reference to a known pattern (grid for calibration), from Sutton et al. [49]

As previously mentioned, a good pattern is crucial to the correlation measurement accuracy. The texture and size of the speckle pattern is entirely dependent on the size of the area of interest, as well as the camera lens and resolution [55]. No standard speckle size exists that works for all situations; however, a similar speckling process is followed for creating the speckle pattern. To speckle, the process typically begins with the application of a basecoat on the surface that contrasts the color of the speckles, this is typically done with a paint roller or spray paint. Once the basecoat has set, common methods to create a speckle pattern include using rollers to apply patterned ink, lightly spray painting directly or with a stencil (with non-uniform paint droplets being ideal speckle dots), or dotting the surface with markers [56].

### **1.3.3. High Temperature Digital Image Correlation**

Many DIC image acquisition and processing procedures have already been established for common room-temperature experiments, with multiple examples documented by Sutton *et al.* [49]. However, procedures to perform high temperature DIC are still being actively investigated due to the numerous issues of obtaining high quality optical images of speckle patterns at elevated temperatures.

Numerous researches have observed that above 600°C, thermal radiation from heated specimens results in significant overexposure of the acquired images [51], [57], [58]. The effect of this overexposure can be seen in Figure 13, where Figure 13(a) is an image of the specimen taken at room temperature and Figure 13(b) is the same specimen at approximately 700°C. Note, the lens aperture and camera shutter speed (exposure time) are identical for both photos.

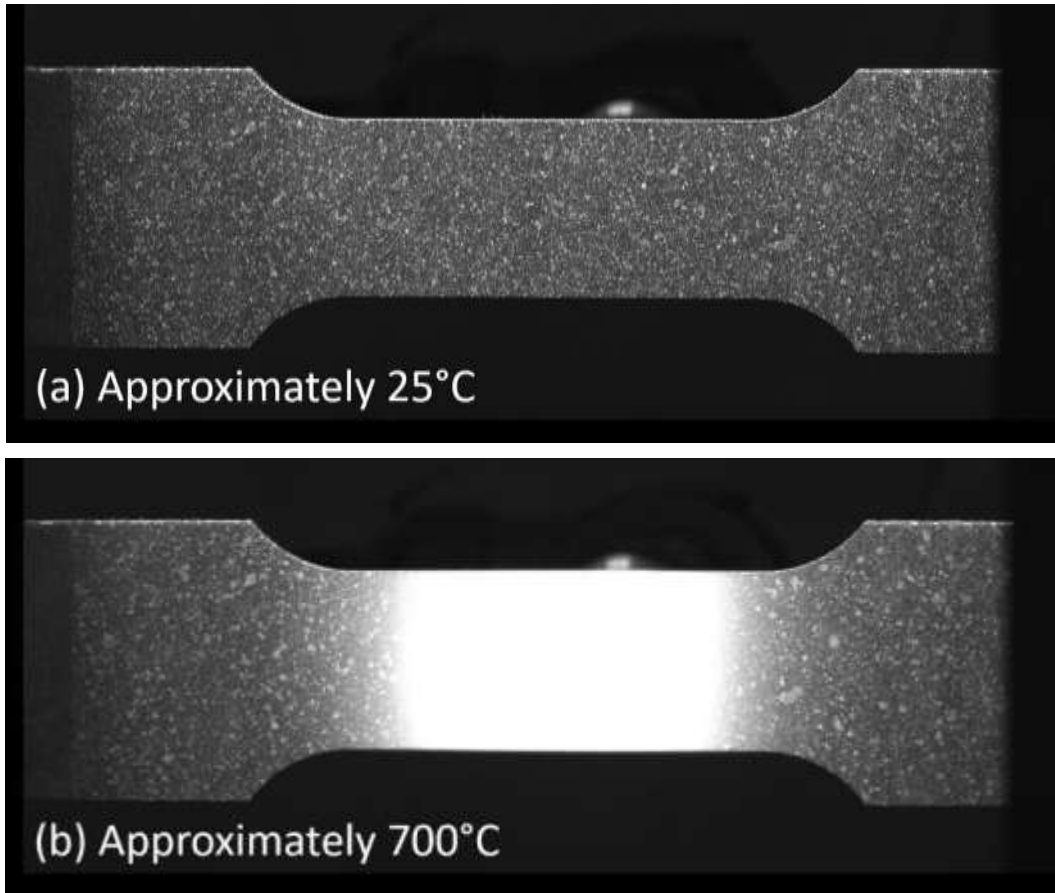


Figure 13: Visual effect of thermal radiation on a speckled specimen when heated from (a) room temperature to (b) approximately 700°C

The reason for the overexposure is due the significant increase in the emission of thermal radiation, in the form of electromagnetic waves, including visible light, with increasing temperature [57]. Many researchers have successfully remedied the issue of overexposure up to temperatures of 2000°C by using bandpass camera filters to reduce the amount of excessive light captured by the camera sensors [59]. Optical bandpass filters are filters are mounted in front of cameras which only allows a certain wavelength range of light to pass through. Since the intensity of shorter waves are lesser than longer waves at any given temperature [57], most researchers have utilized shorter wavelength bandpass filters such as blue (450 nm – 470 nm) or ultraviolet (UV) filters to conduct high temperature DIC. For the reader’s reference, UV waves are shorter than visible light, and the visible light spectrum spans from purple-blue (shorter wavelength) to yellow-red (longer wavelength). Chen *et al.* [53], Grant *et al.* [51], Novak and Zok [60], Pan *et al.* [57], and Wang *et al.* [59] all utilized blue bandpass filters (ranging between 425 nm – 475 nm) to conduct DIC with

on a variety of materials and tests at elevated temperatures ranging from 800°C – 2000°C. Berke and Lambros [58] obtained good DIC results up to 1100°C using UV bandpass filters, and also evaluated the feasibility of using blue bandpass filters.

Often for room temperature tensile tests, additional light should be introduced to allow for better or more evenly illuminated (and typically better quality) images and faster image acquisition rates. Since the use of bandpass filters limit the transmission of light from non-allowable wavelengths, supplemental light should be provided in the permitted wavelength range. It is of course possible to use standard white light (or other broad wavelength) LEDs, however most of the light would be filtered out by the bandpass filters. A literature review of high temperature DIC experiments revealed that most researchers used lights of similar wavelength to the bandpass filter. Chen *et al.* [53], Pan *et al.* [57], Grant *et al.* [51], Wang *et al.* [59], Berke and Lambros [58] and Y. Li *et al.* [45] all used blue (approximately 450 nm) LED lights for additional lighting when using blue bandpass filters. Pan *et al.* [57] and Chen *et al.* [53] used green lights along with green (approximately 550 nm) bandpass filters while Berke and Lambros [58] used UV lights with UV-range bandpass filters for additional light. Figure 14 shows images taken by Berke and Lambros [58] of a speckled nickel superalloy beyond 600°C using UV bandpass filters, showing no significant change in light saturation over a wide range of temperatures.

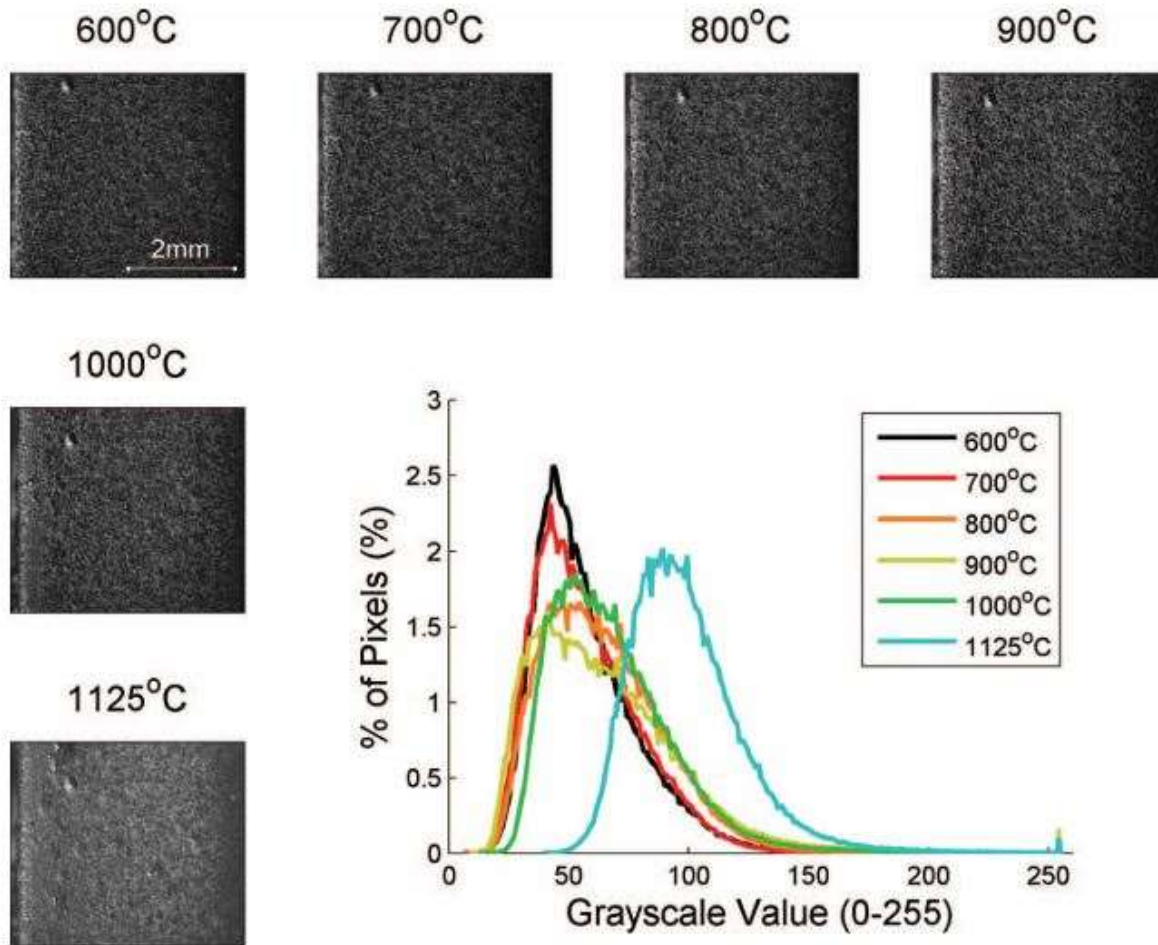


Figure 14: Sample images obtained between 600°C-1125°C using a UV bandpass filter, and the corresponding grey value histograms for each image from Berke and Lambros [58]

Heat haze has been observed when specimens are heated to extreme temperatures [51]. Heat haze occurs when interaction between a hot surface and the air around it creates thermal air currents, resulting in optical distortions in the acquired images. When capturing images of the specimen, this can eventually lead to excess noise in the deformation measurements and the calculated strains. Novak and Zok [60] showed that there was a greater artificial spread in the nodal displacement measurements taken at 800°C compared to room temperature measurements due to heat haze. Once the images were processed, this resulted in greater noise for the calculated strains. However, it was noted that the accuracy of the image and speckle correlations were unaffected, only the spread of the results increased. To mitigate the effect of the heat haze, Novak and Zok [60] recommended the use of an “air knife”, a constant stream of air blowing



across the speckled surface, to reduce the thermal turbulence at the surface of the specimen. Alternatively, Grant *et al.* [51] speculated that a vacuum environment would likely eliminate any heat haze effects but did not test such a solution.

Paints commonly used for room temperature tests are usually incompatible for high temperature DIC analysis for several reasons. The primary issue is that regular paints will burn off or melt at elevated temperatures. For example, general purpose spray paints commonly used for room temperature DIC tests have a temperature rating of 200°F (93°C) [61]. Marker ink intended for high temperature industrial and laboratory purposes, such as an industrial grade high temperature Sharpie marker, can only withstand up to 500°F (260°C) [62]. Additionally, the paint should ideally maintain a consistent colour once heated, to keep the pattern in a high contrast state. Certain high temperature paints may tolerate extreme temperatures but will dull or change colours when heated or cured [53]. Finally, since accurate DIC analysis requires the pattern to deform simultaneously with the base material, the paint must be similarly ductile as the base material to not crack prematurely.

Ceramic coatings are highly heat-resistant and are often used for applications beyond 1000°C, however these coatings are typically very brittle and will crack at very small strains [53]. DIC was conducted on various materials at temperatures up to 1100°C by Chen *et al.* [53] using a “precipitated silica and titanium dioxide” coating. However, to ensure the coating’s heat-resistance, a lengthy curing cycle consisting of various heating (up to 340°C) and cooling stages was required. Depending on the material being tested, these heating and cooling cycles may adversely affect the properties of the material of interest. Pan *et al.* [57] used a cobalt oxide and liquid high temperature adhesive mixture to apply black speckles onto a stainless steel for experiments at 1200°C. The bare surface of the stainless steel acted as the contrasting background for the speckle pattern, and no oxidation issues were reported. Pan *et al.* [57] and Novak and Zok [60] pre-oxidized a Nickel superalloy to achieve a dark background on the specimen surface, before speckling with commercial alumina and zirconia paints using an airbrush. Wang *et al.* [59] also used alumina paint on a Nickel superalloy for small strain testing up to 2000°C. Both Pan *et al.* [57], and Novak

and Zok [60] studied the coefficient of thermal expansion with no additional applied strains while Wang *et al.* [59] only tested at small strains to obtain the Young's modulus. Pan *et al.* [57], Novak and Zok [60], and Wang *et al.* [59] all studied material properties at very low strains, therefore it is unproven if these paints are suitable for high strain experiments. Grant *et al.* [51] abraded the surface of a nickel superalloy with grit paper to achieve a dotted speckle pattern rather than using paint. The contrasting pattern is achieved by the enhanced reflectivity of the scratches compared to the un-abraded regions of the surface.

Aside from premature cracking, typical high temperature coatings have been known to lose adhesion and flake off during large deformations [45]. To increase the adhesion of these coatings, Li *et al.* [45] debossed (or coined) the surface of uncoated PHS specimens to create shallow cavities, which were then painted over with brittle white titanium oxide to act as speckles. Figure 15 shows the procedure utilized by Li *et al.* [45] to promote paint adhesion to a 22MnB5 tensile specimen and the DIC results from the pattern.

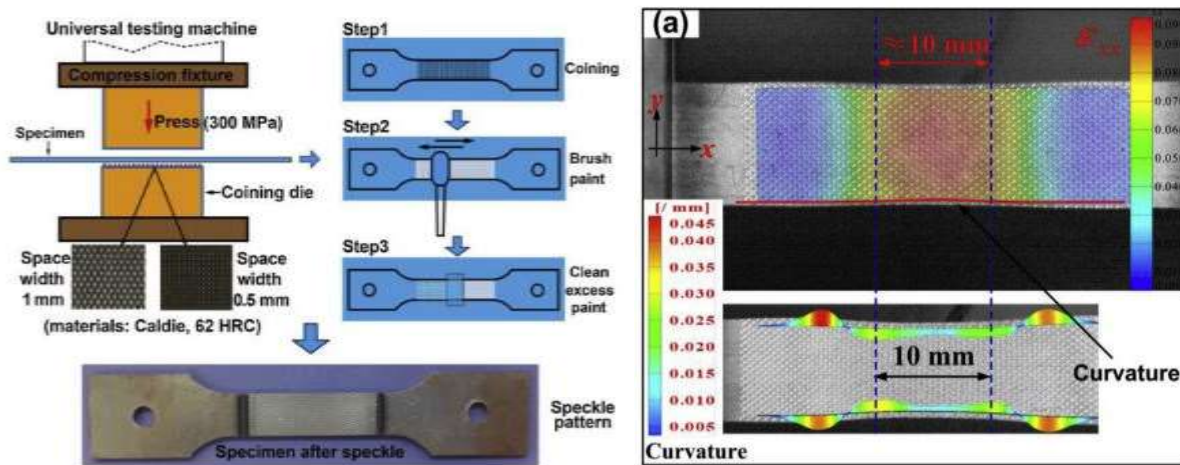


Figure 15: Method of debossing the surface to promote better paint adhesion, and subsequent DIC results by Li *et al.* [45]

Although the procedure developed by Li *et al.* did produce excellent DIC results at high temperatures and high strains, the need to mechanically process the surface prior to testing is time consuming and prohibitive for coated materials.

## 1.4. Numerical Modelling

The development of a cold stamped sheet metal component can be a very complex task due to the numerous variables associated with its manufacturing operation. Factors such as the intrinsic material behavior, friction, geometric complexity, and much more all affect the feasibility and repeatability of forming operations. Historical development of new sheet metal components has involved numerous design and tooling prototypes prior to mass production, which was both time consuming and expensive. Numerical modelling in the form of finite element (FE) analysis has been developed to enable virtual simulations of manufacturing processes to reduce costs and development times [63]. The increased adoption of finite element tools has also enabled the development of better designs, both in terms of part performance as well as manufacturing precision. Finite element tools, available as either commercial software or unique in-house developed solutions, are now widely used tool for predicting the formability of components and optimizing forming operations [64].

Developing accurate models of hot stamping is significantly more challenging than creating models of conventional (cold) stamping operations [65]. Numerous additional complexities are introduced when dealing with even basic hot stamping operations. Not only are the material's mechanical properties temperature dependent (for both the blank and the die material), but temperature dependence must be introduced to almost every other aspect of the process also, such as heat transfer and friction coefficients. Complex heat transfer mechanics involving conduction, convection, and radiation must also be modelled to accurately capture changing temperatures and cooling rates [9]. Additionally, microstructural evolution, primarily in the form of austenite decomposition must be captured in order to accurately predict the component's final properties [66]. Because the mechanical, thermal, and microstructural properties are inter-related, a hot stamping process model must ideally consider the interaction between all three aspects during the entire hot stamping operation for accurate predictions. Figure 16 shows a schematic of the inter-

relations between the mechanical (forming), thermal (heat transfer), and microstructural properties during hot stamping [14].

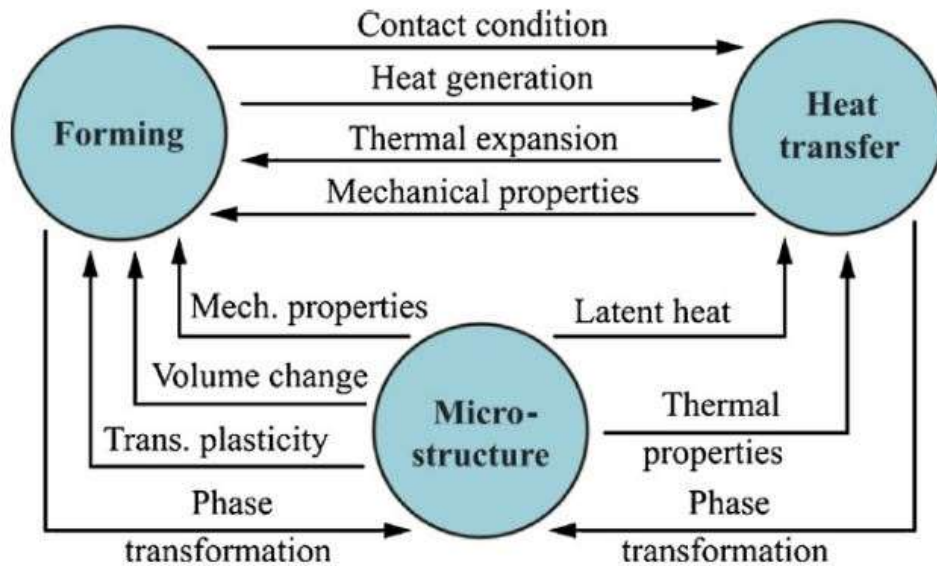


Figure 16: Relationships between the mechanical, thermal, and microstructural aspects of a hot stamping process, from Karbasian and Tekkaya [14]

Despite all the complexities associated with hot stamping modelling, the most important input to any forming model is arguably the intrinsic constitutive behaviour of the material when deformed. Therefore, to enable accurate FE predictions, the material’s hardening behaviour must be characterized and modeled.

#### 1.4.1. Hardening Models

Hardening models or constitutive equations relate the stress to deform a material to the amount of prior deformation (strain). Constitutive equations can be phenomenological or physically-based in relating stress and strain [14]. Phenomenological equations typically involve fitting a desired model to experimental data by means of deriving the necessary variables governing the predicted response. Depending on the complexity of the model, some of these coefficients may have physical meanings while others are non-physical but offer good correlation to experimental data. Physically-based models vary greatly, but the overall intention is to develop a model that represents the intrinsic nature of the material. These models still rely on experimental data but may require much more than just an experimental stress-strain curve to accurately describe the material behaviour.

Constitutive equations are often fit to experimental stress-strain curves (or data) for many reasons such as for interpolation or extrapolation of results, implementation in FE programs, or for comparisons between materials. The most basic equation used to describe the hardening response of common low carbon steels is the power law equation [67],

$$\sigma = K\varepsilon^n \quad (5)$$

Once experimental data is obtained from a standard tensile test, one could fit Equation (5) to the experimental true stress and true strain data points by means of regression analysis to obtain the coefficients  $K$  and  $n$ , the strength and strain-hardening coefficients, respectively. Once the model parameters are determined it is possible to extrapolate the curve to strains well beyond that of the experimental data if so desired. The fit equation may also be used to generate a smooth hardening curve if the experimental data itself is noisy. Additionally, the hardening properties of different materials could also be directly compared by evaluating the differences between the two coefficients.

Equation (5) is known as the power-law (or Hollomon) equation, however not all material hardening behaviours are best represented with by this simple exponentiation relationship. Exponential equations such as the Voce equation, in which strain is exponentially related to stress, is often used for materials that exhibit a plateau in strain hardening [68]. There are also constitutive equations that have both power-law and exponential components, such as the model proposed by Ludwigson [69]. Figure 17 shows an example of two well-known constitutive models, the power-law-type Swift equation and the exponential-type Voce equation, fit to experimental results. Note the differences in immediate hardening at the onset of plastic deformation, as well as the differences in the extrapolated flow stress at high plastic strains.

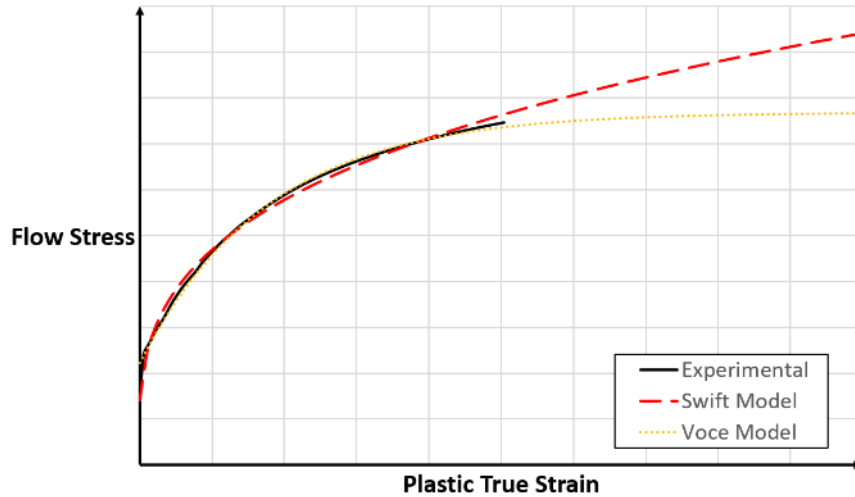


Figure 17: Schematic showing the differences between experimental results (black, solid line), a Swift model (red, dashed line) model fit to the experimental data, and a Voce model (orange, dotted line) fit to the experimental data

All constitutive models discussed up to this point have been equations where stress is solely dependent on strain. However, to characterize PHS materials accurately for hot stamping applications, one must also consider the effects of strain rate and temperature. Capturing the effect of strain rate on the constitutive behaviour of a material is extremely important when the material behaviour is dependent on the rate of loading or when the strain rate is variable during loading. For hot stamping, rapid press speeds are required to complete the forming of the blank while the blank is fully austenitic. Because of this, certain regions of a blank requiring high deformation (high strains) could experience relatively high strain rates during the forming process. Likewise, regions that require less deformation (lower strains) could experience much lower strain rates. PHS 1500 has been shown to be strain rate sensitive in the austenitic state at hot-stamping temperatures by various researchers. Hochholdinger *et al.* [36], Eriksson *et al.* [40], and Naderi *et al.* [47] have all demonstrated the strain rate sensitivity of 22MnB5 materials during isothermal compression tests between 650 – 900°C, in which increased strain rate resulted in increased flow stress. Figure 18, from Naderi *et al.* [47], shows the effect of strain rate between the two subplots (and temperature) on the flow stress of a PHS 1500 materials from compression testing.

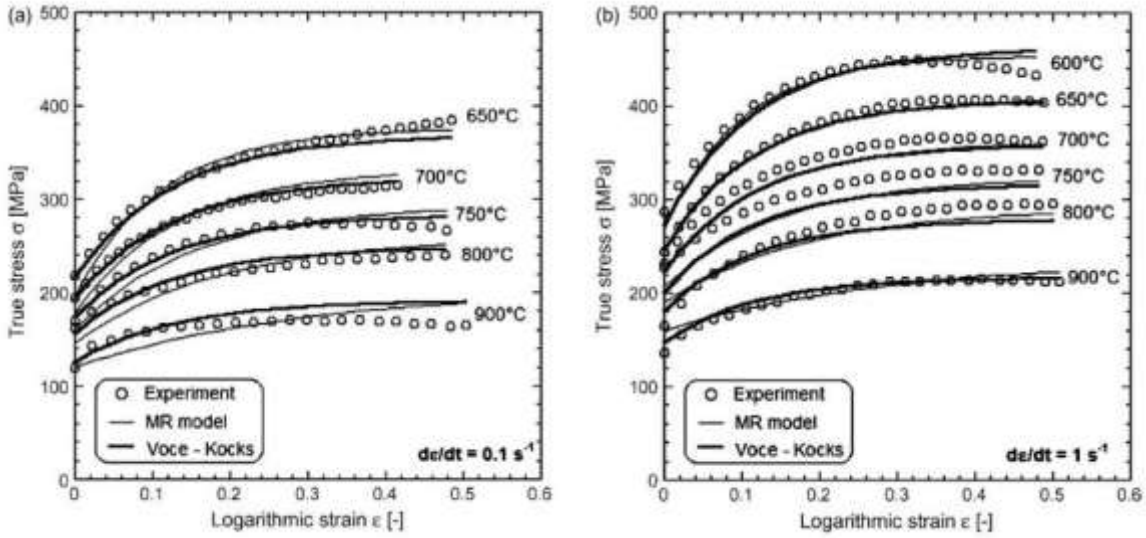


Figure 18: The effect of strain rate and temperature on the stress response of 22MnB5 from isothermal compression testing (from [47])

The same phenomenon has also been captured during isothermal tensile tests, such as those conducted by Merklein and Lechler [42], Li *et al.* [45], Abspoel *et al.* [43]. Figure 19 shows a plot from Merklein and Lechler [42] that shows the influence of strain rate on the flow stress of a PHS 1500 material at 700°C.

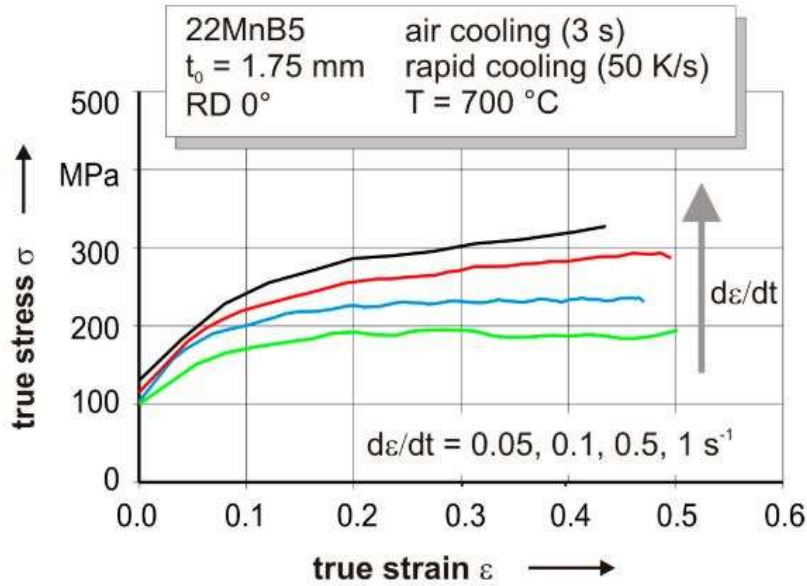


Figure 19: The effect of the strain rate on the stress response of 22MnB5 from a tensile test at 700°C (from [42])

Another important variable required to adequately model the constitutive behaviour of PHS material is temperature dependency. Because the blank is not formed isothermally, different regions of the blank will

be at different temperatures at different times. Typically, steels experience thermal softening, in that the flow stress decreases with increasing temperature [31]. The temperature sensitivity of PHS 1500 has been observed during constant strain rate isothermal constitutive testing between approximately 600°C – 900°C by Hochholdinger *et al.* [36], Eriksson *et al.* [40], Naderi *et al.* [47], Merklein and Lechler [42], and Li *et al.* [45]. Figure 18 from Naderi *et al.* [47] shows the effect of temperature on the flow stress response, in the form of thermal softening at higher temperatures. All experimental results of PHS 1500 reviewed for this current work have shown decreased flow stresses with increasing temperature.

Hochholdinger *et al.* [36], Naderi *et al.* [47] and Merklein and Lechler [42] have also observed that the rate of work hardening decreases with increasing deformation temperature. Work hardening can be defined as the increase in stress response after the onset of yielding and plastic deformation. Both Naderi *et al.* [47] and Merklein and Lechler [42] noted a decrease in work hardening with an increase in temperature. Merklein and Lechler [42] determined a relatively well correlated decaying exponential relationship between work hardening and temperature, shown in Figure 20 for the 0.1s<sup>-1</sup> strain rate condition..

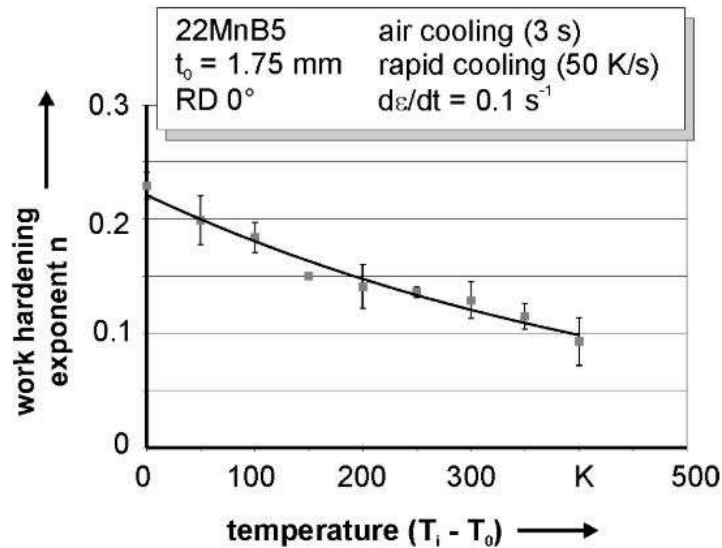


Figure 20: Work hardening exponent  $n$  as a function of temperature difference to the lowest temperature condition, for PHS 1500 (from [42])



Temperature does not only affect the stress response or work hardening rate of PHS materials. Merklein and Lechler [42] also observed a increase in the strain rate sensitivity of PHS 1500 at higher deformation temperatures, shown in Figure 21.

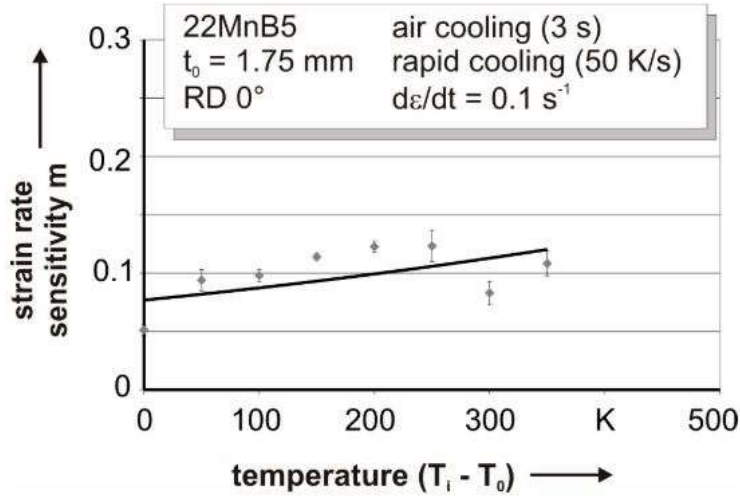


Figure 21: Strain rate sensitivity parameter as a function of increasing temperature difference to the lowest temperature condition, for PHS 1500 (from [42])

To summarize, the temperature and strain rate has been shown to affect various aspects of the constitutive behaviour of PHS materials. Therefore, any constitutive model intended to accurately capture the behaviour of PHS must also incorporate the thermal and strain rate sensitivity of the material.

Several strain rate and temperature dependent material models have already been applied to PHS 1500 by other researchers. Merklein and Lechler [42] used a phenomenological modified Norton-Hoff equation and obtained a good fit to experimental PHS 1500 data between 500-800°C, and 0.01 - 1.0 s<sup>-1</sup> strain rate, shown in Figure 22 by the solid lines.

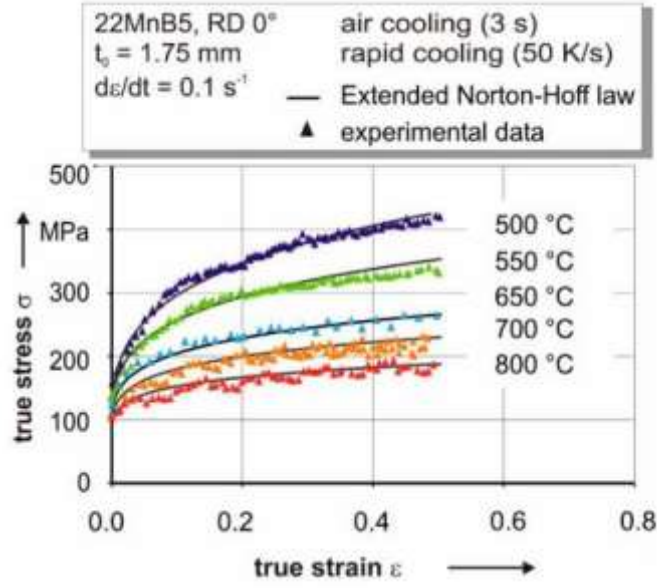


Figure 22: Experimental data of PHS 1500 and the fit modified Norton-Hoff equation fit (solid line) (from [42])

The modified Norton-Hoff equation is a power-law type equation in which both the strain hardening, and strain rate sensitivity exponents are exponentially related to temperature. In addition, both the temperature and strain rate terms were multiplicative to strain. The modified Norton-Hoff equation used by Merklein and Lechler is shown by Equations (6) - (8).

$$\sigma = A e^{\frac{B}{T}} (b + \varepsilon_p)^{n(T)} \dot{\varepsilon}^{m(T)} \quad (6)$$

$$n(T) = n_0 e^{-C_n(T-T_0)} \quad (7)$$

$$m(T) = m_0 e^{-C_m(T-T_0)} \quad (8)$$

Li *et al.* [45] also successfully used the modified Norton-Hoff equation developed by Merklein and Lechler [42] to fit experimental PHS 1500 data up to  $10 \text{ s}^{-1}$  strain rate at various temperature conditions. Li *et al.* [70] compared constitutive fits using the modified Norton-Hoff (N-H) model to the Molinari-Ravichandran (M-R) model for a PHS 1500 and noted that the M-R model better captured the stress saturation behaviour seen at high strains, as shown in Figure 23.

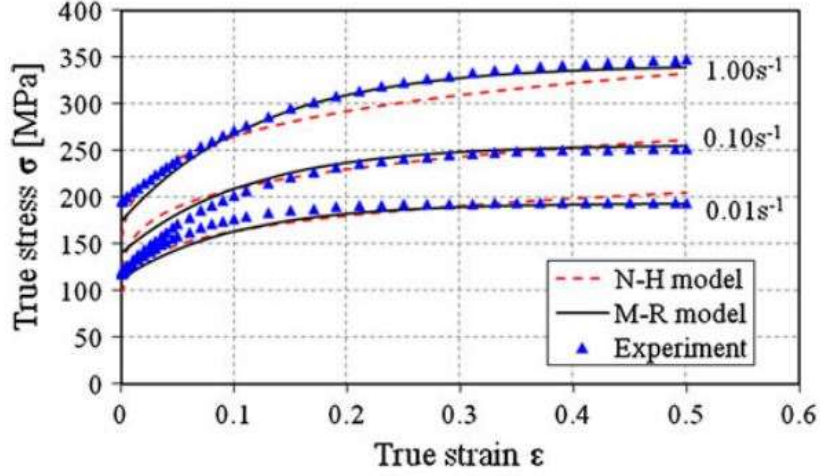


Figure 23: Comparison of the modified Norton-Hoff (N-H) model and the Molinari-Ravichandran (M-R) model fit to experimental PHS 1500 data at 650°C (from [70])

A downside of the M-R model is the complexity of the model, which requires 14 parameters to be identified. The M-R model is shown by Equation (9) [70], in which all parameters except for equivalent strain ( $\bar{\epsilon}$ ), strain rate ( $\dot{\epsilon}$ ), and the temperature terms ( $T, T_0$ ) must be identified to fully define the model.

$$\sigma_h = \sigma_d \left( \frac{\frac{\delta_0}{\delta_{s0} [1 - a_s \left(\frac{\dot{\epsilon}}{\dot{\epsilon}_{s0}}\right)^{\zeta_s} \left(\frac{T}{T_0}\right)^{-v_s}]}{1 - \left(1 - \frac{\delta_s}{\delta_0}\right) \exp(-\delta_{r0} [1 - a_r \left(\frac{\dot{\epsilon}}{\dot{\epsilon}_{r0}}\right)^{\zeta_r} \left(\frac{T}{T_0}\right)^{-v_r} \bar{\epsilon}])}}{\left(\frac{\dot{\epsilon}}{\dot{\epsilon}_0}\right)^{\frac{1}{s}}} \right) \quad (9)$$

Naderi *et al.* [47] compared the fit of the Voce-Kocks model and the M-R model to isothermal uniaxial compression test data for PHS 1500, shown in Figure 18. It was observed that the Voce-Kocks model resulted in a better fit at high strains, however it is important to note that stress-strain curve obtained from compression testing is not directly comparable to tensile tests results due to the higher achievable strains prior to necking or fracture. For reference, the Voce-Kocks model is shown in Equation (10), where the saturation stress ( $\sigma_s$ ) is dependent on temperature and various material parameters, and the relaxation strain ( $\epsilon_r$ ) is dependent on strain rate and temperature.

$$\sigma = \sigma_S + [(\sigma_0 - \sigma_S) \exp\left(\frac{\varepsilon}{\varepsilon_r}\right)] \quad (10)$$

Abspoel *et al.* [43] fit experimental PHS 1500 data to a physically-based model that relates flow stress to the summation of a yield stress ( $\sigma_0$ ), a thermally activated stress component ( $\sigma^*$ , that is also dependent on strain rate), and a strain, temperature, and strain rate dependent work hardening stress ( $\sigma_w$ ), the general structure of the model is shown by Equation (11) [43].

$$\sigma_f = \sigma_0 + \sigma^*(\dot{\varepsilon}, T) + \sigma_w(\varepsilon, \dot{\varepsilon}, T) \quad (11)$$

The physically-based model by Abspoel *et al.* [43] was applied to experimentally determined data, however a relatively poor fit was observed at strain rates greater than  $0.1 \text{ s}^{-1}$ . On the other hand, Åkerström [71] and Li *et al.* [32] found that the common temperature and strain rate dependent Johnson-Cook equation was typically unable to represent the flow stress response of PHS 1500 at elevated temperatures.

#### 1.4.2. Austenite Decomposition Modelling

A critical mechanism of the hot stamping process is the phase change from the highly formable austenitic microstructure at elevated temperatures to the high-strength fully martensitic structure after quenching. In order to accurately capture the behavior of a PHS undergoing the hot stamping process, the phase transformation characteristics of the material must also be modeled [16]. Figure 24 shows a continuous cooling transformation (CCT) diagram for a grade of 22MnB5 from Nikravesh *et al.*[38], showing the temperatures and times required for austenite to decompose into other phases.

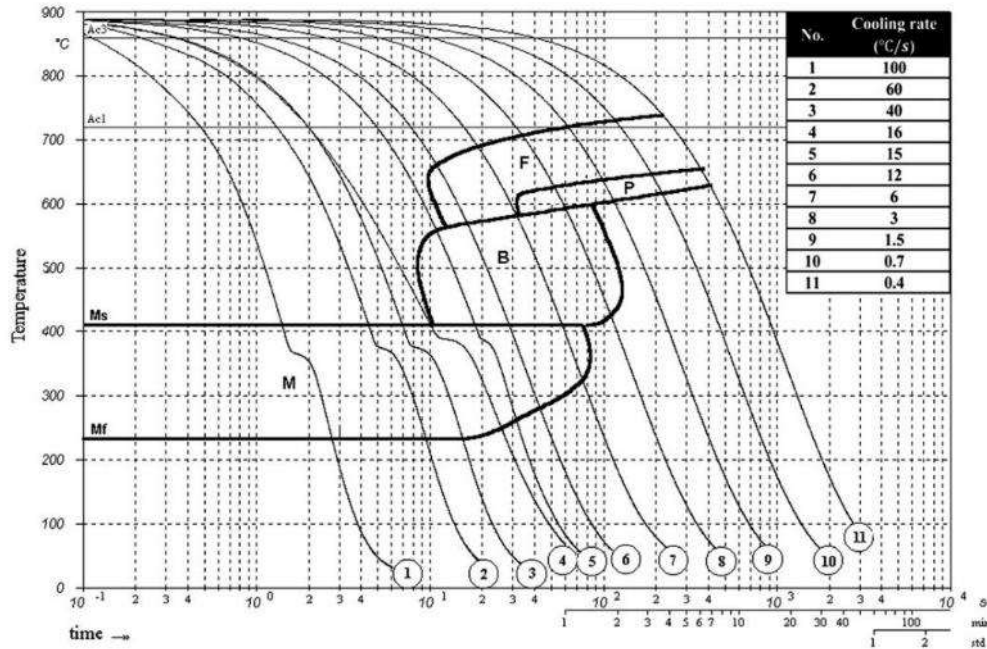


Figure 24: Continuous cooling transformation (CCT) diagram for 22MnB5, with various cooling rates shown (from [38])

Modelling the phase change properties of a PHS is crucial for predicting whether a component will be fully hardened when strength is the only desired attribute, and for developing components with tailored properties that may contain regions of varying strengths (or harnesses) for optimizing other aspects of performance. Specifically, it is critical to model the phase transformation of austenite into ferrite, pearlite, bainite, and martensite depending on time, cooling rate, and temperature state of the material. Bardelcik *et al.* [72] developed a constitutive model (Tailored Crash Model II) that relies on the final phase fractions of ferrite, bainite, and martensite of 22MnB5 to predict the flow stress of the material after hot stamping. The Tailored Crash Model II was developed by fitting the model to experimental results and could predict the post-quenched performance of fully martensitic as well as mixed-phase specimens for a wide range of strain rate conditions. Aside from predicting the strength after hot stamping, a model could also correlate the hardness (or microhardness) to the final phase fractions within the material.

To predict the amount of martensite after quenching, Koistinen and Marburger [73] developed an empirically determined equation to predict the volume fraction of retained austenite after quenching below

the martensite start temperature. The Koistinen and Marburger equation is shown by Equation (12), which can consider the quenching temperature  $T_q$ , and the martensite start temperature  $M_s$  [73].

$$V_\gamma = \exp [-1.10 \times 10^{-2}(M_s - T_q)] \quad (12)$$

Consequently, if the initial amount of austenite is known, and the retained amount of austenite is predicted, then the fraction of martensite in the final microstructure can be calculated. The martensite start temperature can be determined experimentally or by approximation based on the chemical composition of the PHS.

For non-martensite phases, Kirkaldy and Venugopalan [74] developed a widely used austenite decomposition model for the transformation prediction of diffusion-based phases (ferrite, pearlite, bainite) for low alloy steels. The Kirkaldy and Venugopalan model accounts for the effects of initial austenite grain size, chemical composition of the steel, and temperature (undercooling) to predict the rate of phase change. Åkerström and Oldenburg [66] built upon the Kirkaldy and Venugopalan rate equations and applied the austenite decomposition model to create a coupled thermal-mechanical-phase change finite element model for simulating the hot stamping process. The modified Kirkaldy and Venugopalan phase formation rate equation is shown by Equation (13), where  $f(G)$  accounts for the effect of grain size,  $f(C)$  accounts for the material chemical composition,  $f(T)$  is the temperature dependency, and  $f(X_i)$  is the term for the current fraction of formed phases [66].

$$\frac{dX_i}{dt} = f(G)f(C)f(T)f(X_i) \quad (13)$$

The effect of grain size is represented by an increased rate of phase transformation for smaller austenite grain sizes. New implementations of the model have also modeled the effect of changing austenite grain sizes (primarily growth, from heating) and its subsequent effects on the formation rate [75]. Kirkaldy and Venugopalan also developed an equation that reduces the formation rate, as the fraction of formed phases increased. In the original Kirkaldy and Venugopalan model, the effect of increasing various common alloying elements such as Mn, Ni, Cr, and Mo were considered to reduce the rate of transformation.

Åkerström and Oldenburg [66] modified the rate equations to account for the effect of boron on the hardenability of steels, which was critical to accurately represent the actual behavior of 22MnB5 and similar PHS materials. The effect of boron was implemented by applying a reduction factor to the formation rate of ferrite and pearlite phases with increased boron content. The effect of temperature is a critical factor in predicting when phase change occurs, because austenite will not decompose if the material remains above the critical temperatures for phase transformation. The effect of temperature on the rate of phase change is shown by Equation (14), where  $T_{cr} - T$  is the supercooling beyond the critical temperatures for each phase,  $n$  is a constant representing the reaction location,  $Q_i$  is the activation energy value for each phase, and  $R$  is the universal gas constant.

$$f(T) = (T_{cr} - T)^n e^{\frac{Q_i}{RT}} \quad (14)$$

From Equation (14), greater supercooling beyond the critical start temperature for each phase results in a greater rate of transformation. The critical temperatures for ferrite, pearlite, and bainite are determined based on the chemical composition of the material.

Åkerström and Oldenburg [66] integrated both the Koistinen and Marburger equation [73] and the Kirkaldy and Venugopalan [74] model into a austenite decomposition model capable of predicting the formation of the diffusion-less martensite phase, and the diffusion based ferrite, pearlite, bainite phases. Åkerström and Oldenburg [66] also implemented additional factors to account for phase transformation effects that would be relevant to a hot stamping finite element simulation. The effect of latent heat of transformation when austenite decomposes was included in the Åkerström and Oldenburg model [66]. Latent heat typically reduces the amount of undercooling experienced by a hot stamped component, which affects the cooling rate and subsequently feeds back to influence the phase change rate. Åkerström and Oldenburg [66] also accounted for the effects of different thermal properties of each phase, by implementing a mixture law based on the fraction and thermal conductivity of each phase. In conjunction with the phase transformation model, Åkerström and Oldenburg also integrated a hardness prediction model, based on empirical correlations from various sources, depending on the alloying elements of the

material. For example, the microhardness (Vickers, HV) of martensite was taken from Honeycombe [76] and directly correlates hardness to carbon content (C, wt%), as seen by Equation (15).

$$HV = 181.1 + 2031.9C - 1940.1C^2 \quad (15)$$

Figure 25 shows a good correlation between the measured and predicted (calculated) final microhardness of a hot stamped 22MnB5 sheet using the Åkerström and Oldenburg austenite decomposition model [66].

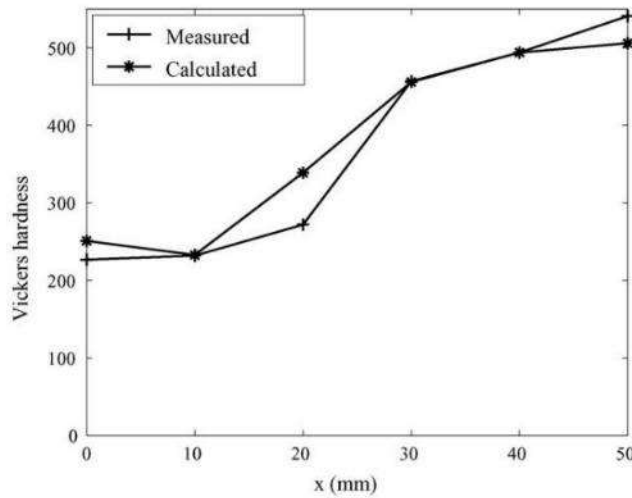


Figure 25: Measured and predicted microhardness of a hot-stamped 22MnB5, from Åkerström and Oldenburg [66]

A limitation of the Åkerström and Oldenburg [66] model is that strain or deformation on the austenite microstructure does not change the final phase fraction predictions. Barcellona and Palmeri [77] conducted extensive experiments on 22MnB5, demonstrating that tensile strains at elevated temperatures (referred to as pre-strain) prior to quenching resulted in the formation of more ferrite and pearlite phases than specimens that experienced no pre-strain. The increased ferrite and pearlite phases, as well as the reduced microhardness measurements clearly indicated a change in the austenite decomposition kinetics due to strain. Figure 26 from Nikravesh *et al.* [38] shows the CCT diagram of 22MnB5 with 40% induced (compressive) deformation during cooling. Compared to the CCT diagram without deformation (Figure 24), deformation causes the CCT diagram to be shifted to the left, leading ferrite, pearlite and bainite phases to begin forming sooner and at higher temperatures.



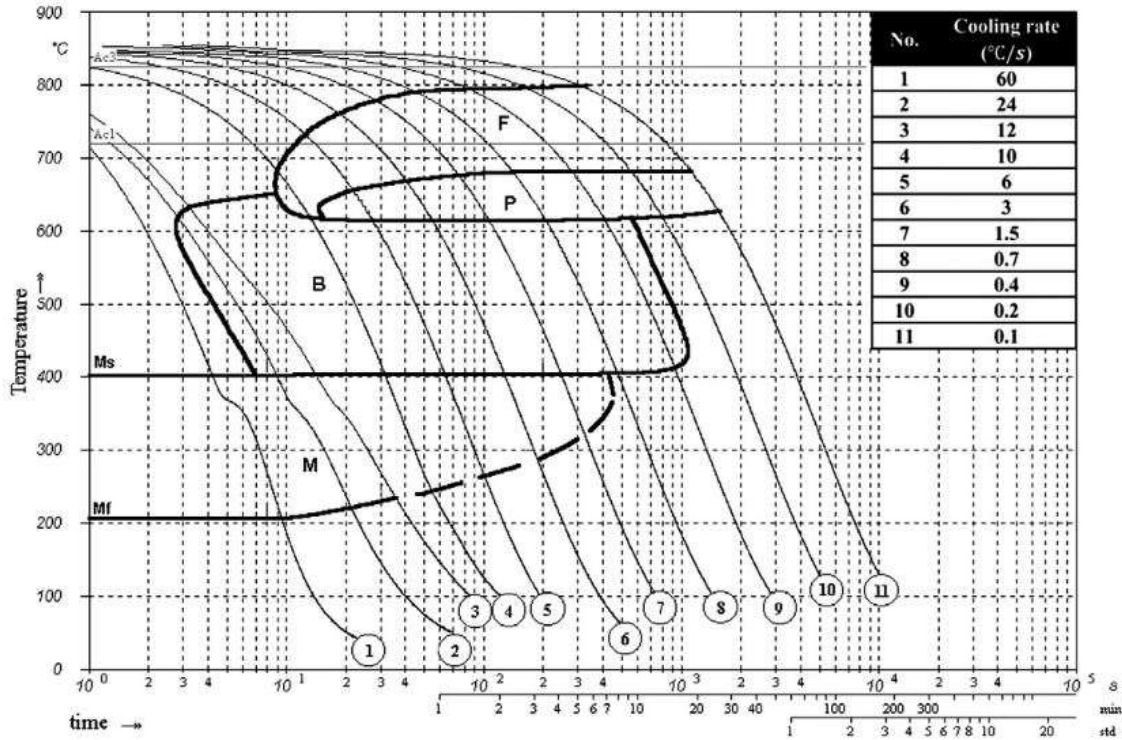


Figure 26: Continuous cooling transformation (CCT) diagram for 22MnB5, with 40% induced compression strain during cooling, with various cooling rates shown (from [38])

To account for the effects of deformation on phase transfer, a modification was made to the Kirkaldy and Venugopalan model by the addition of a scale factor to the activation energy of each phase [75]. The modification to the temperature effect is shown by Equation (16), where  $k_i$  is the deformation scale factor for each phase.

$$f(T) = (T_{cr} - T)^n e^{-k_i \frac{Q_i}{RT}} \quad (16)$$

The deformation scale factor decreases with increasing deformation, reducing the activation energy of each phase which promotes the formation of ferrite, pearlite, and bainite.

For PHS in hot stamping applications, the Åkerström and Oldenburg [66] model is likely the most well-known model to simulate austenite decomposition and predict final phase fractions after hot stamping. The applicability of the Åkerström model can be attributed to its adaption and implementation into the widely used commercial finite element solver, LS-DYNA (MAT\_244) [66], [75].

Hippchen *et al.* [78] demonstrated some limitations of the Åkerström-based model (MAT\_244) in LS-DYNA for predicting the properties of indirect hot stamped and tailored heat treated 22MnB5 components. Compared to experimental results, Hippchen *et al.* showed that the Åkerström-based model overpredicted the amount of ferrite in the final fracture, leading to an inaccurate prediction of final mechanical properties of the tailored heat treated B-pillar [78]. To improve the final martensite prediction, Hippchen *et al.* updated the Koistinen and Marburger equation with additional coefficients to account for the rate of martensite formation based on already-formed phases [78]. Additionally, Hippchen *et al.* introduced new coefficients to change the rate of phase transformation depending on the time history prior to phase formation, making the transformation rate dependent on the cooling rate prior to transformation [78]. Finally, Hippchen *et al.* implemented an approach to calculate phase transformation strains, based on the change in density of the FCC structure austenite phase into its BCC structure of the final phases. Capturing the strains from phase transformation was required to accurately predict residual stresses and strains that could potentially result in geometric variations in the component (such as springback for tailor heat treated parts) [78]. The changes to Åkerström-based model were also implemented in LS-DYNA as MAT\_248 and seems more suitable for indirect hot stamped and tailor heat treated components. Figure 27 shows a comparison of measured results to the predicted results (in the form of geometrical deviation) when using the Åkerström-based model (MAT\_244, left) and the updated Hippchen *et al.* model (MAT\_248, right) [78].

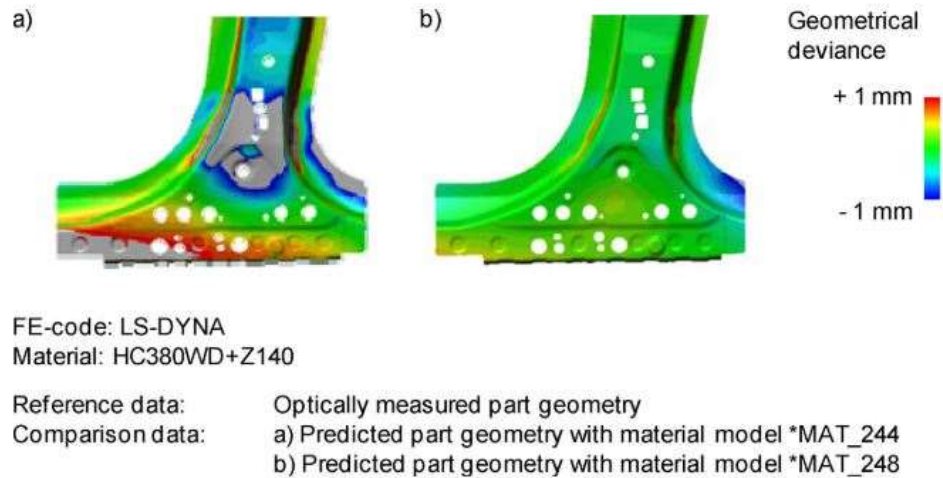


Figure 27: Comparison of geometrical deviance of measured results to predicted results based on the Åkerström-based model (MAT\_244, left) and the Hippchen et al. updated model (MAT\_248, right), taken from Hippchen et al. [78]

Despite the previously mentioned limitations, many researchers have also successfully utilized the Åkerström-based austenite decomposition model for developing hot stamped components with tailored properties. George *et al.* [79] and Omer *et al.* [80] calibrated the activation energies and deformation scale factor of the Åkerström-based model (MAT\_244) in LS-DYNA to experimental phase fraction measurements. The calibrated model was then used to create a finite element model of a tailored heat treat hot stamping process that utilized heated sections of the stamping die to vary the cooling rates along component. Compared to the experimental trials, the simulation with a calibrated material model was capable of predicting the final hardness distribution throughout the component, which varied between a range of 190 HV to 480 HV.

Bourque [81] also investigated the use of the Åkerström-based model in LS-DYNA to predict the final phase fractions and microhardness of two grades of PHS 1800, after quenching at various cooling rates and tempering conditions. The finite element model predicted initial results that poorly correlated to the experimental observations using the default model parameters. However, after calibrating the activation energies of the Åkerström-based model to experimental results, a good correlation was achieved for the micro-hardness values.

## 1.5. Scope of Work

Motivation for the current research is primarily drawn from the lack of literature regarding PHS 1800. Recent comprehensive reviews of hot stamping processes only briefly mention PHS 1800, and most of the research available for hot stamping is directly associated with PHS 1500 only [16], [82]. With regard to the few currently available publications on PHS 1800, none have explored the hardening behaviour of this steel grade under hot stamping conditions. The secondary focus for this research is to develop experimental techniques to test and characterize Al-Si coated PHS materials with digital image correlation. Currently, most researchers utilize uncoated PHS specimens for experimental research, which has several limitations mentioned previously in Section 1.3. The development of a strategy to utilize DIC techniques to measure specimen surface deformation will enable the collection and analysis of higher fidelity constitutive data.

Given this deficit in the published literature concerning PHS 1800, the intent of this research is to develop an experimental procedure to conduct isothermal tensile tests for this new grade utilizing digital image correlation for strain measurement and determination of specimen cross-sectional area. To validate the experimental method, a common grade of PHS 1500 will also be tested in an identical manner and results will be compared to published results in literature as a baseline evaluation of the experimental techniques. Analytical techniques will be developed to process the experimental results to produce material flow curves at various temperatures and strain rates. A temperature and strain rate sensitive constitutive model that is capable of accurately representing the material hardening behaviour will then be fit to the experimental data for finite element analysis. A finite element model of the tensile tests is then constructed, to evaluate the accuracy of the constitutive results.

The implementation of DIC techniques for full-field strain measurements under hot stamping conditions also represents a deficit in the existing literature. Due to the difficulty associated with high temperature DIC, few researchers have applied DIC to high temperature testing of PHS. As mentioned previously, Merklein and Lechler [42] utilized an optical strain measurement method but did not go into detail regarding their methods. Li *et al.* [45] utilized DIC for constitutive testing of PHS 1500, however it

was applied to an uncoated material and required deforming the specimen surface (embossing) to generate the speckle pattern as seen in Figure 15. A goal for the current research is to develop an approach to DIC that is applicable to the Al-Si coated PHS, and without significant modifications to the specimen. Because DIC use for hot stamping test conditions is so rare, few analysis methods have been documented to process the experimental results. Hence, the current work also explores a post-processing strategy to better utilize data from DIC that would not otherwise be available when using traditional measurement technologies.

Because the focus of this research revolves around the deformation behaviour of PHS 1800, it seems appropriate to extend the investigation to the effects of deformation on the microstructural development of the material during hot stamping. As presented earlier, accurate hot stamping predictions are highly dependent on the inter-relation between the PHS material's mechanical, thermal, and microstructural properties. Experiments will be conducted to evaluate the deformation induced effects on phase transformation during quenching. These results will be utilized to update relevant parameters of the popular Åkerström austenite decomposition model to better reflect the PHS 1800 material.

The contents of this thesis are organized as follows: First, the experimental procedure is described, including the two studied materials, laboratory equipment used, and an overview of the experiments conducted. Afterwards, all experimental results for both PHS materials are presented, and relevant discussion topics are included alongside the results. Following the experimental results section, the constitutive modelling aspect of this thesis is presented. For the constitutive modelling section, the modeling procedure and the predicted results are presented and discussed with reference to the experimental observations. To tie everything together, a brief discussion is included to highlight key findings of this research, and a conclusion summarizes the overall outcome of this research. Lastly a list of recommendations is presented with numerous lessons learned for future researchers seeking to conduct constitutive testing of PHS materials.

## 2. Experimental Procedure

### 2.1. Studied Materials

Two grades of PHS were studied in this research. These two materials will be referred to by their nominal ultimate tensile strength (in MPa) after hot stamping. PHS 1800 is a new grade of PHS with a UTS of over 1800 MPa after hot stamping. PHS 1500 is a commonly available PHS and is comparable (in strength and chemical composition) to the widely investigated 22MnB5 alloy. As previously mentioned, the PHS 1500 was selected to be studied in parallel with the PHS 1800 as a baseline, such that the experimental techniques and data processing procedures can be validated against results in the existing literature. Both grades of PHS were received with a type-1 Aluminum-Silicon coating. The studied PHS 1500 sheet measured approximately 1.7 mm thick, which includes a coating thickness of approximately 20-25  $\mu\text{m}$  per side. The PHS 1800 sheet measured approximately 1.6 mm in thickness, with a coating thickness of approximately 25-30  $\mu\text{m}$  per side. The chemical compositions of the studied PHS 1500 and PHS 1800 materials are shown in Table 1.

*Table 1: Chemical compositions of PHS 1500 and PHS 1800 studied in this research*

	<b>C (%)</b>	<b>Si (%)</b>	<b>Mn (%)</b>	<b>P (%)</b>	<b>S (%)</b>	<b>Al (%)</b>	<b>Cr (%)</b>	<b>Ti (%)</b>	<b>B (%)</b>
<b>PHS 1500</b>	0.22	0.25	1.23	0.008		0.03	0.20	0.037	0.004
<b>PHS 1800</b>	0.32	0.57	0.60	0.012	<0.005	0.05	0.31	0.021	0.002

The same grade of PHS1500 used by Bardelcik *et al.* [72] was also used in this research and therefore the chemical composition was also taken from that publication. The chemical composition of the PHS 1800 was determined by inductively coupled plasma mass spectroscopy (ICP or ICP-MS) analysis performed by an ISO 17025 accredited chemical analysis laboratory. ICP-MS analysis was selected as the method of chemical analysis to ensure the low concentrations of boron can be quantified. Three samples were sheared from a single as-received sheet and the coating was removed using mechanical abrasion prior to analysis. The chemical breakdown for PHS 1800 presented in Table 1 is the mean chemical composition of the three prepared samples.

## 2.2. Experimental Equipment

### 2.2.1. Electric Furnace

A Deltech electric furnace was used to heat treat specimens at temperatures ranging from 600°C – 930°C. The temperature of the furnace was regulated by three thermocouples positioned at various depths (inward direction, away from the door) inside the chamber. An internal fan was used to circulate hot air to promote a uniform temperature distribution within the chamber. Depending on the application, specimen placement and extraction was either performed manually or the furnace was coupled with a hydraulic press and a transfer system to allow for automatic specimen processing. Figure 28 shows the electric furnace to the right of the hydraulic press.

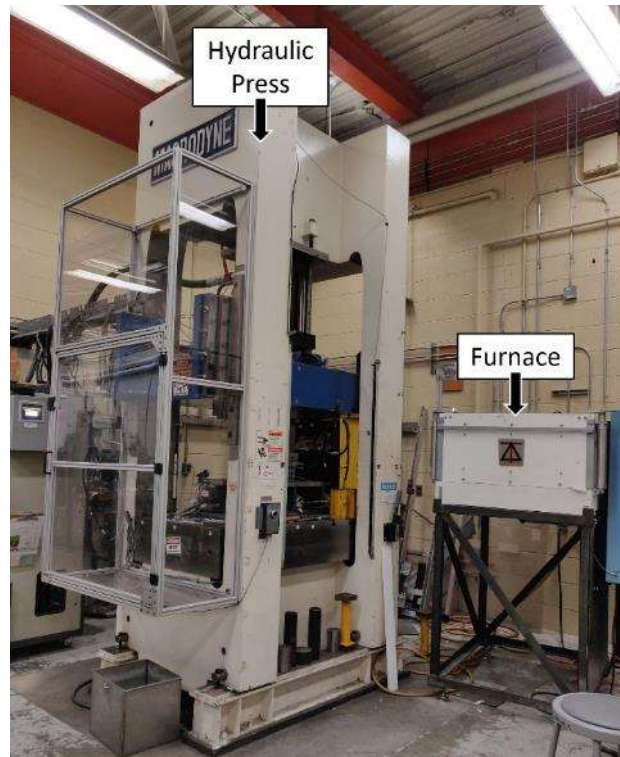


Figure 28: 125 ton Macrodyne hydraulic press (left) and Deltech electric furnace (right) oriented for manual specimen transfer

### 2.2.2. Hydraulic Press

A 125 ton Macrodyne hydraulic press with flat steel dies was used to rapidly quench flat specimens from elevated temperatures to room temperature. The press speed, load, and dwell times were all parameters that could be varied using the controller depending on the intended application. The primary reason for

using the press for quenching was to achieve quench rates comparable to those seen in industrial hot stamping processes. An added benefit of quenching between flat steel dies (versus liquid media, for example) is the preservation of specimen flatness due to the prevention of warpage. An optional feature used with the hydraulic press was a custom designed blank transfer system. The transfer system consists of a motor-driven clamp that translates linearly on fixed rails around the flat dies. The clamp was capable of gripping room-temperature blanks, placing them inside the oven, removing the hot blanks after a certain amount of time in oven, and then placing the heated blank onto the bottom die. A dowel pin was attached on one end of the flat die to assist in locating the blank prior to press hardening. The transfer system was used extensively to automate specimen processing when large quantities of material needed to be heat treated. For smaller batches of heat treating and processing, the press control and any specimen transfer was performed manually by the operator using tongs. For all quenching applications, 25 MPa of pressure was applied to the blank and the quench time was 20 seconds. Figure 28 shows the hydraulic press with the electric furnace oriented alongside for manual blank transfer. When the transfer system was intended to be used, the furnace would be relocated behind the press such that the furnace opening was oriented in-line with the press.

### **2.2.3. Gleeble 3500**

The Gleeble 3500 is a thermal-mechanical universal tester that utilizes resistive heating to rapidly heat specimens prior to or during tension or compression testing. Compressed air, inert gases, or water can be used to rapidly cool specimens within the enclosed test chamber. A thermocouple is typically spot welded onto the surface of the specimen to control and monitor the temperature of the specimen. The primary benefit of resistive heating compared to other heating technologies is the ability to precisely control the heating rate. A downside of resistive heating is that the temperature is only controlled at the location of the thermocouple. In most instances, the thermocouple is welded at the centre of the specimen. Since the jaws gripping the specimen are water-cooled and are not thermally insulated, this means that a non-uniform temperature profile typically develops along the length of the specimen. Force, crosshead displacement, and thermocouple temperature are recorded by the Gleeble. For this research, image acquisition was also



utilized with the Gleeble to enable DIC analysis of surface displacement data. Figure 29 shows the exterior of the Gleeble 3500 used in this work, along with the control panel, control computer, and the thermocouple spot welder.

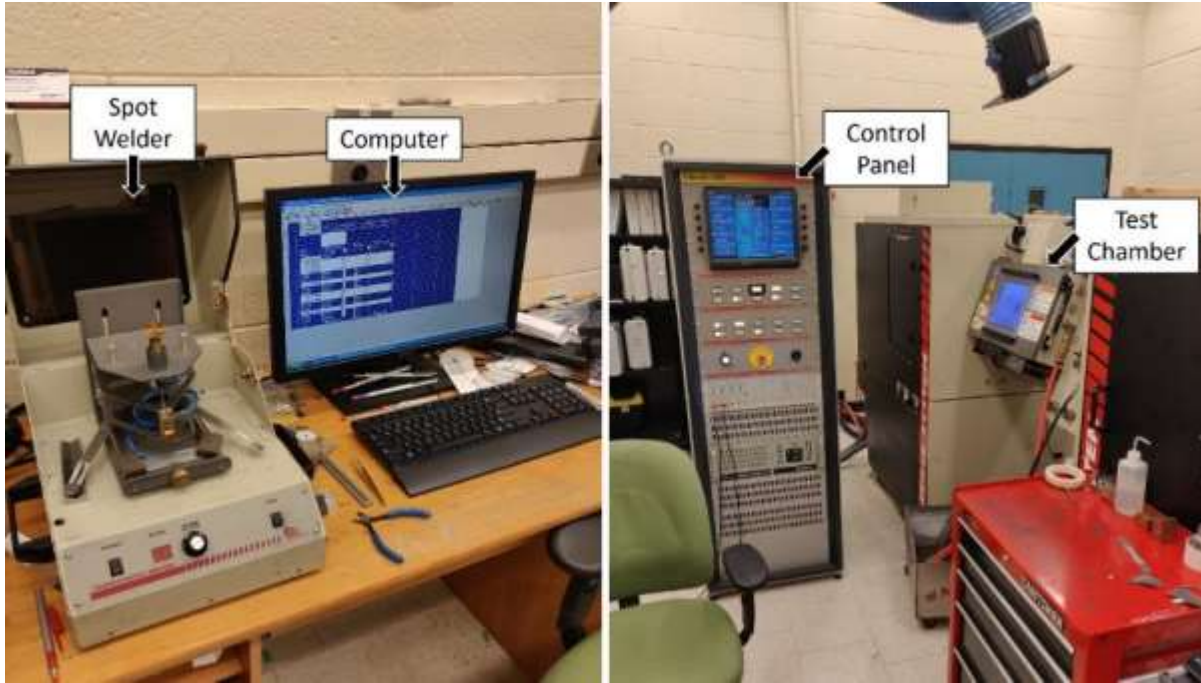
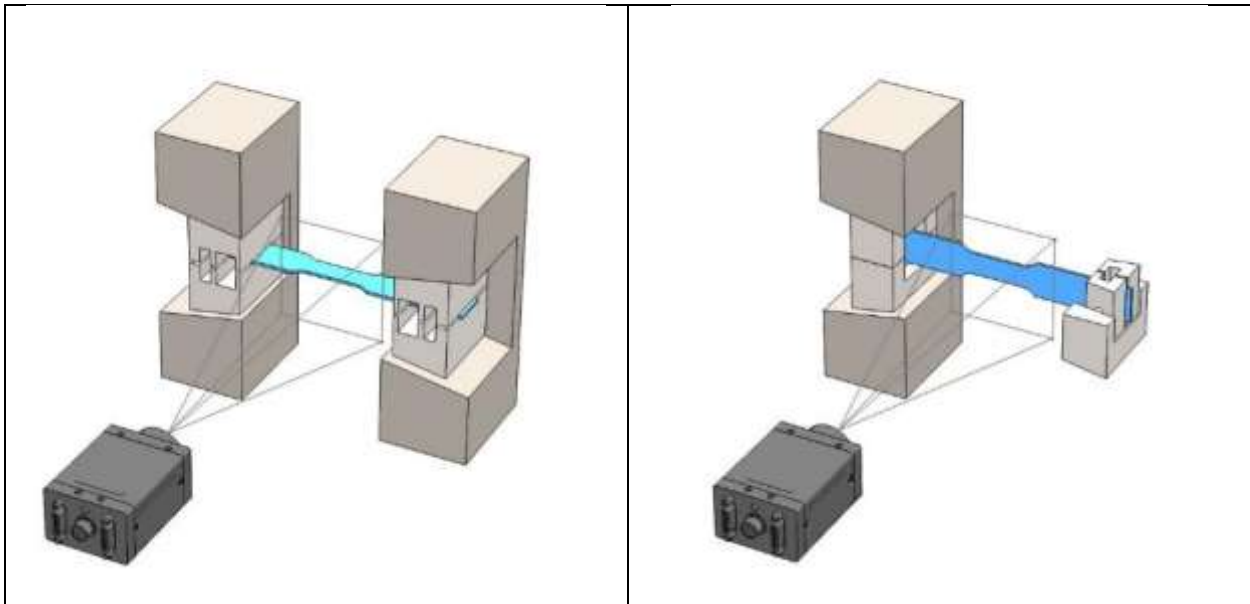


Figure 29: Gleeble 3500 and associated equipment including the thermocouple spot welder, computer for loading test programs, and the control panel for manual Gleeble control

For this research, the Gleeble 3500 was utilized for elevated temperature tensile testing, including heating, and cooling the specimen to follow a representative hot-stamping thermal cycle. To maintain consistent electrical contact between the grips and the specimen, wedge grips with a smooth contact surface were used to clamp the specimen. The lack of knurling on the contact face significantly reduces the contact friction between the wedge grips and the specimen, necessitating the specimens to be pin loaded in order to apply a tensile force without slippage. The default position of the gripped specimen in the Gleeble results in the thickness face being oriented towards the front and rear observation windows of the test chamber. To enable DIC observation of the specimen surface, the specimen needs to be rotated 90° about the specimen's longitudinal axis. This was achieved with a custom designed set of nested wedge grips inspired by Li *et al.* [45], where the outer grips match the profile of standard grips but includes a trapezoidal internal cavity that allowed for another set of wedge grips to be nested within. A second smaller set of inner wedge grips were

then designed to nest inside the outer grips such that when tension is applied, compressive clamping forces was generated. The inner grips clamped about a plane perpendicular to the clamping plane of the outer grips, enabling the specimen to be rotated 90° from its original orientation. A press-fit dowel hole was placed in the inner grips to allow for a dowel pin to be used for pin loading the specimen. Drawings and the CAD for these wedge grips are included in Appendix A. Figure 30 shows a schematic of the camera view with the default and rotated specimen orientation.



*Figure 30: Default specimen orientation (left) and the rotated specimen orientation (right) accomplished with nested wedge grips. The right figure hides the right jaw and top outer grip to better reveal the nested grip assembly.*

Other researchers have utilized bolted grip designs, where the bolt pre-load is solely responsible for providing the clamping force for electrical contact [44]. However, the nested wedge grips offer much more consistent (electrical) contact due to increasing contact pressure with increasing tensile load, rather than the non-uniform contact pressure from the bolt pattern. The experimental setup procedure is also much easier without the need for tightening and loosening several bolts for every specimen. An additional benefit of the nested grips is that the inner grips have been designed to contact the specimen further away from the centre of the specimen.

Cooling (or quenching) the specimen to the desired test temperature after austenitization at a rapid rate is essential to accurately represent the air-cooling and die quenching stages of a conventional hot stamping

process. To accomplish this, an air nozzle feeding pressurized room temperature air is directed at the centre of the specimen during testing. Although water can achieve higher cooling rates, it was not used in this work so as to not interfere with capturing photos for DIC analysis. At first, a flexible plastic coolant hose with a plastic flat nozzle was used. However, if placed too close to the specimen, the plastic nozzle was observed to melt. Additionally, since the nozzle needed to be moved every time specimens were to be removed or installed, the nozzle position was inconsistent between tests, leading to inconsistent cooling results. Lastly, the highly flexible plastic hose experienced significant deflection when high pressure air passed through, again resulting in inconsistent cooling results. To remedy this, a more rigid metal (brass and stainless steel) quench hose was designed and implemented from commercially available pipes and pipe fittings. The quench hose was routed along the side of the Gleeble chamber to avoid interference with the operator or the cameras. A stainless steel spray nozzle was attached to the end of the quench hose such that melting or other temperature damage was avoided. A quick-disconnect hose coupling was utilized along the quench hose such that the assembly can be easily separated when removing and installing specimens, enabling easier setup and a consistent quench nozzle positioning between all experiments. Figure 31 shows the interior of the Gleeble chamber, with the rotated specimens (and nested grips) and the quench hose.

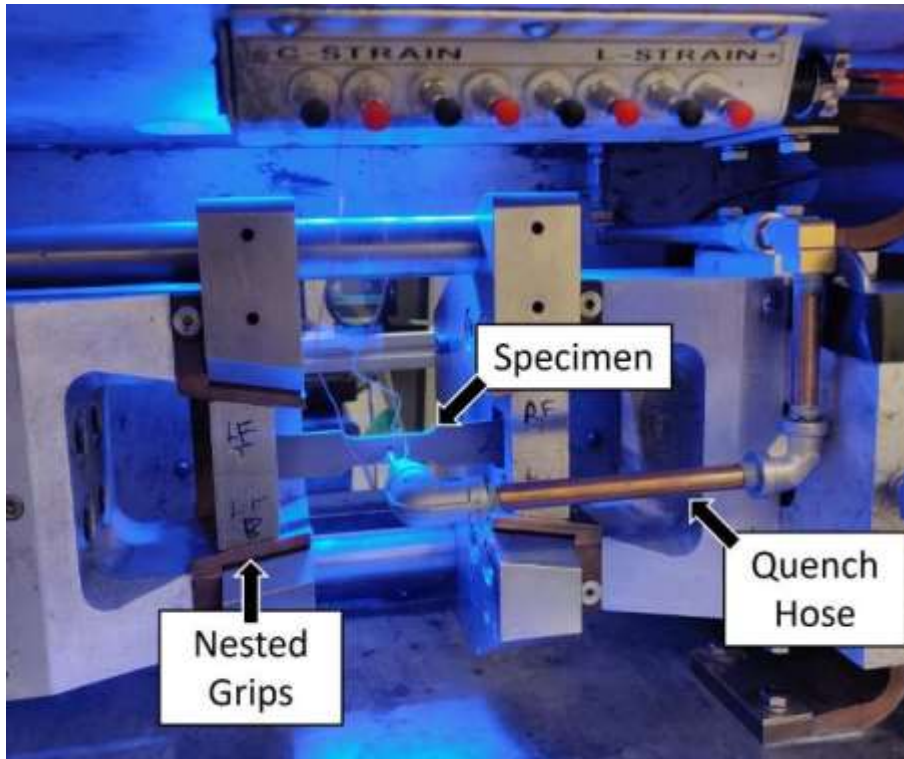


Figure 31: Gleeble chamber interior setup, featuring the nested grips to rotate the specimen orientation, and the air hose for quenching/cooling

#### 2.2.4. MTS Universal Test System

An MTS Criterion Series 45 electromechanical test system was used to perform room-temperature, quasi-static tensile tests. Specimens were clamped using knurled wedge grips and an MTS 685 hydraulic grip supply to achieve sufficient grip pressures to avoid specimen slippage. Tensile tests were conducted by controlling the displacement (stroke) rate of the crosshead. Load and stroke were recorded by the MTS machine; however, all tests were conducted with an external camera system to acquire images for 3D DIC analysis of the specimen surface displacements. Figure 32 shows the MTS frame and the DIC image acquisition setup for room temperature tensile tests.

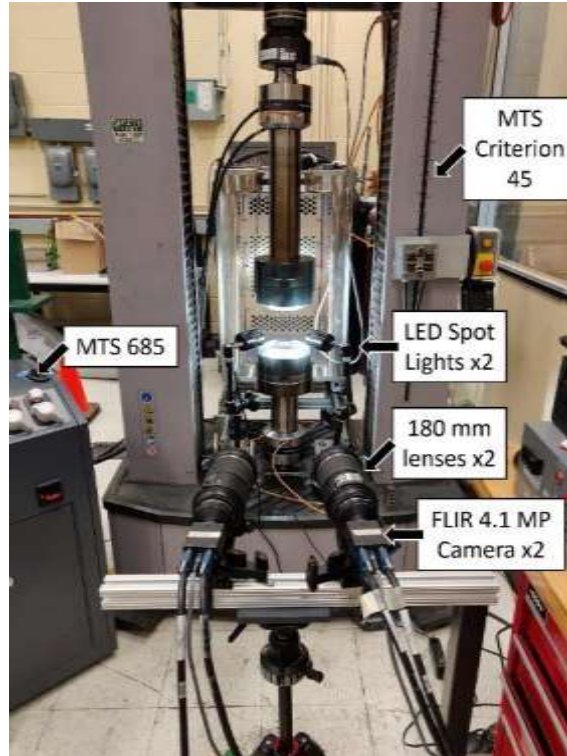


Figure 32: MTS tensile frame and DIC image acquisition setup, MTS 685 hydraulic grip supply partially shown to the left

### 2.2.5. Optical Strain Measurement (Digital Image Correlation) Equipment

Two DIC image acquisition systems were used for this research. The image acquisition system used for room temperature tests were two TAMRON 180 mm F/3.5 macro lenses mounted on two Point Grey (now FLIR) GZL-CL-41C6M-C 4.1 megapixel (MP) cameras, with a maximum acquisition rate of 150 frames per second (FPS). Two spotlights were used to provide uniform lighting conditions on the specimen and were positioned to the sides of the specimen. Figure 32 shows a picture of the DIC setup for room temperature testing on the MTS tensile frame.

For the elevated temperature tests, two Nikon 60 mm f2.8 lenses mounted on two FLIR GZL-CL-22C5M-C 2.2 MP 280 FPS cameras were used to acquire images of the specimen during testing. The 2.2 MP camera sensors were used instead of the higher resolution 4.1 MP sensors because of the higher permissible acquisition rate of 280 frames per second. Even higher acquisition rates would have been more desirable for the highest strain rate tests, however, other available cameras offering higher acquisition rates were lower resolution and were significantly larger in comparison, requiring more physical space than

available. Larger cameras and lenses would be difficult to incorporate around the Gleeble observation window due to the tight spaces and small window area. Two MidOpt BP470 blue bandpass filters (part number BP470-62) were attached to the front of the camera lenses to filter out excessive light at elevated temperatures. To uniformly increase the lighting on the specimen surface, two Smart Vision Lights SC75 blue-colored brick lights (part number SC75-470) were utilized. Blue (470 nm) light was used instead of standard white spotlights such that the light is not filtered out by the bandpass filters. The standard observation window on the Gleeble was replaced with a new, clean pane of borosilicate glass to ensure clear and consistent images. Figure 33 shows a picture of the DIC setup used for elevated temperature tests with the Gleeble.

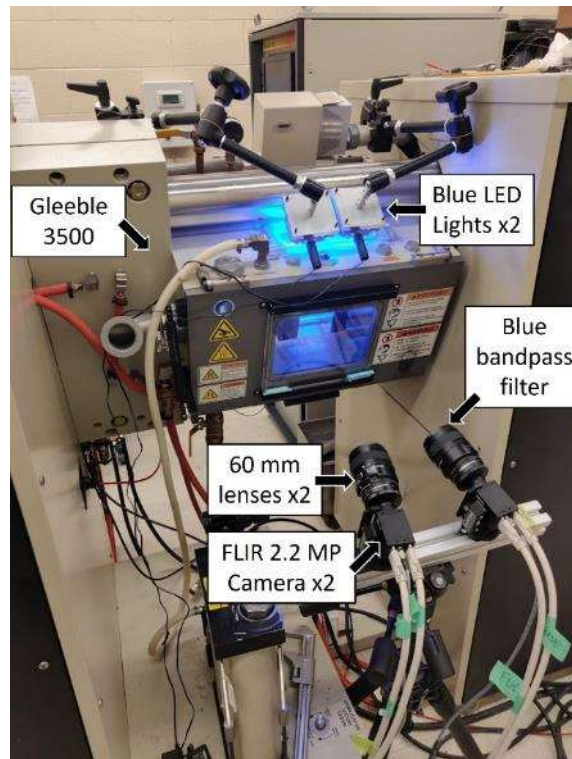


Figure 33: Image acquisition setup for the Gleeble, with both cameras facing the specimen from the rear window and two angled overhead blue LED lights directed through the top window

To interface the aforementioned cameras with a computer for image storage and processing, two frame grabbers (NI PCIe-1433) were installed on the computer with the image acquisition software. To record other data from the test frame (typically analog load cell and crosshead displacement signals), a multifunction data acquisition device (NI USB-6361) was connected to the DIC computer. The images for

DIC analysis were acquired using the software Vic-Snap, and the images were processed with Vic3D (versions 8 and 9) [83] (both software provided by Correlated Solutions) to calculate surface displacements and strains.

### **2.2.6. Metallography and Metallography Equipment**

Metallographic preparation for hardness testing and microscopy analysis was performed on various specimens throughout this research. In general, metallography specimens were first rough cut from small sheets or tensile geometries with a Struers Labotom-5 manual cut-off machine. For select specimens, a Struers Accutom-5 precision cut-off machine was used for a finer surface finish and more precise cuts. Specimens for microscopy were hot mounted with Struers Durofast and Multifast resin using a Buehler SimpliMet 1000 mounting press with the Struers recommended mounting cycle settings. To stand the thin sheet specimen such that the thickness face is exposed after mounting, fixation clips were used to hold specimens upright in the mounting press. After mounting, the specimens were sequentially ground with P800, P1200, P2400, and P4000 silicon carbide grinding paper and then polished with a 3  $\mu\text{m}$  diamond suspension in a Struers TegraPol-15 automatic polishing machine. Specimens used for microscopy were etched with a 5% Nital solution until the grain structure was revealed, then cleaned with methanol and dried prior to observation.

For observing microstructures and taking micrographs, a Keyence VHX-5000 digital optical microscope was utilized. The microscope was calibrated with a Keyence OP-87427 calibration grid prior to every use to ensure accurate length measurements. For micrographs, a Keyence VH-Z500R 500x-5000x variable zoom lens was used to capture the microstructure. Due to the poor image quality at higher magnifications, most micrographs were taken at between 500x-2000x magnification. For macro observations and measurements related to overall specimen dimensions (width, total thickness), a lower magnification VH-Z20R 20x-200x variable zoom lens was used.

### 2.2.7. Microhardness Tester

Hardness tests were performed with a calibrated Wilson Instruments 402 MVD Vickers microhardness tester. All hardness measurements were taken with a 1 kgf indenting force.

## 2.3. Surface Alloying Experiments

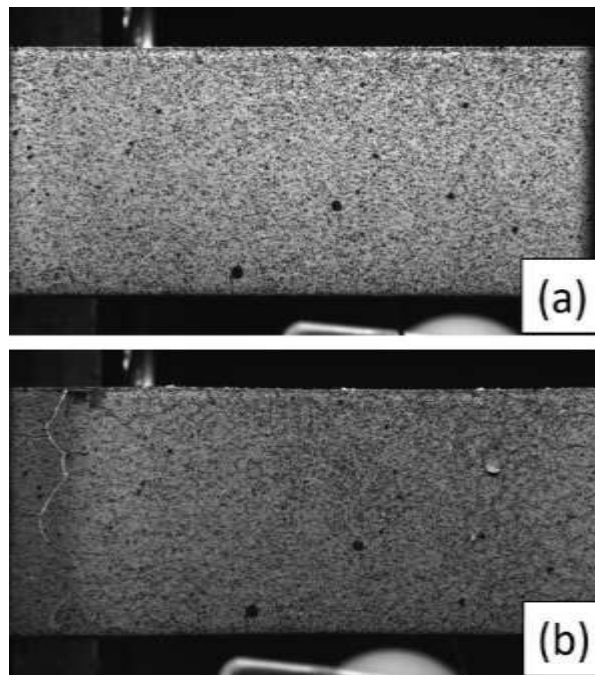
As mentioned in the introduction, various high temperature paints or coatings have been utilized for DIC analysis over 900°C, however past applications have been limited to low strain experiments. PHS in its austenite state is highly ductile, and specimens can be deformed beyond 50% strain during tensile testing (at around 900°C) before fracture. Therefore, a basecoat that is both ductile and high temperature-resistant is essential for the speckle pattern to remain for image capture and DIC analysis. Surface alloying experiments were conducted on both PHS 1500 and PHS 1800 in an attempt to identify a suitable coating that enables a painted pattern for high temperature DIC analysis.

The first issue that needs to be addressed is the Al-Si coating on the as-received material. During heating to the austenitization temperature in a conventional furnace, the Al-Si coating is known to melt at approximately 600°C before resolidifying [19]. For DIC analysis, a liquified coating would ruin any speckle pattern on the Al-Si coating and thus prohibit any meaningful DIC analysis afterwards. The simplest solution is to use uncoated PHS (in the form of uncoated as-received sheet or coated sheets with the coating manually removed) for constitutive testing. This is a common approach utilized by Li *et al.* [45] and Abspoel *et al.* [43], for example; however, to avoid surface oxidation during the test, a vacuum or inert gas environment must be used. There is a desire to develop a test method that avoids the necessity of vacuum or inert gas environments due to the added cost, time, and complexity of each test. In addition, vacuum or inert gas chambers are not readily available or feasible for many other experimental setups or tests. Specifically, it was desired that the developments from this research would also be applicable to high-temperature formability (dome) testing without necessitating the use of a vacuum or inert gas environment. To achieve this, a technique referred to as “surface-alloying” was developed to pre-treat the as-received Al-Si coating prior to constitutive testing such that coating removal is not required. This is done by first heating



and holding the as-received material in an oven beyond the initial coating melting temperature for between 30 seconds to 10 minutes. As the specimen is heated, the coating would melt, resolidify, and then transform to consist of higher melting-point Al-Si-Fe intermetallic alloys (from the surface alloying with the steel substrate). Thus, when the surface-alloyed specimen is heated again to austenitization temperatures prior to tensile testing, the coating would no longer melt during the heating stage.

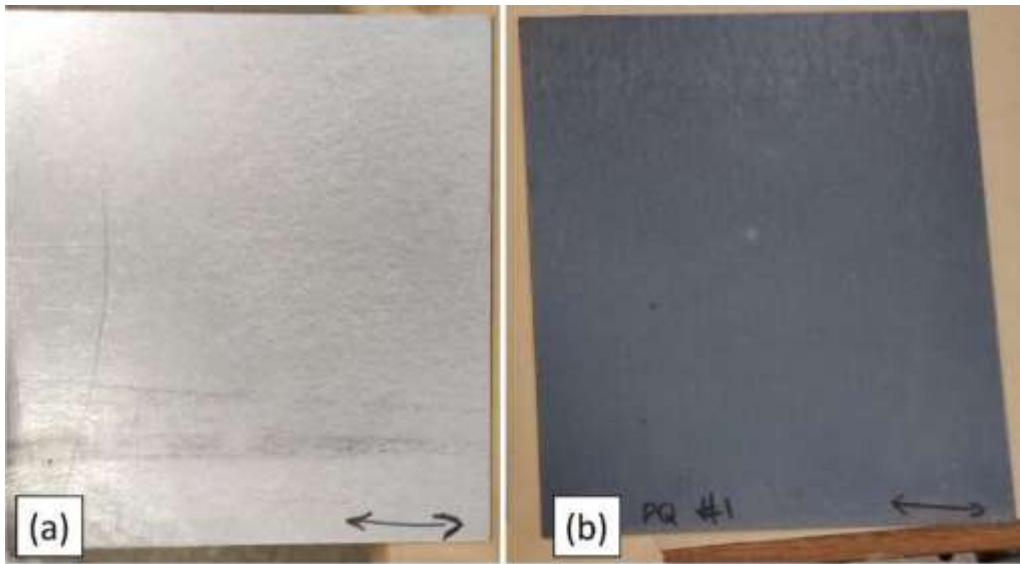
The second issue with high temperature DIC is the brittleness of high temperature paints/coatings as mentioned in the introduction. A preliminary experiment conducted with a commonly available aerosol high-temperature paint (VHT FLAMEPROOF header paint, rated for 704°C-1093°C) showed significant cracking solely due to thermal strains from heating, without any additional applied deformation. Figure 34 shows a picture of a painted specimen (black speckles on white basecoat, both colors are VHT FLAMEPROOF header paints) at 930°C, with cracks throughout the pattern and paint flakes detaching from the surface.



*Figure 34: High temperature aerosol paint speckled pattern at (a) room temperature, and at (b) 930°C*

It was noted however, that only the large continuous basecoat experienced cracking when heated. During preliminary experiments, the small speckles of aerosol paint did not crack during heating or during

deformation. It was also noted that the Al-Si coating of surface alloyed specimens could potentially act as a dark substrate for a speckle pattern, since the Al-Si specimens darken significantly after the surface alloying heat treatment cycle. This darkening can be seen with any Al-Si hot stamped part, where the as-received “silver” surface transforms to a dark grey or dark blue color after press hardening. Figure 35 shows a photo of PHS 1800 in its as-received state and after conventional austenitization (5 minutes in a 930°C oven) and rapid die quenching.



*Figure 35: PHS 1800 flat blanks in the (a) as-received state, (b) after hot stamping*

Additionally, the surface alloyed coating was not observed to crack until extremely high strains (with coating cracks initiating only after the onset of localized necking) during initial tensile experiments. Therefore, rather than assessing the feasibility of various high temperature paints/coatings, additional surface alloying experiments were conducted in order to produce a sufficiently dark Al-Si basecoat for DIC analysis.

The primary challenge associated with developing the surface alloying treatment was ensuring that the time at temperature does not affect the constitutive response of the PHS. Since the surface alloying procedure essentially acts as a short annealing or normalizing treatment, there could be a likelihood of softening in the material response due to potential grain growth and possible austenitization. To minimize the effect of surface alloying on the material response, the lowest treatment temperature and shortest

treatment time was determined. The two process parameters that were varied for the surface alloying experiments were the treatment temperatures (between 600 - 800°C), and the total time in the furnace (30 seconds -15 minutes). The viability of the coating color after treatment was preliminarily evaluated visually and then confirmed by creating a speckle pattern that was evaluated with DIC analysis. After surface alloying, the treated material was compared to the as-received material to evaluate the effects of the surface alloying procedure. Optical micrographs were taken of the materials to compare the microstructure between the as-received and surface alloyed material conditions. Elevated temperature tensile tests were also conducted on as-received and surface alloyed specimens to evaluate the constitutive behaviour before and after the surface alloying process.

To conduct the surface alloying experiments, a full size blank was sheared into many smaller sized 7 inch x 9 inch rectangular blanks. The size of these smaller blanks was selected for ease of manufacturing of tensile specimens after the surface alloying treatment. The electric furnace (Section 2.2.1) was used to heat treat these specimens, and the hydraulic press (Section 2.2.2) with flat dies was used to cool (quench) the blanks afterwards. To surface alloy, the as-received PHS blanks was manually placed in the oven after it was preheated to the desired temperature. Once placed inside the oven, a timer was started to record the total time in the oven. After the desired amount of time, the blanks were manually removed from the oven and were immediately transferred to the hydraulic press. The hydraulic press was used to rapidly quench the blanks, so as to stop any further heat treatment, while maintaining sheet flatness. After die quenching, the blanks (now below 50°C) were removed from the press to air cool until room temperature.

To understand the thermal history of the blanks within the oven, thermocouples were attached to the surface of several modified blanks prior to heat treatment. These thermocouples were connected to a data acquisition system to record the temperature history of the surface, at the centre of the blank. These modified blanks were the same dimensions as the previously mentioned blanks but contained a single 4mm diameter hole that was drilled in the centre to allow for a bolt to pass through. A high temperature resistant K-type thermocouple was then placed in contact with the blank surface at the through hole. The contact tip of the thermocouple was then tightly clamped to the surface of the blank with a M4 stainless steel socket

head bolt, nut and two plain stainless steel washers. This thermocouple was then interfaced with the data acquisition device to record data to a laptop nearby. Temperature data was recorded from prior to manual insertion into the oven, until the blank was removed from the oven. Temperature data for the quenching stage was not recorded since the hydraulic press with flat dies was not compatible with the thermocouple and fasteners. Figure 36 shows a setup of the modified blank, thermocouple and data acquisition system for temperature recording.

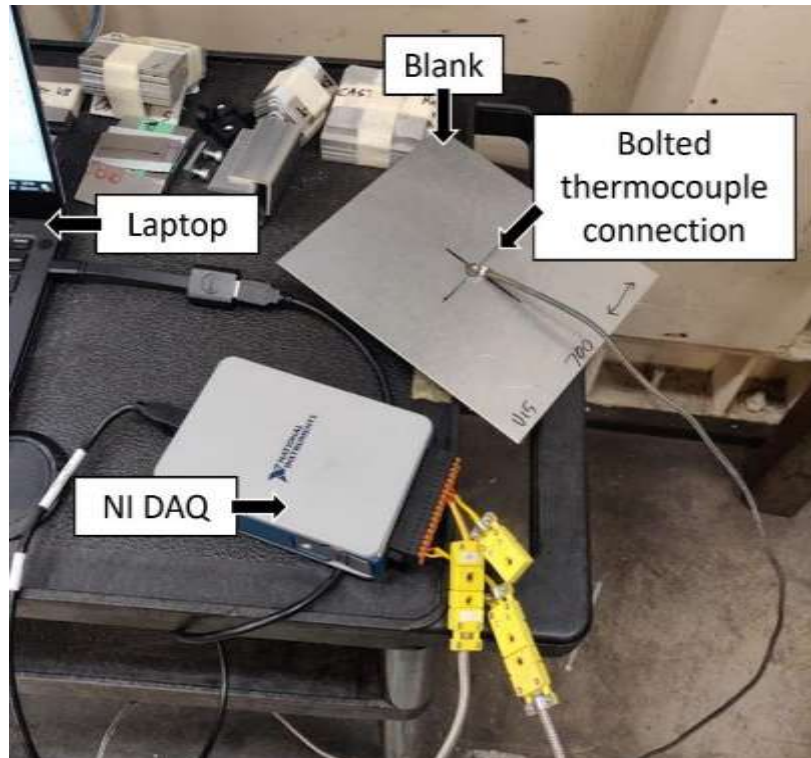


Figure 36: Temperature recording setup for the electric furnace, showing the modified blank and the thermocouple connection

## 2.4. Room Temperature Tensile Tests

Quasi-static room temperature tensile tests were conducted on quenched PHS 1500 and PHS 1800 to evaluate the critically quenched (fully martensitic) strength of both materials after hot stamping. To prepare the specimens, small as-received blanks were placed into a preheated electric furnace at 930°C for 5 minutes to completely austenitize the material. These blanks were then removed from the oven and placed into the hydraulic press with flat dies to rapidly quench the blank, forming a fully martensitic microstructure. After quenching, the blanks were water jet cut into smaller pieces and then CNC machined to the final tensile

specimen geometry. Prior to the tensile test, specimens were speckled by first painting a white background with Rust-Oleum Painter's Touch White Primer spray paint. After air drying, the specimen was then lightly painted with Rust-Oleum Painter's Touch Flat Black Primer spray paint to achieve a fine speckle pattern.

The MTS tensile frame (Section 2.2.4) was used to conduct quasi-static room temperature tensile tests, and the room temperature 3D DIC acquisition setup (Section 2.2.5) was used to record the surface deformation of the specimens. To set up the test, a single speckled specimen was first clamped to the jaws of the tensile tester to focus the cameras and adjust the lighting to achieve high quality images for DIC analysis. The cameras were set up in accordance to the recommended positions and angles based on the lens size from the testing guide by Correlated Solutions [54]. After this, a calibration grid was used to calibrate the camera setup as per the recommended calibration practices from the testing guide [54]. To test, specimens were longitudinally aligned with the tensile frame with a carpenter square and then clamped from both ends to the jaws of the tensile tester. The load cell was then zeroed to eliminate any residual forces from the high pressure clamping process. Image acquisition is then initiated, followed by the test program. Specimens were loaded at a crosshead speed of 0.025 mm/s, which roughly corresponds to a strain rate of  $0.001\text{s}^{-1}$  (specimen gauge length of 25 mm). Specimens were pulled to fracture, at which point the testing is completed. Images were acquired at a fixed interval that resulted in approximately 500-600 total images (per camera) over the duration of the test.

## **2.5. Elevated Temperature Tensile Tests**

### **2.5.1. General Considerations**

As mentioned in Section 2.2.3, several modifications were made to the Gleeble 3500 to better enable high temperature constitutive testing of PHS with DIC analysis. This involved implementing the nested grips to rotate the specimen, orienting the specimen face to the cameras. A rigid quench hose was designed and implemented to allow for consistent quenching between repeat experiments. Additionally, tubular ceramic insulators were placed around the thermocouple ends that were attached to the specimen to prevent contact between the thermocouples during testing. During preliminary testing, thermocouple contact was

observed at elevated temperatures when the thermocouples sag onto one another due to high ambient temperatures. Unintended contact between the thermocouples wires interfered with the temperature reading and results in loss of temperature control during testing.

### **2.5.2. Specimen Design**

In the Gleeble thermo-mechanical simulator, the grips that hold the specimen not only provide electrical contact to supply the current but also draw heat away from the centre of the specimen due to conductive heat transfer. Because of this, a non-uniform temperature profile develops longitudinally along the specimen when heated, where the centre of the specimen is the hottest [39]. The temperature difference between the centre of the specimen and the grips are further amplified by the water-cooled jaws that hold the grips. Understanding and characterizing the temperature profile is extremely important to the determination of the flow curve, because a non-isothermal gauge region would not result in uniform deformation within the gauge region during testing.

Li *et al.* [45] studied the temperature profile for a custom tensile geometry and showed a increase in the temperature uniformity at the centre of specimen with increased grip span. Li *et al.* [45] denoted this region as the uniform temperature zone (UTZ) and analyzed the deformation data within this region. Gui *et al.* [84] observed a 8 mm uniform temperature region at the centre of a 35 mm gauge length specimen and therefore only considered the 8 mm region as the effective gauge length for strain calculations. Abspoel *et al.* [43] also studied the temperature profile for a custom tensile geometry and developed several modifications to increase the temperature uniformity in the gauge region. The final design was quite complex, requiring electrical shunts to be attached to the specimen, however it was capable of maintaining less than a 10°C variation in temperature within a 30 mm gauge length.

Ultimately, most specimen modification principles can be traced to a study of specimen geometry and its corresponding effect on the temperature profile along the length of the specimen by Walsh *et al.* [39]. Although Walsh *et al.* [39] performed the studies on round specimens, the same principles and conclusions can also be applied to flat specimens since the results only addressed temperature variation along the

longitudinal direction of the specimen (and did not consider temperature variation within the cross-section) and were based on geometric size rather than shape. To summarize their findings, a specimen with lower thermal conductivity (material property), smaller cross-sectional area (geometric), and greater span between grips (geometric) resulted in lower temperature variation along the length of the specimen [39]. Since the thermal conductivity of the material cannot be changed, all modifications were focused on the geometry of the specimen.

A custom tensile geometry was developed to suit the needs of the current research, partially following the principles outlined by Walsh *et al.* [39] to minimize the temperature variation along the length, and partially to achieve consistent image quality for reliable DIC analysis. A standard specimen geometry was first selected as the starting point so as to not deviate significantly from commonly accepted industry standards. Two common specimen geometries are the ASTM E8 [85] specimen and the JIS #5 [86] specimen, both of which are intended for sheet metal/plate materials. The ASTM E8 geometry is much longer and slender design than the JIS #5, with a gauge length to gauge width ratio of 4:1, however it would need to be scaled down significantly to fit in the Gleeble while still allowing for enough travel to pull specimens to failure. For reference, the Gleeble 3500 only allowed for approximately 4.4" or 112 mm of grip span at full stroke. Although the slenderness of the design is attractive for minimizing the temperature variation, it was noted from initial experimentation that specimens with a greater gauge width provided substantially more surface area, allowing a better quality speckle pattern. Not only does a larger speckled area provide more data, but the speckle pattern was also noted to be less susceptible to edge disruptions such as burrs from manufacturing, oxidation on the thickness (machined) face during heating, and bright reflections from the machined edge. Therefore, the JIS #5 geometry, with a gauge length to gauge width ratio of 2:1, was selected as the base design for the custom specimen geometry. Several modifications were made to the tensile specimen geometry to reduce temperature variation along the specimen and reduce the likelihood of unwanted failure modes. Figure 37 shows a drawing of the geometry of the modified half scale JIS #5 (Modified-mini-JIS or MMJIS) specimen for Gleeble use. To fit the specimen within the Gleeble and reduce the cross-sectional area to minimize temperature variation, the JIS #5 specimen was

half scaled, resulting in a 12.5 mm gauge width and 25 mm gauge length. Zhumagulov [87] evaluated the difference between a regular scale JIS #5 specimen and a half scale JIS #5 specimen at room temperature and showed good agreement in engineering stress-strain results between the two specimen sizes. To reduce the temperature variation along the gauge length, the grip region of the half scale JIS #5 was lengthened to increase the span of the specimen. Additionally, a 5 mm diameter hole was placed along the centreline of the specimen, as close to the ends of the grip region as possible to maintain a long span, while ensuring no bearing damage or tear-out occurred when the specimen was pin loaded. The holes were placed 12 mm from the end edges of the specimen based on a simple shear tear out equation [88]. The width of the grip region was increased from 19 mm to 20 mm to minimize the likelihood of tension failure at the pin hole. It should be noted that the grip region was anticipated to remain around room temperature (due to the water cooled jaws), with an expected as-received tensile strength of approximately 500-600 MPa, while the hotter austenite centre was expected to deform at a much lower flow stress, depending on the specific test temperature and strain rate. The hole diameter was determined to be 5 mm, which enabled the use of the standard 3/16 inch (4.8 mm) diameter dowel pins to load the specimen without failure of the pin.

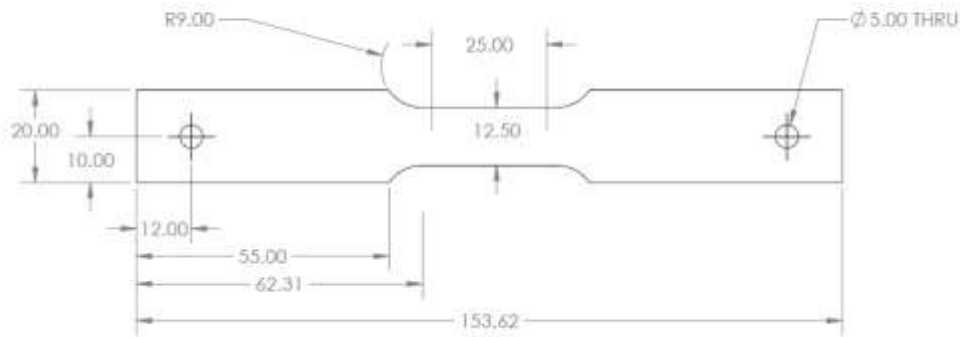


Figure 37: The modified half scale JIS #5 (MMJIS) specimen for Gleeble use, with critical dimensions labeled



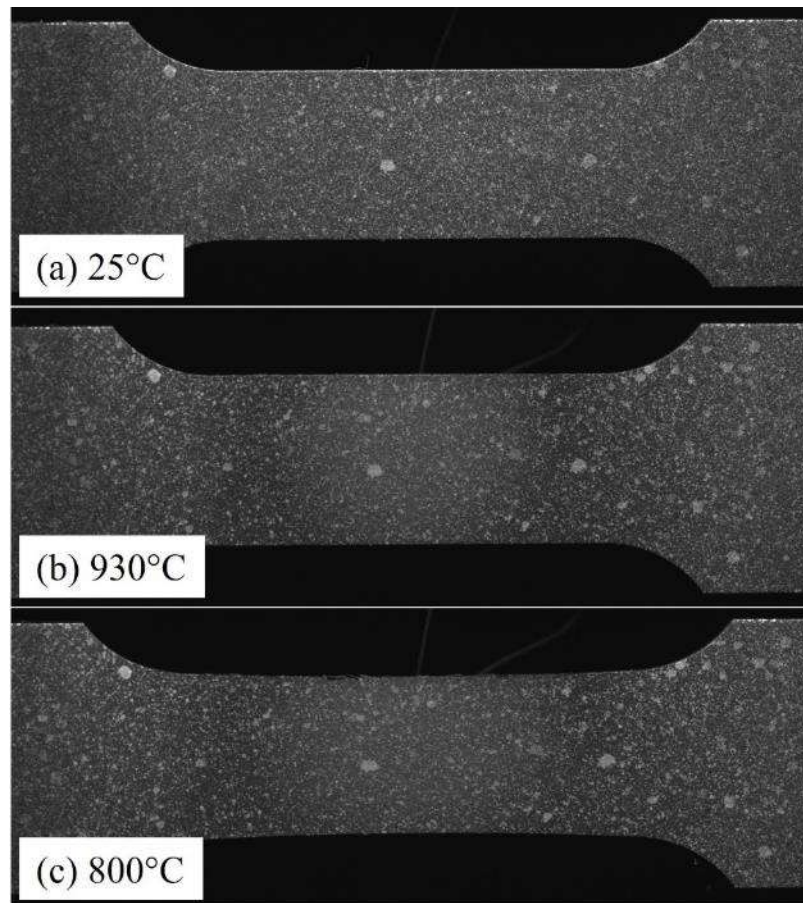
### 2.5.3. Surface Alloying Comparison

As mentioned in Section 2.3, surface alloying experiments were conducted to determine a process that would result in a suitable Al-Si coating for DIC image acquisition. For PHS 1500, the final surface alloying heat treatment cycle was determined to be 7 minutes at 700°C. For PHS 1800, the final surface alloying cycle was determined to be 10 minutes at 700°C. 700°C was selected because it was below the austenitization temperature of PHS 1500 and PHS 1800, which is approximately 800°C [9]. The 7 and 10 minute durations in the oven were determined experimentally to darken the coating to a dark grey color, which is necessary for creating the speckle pattern. A detailed discussion of the determination of these times and temperatures is provided in Section 3.2.

To conduct the surface alloying process, full-sized PHS blanks were cut into smaller rectangular blanks (approximately 7 inch x 9 inch) to fit between the flat quenching dies. The blank was then placed into the preheated electric furnace (Section 2.2.1) for a total time of 7 and 10 minutes for PHS 1500 and PHS 1800 respectively. After the appropriate time in the furnace, the blank was extracted, and die quenched for 20 seconds until approximately room temperature. The surface alloyed blank was then labeled, wrapped with masking paper to protect the coating from scratches, and stored. This process was repeated until a sufficient number of blanks were produced.

After surface alloying, the blanks were sheared into small rectangular blanks the width of a single specimen. These small blanks were then CNC machined to the final specimen geometry. Specimens were stored and transported with masking paper around each specimen to avoid scratches or other damage to the dark surface coating. In preparation for tensile testing, the specimens were speckled with a white high-temperature resistant aerosol paint (VHT FLAMEPROOF header paint) to create a fine, random speckle pattern. The header paint was ideal for the purposes of this research project as it was readily available at many major retail stores in Canada at the time of research. Additionally, despite the paint instructions recommending a sophisticated alternating heating and cooling curing cycle, no such cycle was necessary to achieve the desired high temperature performance. Prior to testing, a pair of thermocouples were spot

welded to the back side (unspeckled face) of the specimen for Gleeble temperature control. The specimen could then be assembled to the grips, and then placed within the Gleeble test machine for tensile testing. Figure 38 shows pictures captured from the DIC camera system of a speckled specimen at room temperature (prior to heating), at 930°C (after heating), and during deformation at 800°C.



*Figure 38: Images of a speckled specimen (a) at room temperature (25°C), (b) after the heating stage (930°C), (c) after quenching and during deformation (800°C)*

#### **2.5.4. Test Program**

A test program that resembles an industrial hot stamping cycle was used to process the specimen prior to the tensile test. The test program can be distinguished by 5 stages which include heating, soaking, quenching, stabilization, and tensile testing. At first, the specimen was heated from room temperature (approximately 25°C) to 930°C at a rate of 15°C/s. Typically, target austenitization temperatures between 900-950°C are reported in literature [9]. The heating rate of 15°C/s was similar to heat rates used by other

researchers like Merklein and Lechler (16°C/s) [42] and Abspoel *et al.* (15°C/s) [43]. Afterwards, the specimen is held at 930°C for 4 minutes to ensure a fully austenite microstructure. This is representative of the time a blank would remain in a roller hearth oven, however times can vary between 3-8 minutes depending on sheet thickness and/or the oven temperature [9]. After soaking the specimen at 930°C, the specimen is then cooled by compressed air at a cooling rate of 50°C/s to the desired tensile test temperature. This step represents the industrial processes of blank removal from the oven, placement into the forming press, and the approximately die quenching rate. Although higher cooling rates may be more representative of die quenching rates, it is not possible to consistently achieve higher cooling rates with compressed air cooling in the Gleeble. After being cooled, the specimen is rested for 5 seconds as thermal irregularities stabilize along the length of the specimen. Thermal irregularities can be observed immediately after the air quenching stops and can be seen by a slight temperature increase due to the resistive heating being unbalanced by the stoppage of air cooling. This step is not representative of any stage in the industrial hot stamping process, however, is necessary in ensuring that the centre of the specimen is at the correct temperature prior to the tensile test. Finally, after 5 seconds of rest, the specimen is loaded in tension at a constant crosshead velocity (varying between 0.25 – 38.0 mm/s) to achieve the desired strain rate condition until the specimen fractures. All data collection concludes at this point. Lastly, the specimen is air quenched at maximum pressure for 30 – 60 seconds to cool the specimen to room temperature for handling and removal, however this is irrelevant to the test results. Figure 39 shows a schematic of the Gleeble test program and the temperature cycle every specimen undergoes prior to tensile testing.

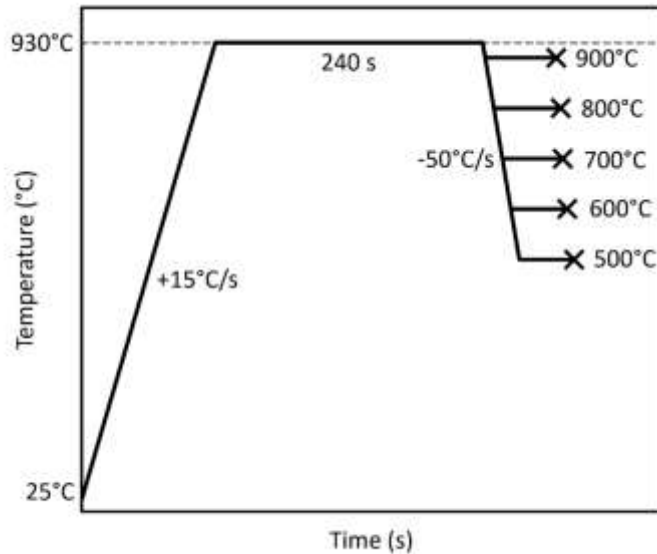


Figure 39: Schematic of the temperature-time tensile test program for elevated temperature testing of PHS 1500 and PHS 1800

At the start of the test procedure described in the previous paragraph, a 0.2 kN tension force (approximately 10 MPa tensile stress) was applied to the specimen to ensure the specimen does not buckle against the grips due to thermal expansion when heated. Additionally, preliminary screening experiments were conducted to determine the appropriate displacement rate in order to achieve the desired strain rate. Image acquisition for DIC analysis was initiated prior to heating and was stopped after the specimen fractures.

Isothermal tensile tests were conducted at five temperature conditions and between three to five strain rate conditions. The temperature conditions were selected to be between 500°C and 900°C, at 100°C increments. The 600°C-800°C temperature conditions capture the primary temperature range in which forming occurs in an industrial hot stamping process [9]. The 500°C and 900°C conditions were selected to provide more insight into the material behaviour at the upper and lower limits of the forming process. The targeted strain rate conditions varied from  $0.01\text{s}^{-1}$ ,  $0.05\text{s}^{-1}$ ,  $0.1\text{s}^{-1}$ ,  $0.5\text{s}^{-1}$ , and  $1\text{s}^{-1}$ . Strain rates above  $0.1\text{s}^{-1}$  are more representative of strain rates observed in industrial hot stamping processes, where a part would be fully formed (experiencing about 20-30% strain) within 1s of high speed deformation. The lower strain rate conditions were evaluated to provide additional insight into the material behaviour, especially in regard to

strain rate sensitivity of the hardening behaviour. A  $0.05\text{s}^{-1}$  strain rate condition test was conducted at  $900^\circ\text{C}$ , before it was determined that a  $0.01\text{s}^{-1}$  strain rate condition was also feasible. No  $0.01\text{s}^{-1}$  strain rate condition tests were conducted at  $500^\circ\text{C}$  and  $600^\circ\text{C}$ , because the long duration of the test would result in considerable pearlite and bainite formation, rendering the results mostly irrelevant as all forming should be completed while the microstructure phase is primarily austenite. Three repeat tests were conducted for each test condition, and the average standard deviation of the true stress at each test condition is calculated as a measure of repeatability. Table 2 below shows a test matrix of the isothermal tensile tests conducted for this research.

*Table 2: Proposed tensile test matrix for both PHS materials*

Temperature ( $^\circ\text{C}$ )	Target Strain Rates (1/s)				
	0.01	0.05	0.1	0.5	1
900	x	x	x	x	x
800	x		x	x	x
700	x		x	x	x
600			x	x	x
500			x	x	x

Ideally, tests at even higher strain rates, such as at  $10\text{s}^{-1}$ , should also be conducted. However, the cameras utilized for this research would not be able to capture a sufficient quantity of images within the test duration. Higher frame rate cameras were available; however, they were much larger and bulkier to adequately fit a pair for 3D DIC analysis. An additional limitation was the time required for the Gleeble 3500 crosshead to accelerated to the desired velocity. For even faster deformation rates, this acceleration ramp up time was substantial, resulting in a non-constant strain rate during testing.

### **2.5.5. Results Post Processing**

Images acquired during the experiments were processed using the commercial DIC software Vic3D 8 (and later, version 9) by Correlated Solutions [83]. The digital images were first imported, then the area of interest (the speckled gauge region) was manually identified. Afterwards, an appropriate processing step (8 pixel length) and subset size (35 pixel length) was selected based on the recommended settings to minimize

noise. The images were processed with the zero-normalized squared differences correlation criterion to minimize the effect of lighting changes (due to heating, cooling) on the results [55]. The default settings were used for the remaining analysis parameters. The analysis settings used for the current research is summarized in Table 3.

*Table 3: DIC analysis settings used to process speckle pattern images from tensile testing*

Subset size (pixels)	35
Step size (pixels)	8
Subset weighting	Gaussian (default setting)
Correlation interpolation	Optimized 8-tap (default setting)
Correlation criterion	Zero-mean normalized sum of square differences
Strain filter size	27

Finally, the logarithmic (Hencky) strains were computed from the deformation results using default strain computation parameters. Figure 40 shows a raw captured photograph at 800°C and 30% extensometer elongation, and the post-processed image showing the principal ( $\epsilon_1$ ) strain field and a virtual extensometer.

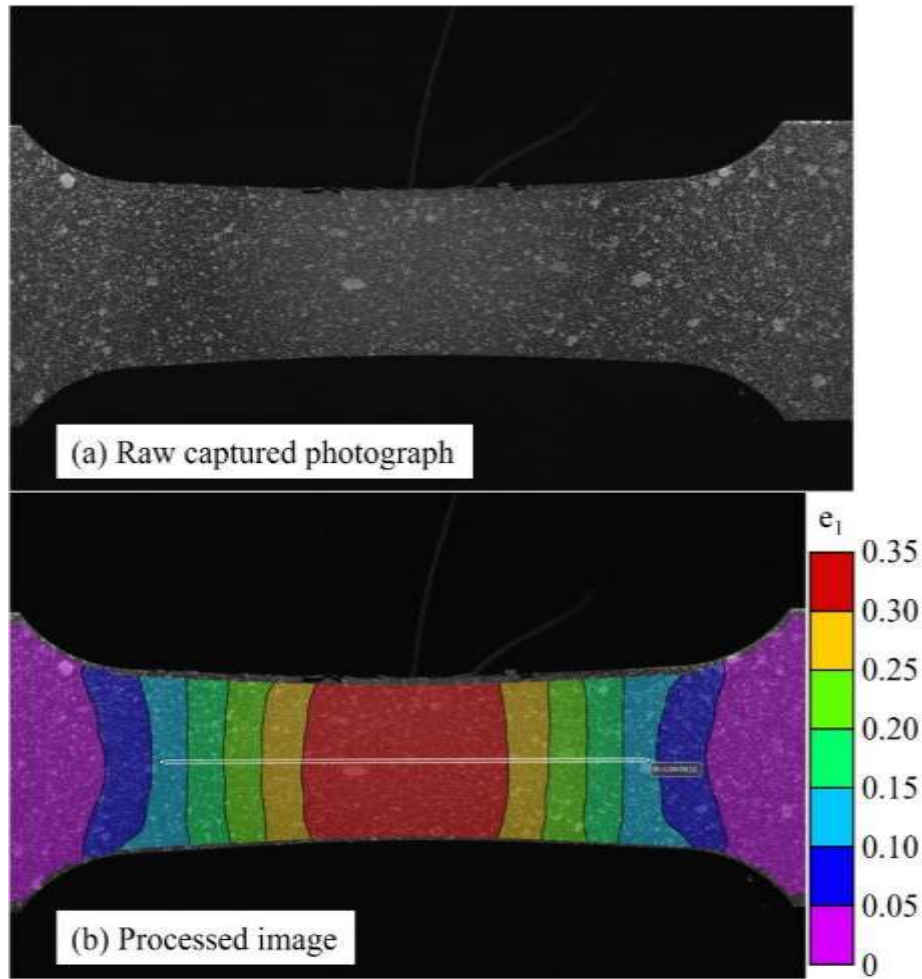


Figure 40: (a) raw captured image at 800°C and (b) the processed image showing the principal ( $e_1$ ) strain field

Typically, a virtual extensometer (a virtual ruler measuring the displacement of two selected points) is used on DIC results within the gauge length to determine gauge displacement and therefore strain. However, this was not feasible due to the non-uniform temperature profile along the length of heated specimens in this study. Rather than using a shorter virtual strain gauge spanning the uniform temperature region at the centre of the specimen to determine deformation strains, an alternative area reduction method (ARM) by Omer *et al.* [89] was utilized that only required data at the centre of the specimen where the temperature is controlled by the Gleeble apparatus. Using the ARM, the change in cross-sectional area can be calculated from the surface strains captured by DIC analysis. This was accomplished by tracking the change in the width of the specimen from DIC data and extracting the longitudinal and transverse surface strains at the centre of the specimen. In order to extract discrete data from the DIC results, the cross-section at the centre

of the specimen is first discretized into numerous sub elements. The thickness strains ( $\varepsilon_z$ ) of each sub element can then be computed by assuming volume conservation during plastic deformation, shown by Equation (17) where  $\varepsilon_x$  and  $\varepsilon_y$  are the surface strains in the x and y directions [89].

$$\varepsilon_z = -\varepsilon_x - \varepsilon_y \quad (17)$$

With thickness strains determined, the dimensional change of each sub element can then be determined by relating the thickness strain to the change in thickness. Equation (18) shows the relationship between thickness change and thickness strain, where  $t_i$  is the current thickness of the  $i$ -th element and is the variable to be solved,  $t_{0,i}$  is the thickness in the previous increment (initial thickness), and  $\varepsilon_{z,i}$  is the thickness strain.

$$\ln\left(\frac{t_i}{t_{0,i}}\right) = \varepsilon_{z,i} \quad (18)$$

By summing the new area of each sub element, the new total cross sectional area of the specimen can be calculated. Equation (19) shows the summation of the calculated thickness  $t_i$ , and measured width  $w_i$  to determine the instantaneous cross-sectional area at any given time.

$$A = \sum t_i w_i \quad (19)$$

Figure 41 illustrates how the cross-section profile at the centre of the specimen is determined by discretization. Figure 41 also shows the orientation of the strains to show how thickness strains can be derived from surface planar strains via volume conservation. Once the change of each sub element is determined, summing the area of each sub element in the cross-sectional plane results in the total cross sectional area of the tensile specimen.



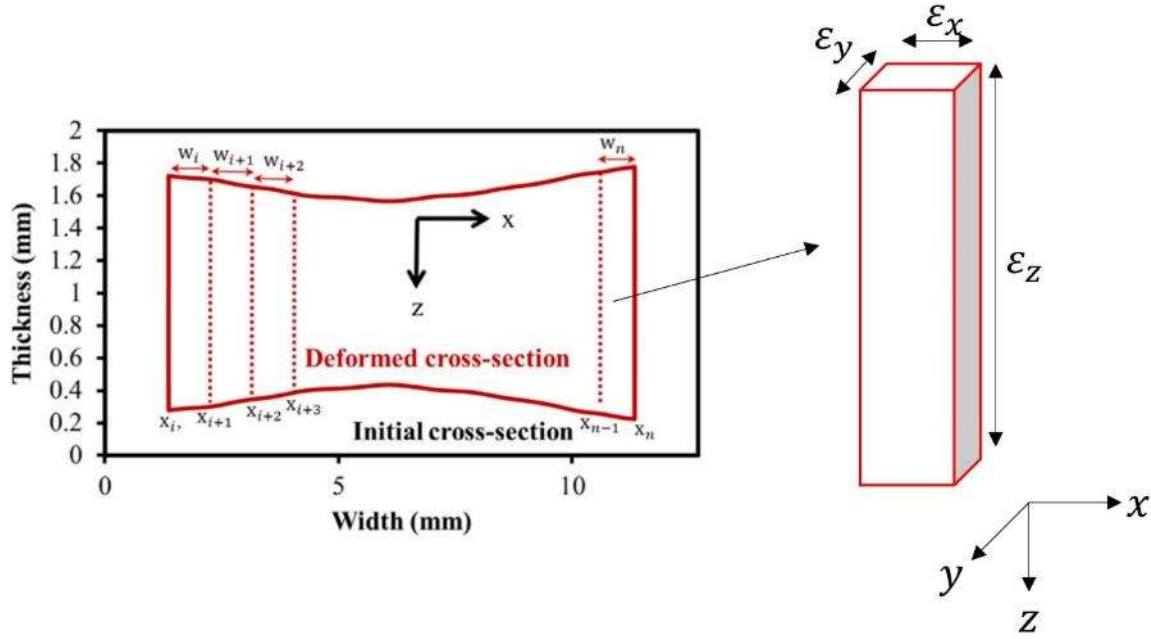


Figure 41: Constructed cross-section profile using the area reduction method and an example of how strains are applied to the discretized sections, adapted from Omer et al.[89]

To determine the true stress experienced by the specimen, the standard force over area equation shown in Equation (20), where  $F_i$  and  $A_i$  are the instantaneous force and instantaneous (cross-sectional) area, respectively.

$$\sigma_{true} = \frac{F_i}{A_i} \quad (20)$$

Instantaneous force is obtained from the tensile tester load cell and instantaneous cross-sectional area is derived from the area reduction method described. To determine the true plastic strain, which will be utilized for flow curve fitting, Equation (21) can be utilized based on changes to the cross-sectional area rather than longitudinal gauge deformation [89]. In Equation (21)  $A_0$  is the initial cross-sectional area,  $A_i$  instantaneous cross-sectional area,  $\sigma$  is true stress, and  $E$  is the elastic modulus. For reference, the first component of Equation (21) is simply the true (total) strain at the centre of the specimen.

$$\epsilon_{true, plastic} = \ln\left(\frac{A_0}{A_i}\right) - \frac{\sigma}{E} = \epsilon_{total} - \epsilon_{elastic} \quad (21)$$

The significant advantage of using the ARM is that the tensile test results are extracted from the centre of the specimen, which is the only location on the specimen that is precisely maintained at the desired deformation temperature for a tensile test on the Gleeble 3500. If using a virtual (or physical) extensometer, the effective gauge length (length of uniform deformation), would be very short, and would need to be determined for every temperature condition depending on the steady temperature variation along the specimen.

As a comparison, the stress-strain curves as determined by virtual extensometer and by using the ARM are shown in Figure 42.

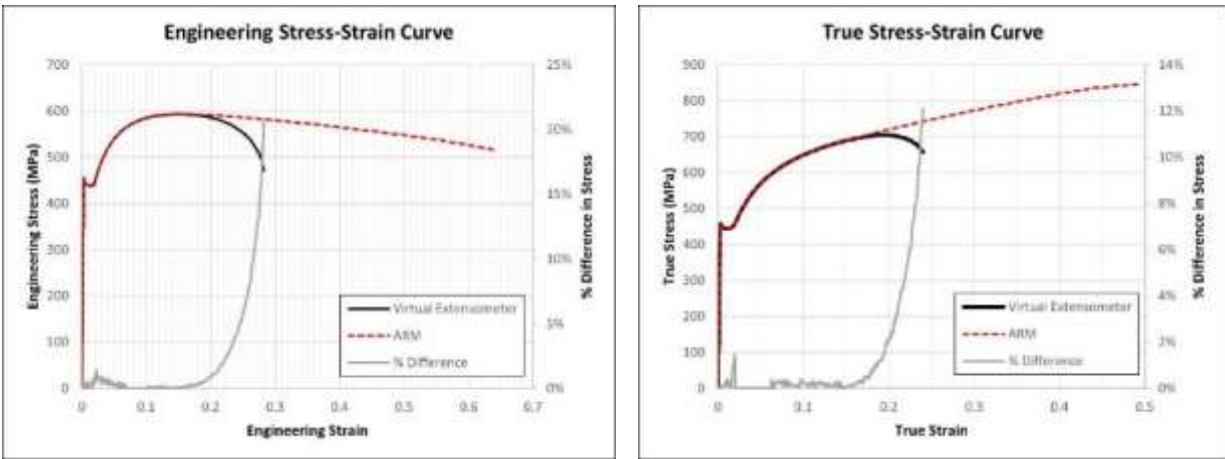


Figure 42: Engineering (left) and true (right) stress strain curves as calculated from results of a tensile test, using a virtual extensometer and the area reduction method (ARM)

The tensile test shown in Figure 42 was conducted on an as-received sheet of PHS 1500 at room temperature, at  $0.02 \text{ s}^{-1}$ . There is a maximum error of less than 2% between the results determined from the virtual extensometer compared to the results calculated from ARM. For the true stress-strain curves, the result is plotted to the point of specimen fracture. The ARM curve is the direct result of the ARM calculations, while the true-stress strain curve from the virtual extensometer was converted from engineering stress and strain via Equations (22) and (23). For the engineering stress-strain curve, the ARM curve was converted from the true stress-strain data whereas the virtual extensometer curve is obtained directly from the extensometer and load measurements. It should be noted that the equations to convert

uniaxial true stress and strain to engineering stress and strain are only valid until the onset of diffuse necking, therefore the converted data beyond the necking point are shown for reference only.

For reference, true strain or true stress can be converted to engineering strain or engineering stress by Equations (22) and (23), respectively [88].

$$\varepsilon_{engineering} = e^{\varepsilon_{true}} - 1 \quad (22)$$

$$\sigma_{engineering} = \frac{\sigma_{true}}{(1 + \varepsilon_{engineering})} \quad (23)$$

The procedure for applying ARM for experimental results analysis was performed in an identical manner to that presented by Omer *et al.* [89]. First, the speckled images taken during the test were calibrated and processed to obtain surface deformations and strains as described previously. After processing the deformation results to obtain surface strains, a line slice was drawn across specimen at the centre of the specimen, to extract 200 discrete data points. The surface displacements and strains at this centre line slice was then exported from Vic3D as a csv file, with data points recorded at every processed image. The data was then imported into MATLAB [90] for further data processing, fitting, and plotting purposes.

Using MATLAB, the area reduction method (ARM) was applied to the data exported from the digital image correlation software using Equations (17) - (21) highlighted above to obtain true tensile stresses and strains. Since a total of three repeat experiments were conducted at each test condition, the mean flow curve for each test condition was determined. In addition to the stress and strain data, instantaneous and average strain rates were computed for each test. The instantaneous strain rate was calculated by dividing the ARM calculated strain increment by the time increment between each data point. Due to the small time increments between each data point, noise from the strain calculation resulted in significant fluctuations in the instantaneous strain rate data. Smoothing was applied to the strain rate data to prevent negative instantaneous strain rate values and noisy fluctuations from being used for further calculations. The linear regression smoothing method in MATLAB was utilized with a smoothing window of 10% of the total flow

curve data to process the strain rate data to eliminate extreme fluctuations. The instantaneous strain rate was used for the fitting of the constitutive model to the experimental data.

The non-linear least squares curve fitting 'lsqcurvefit' function in MATLAB was used to fit the constitutive equation to the experimental data by solving for all unknown coefficients simultaneously. The non-linear least squares curve fitting function is a general purpose least-squares regression solver intended for determining coefficients of nonlinear equations [91]. The least-squares regression solver seeks to minimize the residuals of the fit and experimental data points using a trust-region-reflective algorithm, which iteratively reduces the domain of potential solutions until the solution converges on the minimum residual [91]. To better constrain the problem for faster solution times, an upper and lower bound, as well as an initial guess was set for all coefficients. The initial values used were simply the Norton-Hoff coefficients identified for PHS 1500 by Merklein and Lechler [42]. The upper and lower bounds were conservatively set to be 2 orders of magnitude above and below the initial values, with the expectation that the solution would be somewhat similar to the initial values. To utilize the 'lsqcurvefit' function, the modified Norton-Hoff equation (Equations (6) - (8)) was first defined symbolically in MATLAB. Afterwards, the initial values and bounds of each coefficient were defined, then all experimental data (true stress, plastic strain, strain rate, and temperature) were referenced by the function. As previously mentioned, the smoothed instantaneous strain rate was referenced at each data point, rather than the average strain rate for the test condition. Conversely, a constant temperature (the target temperature of the test condition) was used for simplicity instead of the instantaneous thermocouple reading, as the temperature at the centre of the specimen was precisely maintained at the desired temperature.

### **2.5.6. Thermal Characterization**

Various thermocouples were attached along the length of the tensile test specimens to measure the temperature variation along the specimen. The specimens were then subjected to the same thermal cycle as the elevated temperature tests, shown in Figure 39, but without the applied deformation. Four thermocouples were attached to each specimen, one at the centre, two 5 mm from the centre (both sides), and one 10 mm from the centre. A total of four repeat tests were conducted at each temperature, with the

thermocouple position mirrored for half of the repeats, to assess the thermal symmetry of the specimen. These thermal characterization tests were conducted prior to any tensile testing to ensure thermal stability and symmetry in the test setup. The air nozzle position was adjusted until thermal symmetry was achieved in the specimen.

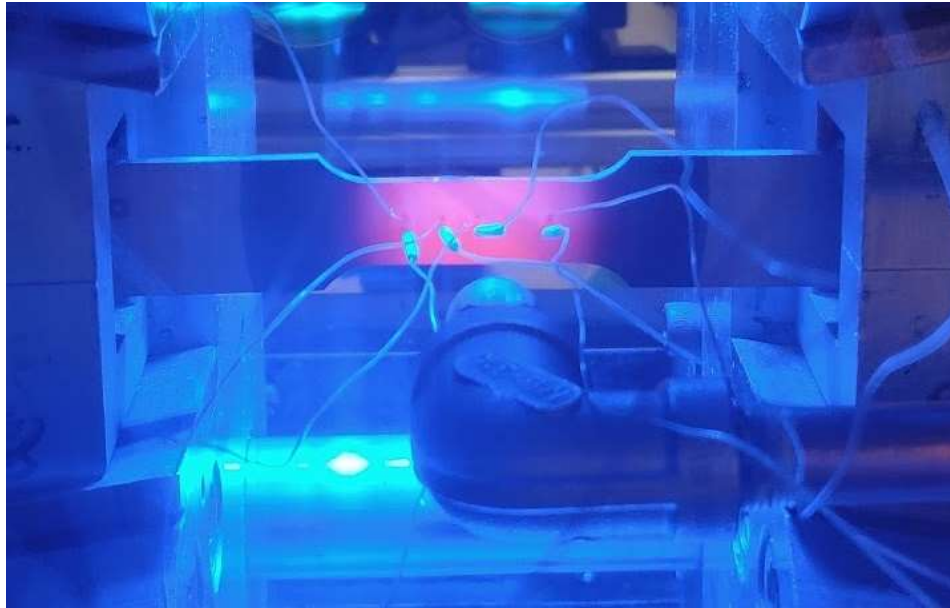


Figure 43: Photograph of specimen with multiple thermocouples (with wire insulators) attached for thermal characterization, during the heating stage

## 2.6. Phase Transformation Experiments

Phase transformation is an inherent aspect of the hot stamping process for PHS materials. Both the thermal and mechanical parameters of any hot stamping process significantly affect the phase change mechanisms. Thermal aspects include the cooling rate and the deformation start and end temperatures, determine the active phase transformations during forming, as well as the final phases in the formed component. Mechanical deformation has also been shown to affect the rate of phase formation, as observed by Åkerström *et al.* [66] and Nikravesh *et al.* [38]. To better understand the effects of hot-stamping parameters on the phase transformation of PHS 1800, experiments considering constant cooling rate with induced deformation were conducted with the Gleeble thermomechanical simulator. The first aspect of these experiments is to solely evaluate the effects of cooling rate on the final phases formed and hardness (after quenching). Afterwards, simultaneous quenching and deformation was applied to the specimens, to

determine the effects of tensile deformation on the final phases and hardness. These experiments follow a similar strategy and methodology utilized by Bardelcik *et al.* [72] for phase evolution characterization of PHS 1500. The results from these experiments, in the form of phase fractions and Vickers microhardness measurements, can then be used to determine relevant material parameters in the Åkerström austenite decomposition model [66] highlighted in the background. This updated model will then enable the prediction of microstructure evolution and final hardness of a hot stamping process by finite element analysis.

For the initial zero-deformation experiments, the test program consisted of a heating and soaking stage that was identical to the heating and soaking stage of the elevated temperature tensile test program. The specimen was first heated to 930°C from room temperature (approximately 25°C) at 15°C/s, then held at 930°C for 4 minutes to fully austenitize. This was followed by compressed air quenching to cool the centre of the specimen at a constant rate to below 100°C, which is well below the martensite finish temperature of approximately 200°C. Three cooling rate conditions were selected to evaluate the austenite decomposition of the material, 5°C/s, 10°C/s, and 50°C/s. The two lower cooling rates were selected to represent the cooling rates seen by parts in an industrial hot stamping process, where ideal contact conditions may not be possible, such as near-vertical sidewalls of channel geometries. Alternatively, these lower cooling rates could also be utilized by manufacturers to produce tailored parts utilizing heated dies other tailored cooling strategies. These low cooling rates were expected to produce mixed phase fractions, which is traditionally undesirable as it would reduce the strength of the PHS component. The high cooling rate condition is desirable for hot stamped components that require a fully martensitic final microstructure. After quenching, the specimens were sectioned at the centre (where the temperature and cooling rates were controlled precisely by the control thermocouple), then mounted, ground and polished using the equipment described in Section 2.2.6. The hardness of each mounted specimen were then measured by a Vickers microhardness tester. Afterwards, all specimens were etched with a 2% nital solution to reveal the microstructure to allow for observation under an optical microscope at up to 2000x magnification. For phase fraction identification,

the specimens were observed with a FEI Quanta 250 scanning electron microscope (SEM) to obtain micrographs at 4000x magnification. The various structures observed in the micrograph were manually identified based on grain structure and grain boundaries, then an image analysis software was used to apply different colors to each phase, where fractions of each phase were quantified by pixel count. The strategy utilized in this research was based on the procedures highlighted in Bardelcik *et al.* [72] and Bourque [81]. Three images were obtained and processed from each specimen at varying locations to evaluate any variation within the specimen.

For the experiments involving deformation, the heating and soaking program were identical to the zero-deformation condition. Again, compressed air quenching begins after the soaking stage, at the three cooling rate conditions (5°C/s, 10°C/s, and 50°C/s). During the quenching, non-isothermal deformation was induced via tensile displacement and was initiated beginning at 800°C, which represents the temperature at which forming could potentially begin in an industrial hot stamping process. To best represent how components are deformed in a real hot stamping process, the displacement loading was prescribed simultaneously with the quenching. Two deformation conditions, 10% and 20% true strain at 0.1 s<sup>-1</sup>, were conducted to evaluate the effects of increasing strain. Since the same tensile geometry from the tensile tests were utilized, the amount of crosshead displacement to achieve the desired strain level was known and used. During (and after) deformation, the specimen continues to cool at the constant prescribed cooling rate, until the specimen centre temperature was measured below 100°C. Afterwards, the specimens were sectioned at the middle (where cooling rate, and deformation amount was controlled), mounted, prepared, microhardness tested, and observed with an optical microscope and SEM to determine final phase fractions. A schematic representation of both the zero-deformation and induced deformation constant cooling rate test programs is shown in Figure 44

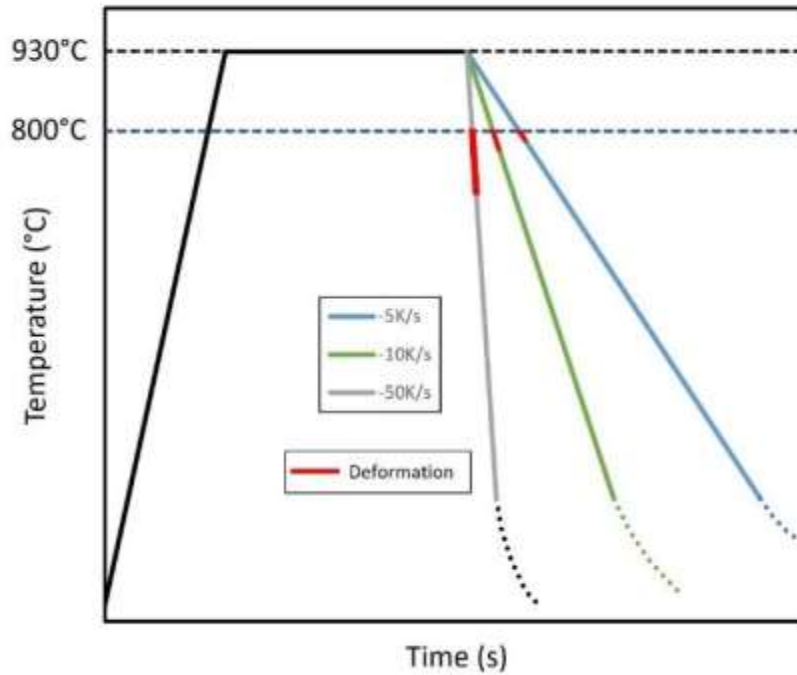


Figure 44: Schematic of the constant cooling rate and induced deformation test program, red lines indicate when deformation took place

The goal of these quench and deformation experiments was to determine the effect of temperature change (cooling rate) and deformation on the rate of ferrite, pearlite, and bainite formation from austenite. The experimental results, in the form of hardness and final phase fraction measurements, were then used to determine the activation energy parameters (shown in Equation (14)) for the Åkerström and Oldenburg [66] model (MAT\_244) in LS-DYNA by means of metamodel-based optimization using LS-OPT. LS-OPT is an optimization tool that directly interfaces with LS-DYNA to compute optimal solutions with specifically defined constraints and objectives. It is widely used to determine material properties or parameters based on the comparison of experimental results to predicted results. LS-OPT was used to determine the activation energies, and afterwards, the deformation scale factors (shown in Equation (16)) by varying the relevant parameters to minimize the residual between predicted results and experimental results. This follows a similar strategy utilized by Omer *et al.* [80] for tailored cooling experiments with PHS 1500. A detailed explanation of how the material parameters were derived can be found in Chapter 5.



### 3. Experimental Results

#### 3.1. PHS 1500 and PHS 1800 Post-Quench Tensile Test Results

Figure 45 shows engineering stress-strain curves of critically quenched (fully martensitic) PHS 1500 and PHS 1800 obtained from room temperature tensile testing. Three repeat tests were conducted for each steel grade.

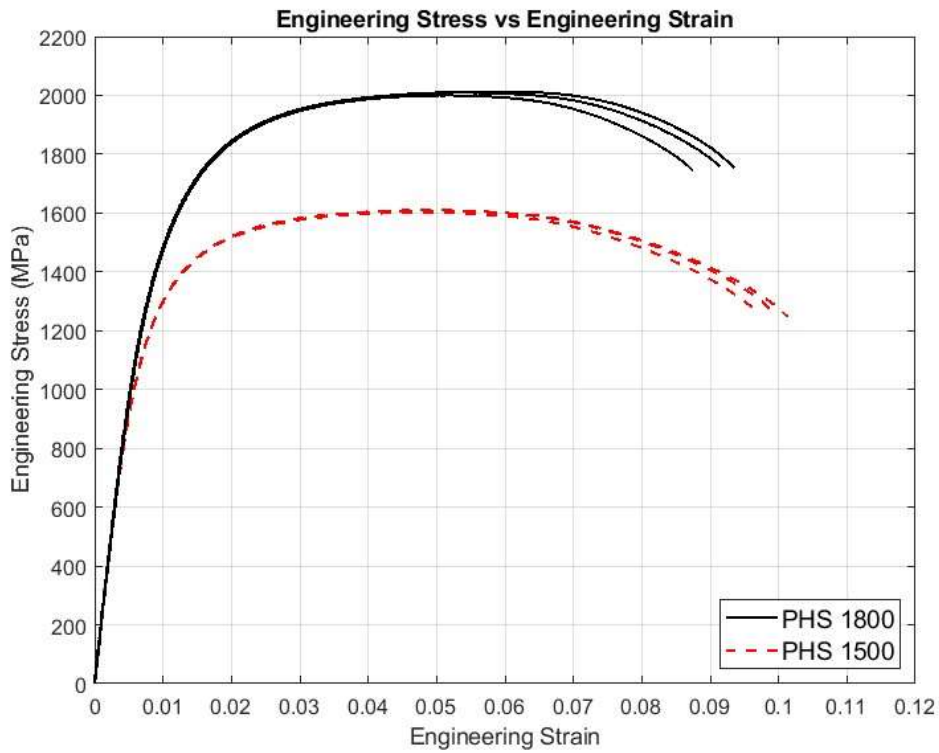


Figure 45: Engineering stress-strain curve of critically quenched (fully martensitic) PHS 1500, at room temperature, from quasi-static ( $0.001\text{ s}^{-1}$ ) tensile test

The quasi-static room temperature tensile test results of critically quenched PHS 1500 and PHS 1800 are summarized in Table 4. The mean values and the standard deviation between the three repeat tests are included.

Table 4: Mechanical properties of quenched PHS 1500 and PHS 1800 from quasi-static room temperature tensile tests

Material	Yield Strength (MPa)	Tensile Strength (MPa)	Total Elongation (%)
PHS 1500	1157 ± 1	1606 ± 4	9.9 ± 0.2
PHS 1800	1365 ± 3	2004 ± 8	9.1 ± 0.3

The yield strength is determined using the 0.2% offset criteria, and the tensile strength is determined by the maximum engineering stress (maximum load). The total elongation is represented in terms of engineering strain and is the strain at which the specimen separates.

For PHS 1500, the yield and tensile strengths are slightly higher than typical values found in literature, such as in hot stamping review papers by Karbasian and Tekkaya [14] or Taylor and Clough [9]. This difference in strength is not unexpected due to potentially different chemical compositions of the tested material, and variations in processing parameters such as the cooling rate during quenching. It has been shown by Bardelcik *et al.* [92] that higher cooling rates corresponds to increased yield and ultimate strengths, even during quasi-static test conditions.

The PHS 1800 tested in this research is shown to have a tensile strength of 2,000 MPa, a 25% increase in ultimate strength compared to the PHS 1500 material. The yield strength of PHS 1800 is also 18% greater than PHS 1500. For PHS 1800, the increase in strength leads to lower ductility, observed by the approximately 8% reduction in total elongation when compared to PHS 1500. For structural, high-strength applications, this 18-25% increase in strength could potentially result in significant weight savings in the final component, by enabling the use of thinner blanks. It is apparent that PHS 1800 would be a highly desirable grade of PHS to adopt, purely from a strength perspective.

## 3.2. Surface Alloying Results

### 3.2.1. As-Received Coating Micrographs and Measurements

Figure 46 shows the microstructure of the base material and the Al-Si coating for an as-received PHS 1500 specimen. The as-received base material consists of a ferritic-pearlitic microstructure with fine

carbides disbursed throughout. The base microstructure is similar to most other PHS 1500/22MnB5 microstructures presented in the literature by Merklein and Lechler [42] and Järvinen *et al.* [93], for example. The as-received coating seen in Figure 46 shows a type 1 Al-Si coating consisting of an Al matrix, with patches of Si slivers distributed throughout, and an intermetallic interface with the base material. The thickness of the as-received coating (from the surface and including the intermetallic layer, to the base material) is approximately 20  $\mu\text{m}$  as measured with a calibrated optical microscope.

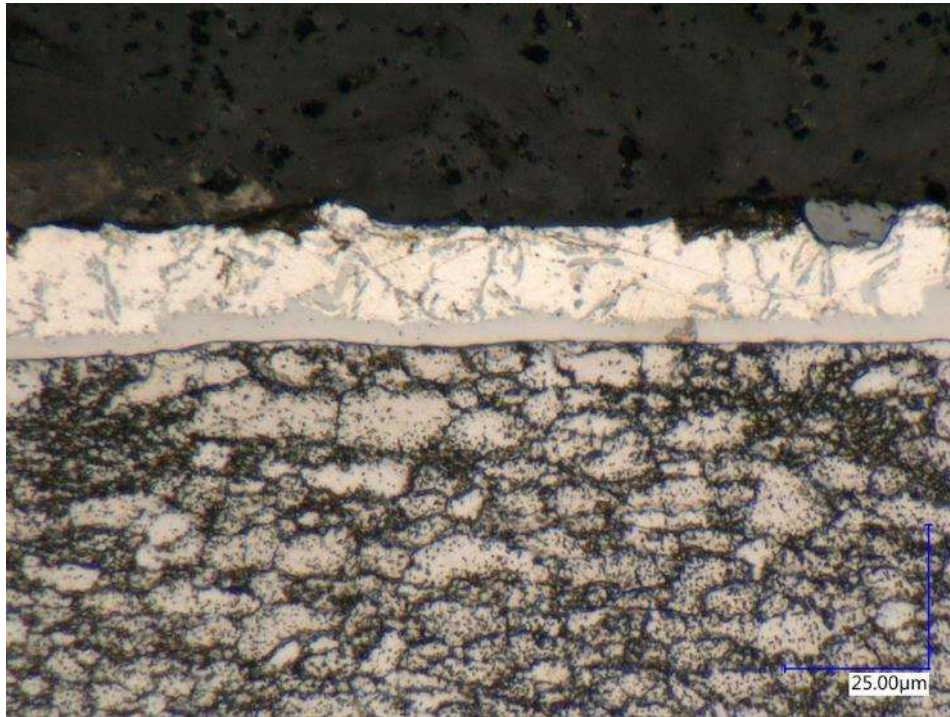


Figure 46: As-received microstructure of PHS 1500 and Al-Si coating viewed with a optical microscope

Figure 47 shows the microstructure of the base material and the Al-Si coating for an as-received PHS 1800 specimen. The base microstructure of as-received PHS 1800 is very similar to that of the as-received PHS 1500 seen in Figure 46. Likewise, the Al-Si coating for the as-received PHS 1800 is also very similar to that of PHS 1500, consisting of an Al matrix and Si aggregates. The Al-Si coating on PHS 1800 is observed have much more voids or inclusions, however that may be a by-product of polishing dissimilar materials (aluminum coating and steel base material) during specimen preparation. In general, the as-received Al-Si coating of both studied materials are identical to typical PHS Al-Si coatings found in the literature, as seen by micrographs from Merklein and Lechler [42], and Borsetto *et al.* [94].



Figure 47: As-received microstructure of PHS 1800 and Al-Si coating viewed with an optical microscope

### 3.2.2. Selected Heating Profile and Surface Alloying Results

Figure 48 shows the temperature-time histories (planned profile and actual temperature measurements) for the selected surface alloying heat treatment cycle for PHS 1500 and PHS 1800. The times shown in the figure (7 minutes and 10 minutes for PHS 1500 and PHS 1800, respectively) are the total time each specimen is inside the heat treat oven. The required time for surface alloying was determined experimentally by treating specimens at various times and evaluating the surface color of the specimen after removal from the oven and quenching to room temperature. The surface temperature of the blank was measured during the surface alloying heat treatment process by a thermocouple at the centre of the blank, contacting the surface of the blank. A red marker with the time label indicates when the measured temperature reaches 700°C. Figure 48(a) shows that the surface temperature of a PHS 1500 blank increases rapidly to approximately 550°C, then slowly increases to 700°C at almost exactly the 7<sup>th</sup> minute in the oven. Figure 48(b) shows the temperature-time plot for a PHS 1800 blank, which follows a similar heating profile to PHS 1500. For PHS 1800, the additional 3 minutes at 700°C was needed to create a sufficiently darkened

surface necessary for applying an adequately contrasting speckle pattern. The difference in soaking time between the two materials can likely be attributed to the difference in the coating thickness for the PHS 1500 and PHS 1800 materials used in this study, where the PHS 1800 blanks had an approximately 5  $\mu\text{m}$  thicker Al-Si coating.

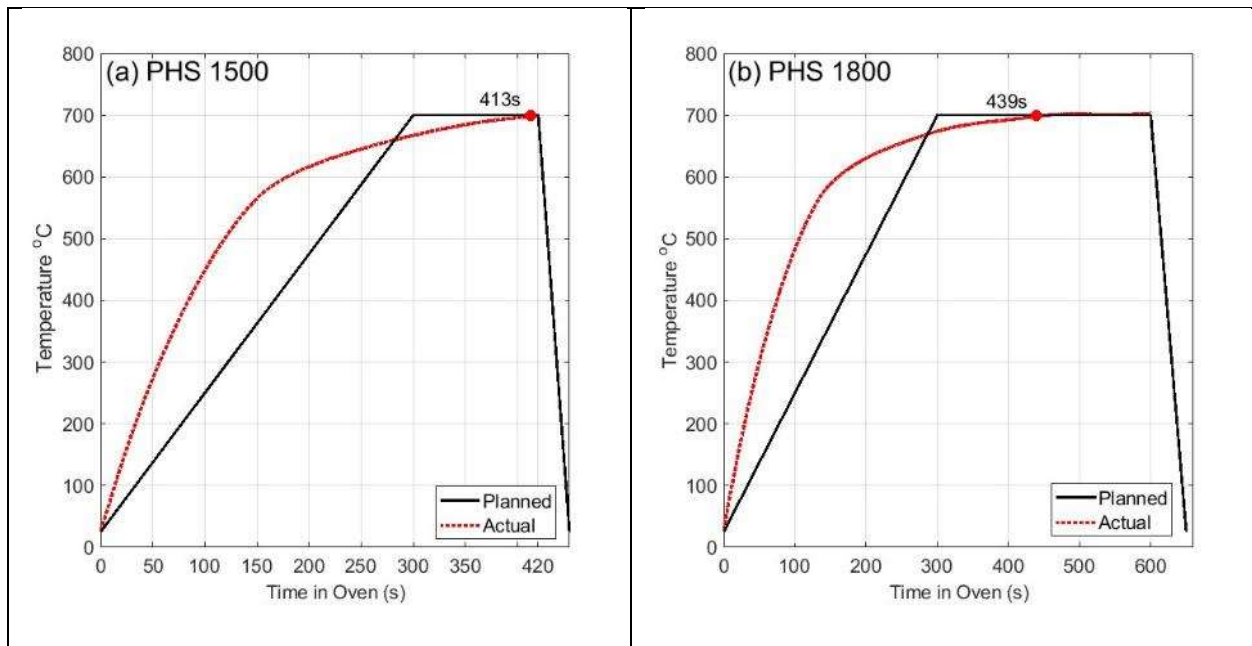


Figure 48: Selected surface alloying heat treatment cycle for (a) PHS 1500 and (b) PHS 1800

Figure 49 shows specimens from the initial surface alloying trials to determine the effect of soaking time on the appearance of PHS 1800 specimens, for a minimum of 30 seconds at 700°C (left most specimen) and increasing to 10 minutes at 700°C (right most specimen).

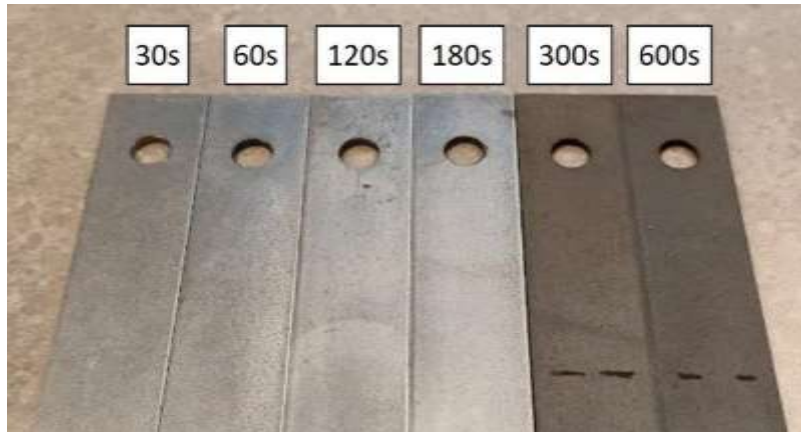


Figure 49: Effect of surface alloying time on the surface appearance, starting with 30 seconds at 700°C (far left) and increasing to 10 minutes at 700°C (far right)

Figure 50 shows photographs of the physical appearance of PHS 1800 in its as-received state, and after surface alloying to the treatment cycle shown in Figure 48. The surface alloyed blank was treated at 700°C for 10 minutes (total time in oven) then quenched to room temperature between flat dies on a hydraulic press. It can be seen that the surface alloying heat treatment process transforms the initial shiny and silver surface coating into a dull grey color. This darkened surface therefore enables the application of white speckles to form a contrasting speckle pattern for digital image correlation. PHS 1500 experienced a similar color transformation but only required 7 minutes at 700°C to achieve a darkened color similar to that shown in Figure 50(b).

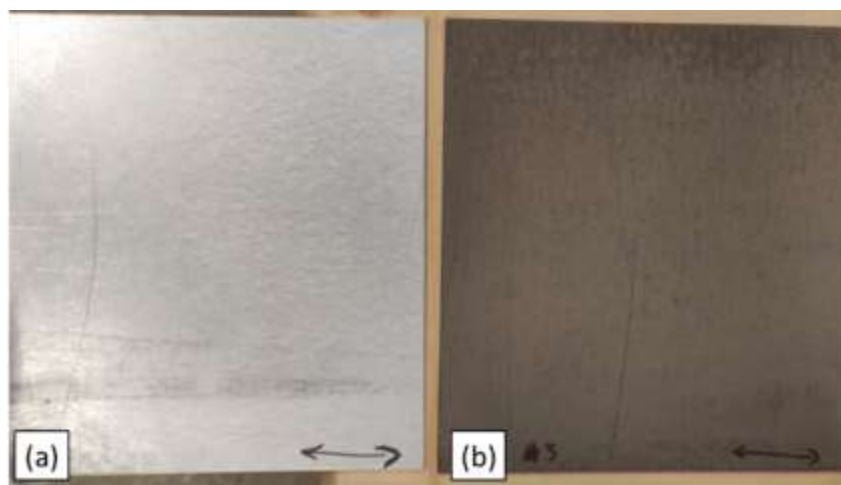


Figure 50: Physical appearance of PHS 1800 (a) in its as-received state, (b) after surface alloying

### 3.2.3. Microstructure Comparison After Surface Alloying Treatment

Figure 51 shows the microstructure of as-received and surface-alloyed PHS 1800 along the coating and base material interface. As discussed previously, the as-received coating shows a typical type 1 Al-Si coating seen in existing literature with a primarily Al matrix, Si patches, and an intermetallic interface to the base PHS material. After surface alloying, the coating has clearly evolved to a more homogenous microstructure, however the distinct intermetallic layers normally seen in fully developed Al-Si coatings is not yet apparent. The steel substrate also changes somewhat after surface alloying, in the form of possibly enlarged ferrite grains and a reduction in size of large pearlite structures (large dark patches).

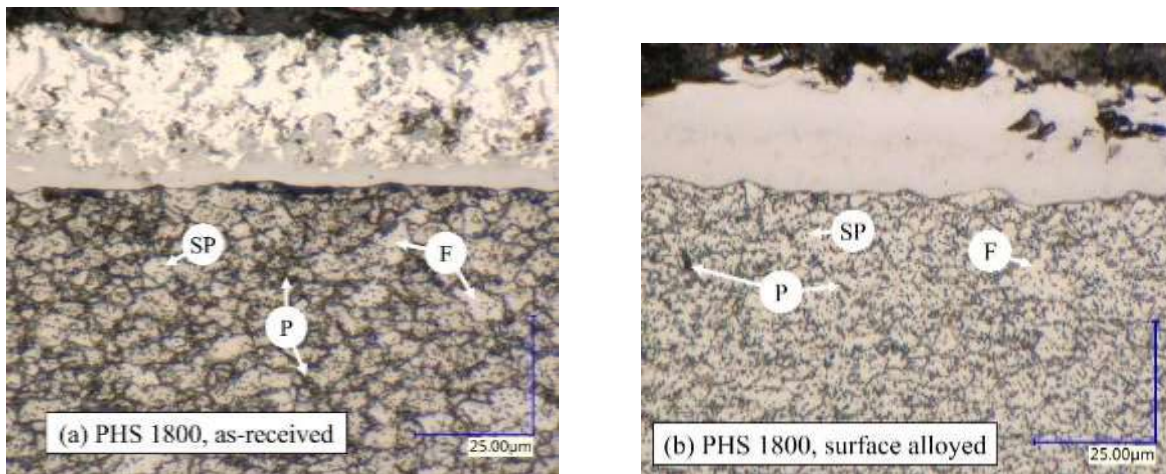


Figure 51: (a) As-received PHS 1800, (b) post surface-alloyed PHS 1800 micrographs at 2000x magnification (F: ferrite, P: pearlite, SP: spheroidized pearlite (dark dots))

Figure 52 shows a comparison of the microstructure of a PHS 1800 specimen subjected to a conventional austenitization and quenching (CAQ) treatment comprising of a 5 minute soak at 930°C followed by rapid die quenching (referred to herein as CAQ treatment) to a sample that was first surface alloyed for 10 minutes at 700°C prior to CAQ. Both specimens have a fully martensitic microstructure as well as the fully developed Al-Si coating with distinct intermetallic layers as seen in Yakubtsov and Sohmshtetty [19] or Borsetto *et al.* [94].

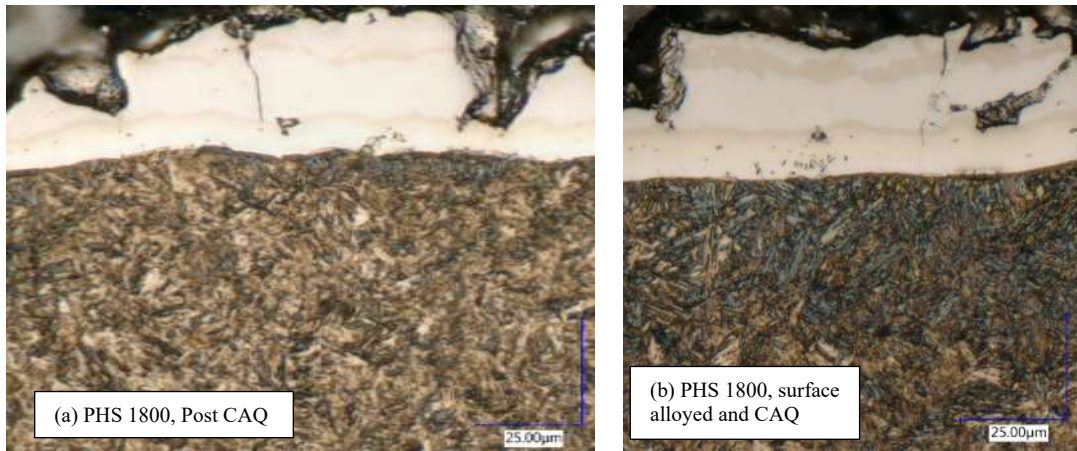


Figure 52: (a) Critically quenched PHS 1800, and surface-alloyed then critically quenched PHS 1800 (b) at 2000x magnification

For every optical micrograph taken of the coating, the average thickness of the coating was measured for reference. As previously mentioned, this average coating thickness is subtracted from the measured thickness of each tensile specimen when determining initial cross-sectional area, for stress calculations since the coating exhibits extensive cracking and is not viewed as load-bearing. The thickness measurement was taken from the outer edge to the beginning of the base material. For the as-received condition, the coating thickness measurement included the thin intermetallic layer. The coating measurements for PHS 1800 are summarized in Table 5.

Table 5: PHS 1800 coating thickness measurements in various conditions,  $N = 8$

As received	After surface alloying	Post CAQ (no surface alloying)	Post surface alloying and CAQ
$29.9 \pm 1.8 \mu\text{m}$	$25.3 \pm 2.3 \mu\text{m}$	$30.1 \pm 4.0 \mu\text{m}$	$32.1 \pm 4.4 \mu\text{m}$

### 3.2.4. Elevated Temperature Surface Alloyed Tensile Test Comparison

Prior to elevated temperature tensile testing with digital image correlation measurements, a brief comparison of as-received and surface alloyed specimens were conducted for both PHS 1500 and PHS 1800. This comparison comprised a comparison of the engineering stress versus engineering strain curves for both conditions of both materials, at varying temperatures and strain rates. Crosshead displacement measurements were used to determine the engineering strain because digital image correlation was not possible for non-surface alloyed specimens. It should be noted that crosshead displacement includes the



potential effect of machine compliance and therefore renders subsequent strain measurement inaccurate. However, the results are still valuable for comparison purposes to detect whether any relative differences in material performance can be identified.

Three repeat tests were conducted for each material and test condition and the mean result is plotted in Figure 53 and Figure 54. For reference, the individual result of every repeat test is plotted in Figure 100 and Figure 101 in Appendix B. The ultimate tensile strength (UTS) is indicated for all curves. Figure 53 shows the engineering stress-strain curves of the as-received (AR) and surface alloyed (SA) PHS 1500 tested at two different temperature and strain rate conditions.

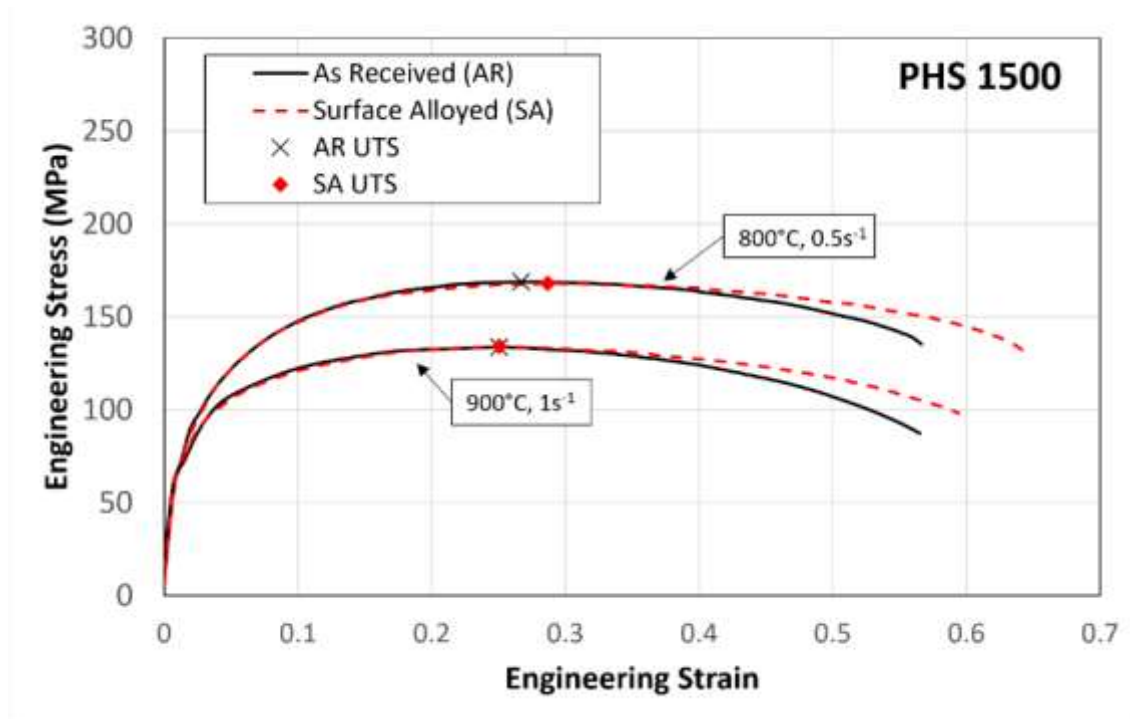


Figure 53: Engineering stress-strain curves of as-received and surface alloyed PHS 1500 from isothermal tensile tests at 800°C and 0.5s<sup>-1</sup>, and at 900°C and 1s<sup>-1</sup>

For the 900°C condition, the UTS for both material conditions are nearly identical both in terms of stress and strain values. For the 800°C condition, the UTS the for the surface alloyed condition is marginally lower and occurs at higher strain. This variation could be indicative of some mechanical softening as a result of the surface alloying treatment; however, the difference is less than 3%. In terms of the overall flow curves, both temperature conditions follow a nearly identical behaviour from yield up to the UTS. Nearly

the same flow stresses are observed, and the strain hardening rate is nearly identical. Beyond the UTS, the surface-alloyed specimens experience slightly greater total elongation, once again suggesting mechanical softening in the surface alloying specimens due to the time at elevated temperatures.

Figure 54 shows engineering stress-strain curves of as-received and surface alloyed PHS 1800 tested at two different temperature and strain rate conditions. Three repeat tests were conducted for each material and test condition and the mean result is plotted. The ultimate tensile strength (UTS) is plotted for all curves. For the 800°C condition, the flow curves are nearly identical for both material conditions up to the UTS. For the 700°C condition, the surface alloyed material shows slightly lower stress when compared to the as received condition, but the difference is within 4%. Similar to the PHS 1500 results, the surface alloyed specimens experience greater total elongation, especially at the 700°C condition.

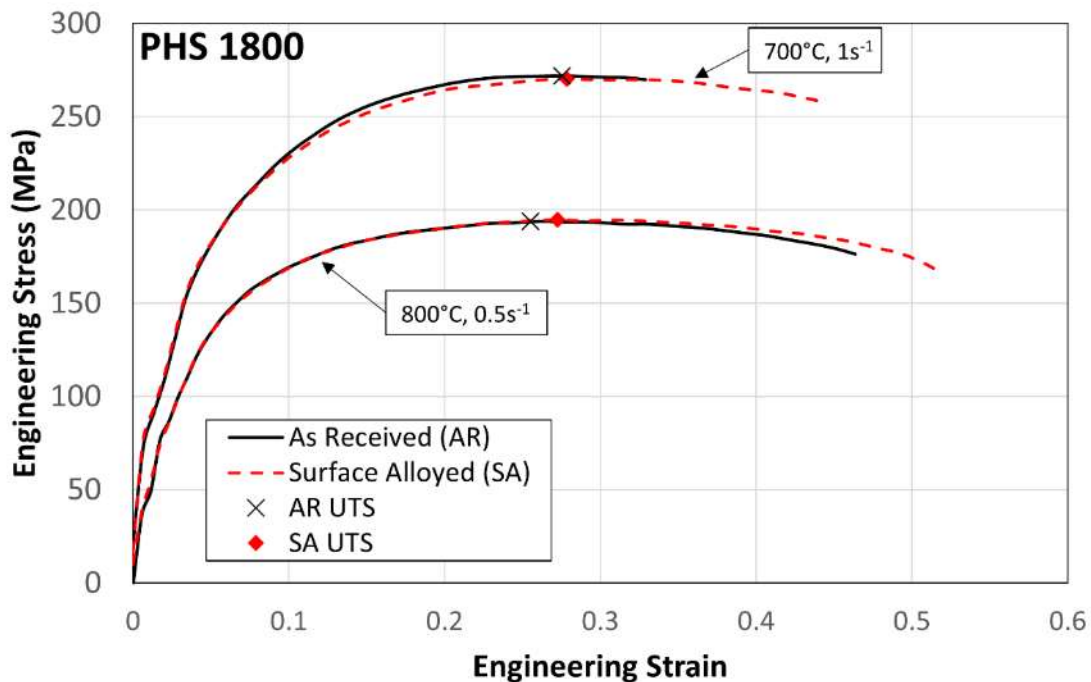


Figure 54: Engineering stress-strain curves of as-received and surface alloyed PHS 1800 from isothermal tensile tests at 700°C and 1s<sup>-1</sup>, and at 800°C and 0.5s<sup>-1</sup>

Both Figure 53 and Figure 54 show that the stress-strain curves from the beginning of the tensile test up to the UTS for the as-received and surface alloyed specimens are nearly identical. Beyond the UTS, the surface alloyed specimens clearly display greater ductility, in the form of increased total elongation prior

to fracture. Because the tensile test is performed after austenitization, the surface alloying heat treatment must have an effect on the fully austenitic microstructure at the time of testing. One possible explanation could be greater austenite grain sizes at the time of testing, as a result of grain growth during surface alloying.

As mentioned previously in the introduction, the flow curve obtained from a tensile test only maintains a uniaxial stress state up to the onset of necking, which occurs at the UTS. Consequently, in general, only tensile test data up to the UTS is utilized to generate a material flow curve unless a correction is applied. Because surface alloying only alters the flow curve beyond the UTS, it is deemed that surface alloying has no effect on the primary focus of this research, which is generating the material flow curves from experimental data up to the point of necking.

### **3.3. PHS 1500 Elevated Temperature Tensile Test Results**

#### **3.3.1. Results Overview**

Figure 55 shows a compilation of the experimentally determined PHS 1500 flow curves at varying temperature and strain rates. The average result from three repeat tests at each test condition is shown. The variability of the repeat test data is quantified in Table 6 below.

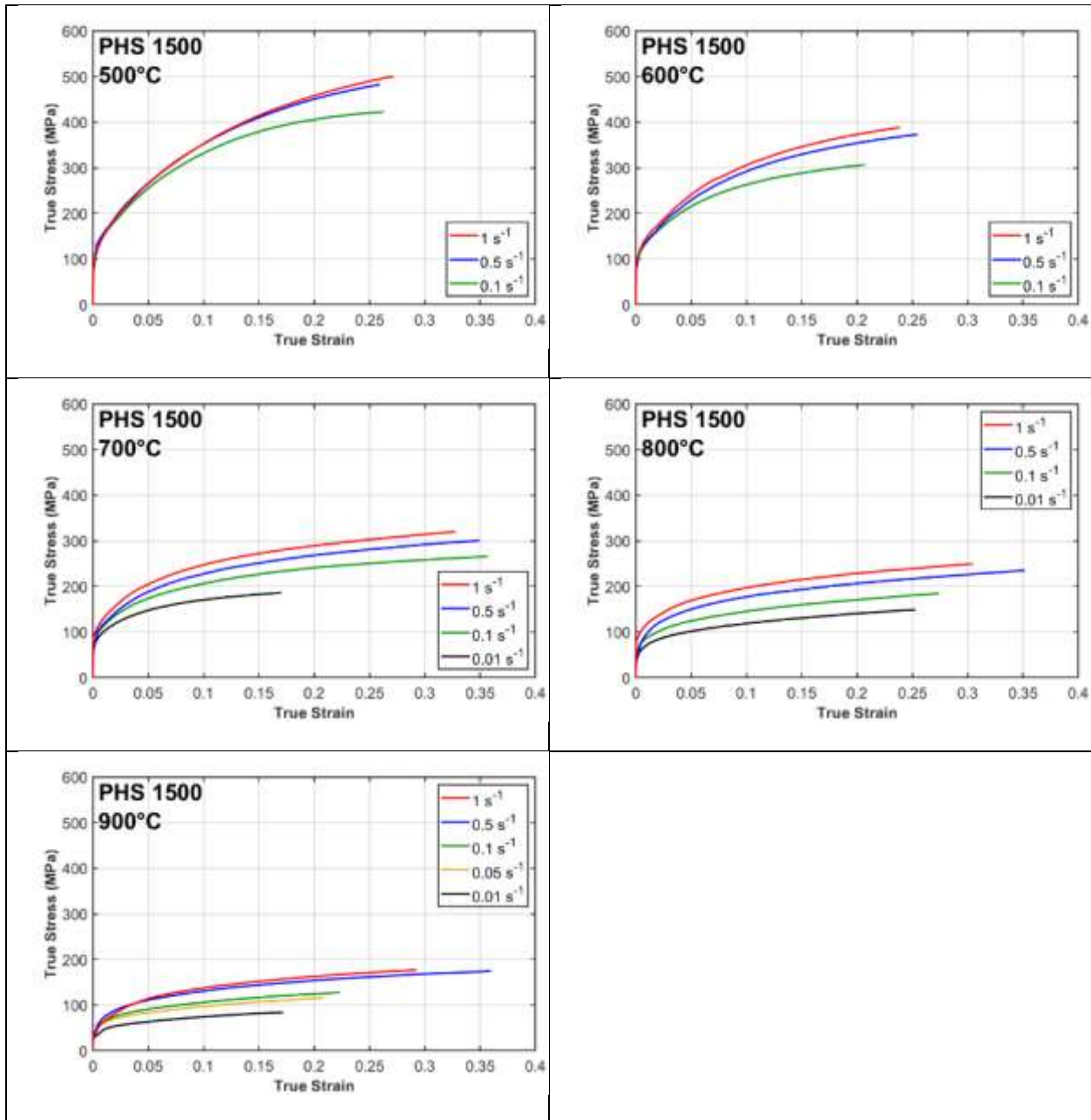


Figure 55: Experimental PHS 1500 flow curves at various temperatures and strain rate conditions after austenitization

For all flow curves, it can be seen that flow stress increases with decreasing temperature (at the same strain rate), and flow stress increases with increasing strain rate (at the same temperature). Greater work hardening can be observed at lower temperatures, especially at 500°C, where flow stresses increase significantly after yielding from approximately 100 MPa to 500 MPa. At 700°C and 800°C, the flow curves are clearly distinguishable when at  $0.5\text{s}^{-1}$  and  $1\text{s}^{-1}$ . Conversely, the higher strain rate conditions at 500°C

and 600°C are nearly identical, indicating less strain rate sensitivity at lower temperatures. For reference, flow curves are presented in consistent strain rate sub-plots in Figure 102 in Appendix C.

The variability of the test data is assessed based on the average standard deviation of true stress between all repeats, summarized in Table 6 for every tensile test condition for PHS 1500. The values presented are calculated by taking the standard deviation of true stress data at every strain data point, for all three repeat tests, then taking the average of all standard deviations. This average standard deviation value can be treated as a measure of variation of true stress response between each test, with a greater standard deviation value indicating a greater variation between the repeat tests. The highest standard deviations are found at the lower temperatures and higher strain rates, potentially indicating greater variability at those conditions. In general, the average standard deviation value is low, indicating good repeatability for all test conditions. For reference, all repeat test results for a few select conditions are shown in Figure 102 in Appendix B.

*Table 6: Average of standard deviation of true stress between all repeats, for every tensile test condition of PHS 1500*

<b>PHS 1500</b>					
Temperature (°C)	Average standard deviation of true stress for all repeats (MPa)				
	0.01 s <sup>-1</sup>	0.05 s <sup>-1</sup>	0.1 s <sup>-1</sup>	0.5 s <sup>-1</sup>	1 s <sup>-1</sup>
900	1.0	1.5	1.6	1.6	2.5
800	1.5		3.5	3.6	2.7
700	2.1		2.5	3.8	3.4
600			2.6	3.9	2.4
500			3.0	3.4	4.6

### 3.3.2. Temperature Effects

Figure 56 shows the flow stress of PHS 1500 at 0.05, 0.10 and 0.15 true strain for all strain rate conditions, plotted versus the test temperature. The average flow stress is plotted by a circular dot marker and error bars indicate the standard deviation between the three repeat tests at each test condition. For all conditions, less than 3% difference was observed between repeat tests at each test condition.

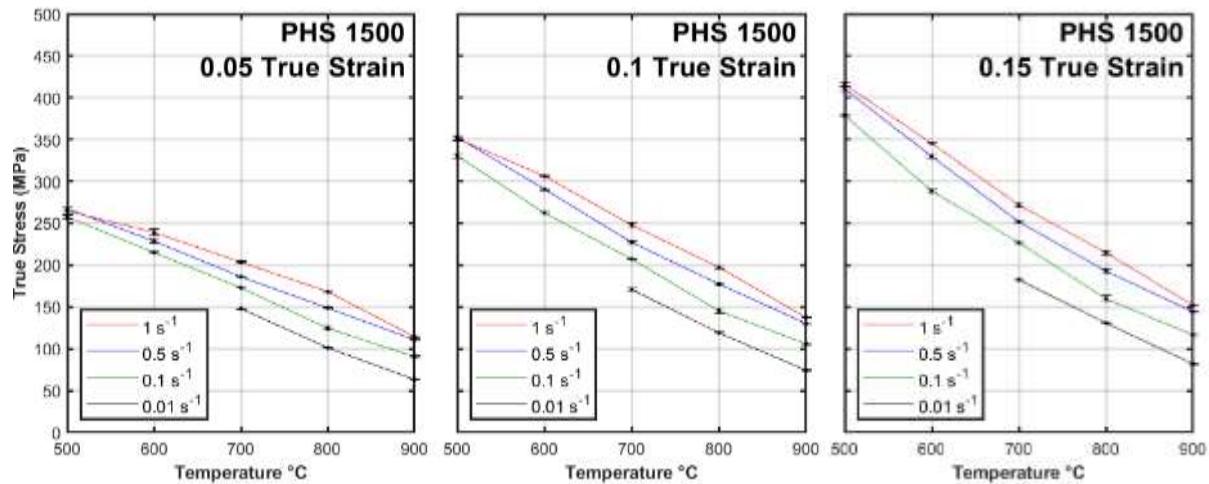


Figure 56: PHS 1500 flow stress values at various strain values and strain rates, versus temperature with error bars showing +/- 1 standard deviation of the flow stress values

At all three strain values, an approximately linear increase in flow stress with respect to decreasing temperature can be observed for all strain rates. Between the three subplots, it is apparent that with increasing strain, temperature has an effect on the flow stress. At 500°C and 600°C, the amount of strain hardening (quantified by the increase in flow stress with increasing strain) is notably greater than the amount of strain hardening at temperatures above 700°C. This relationship between flow stress and temperature indicates a relationship between strain hardening and temperature. This behaviour can be described as an increase in strain hardening sensitivity with decreasing temperature.

### 3.3.3. Strain Rate Effects

Figure 57 shows the flow stress of PHS 1500 at various strains for all temperature conditions, plotted with strain rate along the x-axis. The average flow stress is plotted by a circular dot marker and error bars indicate the standard deviation between the three repeat tests at each test condition.

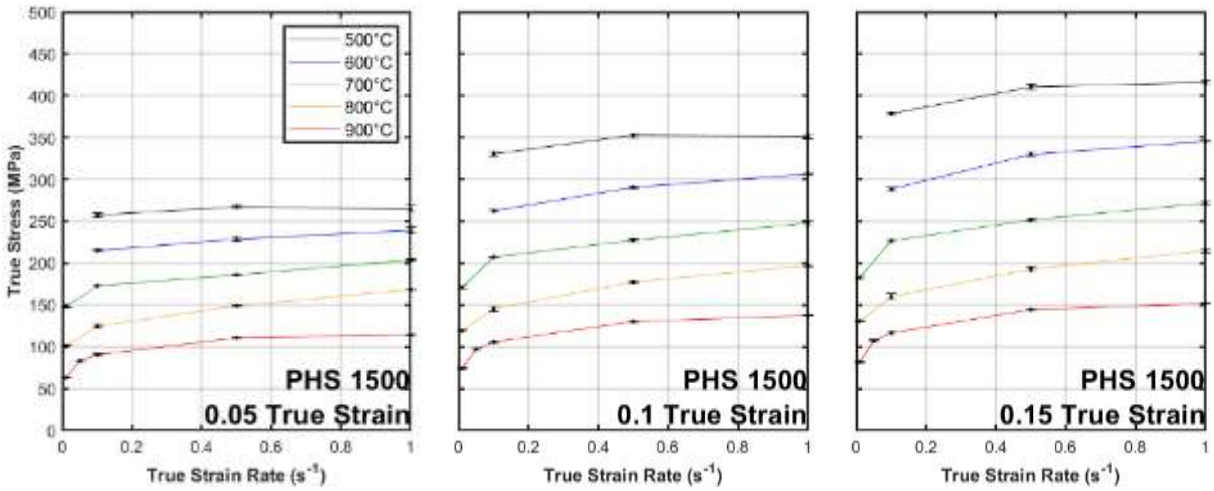


Figure 57: PHS 1500 flow stress values at various strain values and temperatures, versus strain rate with error bars showing +/- 1 standard deviation of the flow stress values

Figure 57 shows a consistent trend across all temperatures and strains, where a greater strain rate results in greater flow stress. However, unlike temperature, this relationship between flow stress and strain rate seems logarithmic instead of linear, with the strain rate sensitivity of the flow stress decreasing with increasing strain rate.

To better visualize the logarithmic relationship between strain rate and flow stress, the strain rate is plotted on a logarithmic scale in Figure 58. While a few exceptions to the relationship can be identified, notably between the 0.5s<sup>-1</sup> and 1s<sup>-1</sup> data points at 500°C, the logarithmic relation between strain rate and flow stress generally applies to PHS 1500.

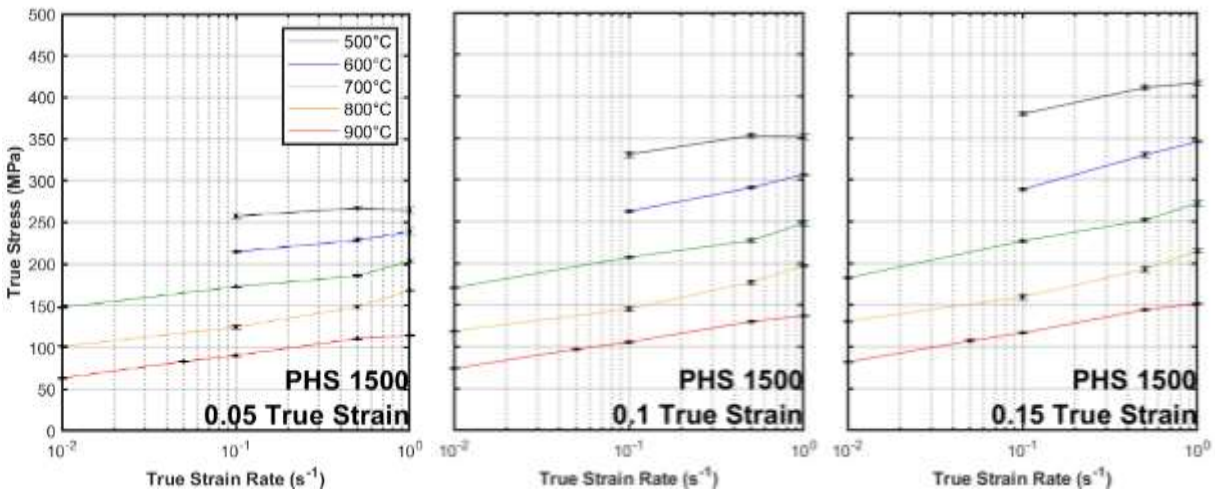


Figure 58: PHS 1500 flow stress values at various strain values and temperatures, versus strain rate on a log scale with error bars showing +/- 1 standard deviation of the flow stress values

### 3.3.4. Comparison To Other Published Data for PHS1500

Figure 59 shows a comparison of the experimentally determined flow curves in this research to results published in the literature from multiple sources. It should be noted that the material, test program, and test conditions vary slightly between all sources, so this is not a direct comparison or repeat study. Dashed lines represent line plot data taken from various sources, while the squares represent data published in symbol form. Sources of all data are cited in the figure. Solid lines indicate the flow curves obtained in this present research with the Al-Si coated PHS 1500 material of chemical composition presented in Table 1. In general, there exists slight discrepancies between the flow curves from all sources, at all conditions. At 500°C the flow curves from the current study are significantly different to all other compared flow curves. Between 600°C and 900°C however, the results obtained in the current study is either extremely similar or lies between the results from the cited data. Prior to 0.15 strain, all results at 600°C and 700°C are extremely similar for both strain rate conditions. At 800°C, the present work is nearly identical to the results obtained by Merklein and Lecher [42] and Abspoel *et al.* [43]. Conversely at 900°C, the present work is extremely similar to the results published by Abspoel *et al.* [43], but is notably different to results by Merklein and Lechler [42] at 0.1s<sup>-1</sup>. Although it may not be appropriate to directly compare results when materials and test parameters differ, the similarity in flow curves between 600°C - 800°C is indicative that the test method



used in this current research, which includes the use of surface-alloying and digital image correlation measurement techniques, is a valid approach to determining the flow curves of hot stamped materials.

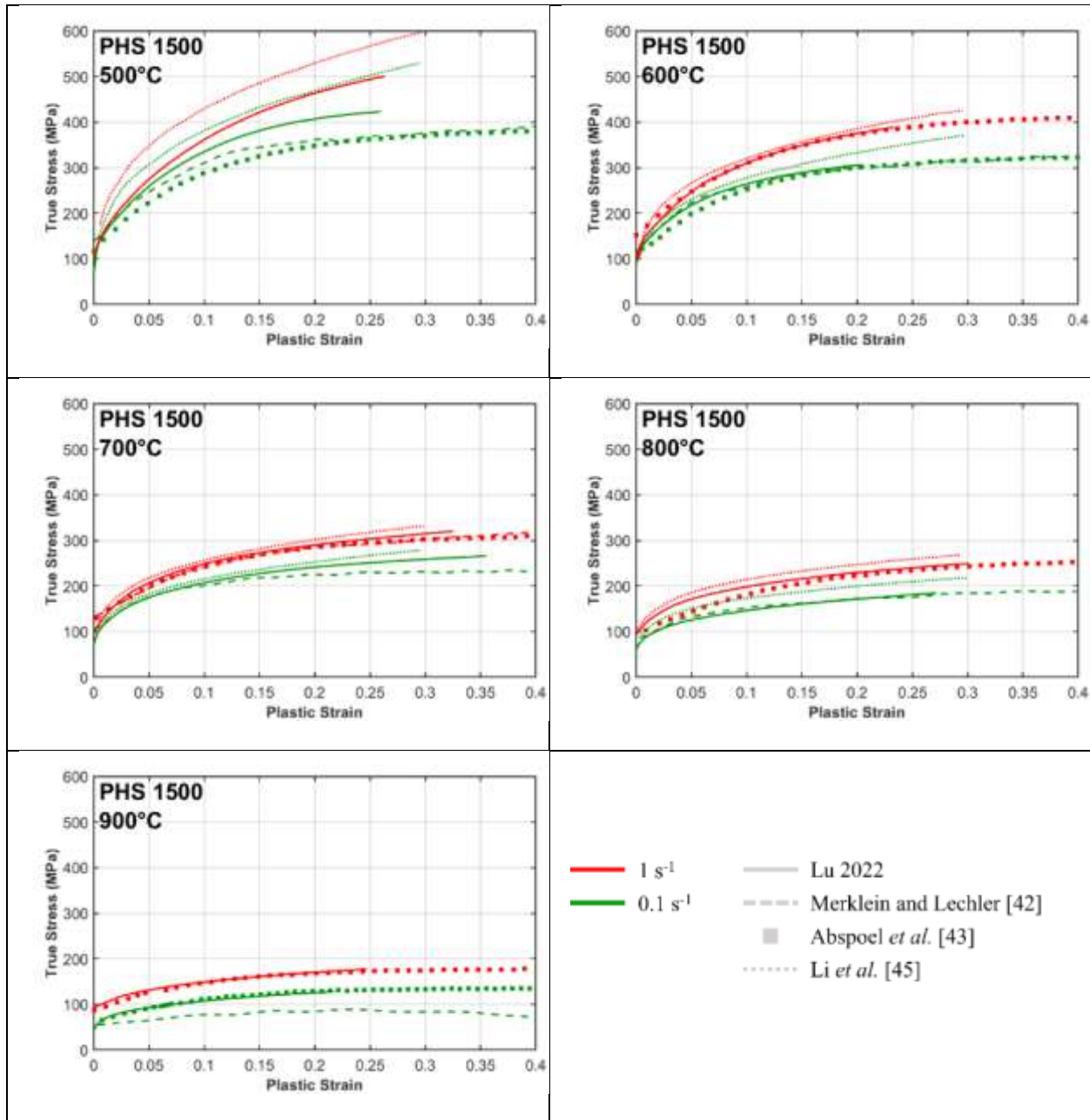


Figure 59: Experimental PHS 1500 results from this work compared to PHS 1500 flow curves published by Merklein and Lechler [42], Abspoel et al. [43], and Li et al. [45]

A summary of the materials tested and adopted test parameters by the referenced studies are compared below in Table 7. All tested materials are PHS 1500 or 22MnB5 equivalents, however specific chemical compositions are not identified by any of the sources. In terms of the processing parameters, all studies

followed similar heating rates, soak temperatures, soak times, and stabilization times prior to tensile testing. The primary difference between the current research and the compared sources is the cooling rate, which is notably lower than either Merklein and Lecher [42] and Li *et al.* [45]. This difference in cooling rate could explain the difference in the results at lower temperatures (500 - 600°C) due to the onset of bainite or pearlite formation in the current work, resulting in significantly different hardening responses at lower temperatures. The rate of austenite decomposition may be further influenced by the specific chemical composition of the tested materials.

Table 7: Summary of test parameters between the current research and PHS 1500 flow curve results obtained from literature

	<b>Current Research</b>	<b>Merklein and Lechler [42]</b>	<b>Abspoel <i>et al.</i> [43]</b>	<b>Li <i>et al.</i> [45]</b>
<b>Material</b>	PHS 1500 1.7 mm	USIBOR 1500P, 1.75 mm	“Regular 22MnB5” 1.5 mm	B1500HS 1.4 mm
<b>Heating Rate</b>	+15 K/s	+16 K/s	+15 K/s	+10 K/s
<b>Soak Temperature</b>	930°C	950°C	900°C	900°C
<b>Soak Time</b>	4 min	3 min	4 min	5 min
<b>Cooling Rate</b>	-50 K/s	-80 K/s	-	-70 K/s
<b>Stabilization Time</b>	5 s	5 s	-	5 s
<b>Displacement Measurement Method</b>	DIC	“Optical measuring system ARAMIS”, possibly DIC	“Retractable strain gauge or crosshead displacement”	DIC

### 3.4. PHS 1800 Elevated Temperature Tensile Test Results

#### 3.4.1. Results Overview

Figure 60 shows the experimentally determined PHS 1800 flow curves at various temperatures and strain rates. The variability of the repeat test data is quantified in Table 8 below. In each subplot, it is apparent that flow stress increases with increasing strain rate. Between the subplots, flow stress decreases with increasing temperature across the entire temperature range. In general, flow stresses increase more substantially with increasing strain at lower temperatures, indicating greater work hardening at lower temperatures. At 700°C and 800°C, the flow curves obtained at strain rates of 0.5s<sup>-1</sup> and 1s<sup>-1</sup> are clearly distinguishable from one another, however this is not the case at other temperatures, indicating a potential

non-linear relationship between strain rate sensitivity and temperature. For reference, flow curves are presented in strain rate sub-plots in Figure 105 in Appendix C.

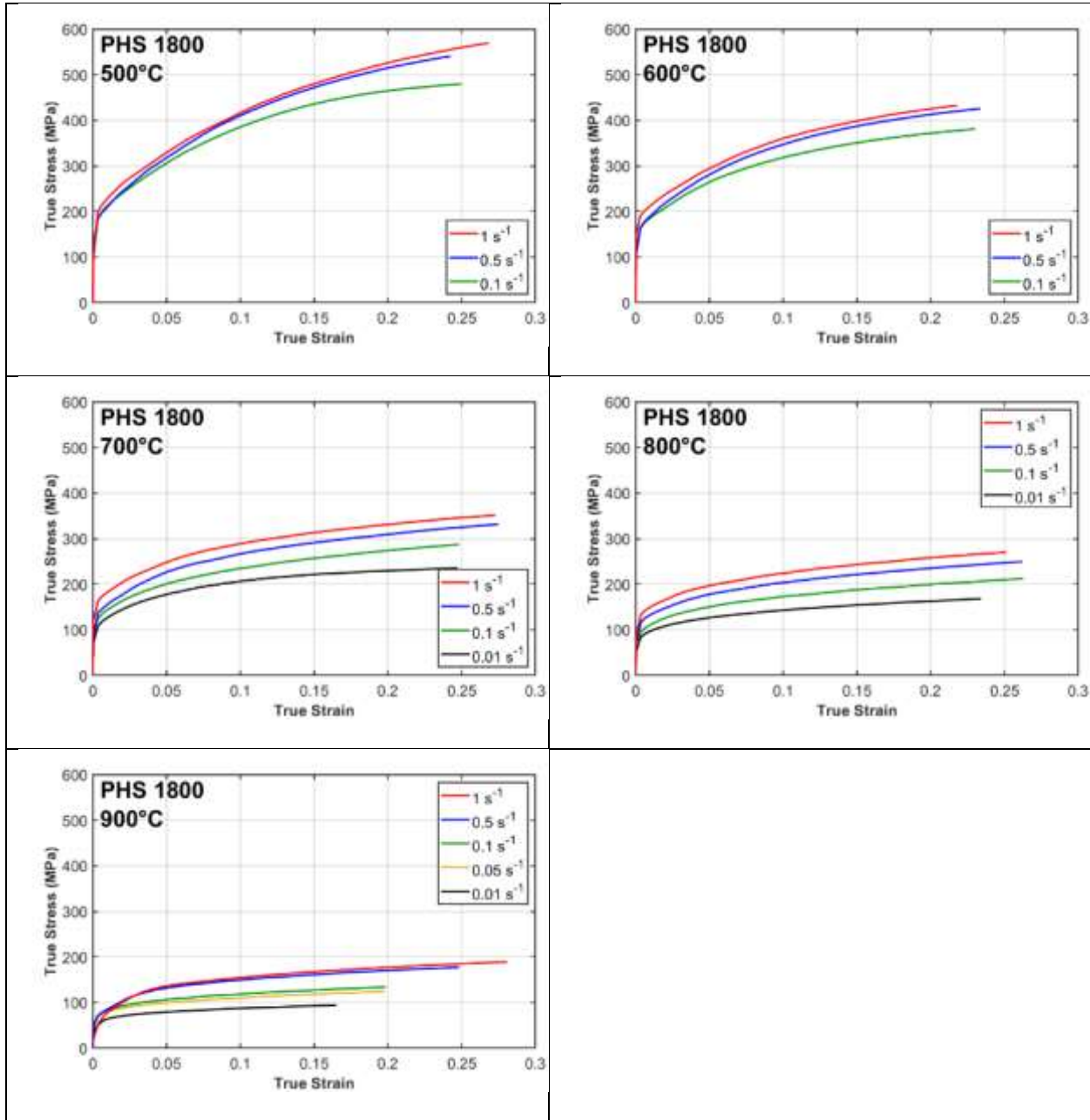


Figure 60: Experimental PHS 1800 flow curves at various temperature and strain rate conditions after austenitization

Table 8 shows the average standard deviation of true stress between all repeats, for every tensile test condition for PHS 1800. Similar to PHS 1500, the highest standard deviations are found at the lower temperatures and higher strain rates, potentially indicating greater variability at those conditions. For reference, all repeat test results of a few select conditions are plotted in Figure 103 in Appendix B

Table 8: Average of standard deviation of true stress between all repeats, for every tensile test condition of PHS 1800

<b>PHS 1800</b>					
Temperature (°C)	Average standard deviation of true stress for all repeats (MPa)				
	0.01 s <sup>-1</sup>	0.05 s <sup>-1</sup>	0.1 s <sup>-1</sup>	0.5 s <sup>-1</sup>	1 s <sup>-1</sup>
900	2.7	1.5	2.2	8.3	4.0
800	2.1		4.8	4.7	5.7
700	2.7		2.5	5.4	6.3
600			4.4	3	7.8
500			8.5	4.2	6.1

### 3.4.2. Temperature Effects

Figure 61 show the flow stress at various strains and strain rates, plotted against temperature. The purpose of each subplot is to showcase any potential relationship between flow stress and temperature. Comparing between the subplots provides insights to any potential changes in the relationship between flow stress and temperature. In general, a linear relationship can be observed between flow stress and temperature, for all strains and strain rates. Similar to PHS 1500, greater work hardening can be observed at the lower temperatures (500°C, 600°C), relative to the higher temperature conditions.

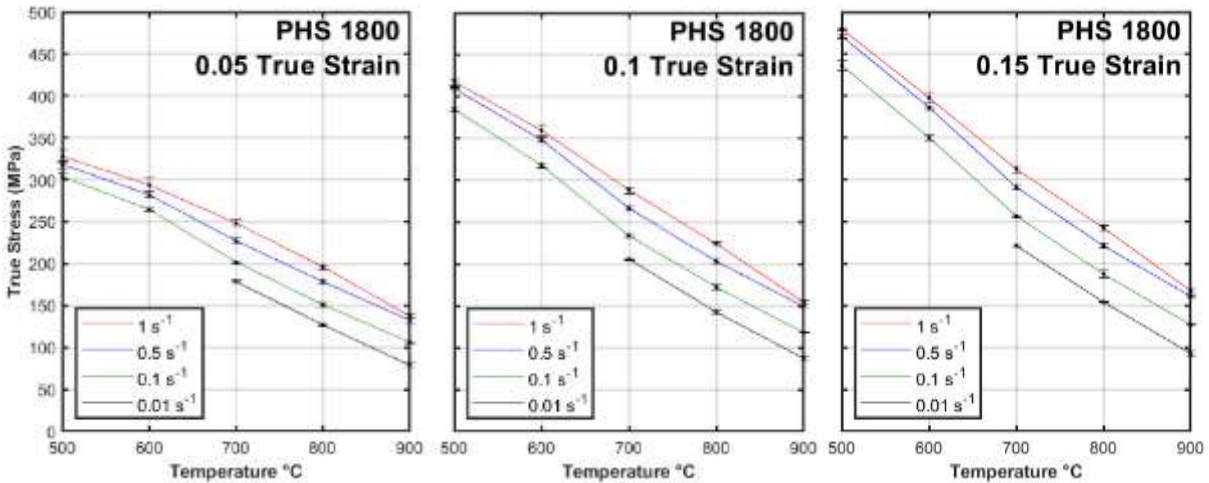


Figure 61: PHS 1800 flow stress values at various strain values and strain rates, versus temperature with error bars showing +/- 1 standard deviation of the flow stress values

### 3.4.3. Strain Rate Effects

Figure 62 shows the flow stress at various strains and temperatures, plotted against strain rate. This figure is intended to highlight the relationship between any changes in flow stress and strain rate. In general, a logarithmic relationship can be observed at almost all temperatures and strain rates. Notable exceptions to this trend occur at 500°C and 600°C at 0.05 strain, which may indicate a linear relationship, however, this is likely due to the lack of lower strain rate data. As discussed previously, the lowest rate ( $0.01\text{s}^{-1}$ ) tests were not performed at 500°C and 600°C due to likelihood of undesirable phase changes during the test.

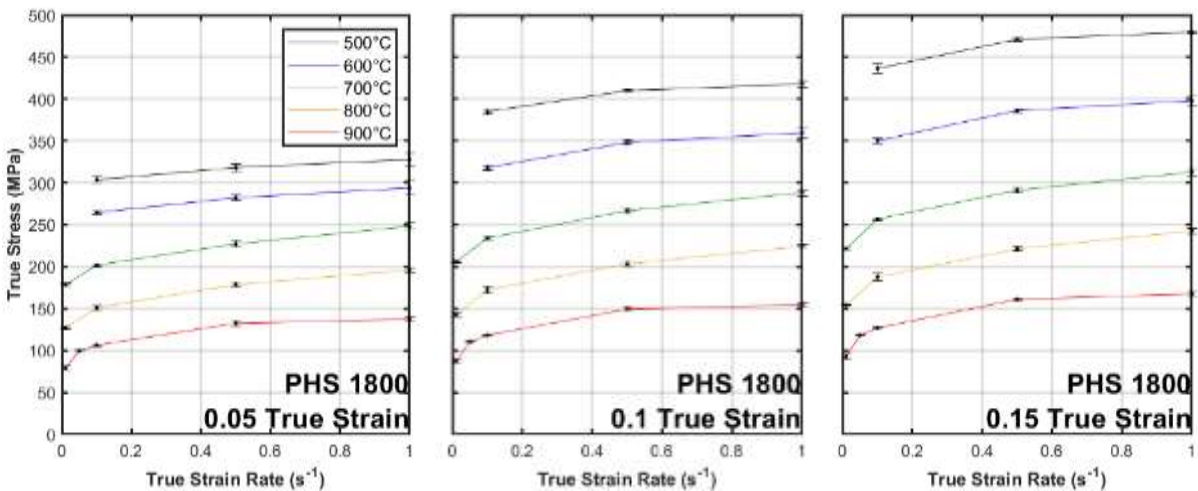


Figure 62: PHS 1800 flow stress values at various strain values and temperatures, versus strain rate with error bars showing  $\pm 1$  standard deviation of the flow stress values

Figure 63 shows the flow stress and strain rate plot for PHS 1800 but presented with strain rate on a logarithmic scale. As noted previously, a logarithmic relationship between flow stress and strain rate is evident for most temperature conditions. Certain exceptions can be observed, for example, the true stress tends to plateau between  $0.5\text{s}^{-1}$  and  $1\text{s}^{-1}$  at 900°C, however the logarithmic relation seems appropriate for all other conditions.

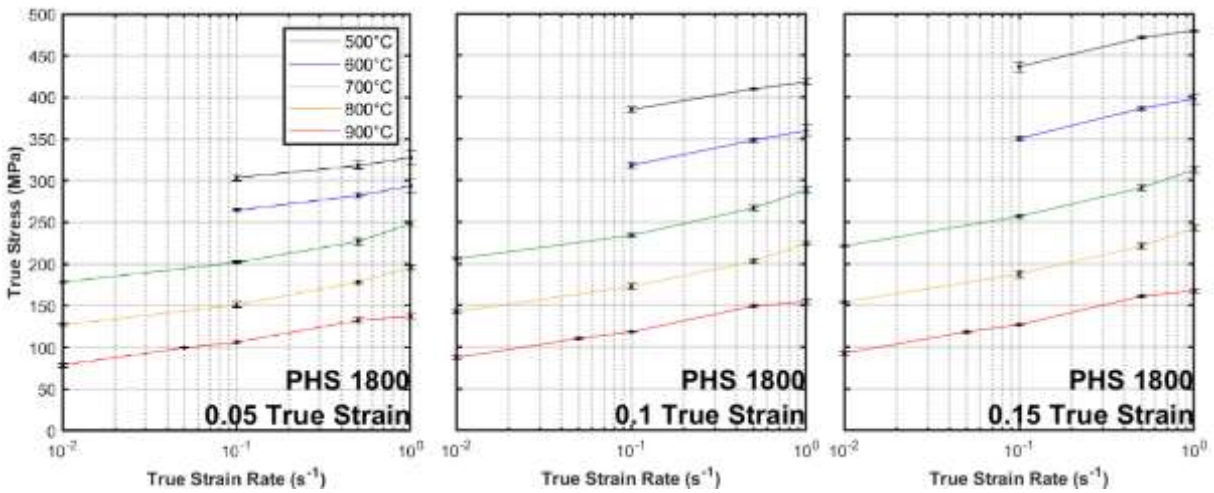


Figure 63: PHS 1800 flow stress values at various strain values and temperatures, versus strain rate on a log scale with error bars showing +/- 1 standard deviation of the flow stress values

### 3.5. Comparison of PHS 1500 and PHS 1800

Figure 64 shows a visual comparison of the PHS 1500 and PHS 1800 flow curves overlaid on each subplot. For all conditions, PHS 1800 exhibits a greater flow stress response compared to PHS 1500. At 5% strain, PHS 1800 experiences approximately 20% greater flow stress than PHS 1500 for all conditions. This difference in strength decreases with increasing strain. At 15% strain, PHS 1800 shows approximately 15% greater stress response than PHS 1500 for all conditions. In general, when comparing the behaviour of the flow curves, both materials display similar amounts of strain hardening at each test condition. At 500°C and 600°C, both materials experience necking at similar strains. However, at higher temperatures, PHS 1800 necks at lower strains (up to a 31% decrease) compared to PHS 1500, with a notable exception at 700°C and 0.01s<sup>-1</sup>.

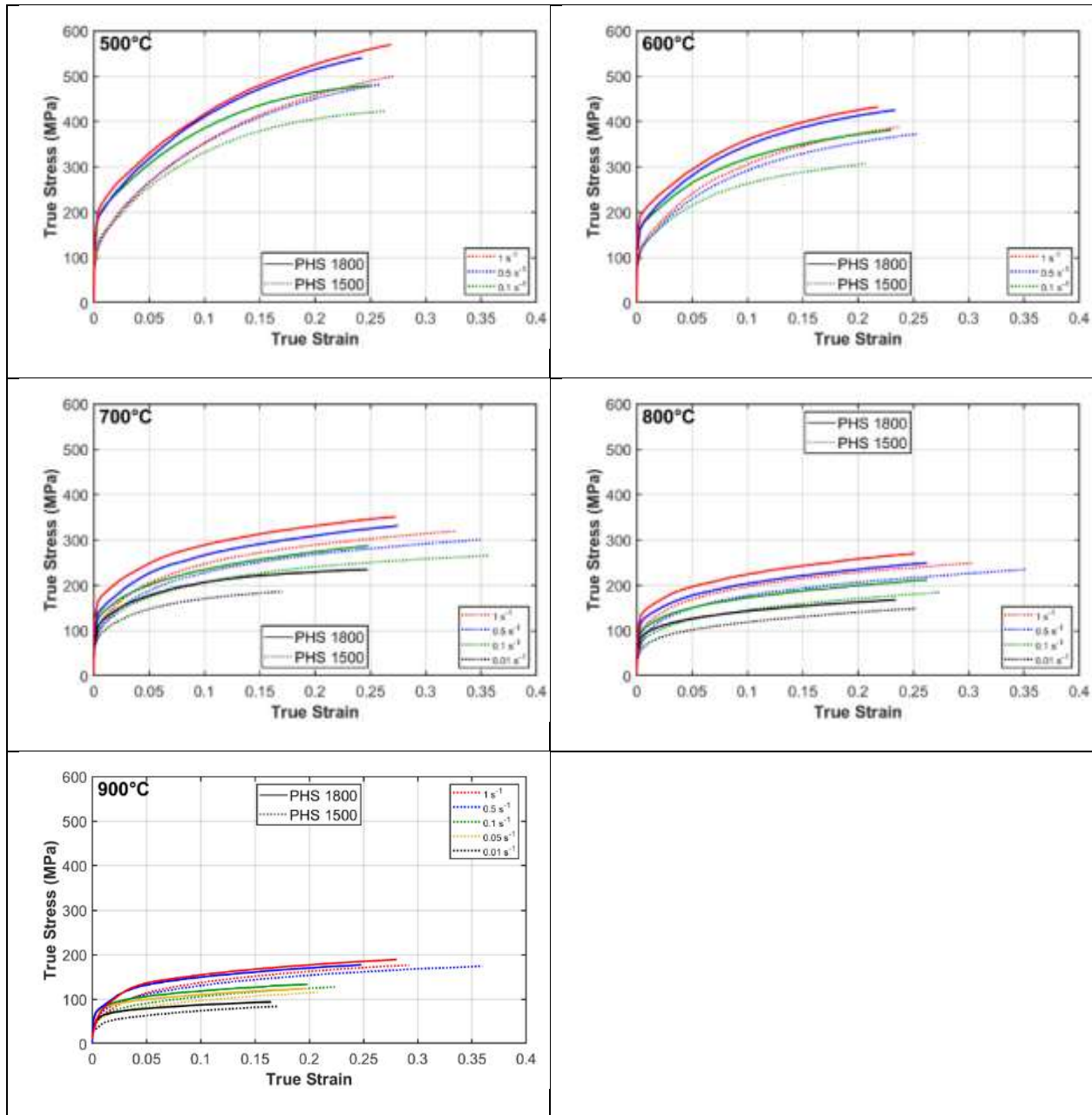


Figure 64: Experimental PHS 1800 (solid lines) and PHS 1500 (dotted lines) flow curves at various temperature and strain rate conditions after austenitization

### 3.6. Elevated Temperature Tensile Test Thermal Characterization

Figure 65 shows the thermocouple measurements of surface temperature along the length of the tensile specimen, taken after cooling from 930°C to various temperatures after 5s of rest for thermal stabilization. For clarity, only the average measurement value is shown. The maximum variation between measurements

at any location is below 3°C. A fourth-order polynomial curve is fit to each set of measured temperatures and is shown by the dotted lines.

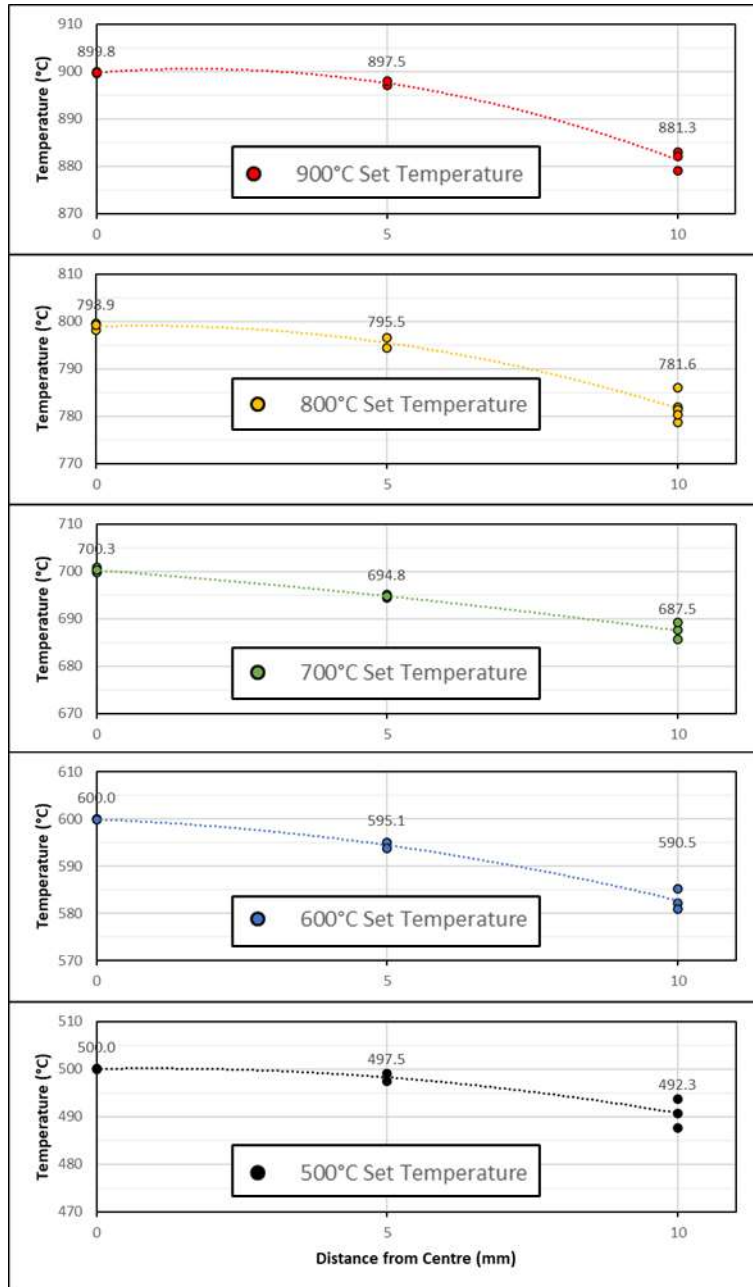


Figure 65: Average surface temperature along the length of the tensile specimen, after quenching to various deformation temperatures

For all temperatures evaluated in this study, there is a variation of less than 5°C from the set temperature within 5 mm from the centre of the specimen. A greater drop-off in temperature is observed at 10 mm from



the centre, varying from 8°C to 19°C depending on the centre temperature. The trends of these results are in line with expectations outline by Walsh *et al.* [39]. The main purpose of these temperature readings is for determining the validity of the test setup and ensuring that centre of the specimen is actually at the desired test temperature prior to testing. It is possible to utilize this data to determine a uniform temperature region about the centre of the specimen for a reduced length virtual (or physical) extensometer for strain measurements, similar to the strategy employed by Li *et al.* [45]. For all tested temperatures, it can be assumed that a uniform temperature region of +/- 5 mm (for a 10 mm extensometer, centred about the specimen centre) exists about the centre of the specimen, assuming that a deviation of 5°C from the target temperature is acceptable. If a deviation of less than 3°C is acceptable, then a further reduced +/- 2.5 mm region (5 mm extensometer) about the specimen centre is required. A comparison between results generated with a reduced extensometer to results obtained using the ARM (or to results obtained by a full-length extensometer) is beyond the scope of this research.

### **3.7. PHS 1800 Phase Transformation Results**

#### **3.7.1. Temperature History**

Figure 66 shows the measured surface temperature and the cooling rate versus time for both the zero-deformation and induced deformation phase transformation experiments for the 5°C/s cooling rate condition. The cooling rate data is inherently noisy since it represents a time derivative of measured thermocouple data. For the zero-deformation experiments, a relatively constant cooling rate of 5°C/s was achieved immediately after the initiation of cooling. This cooling rate was maintained until the end of the experiment at 100°C, 166 seconds after the onset of cooling. There is essentially no deviation from the programmed temperature vs. time profile. For the induced deformation condition, a significant change in the cooling rate can be observed at approximately 800°C, with fluctuations lasting around a second. This spike in the cooling rate occurs exactly during when the deformation is prescribed to the specimen. This change in the cooling rate can likely be attributed to the change in the position of the specimen (and thermocouple position) relative to the cooling nozzle, and the development of thermal/resistive heating

instabilities during deformation. Looking at the measured temperature, it can be observed that there is nearly negligible deviation when compared to the program temperature. After deformation, the cooling rate stabilizes immediately and remains consistent until the end of test, similar to the zero-deformation temperature profile.

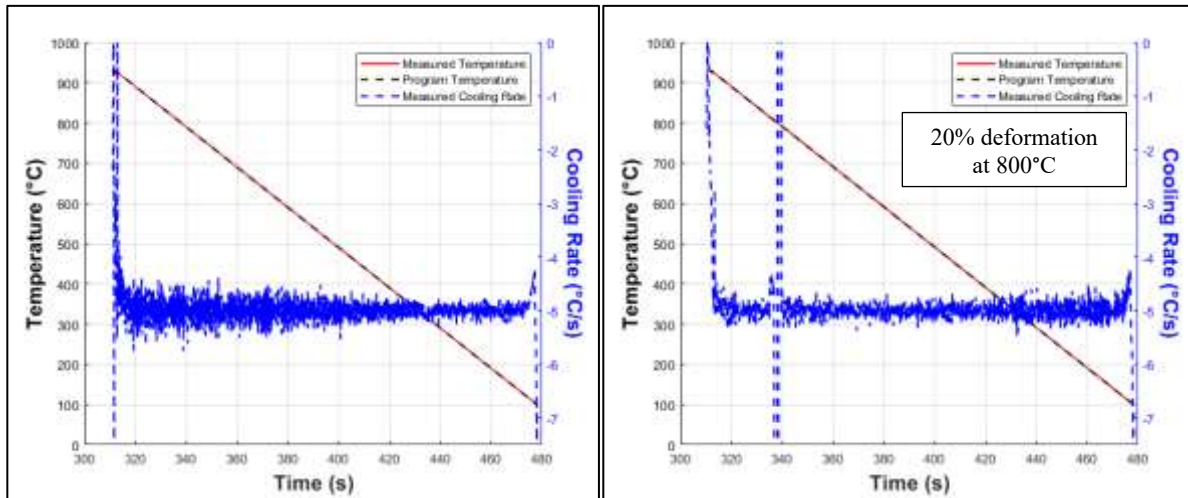


Figure 66: Measured temperature and cooling rate vs time from a 5°C/s cooling rate condition experiment with zero-deformation experiment (left) and a 20% deformation experiment (right)

Figure 67 shows the measured surface temperature and the cooling rate versus time for both the zero-deformation and induced deformation phase transformation experiments for the 10°C/s cooling rate condition. In general, the behaviour of the temperature and cooling rate curves are quite similar to the 5°C/s cooling rate results for both the zero-deformation and induced deformation experiments. Slightly greater noise can be observed in the cooling rate when compared to the 5°C/s condition results, however the average cooling rate is still maintained at the desired 10°C/s. At approximately 350°C, there is a sudden change in the cooling rate, due to the onset of martensite transformation causing thermal instabilities within the specimen. This fluctuation in cooling rate subsequently stabilizes and the desired 10°C/s is maintained until the end of the test.

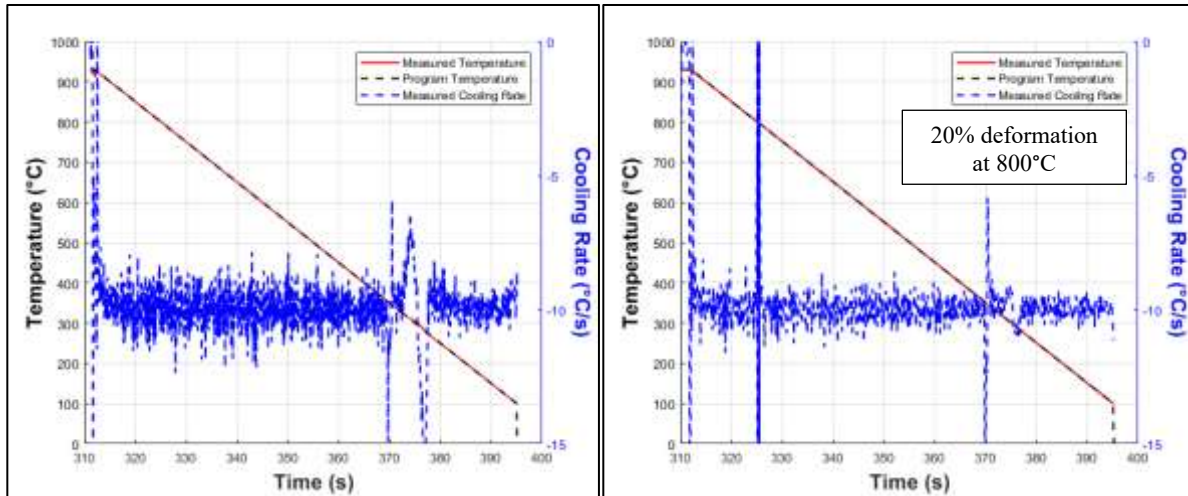


Figure 67: Measured temperature and cooling rate vs time from a 10°C/s cooling rate condition experiment with zero-deformation experiment (left) and a 20% deformation experiment (right)

Figure 68 shows the measured surface temperature and the cooling rate versus time for both the zero-deformation and induced deformation phase transformation experiments for the 50°C/s cooling rate condition. Unlike the results for the other cooling rate conditions, the desired cooling rate of 50°C/s is only maintained until approximately 350°C, the onset of martensite transformation. After which, the latent heat of martensite transformation heats the specimen, resulting in a significantly reduced cooling rate. At temperatures below 350°C, it can be seen that a cooling rate of only 5°C/s - 20°C/s can be maintained until the end of the test for both deformation conditions. As such, the measured temperature deviates significantly from the programmed temperature profile. This reduction in cooling rate is a limitation of using compressed air cooling and could perhaps be mitigated if liquid cooling was utilized. Because the specimen is rapidly cooled to 350°C at the desired cooling rate of 50°C/s, it is assumed that there is little time for ferrite, pearlite, bainite phases to form, and thus the intent of the high cooling rate is accomplished. Therefore, the hardness and phase fraction results from this experiment were deemed acceptable for the purposes of this study.

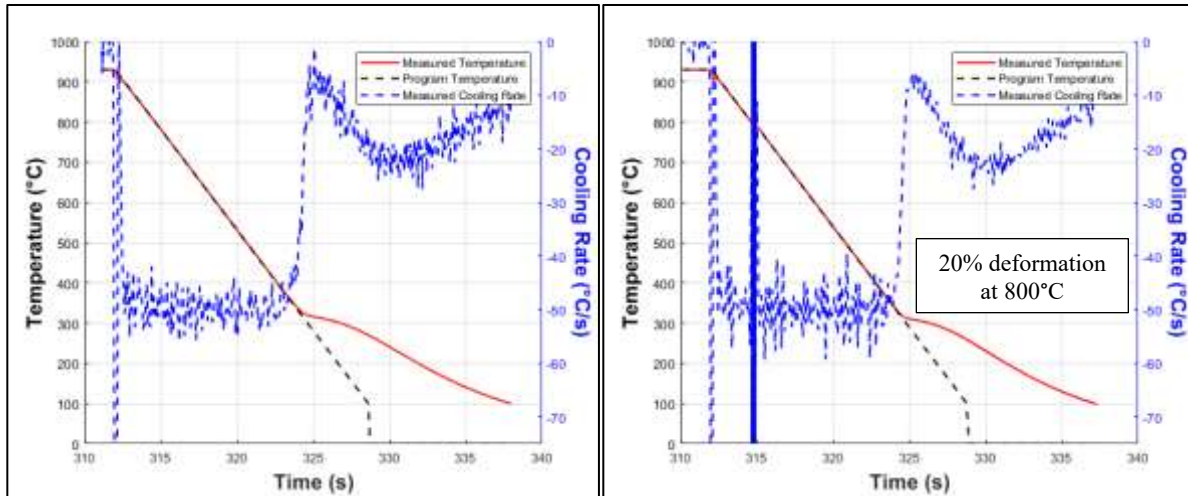


Figure 68: Measured temperature and cooling rate vs time from a 50°C/s cooling rate condition experiment with zero-deformation experiment (left) and a 20% deformation experiment (right)

### 3.7.2. Hardness Results

Figure 69 shows the average Vickers microhardness taken from specimens that were quenched at varying cooling rates and simultaneously deformed using the Gleeble. A minimum of 17 measurements was taken across the width of each specimen. Error bars are included in the figure to represent +/- 1 standard deviation of the measurements. Measurements near the uncoated (machined) faces were discarded due to the possibility of decarburization affecting the results.

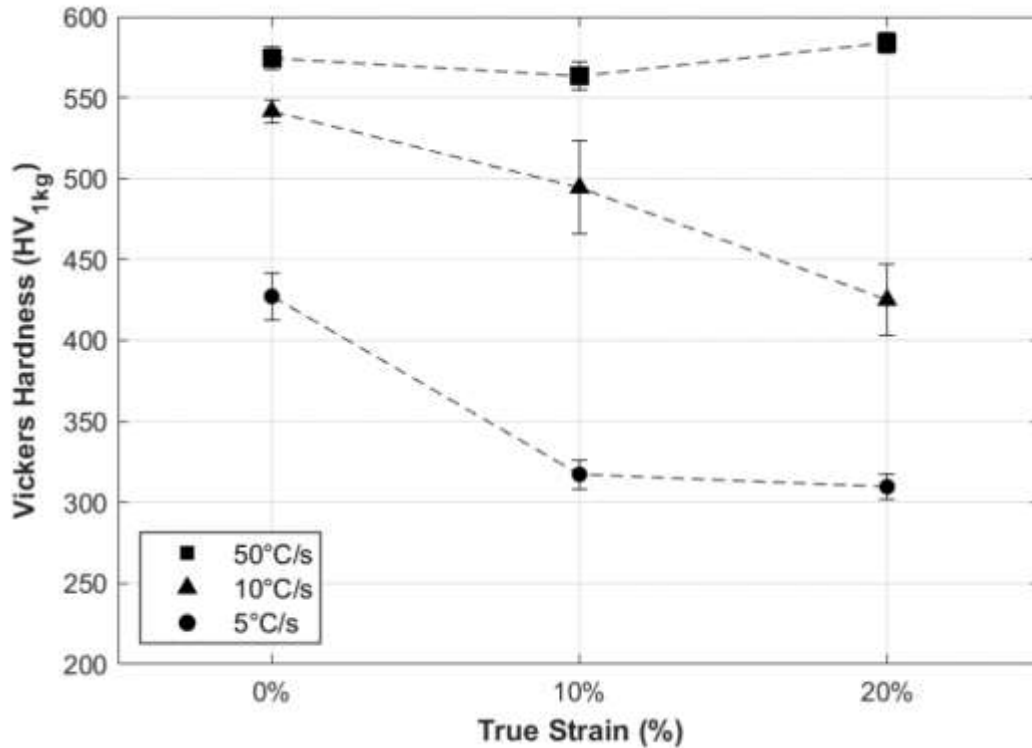


Figure 69: Measured Vickers microhardness of PHS 1800 after quenching to room temperature at various cooling rates and with various levels of applied deformation. Error bars indicate +/- 1 standard deviation of each measurement set

For the zero deformation conditions, it can be seen that the lower cooling rates result in lower hardness values. When quenched at 50°C/s, it is apparent that the critical cooling rate (cooling rate to achieve a fully martensite microstructure) for PHS 1800 is achieved as observed by the high microhardness values beyond 550HV. This high hardness value is in line with hardness values reported in the literature by Barcellona and Palmeri [77], and Holzweissig *et al.* [95] for a fully martensitic PHS microstructure.

The specimens cooled at 50°C/s experienced a slight reduction (11 HV) in hardness when deformed to 10% tensile strain, and a slight increase (10 HV) in hardness when deformed to 20% tensile strain. T-tests were conducted on the hardness measurements to compare the deformed condition results to the zero-deformation results and showed statistically significant differences between the hardness results beyond just measurement error. The hardness fluctuation with increasing tensile strain at 50°C/s indicates a non-linear relationship between final hardness of the fully martensite structure and applied strains in the austenite state. For the specimens cooled at 10°C/s, the hardness values decreased with increasing

deformation almost in a linear fashion. Additionally, the variability of hardness measurements (as represented by the standard deviation error bars in Figure 69) also increased with increasing deformation. For the specimens cooled at 5°C/s, hardness decreased significantly at 10% strain and stabilized at approximately 320 HV, with no further change when compared to the 20% strain specimen.

### **3.7.3. Optical Micrographs and Phase Fractions**

Figure 70 shows the microstructure of PHS 1800 after quenching at 50°C/s and with various levels of tensile deformation applied at 800°C. A fully martensitic microstructure composed of primarily fine grains with sparsely dispersed large lath structures can be observed for all three deformation levels.

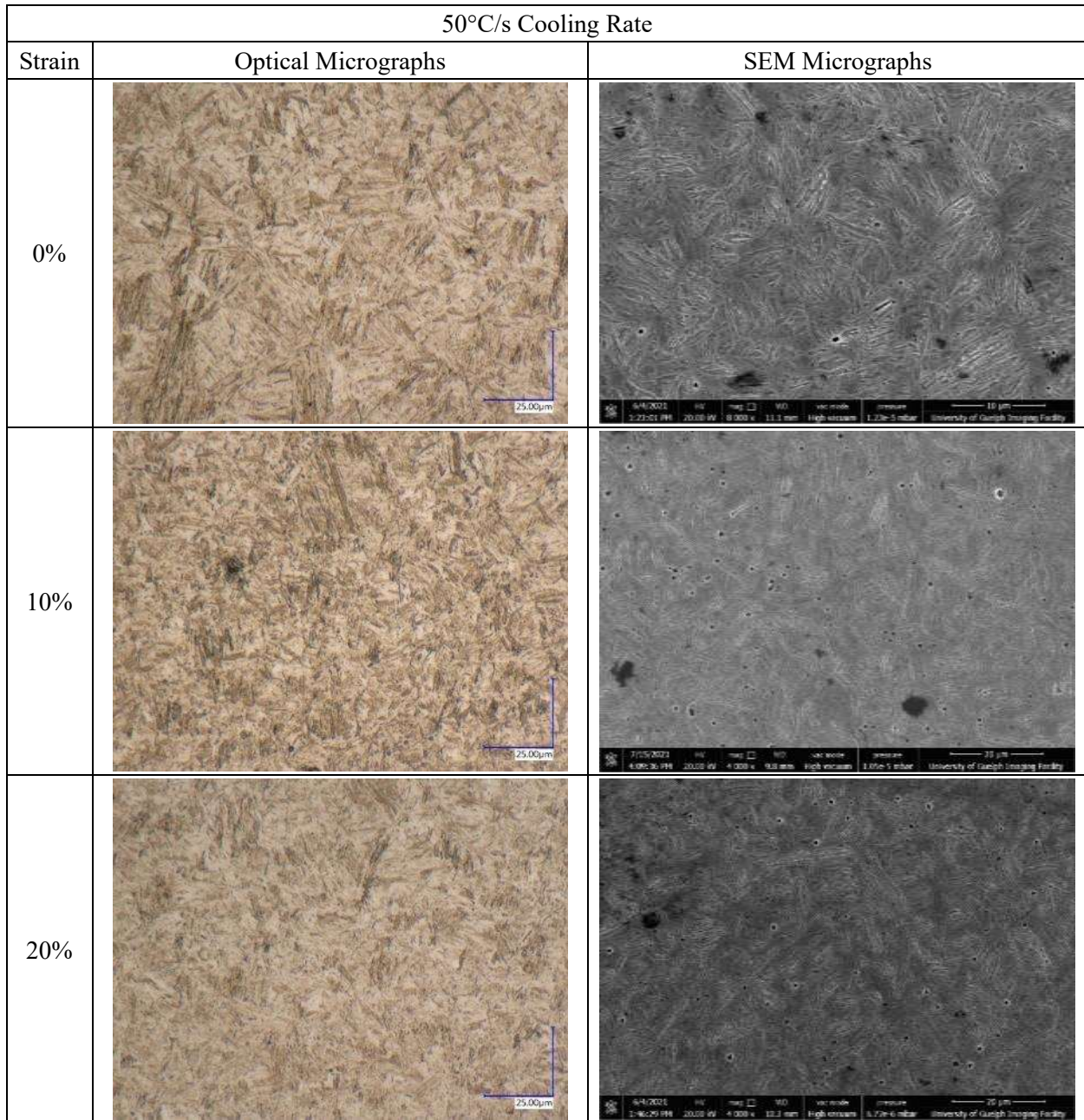


Figure 70: Optical and SEM micrographs of PHS 1800 after quenching at 50°C/s and with varying levels of applied deformation at 800°C

Figure 71 shows the microstructure of PHS 1800 after quenching at a constant cooling rate of 10°C/s with various levels of deformation induced at 800°C. In the zero deformation (0% true strain) condition, the microstructure is composed of primarily martensite (bronze colored regions in the optical micrograph) with sparsely scattered colonies of ferrite (white patches surrounded by dark boundaries in the optical micrograph), and trace amounts of bainite. For the SEM micrographs, martensite is observed as the

primarily light grey matrix while ferrite colonies are identified by dark grey islands surrounded by white outlines. With increasing deformation, a greater area fraction of ferrite can be observed throughout the micrograph. At 10% strain, ferrite becomes widely dispersed among the martensite matrix and continues to increase for the specimen deformed to 20% strain. This increasing concentration of ferrite explains both the decrease in the hardness measurements, as well as the increase in the variation of the hardness measurements with respect to deformation reported in Figure 69. Hardness measurements taken on predominantly martensitic patches would result in higher hardness measurements whereas measurements taken on areas with more ferrite grains would result in lower hardness values. When the microstructure becomes increasingly dual-phase at greater applied strains, greater variance in the hardness measurements occurs due to the increased likelihood of sampling mostly one phase over the other.



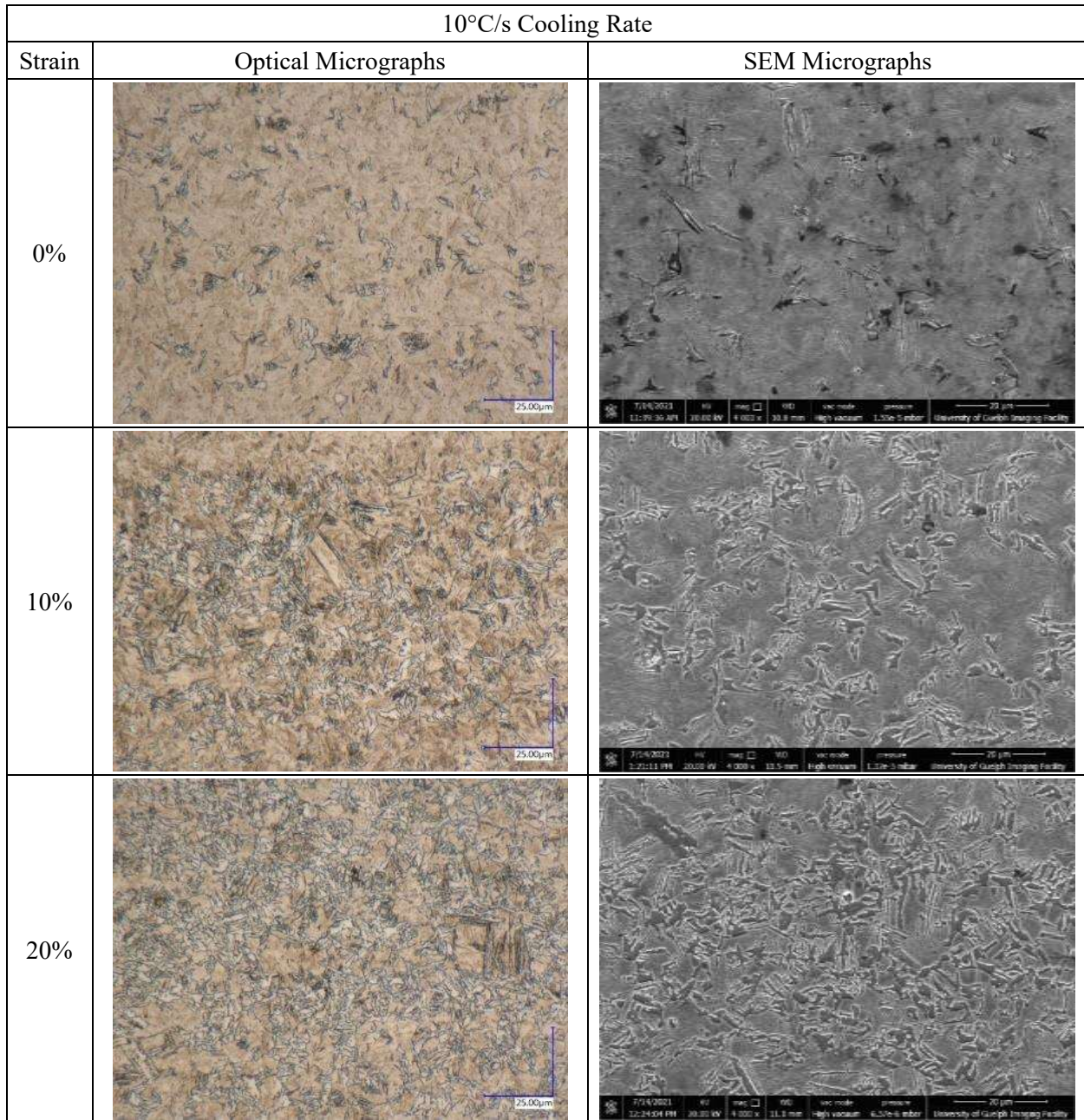


Figure 71: Optical and SEM micrographs of PHS 1800 after quenching at 10°C/s and with varying levels of applied deformation at 800°C

Figure 72 shows the microstructure of PHS 1800 after quenching at 5°C/s with deformation induced at 800°C. With no induced deformation, the microstructure is mostly martensitic with a significant fraction of ferrite. Some bainite is also evidenced by the patches of feather-like texture in the SEM micrograph. Comparing optical micrographs, the zero-deformation microstructure quenched at 5°C/s is quite similar to that of the 10°C/s specimen with 20% deformation. This similarity is further highlighted by comparing the

hardness values seen in Figure 69 for the 5°C/s with 0% deformation, and 10°C/s with 20% deformation conditions. For the 10% and 20% strained conditions, both the optical and SEM micrographs seem similar, consisting of nearly an equal distribution of ferrite and martensite. The reduced area fraction of martensite is also apparent in the hardness results, as observed by the drop in microhardness with induced deformation. Because of the uniformly fine distribution of both phases throughout the entire observed area, the variance of the hardness measurements for the 10% and 20% strained specimens is actually lower than the less uniform microstructure at 0% strain.

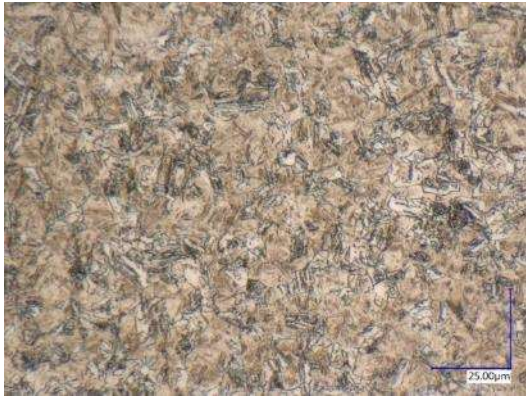
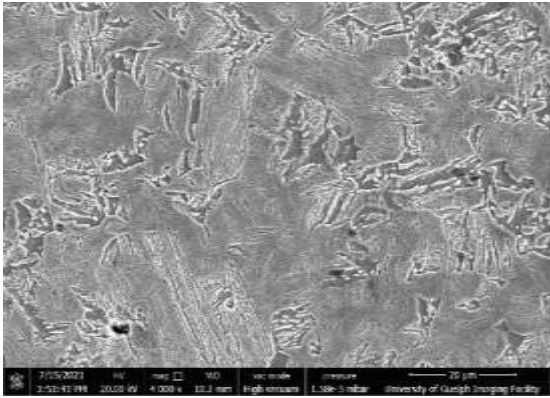
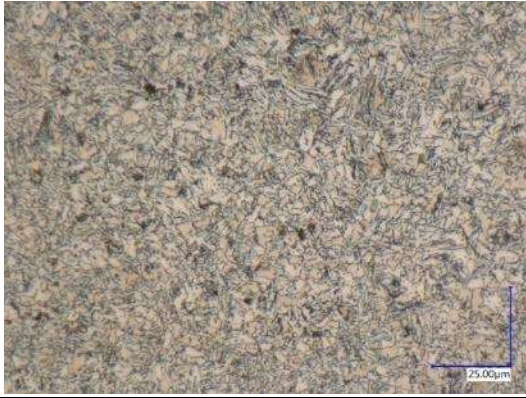
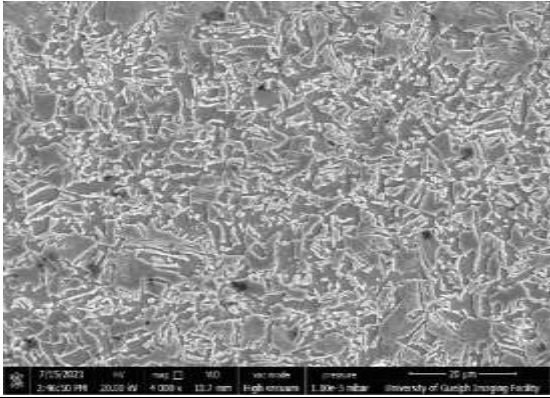

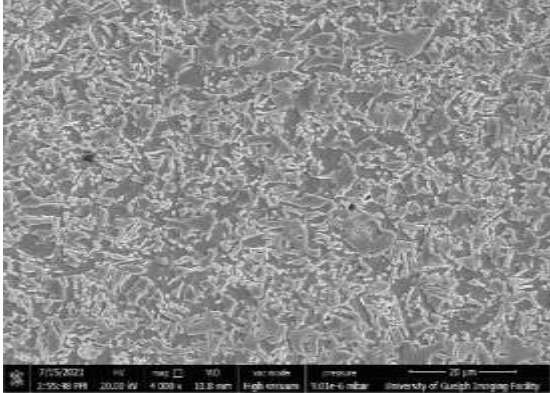
5°C/s Cooling Rate		
Strain	Optical Micrographs	SEM Micrographs
0%		
10%		
20%		

Figure 72: Optical and SEM micrographs of PHS 1800 after quenching at 5°C/s and with varying levels of applied deformation at 800°C

As mentioned in Section 2.6, these area fractions were determined first by identifying phases based on grain structure and boundaries. Then, ferrite and bainite phases were manually segmented from the rest of the microstructure by color coding to easily distinguish colors. The area fractions of each phase were then calculated by counting the number of pixels of each color (representing each phase), and dividing by the total number of pixels in the micrograph. Figure 73 shows an example of a processed micrograph for a

sample cooled at 10°C/s with 10% applied deformation, with the martensite areas colored green, ferrite patches as red, and bainite structures colored blue.

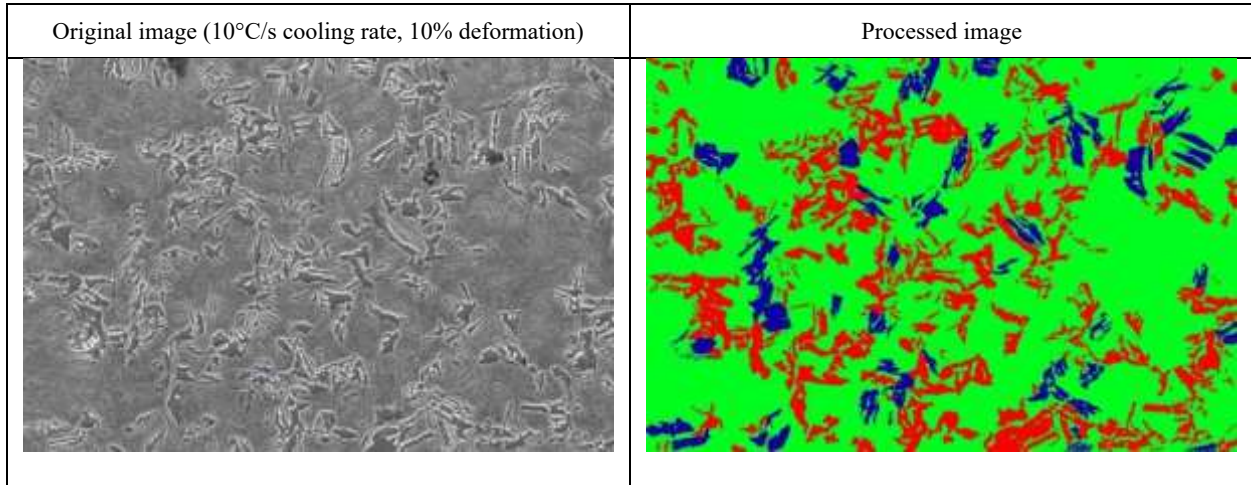


Figure 73: Comparison of original SEM micrograph and processed image of a PHS 1800 sample cooled at 10°C/s with 10% applied deformation. For the processed image, martensite phases are green, ferrite phases are red, and bainite structures are blue

Table 9 summarizes the average area fractions of ferrite, bainite, and martensite from the quenched and deformed specimens. A total of three SEM micrographs were taken at different locations on each specimen and analyzed, then the average phase fraction results are presented along with the standard deviation of the measurements. The standard deviation was calculated from phase area fraction values from the three micrographs taken for each condition. The error associated with the possibility of misidentification of the phases also exists, however cannot be easily quantified.

Table 9: Average area fractions and standard deviations for ferrite, bainite, and martensite of PHS 1800 specimens quenched at various cooling rates with varying levels of deformation

Cooling Rate (°C/s)	True Strain (%)	Ferrite (%)	Bainite (%)	Martensite (%)
50°C/s	0	-	-	100
	10	-	-	100
	20	-	-	100
10°C/s	0	6 ± 1	2 ± 1	91 ± 2
	10	20 ± 1	7 ± 1	73 ± 1
	20	30 ± 3	6 ± 2	64 ± 4
5°C/s	0	17 ± 8	16 ± 3	67 ± 10
	10	49 ± 3	6 ± 1	46 ± 4
	20	51 ± 2	2 ± 1	46 ± 2

As previously discussed, all specimens quenched at 50°C/s are completely martensitic, regardless of deformation amount. For the specimens quenched at 10°C/s, ferrite area fraction increases steadily with increasing deformation, resulting in a steady decrease of martensite. The specimen quenched at 5°C/s with zero-deformation features a relatively complex microstructure, hence the large standard deviation. With deformation, the 5°C/s specimen experiences a plateau in ferrite phases between 10% and 20% strain, resulting in a largely similar overall phase composition between the two deformation conditions (and similar hardness in Figure 69).

## **4. PHS 1800 Constitutive Modelling**

### **4.1. Constitutive Model Fitting**

An initial fitting exercise was performed in order to fit the modified Norton-Hoff equation (equation (6)) from [42] to the measured data. Figure 74 shows the PHS 1800 flow curves generated by fitting equation (6) (dashed lines) overlaid on the experimental results (solid lines). The fit flow curves are extrapolated beyond the experimental data for reference.

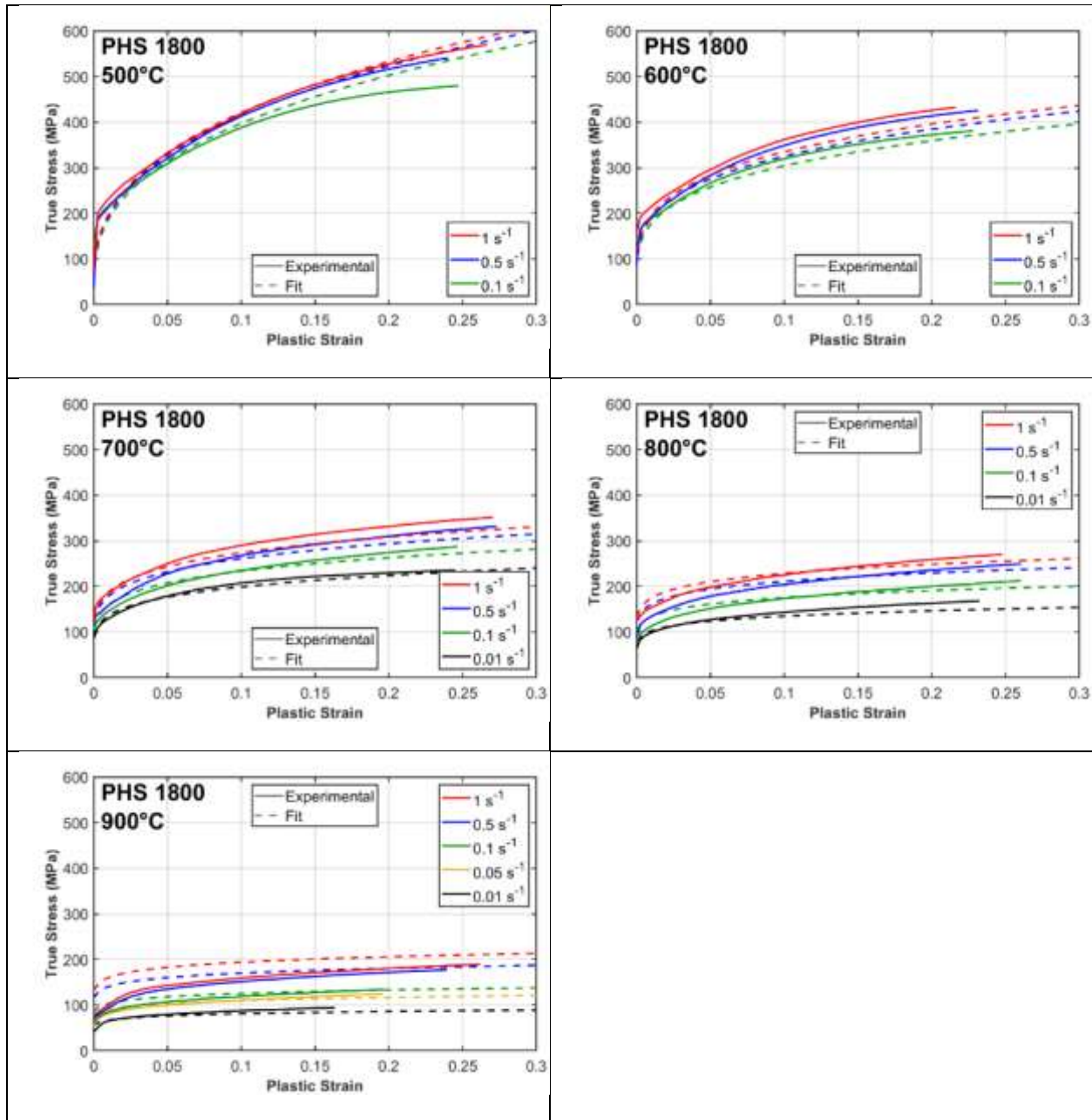


Figure 74: Experimental (solid) and fit (dash) flow curves of PHS 1800, fit to the modified Norton-Hoff equation (equation (6)) proposed by Merklein and Lechler [42]

As previously described, the coefficients of the modified Norton-Hoff equation are determined by least squares regression fitting of the model to all experimental results using MATLAB. The R-squared value of the fit is 0.8862. At higher strain rates, the model seems incapable of capturing the strain hardening behaviour observed in the experimental results. At 800°C and 900°C, for the 0.5s<sup>-1</sup> and 1s<sup>-1</sup> conditions, the fit curves under-represent the amount of strain hardening and reach saturation prematurely. Conversely, at

500°C and 600°C, the fit strain hardening behaviour matches the experimental observation at low strains but deviates significantly at higher strains. In general, the modified Norton-Hoff equation (equation (6)) utilized by Merklein and Lechler [42] seems appropriate for the lower strain rate conditions, and for flow curves experiencing a steady reduction in strain hardening with increasing temperature.

In order to improve the modified Norton-Hoff equation for fitting to the results of this research, the evolution of both the strain hardening exponent ( $n$ ) and strain rate sensitivity coefficient ( $m$ ) with respect to temperature was investigated. This was performed by fitting the modified Norton-Hoff equation to each experimental flow curve individually, while holding the  $A$ ,  $B$ , and  $b$  parameters constant to obtain the best fit  $n$  and  $m$  values. Figure 75 shows the best fit strain hardening exponent ( $n$ -value) for all flow curves at all temperature conditions (shown in degrees Kelvin).

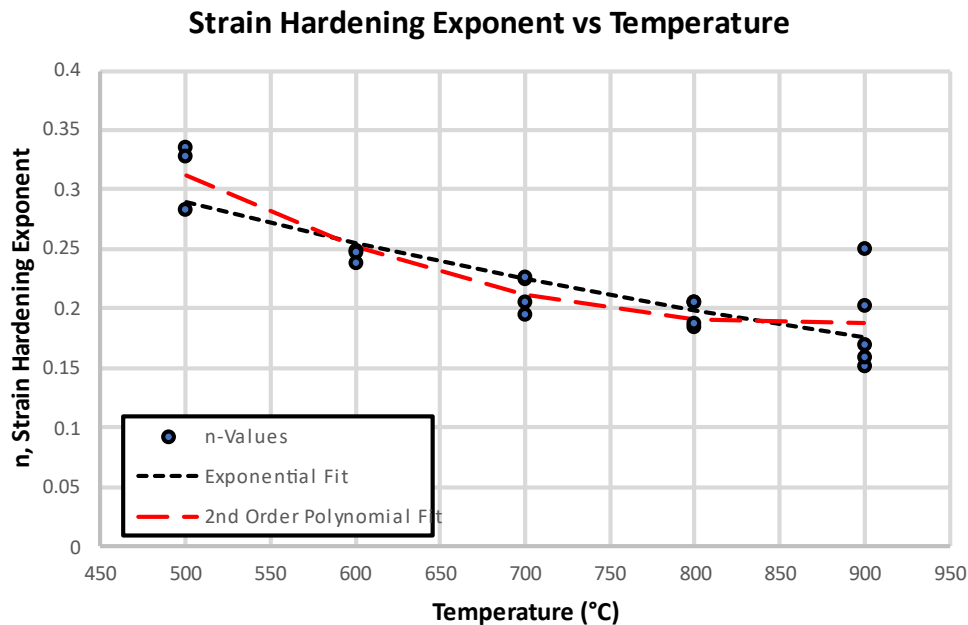


Figure 75: Best fit strain hardening exponent ( $n$ ) for every PHS 1800 flow curve

Observing the overall trend of the scatter plot, a plateau or possible inflection is seen between 800°C and 900°C (1073K – 1173K). There is also relatively high variation in the  $n$ -values at 900°C. In general, the exponential relationship of the strain hardening exponent with respect to temperature does not adequately represent the observed data. Additionally, the exponential relationship cannot capture the sharp



drop in n-value between 500°C to 700°C (773K – 973K). A proposed change to the exponential relationship is to use a second-order polynomial equation to represent the change in n-value versus temperature. A second-order polynomial would be more capable of representing the plateau or inflection in the observed data, while simultaneously capturing a greater change in the n-value at lower temperatures. The best fit second-order polynomial equation is shown in Figure 75, as the red dashed lines, and results in an R-squared value of 0.7935. For reference, the best fit exponential relation results in a R-squared value of 0.7260.

An analysis of the strain rate sensitivity coefficient,  $m$ , was also conducted following the same methodology as previous described and is shown in Figure 76.

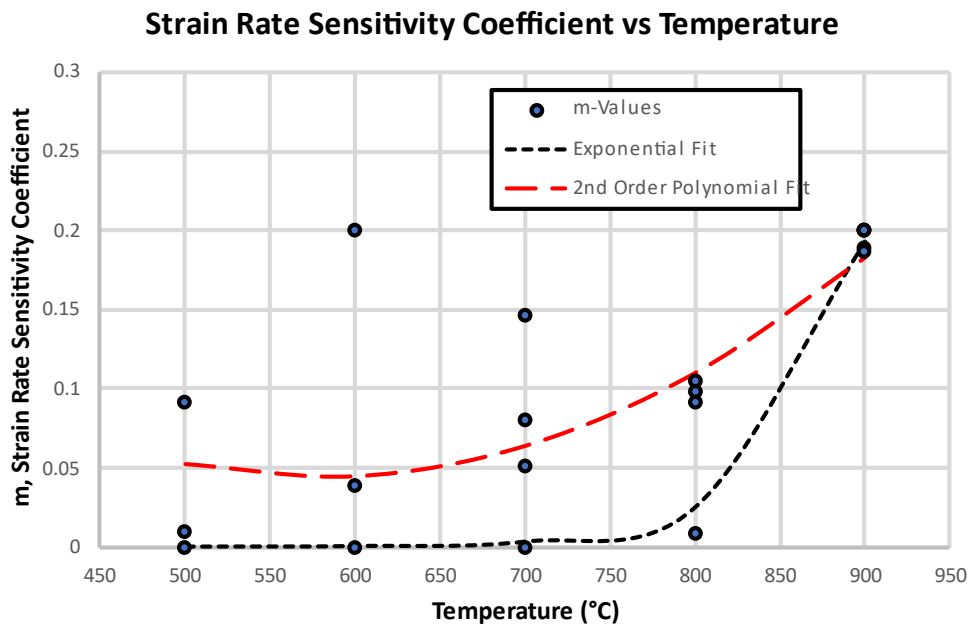


Figure 76: Best fit strain rate sensitivity coefficient ( $m$ ) for all PHS 1800 flow curves

No clear trends can be observed from the distribution of the strain rate sensitivity coefficients ( $m$ -value) with respect to temperature, except that the values are all nearly identical at 900°C (1173K). This observation could indicate that the strain rate sensitivity coefficient is not closely correlated with temperature, contrary to the PHS 1500 results shown by Merklein and Lechler [42]. However, no clear relation between the  $m$ -value and any other parameters (such as strain rate) could be easily identified. Both best fit exponential and second-order polynomial relations were applied to the  $m$ -values with respect to

temperature. Poor correlation is observed for both relations; however, the exponential relation is trivially better with a R-squared of 0.5621 compared to 0.5007 for the polynomial fit. To be consistent, both the strain hardening and strain rate sensitivity coefficient relationship to temperature were modified to be a 2<sup>nd</sup> order polynomial function of temperature, shown by Equations (24) - (26). The remaining parameters of the modified Norton-Hoff equation presented by Merklein and Lechler [42], shown by Equation (6), remain unchanged.

$$\sigma = Ae^{\frac{B}{T}}(b + \varepsilon_p)^{n(T)}\dot{\varepsilon}^{m(T)} \quad (24)$$

$$n(T) = n_1T^2 + n_2T + n_3 \quad (25)$$

$$m(T) = m_1T^2 + m_2T + m_3 \quad (26)$$

It should be noted that the n-values, m-values, and best fit equations presented in Figure 75 and Figure 76 will not necessarily have the same values obtained in the final fitting of second-order polynomial Norton-Hoff equation. The reason for this is that the fitting of the results in Figure 75 and Figure 76 are completely unconstrained to a temperature relationship, to avoid assuming and enforcing the results to any equation. In the fitting of the second-order polynomial Norton-Hoff equation, the n and m values are constrained to a second-order polynomial relation with temperature, resulting in the determination of a completely different set of best-fit coefficients to minimize the residuals.

Figure 77 shows the flow curves generated by the further modified Norton-Hoff equation (referred to as the second order polynomial Norton-Hoff equation), with second-order polynomial relations for the strain hardening and strain rate sensitivity coefficients (dashed lines) overlaid on the experimental results (solid lines). The coefficients of the second order polynomial Norton-Hoff equation are determined in an identical manner to the previously discussed results.

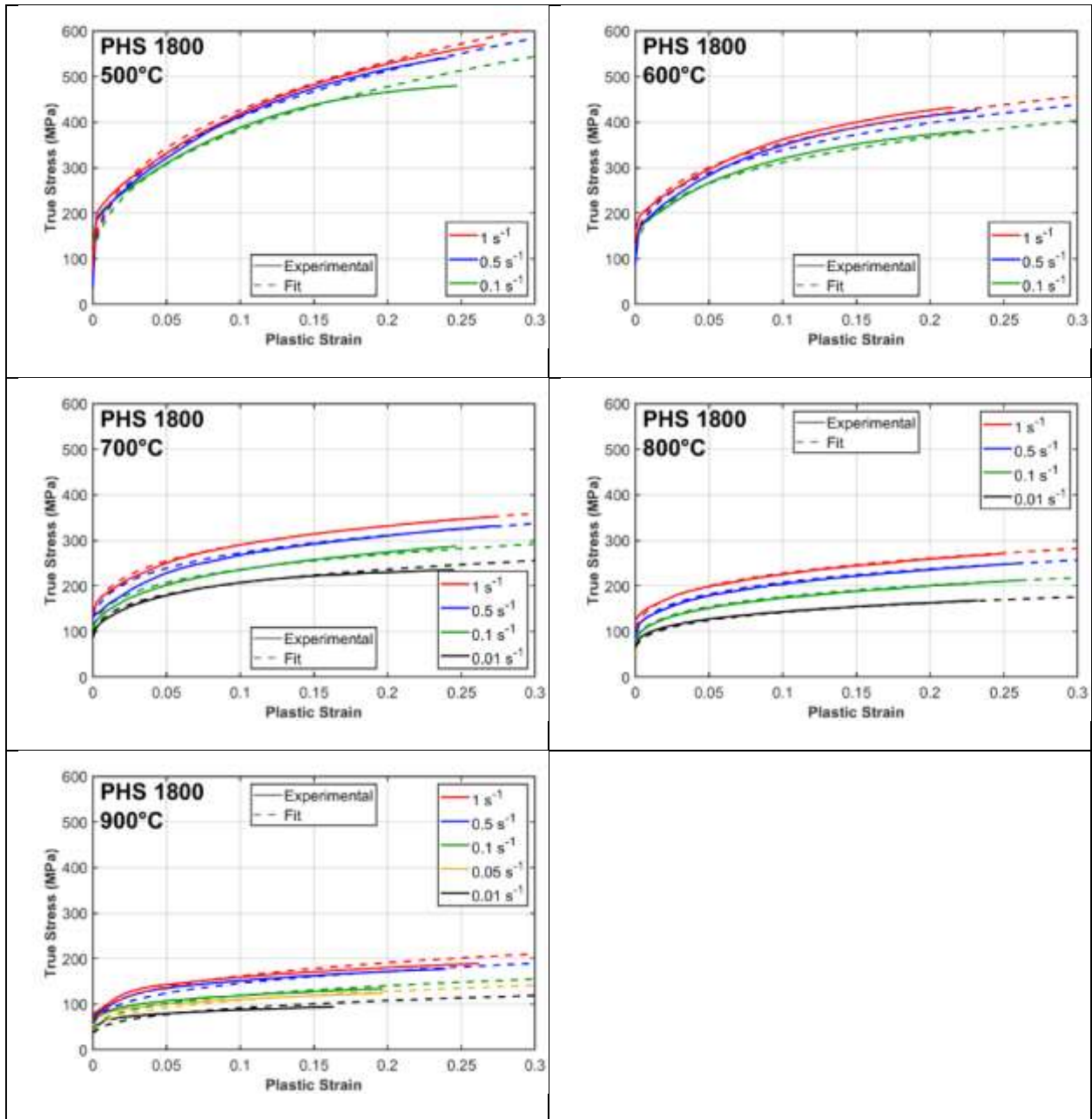


Figure 77: Experimental (solid) and fit (dash) flow curves of PHS 1800 fit to the modified second order polynomial Norton-Hoff equation

In general, the fit curves and the experimental curves are in very good agreement at 600°C and 800°C for all strain rates. At the other temperatures, the change in the work hardening relationship with temperature has a significant effect on the fit results. For the 500°C and 600°C results, the fit curves display greater work hardening at high strains in comparison to the experimental results. At 900°C, the fit results demonstrate slightly greater work hardening throughout the entire strain range for all strain rate conditions.

Compared to the fit results using the Norton-Hoff equation by Merklein and Lechler [42] shown in Figure 74, a much better fit is achieved.

The coefficients for the second order polynomial Norton-Hoff are shown in Table 10 for reference.

Table 10: Coefficients for the Modified Norton-Hoff equation for PHS 1800, obtained by fitting Equations (24) - (26) to the experimental flow curves

<b>A (MPa s<sup>m</sup>)</b>	<b>B (K)</b>	<b>b</b>	<b>n1 (K<sup>-2</sup>)</b>	<b>n2 (K<sup>-1</sup>)</b>	<b>n3</b>	<b>m1 (K<sup>-2</sup>)</b>	<b>m2 (K<sup>-1</sup>)</b>	<b>m3</b>
27.454	2680.108	0.00169	2.253e-6	-4.629e-3	2.551	3.199e-7	-4.126e-4	0.176

The fit coefficients shown in Table 10 resulted in a R-squared of 0.971, calculated by comparing all experimental stress and strain data points (from every temperature and strain rate condition) to the corresponding fit values. To evaluate the fit at each temperature and strain rates condition, the R-squared of the fit was calculated with respect to the experimental flow curve at each test condition and is tabulated in Table 11.

Table 11: R-Squared of the fit flow curves compared to the experimental flow curves, using the coefficients from Table 10

Temperature Condition (°C)	Strain Rate Condition (s <sup>-1</sup> )	R-Squared
500°C	0.1	0.977
	0.5	0.989
	1	0.993
600°C	0.1	0.967
	0.5	0.962
	1	0.976
700°C	0.01	0.983
	0.1	0.982
	0.5	0.976
	1	0.989
800°C	0.01	0.954
	0.1	0.995
	0.5	0.996
	1	0.975
900°C	0.01	0.723
	0.05	0.778
	0.1	0.840
	0.5	0.947
	1	0.871

It should be noted that the individual R-squared values do not average to cumulative R-squared value of 0.971 because different test conditions have differing quantities of data points (due to varying data acquisition rates for varying strain rate conditions). The R-squared value is also not necessarily a good indicator of fit quality or model quality, however the values are included for reference. As an example, all flow curves for the 500°C condition show a high R-squared value, but the fit curve clearly shows greater strain hardening than the experimental observations at high strains. Conversely, at 900°C, the fit curves are unable to capture the relatively low strain hardening behaviour, resulting in a relatively low R-squared value for all strain rate conditions. The low R-squared value for the 900°C fits may indicate that the second-order polynomial Norton-Hoff equation does not account for all relevant parameters to accurately capture the flow curve behaviour and may not be a suitable constitutive equation for PHS at this high temperature. With the exception of the 900°C temperature condition, the second-order polynomial Norton-Hoff equation adequately captures the material flow behaviour at all tested conditions with high degree of accuracy.

PHS 1500 was also fit to the second-order polynomial Norton-Hoff equation and results can be found in Appendix D. A similar improvement was observed by imposing a second-order polynomial relation between temperature and both the strain hardening and strain rate coefficients. Investigating the constitutive fitting of PHS 1500 was beyond the scope of the current work and will not be discussed in detail.

## **4.2. Finite Element Model Setup**

A finite element (FE) model of the elevated temperature tensile tests presented in Section 2.5 was constructed to conduct simulations of tensile tests at select temperature and strain rate conditions. This virtual replication of the experiment was used in conjunction with the fit flow curves as a verification of the experimental method and the accuracy of the fit flow curves. Figure 78 shows the finite element mesh and boundary conditions for the FE replication of the tensile tests conducted in this research. A 1/4-symmetry model was used to reduce computation time. To enforce the correct boundary conditions, planar symmetry conditions were applied at the two symmetry faces at the centre (longitudinal and width axes) of the specimen. A fine and uniform mesh size was used within the gauge length of the specimen geometry to

obtain high resolution results in the region of interest. A high resolution prediction was important to accurately predict the deformation at the centre, which is needed to replicate the ARM calculations virtually and provide a direct comparison of the experimental and simulated results. Fully integrated selective reduced 8-node hexahedral elements were used instead of shell elements to provide a high resolution discretization to capture through-thickness deformation (and strain) results to capture the thinning behaviour of the specimen during the tensile test. The use of multiple solid elements to represent the thickness of the specimen allows the extraction of surface strains (from the surface elements) to enable virtual ARM calculations. It may be feasible to achieve similar results with shell elements and the use of multiple through-thickness integration points, however, the exploration of such modeling strategy is beyond the scope of this research. The grips to pull the specimen were not modeled to simplify and reduce the runtime of the simulation. Since the deformation is concentrated within the gauge length, excluding the grips at the ends of the specimen is assumed to have no effect on the results.

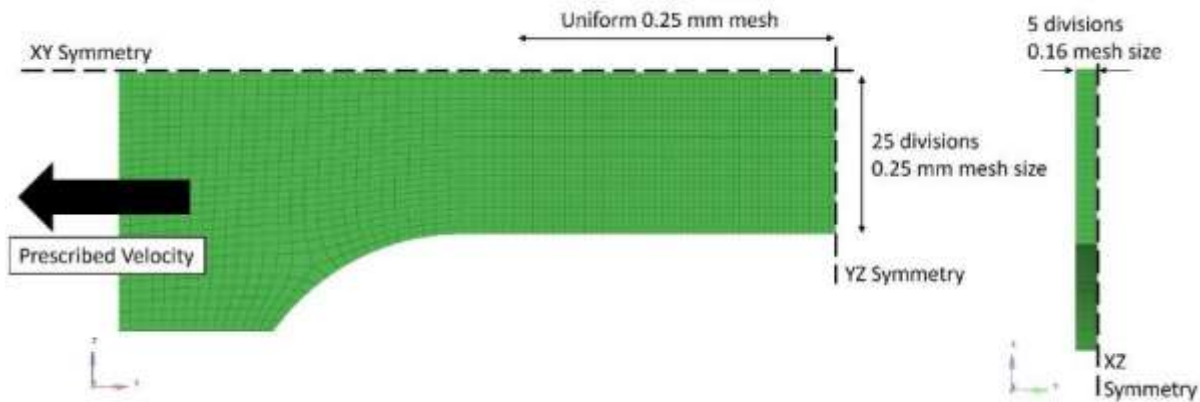


Figure 78: Tensile test finite element mesh and mechanical boundary condition setup to validate fit flow curves

An isotropic temperature and strain rate sensitive material model (MAT\_106 in LS-DYNA) was used to apply the fit flow curves presented in the previous section. Because phase change or hardness predictions are irrelevant to the constitutive model predictions during hot stamping, it was not necessary to use a material card that included phase change mechanics.

In order to represent the temperature distribution across the gauge of the tensile specimen, the experimentally determined temperature profile shown in Figure 65 was applied to the model as the initial

thermal condition. The temperatures beyond the reduced gauge region were determined by extrapolation of the fourth-order polynomial fit of the temperature profile. The temperature profile was prescribed by applying the measured temperatures to the nodes at the measurement locations, and then solving for the temperatures at all other nodes by letting the model achieve thermal equilibrium in an implicit thermal simulation. Figure 79 shows the prescribed temperature boundary conditions prior to solving for the temperature distribution. An interpolated temperature value at 2.5mm from the centre was calculated and applied to better capture a fourth-order temperature variation near the centre of the specimen (rather than a linear temperature variation between the centre and 5mm from centre).

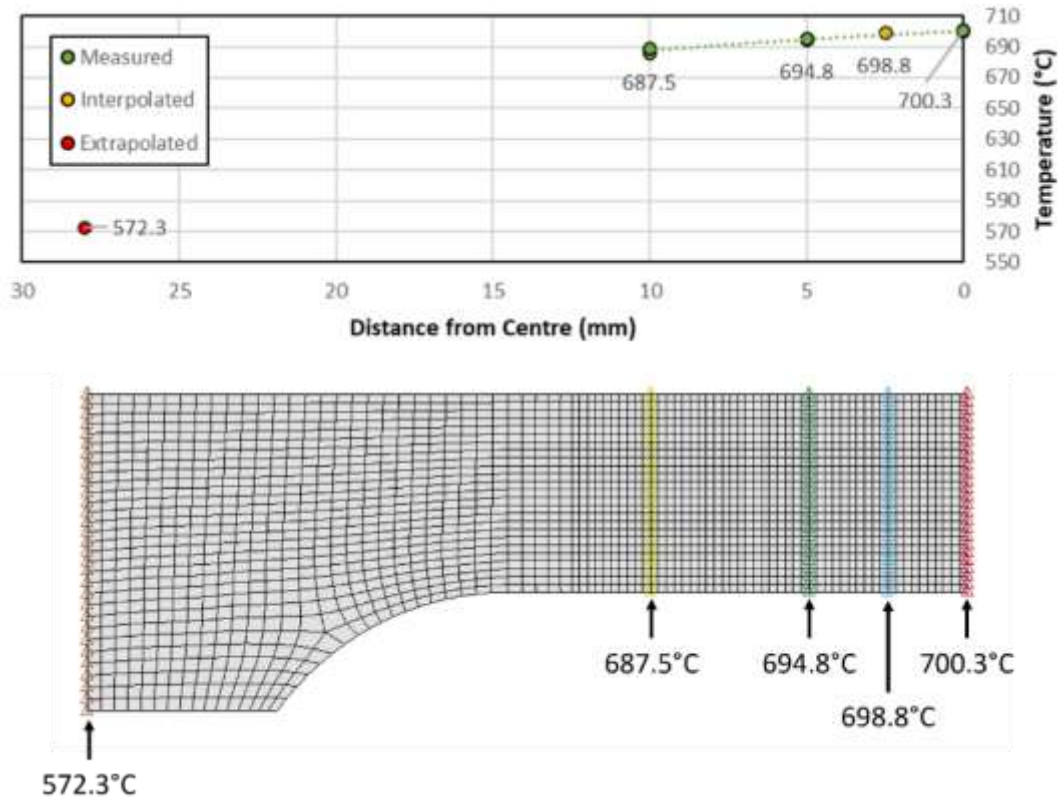


Figure 79: Prescribed temperature boundary conditions to the tensile test finite element model, based on experimentally measured results

This modelling strategy of applying the measured temperature distribution was utilized to significantly reduce the complexity of the model but could be a source of error in the final result. A more realistic way of modeling the thermal condition could be by modeling the resistive heating, convection, radiation, and the conductive heat transfer at the grips contacting the specimen. However, determining the boundary

conditions for such a model would be both experimentally and computationally intensive. Ganapathy *et al.* [44] employed a strategy to derive the temperature distribution along the specimen by modelling the resistive heating with an electro-magnetic solver, however, the complexities of such a model are beyond the scope of the current research. Figure 80 shows the temperature profile applied to the tensile test finite element model prior to deformation.

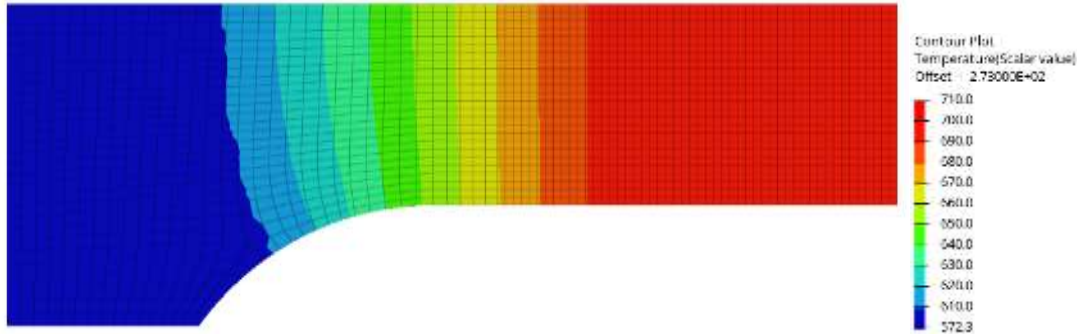


Figure 80: Temperature profile applied to the tensile test finite element model shown in °C, based on experimentally collected surface temperatures for tensile tests conducted at 700°C

### 4.3. Finite Element Model Results

Figure 81 shows a comparison of the maximum principal strain contours from DIC analysis and the FEA for the 800°C and 0.1s<sup>-1</sup> condition, at 7.5 mm of deformation. Visually, the predicted strain contours within the specimen's gauge (reduced) region clearly resemble the DIC results. Towards the grip section, a discrepancy between the predicted results becomes apparent when comparing the purple (0.00 – 0.05 strain range) contour. This underprediction in strain near the grip section of the specimen is likely due to potential differences in the extrapolated prescribed temperature profile versus the actual temperature experienced by the specimen during the experiment. As previously mentioned, the temperature profile beyond 10mm of the centre of the specimen was extrapolated by a best-fit fourth-order polynomial. If the extrapolated temperature profile is significantly lower than the actual temperature near the grip region, then the predicted strength would be much higher than in reality, resulting in less deformation taking place near the grip region. Ultimately, only the accuracy of the results near the center of the specimen is relevant, due to the use of the area reduction method to measure strain and calculate stress.



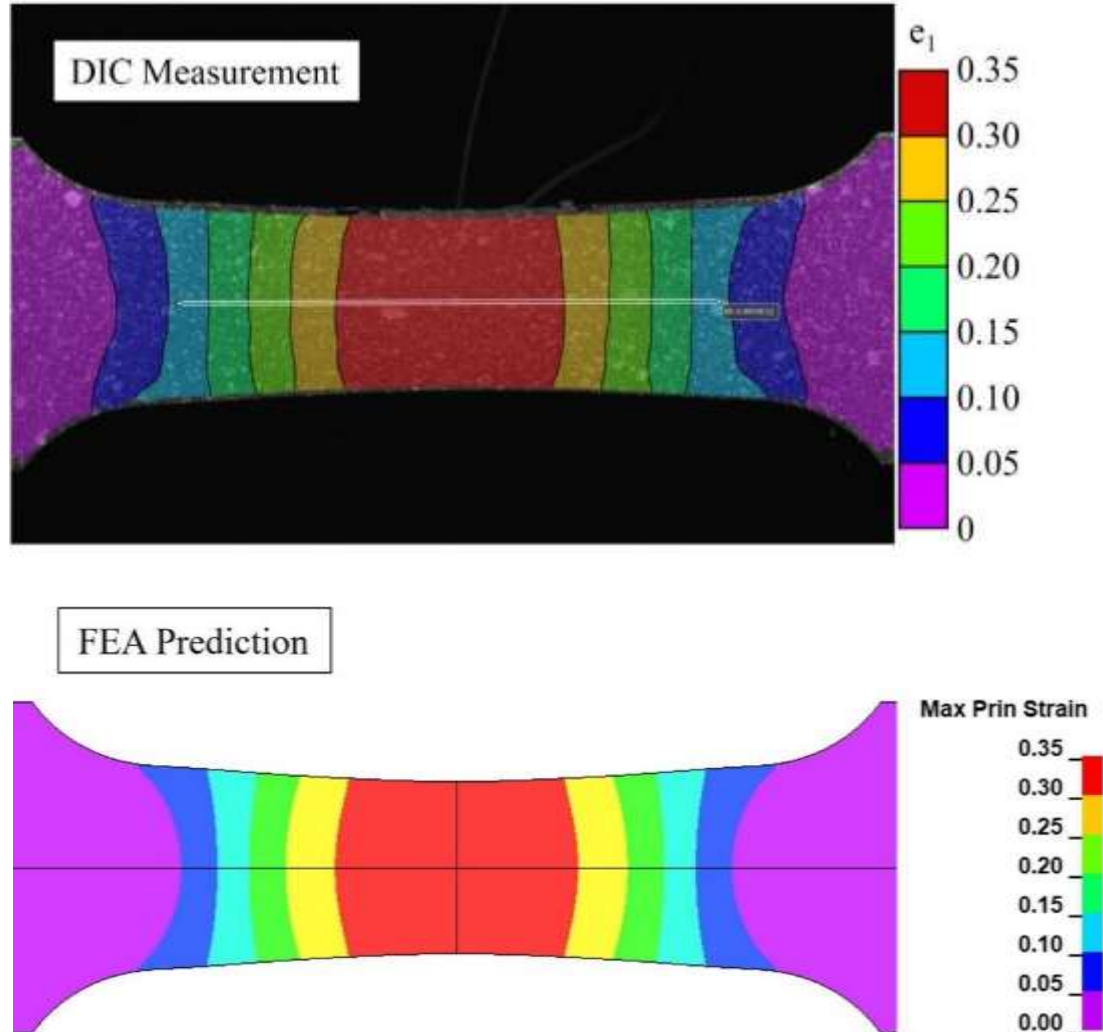


Figure 81: Comparison of principal strain contours generated by digital image correlation (DIC) measurements (top) and FEA predictions (bottom) for the 800°C and 0.1s<sup>-1</sup> test condition

Figure 82 shows a comparison FEA predicted flow curve and the input flow curve for the 800°C and 0.1s<sup>-1</sup> condition. An excellent correlation is achieved until extremely high strains. There is a gradual increase in the error between the predicted and input flow curve with increasing strain, which can be partially explained by the necking of the specimen in the model, leading to a gradual increase in the stress response. Additionally, strain rate steadily increases as deformation localizes in the center, which would lead to an increased stress response compared to plotted input flow curve which is shown at a constant strain rate.

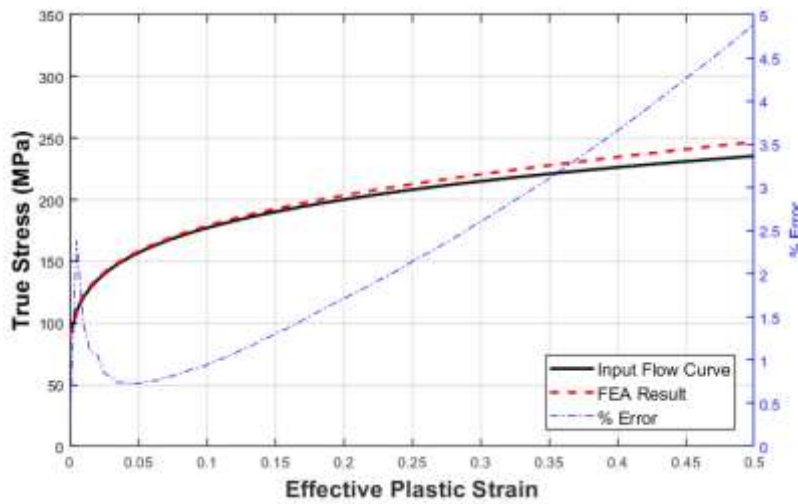


Figure 82: Comparison of FEA prediction versus the input flow curve for the 800°C and 0.1s<sup>-1</sup> test condition

Figure 83 shows a comparison of the flow curve obtained from DIC analysis of the hot tensile test experiment and the FEA prediction, for the 800°C and 0.1s<sup>-1</sup> strain rate condition. When compared to the experimental results, the FEA predictions show a notable difference at low strains. Up to 8% error occurs at the beginning of the flow curve, as the FEA model overpredicts the initial flow stresses at low strains. The error between the predicted and experimental curve then steadily decreases until the end of the available experimental data, at approximately 25% plastic strain. Overall, for the 800°C and 0.1s<sup>-1</sup> test condition, a good correlation between the experimental data and FEA prediction.

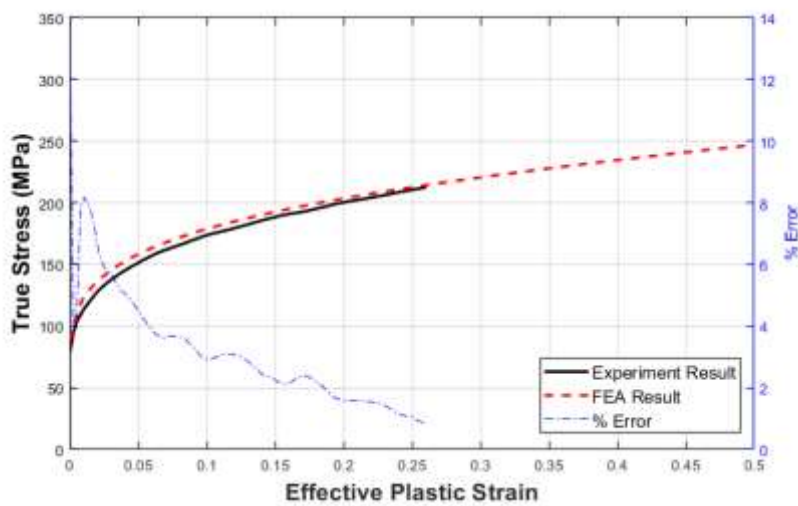


Figure 83: Comparison of FEA prediction and experimentally obtained flow curve for the 800°C and 0.1s<sup>-1</sup> test condition

FEA of the tensile test were also performed at the 700°C and 0.01s<sup>-1</sup> strain rate condition to evaluate the model a lower temperature and strain condition. Figure 84 shows a comparison of the input flow curve and the predicted results for the 700°C and 0.01s<sup>-1</sup> strain rate condition. Similar to Figure 82, there is a high initial error immediately after the onset of yielding. Afterwards, the predicted results are reasonably similar to the input, followed by increased error with increasing strain due to necking of the specimen.

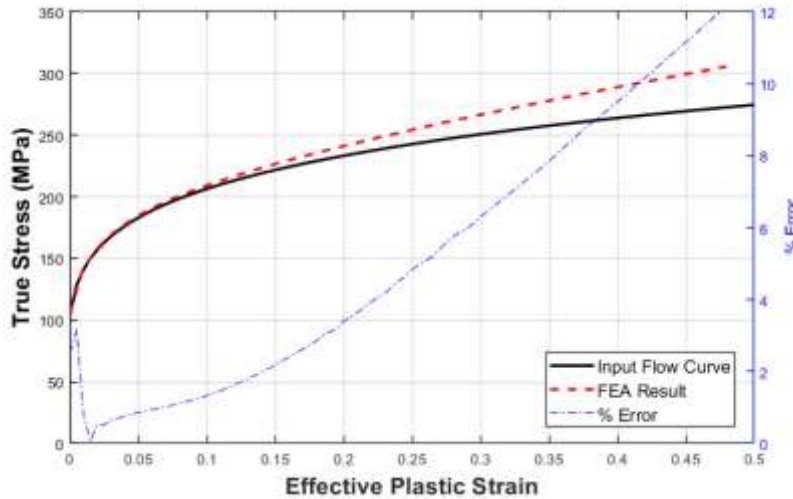


Figure 84: Comparison of FEA prediction versus the input flow curve for the 700°C and 0.01s<sup>-1</sup> test condition

Figure 85 shows a comparison of the FEA predictions to the experimental flow curve at 700°C and 0.01s<sup>-1</sup> strain rate. A high error is observed at the beginning of the curve, due to the overprediction of the initial flow stress. The error of the predicted results gradually decreases until the predicted flow stress diverges again from the experimental results at higher strains. After 0.1 strain, the predicted flow stress experiences greater strain hardening than the experimental results, resulting in a gradually increasing overprediction in flow stress.

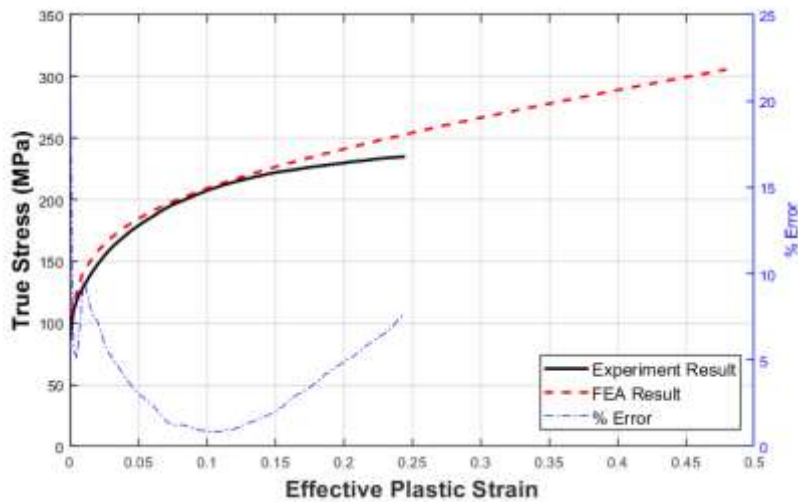


Figure 85: Comparison of FEA prediction and experimentally obtained flow curve for the 700°C and 0.01s<sup>-1</sup> test condition

Overall, a maximum error of 12% is observed when comparing the predicted flow curve (load and displacement result) to the experimental results or the fit flow curves. The prediction error is low for the majority of the predicted flow curve, with greater error observed typically at the initial onset of yield and at high plastic strains. For all the comparisons presented, the most significant source of error is from the poor fitting of the second-order polynomial Norton-Hoff model to the experimental results. It is clear that the difference between the FEA predicted and experimental flow curves mirror the difference between the fit and experimental curves shown in Figure 77. For the 800°C and 0.1s<sup>-1</sup> condition, the fit curve in Figure 77 exhibits slightly greater flow stress than the experimental. Similarly for the 700°C and 0.01s<sup>-1</sup> condition, the fit curve exhibits a greater work hardening rate than the experimental flow curve. In order to improve the accuracy of the FEA predictions, it is necessary to utilize a better constitutive model that can better capture the effects of strain, strain rate, temperature on the flow stress. It can be concluded that the FE model is setup adequately (in terms of geometry simplification, meshing, and applied boundary condition) to predict the mechanical behaviour of PHS 1800, and that the main source of error is due to differences in the fit curve versus the experimental results and not the FE model itself.

## 5. Phase Transformation Modelling

### 5.1. Finite Element Model to Determine Activation Energy

In order to determine the phase transformation activation energies of PHS 1800, a simplified finite element model was created to act as a digital twin of the experiment. A single (four-node shell) element model (Figure 86) was created in LS-DYNA to represent the centre of the specimen during the phase transformation experiments. This single element model was employed to minimize computation time, which was essential for the iterative optimization aspect of this work. The lower left node was fixed to fully constrained the model, while all remaining nodes were constrained to allow for free planar thermal expansion. The experimental temperature histories for the no-deformation cases shown in Figure 66 - Figure 68 were applied to all four nodes of element, such that the element temperature followed the measured temperature history in the experiments. The finite element model for these zero-deformation phase transformation experiments is shown in Figure 86. (The effect of deformation on phase transformation prediction is considered in Section 5.2.)

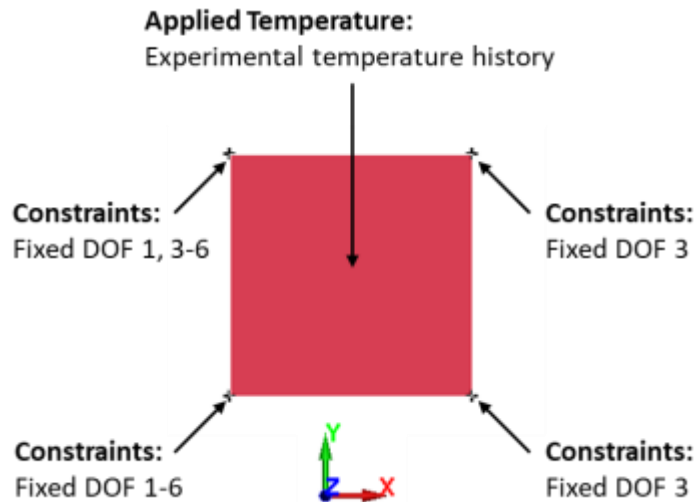


Figure 86: Single element model of the zero-deformation phase transformation experiments

MAT\_244, the material card available in LS-Dyna for press-hardenable steels (based on the Åkerström model) was applied to the element. The flow curves from Section 4.1 were utilized, however the mechanical response was not critical to obtaining accurate results for the zero-deformation tests. Commonly accepted

values of density ( $7830 \text{ kg/m}^3$ ), a constant elastic modulus (207 GPa), and Poisson's ratio (0.3) for steel at room temperature were used for simplicity because density and elastic strains have no direct effect on the phase change model. The default MAT\_244 parameters were used with the exception of the chemical composition, which was updated to the actual chemical composition of PHS 1800 shown in Table 1. Starting with the default MAT\_244 activation energy values, a baseline final phase composition and final microhardness value can be obtained.

The goal of the constant cooling rate experiments was to determine the effect of temperature change (cooling rate) and deformation on the rate of ferrite, pearlite, and bainite formation. The experimental results, in the form of hardness and final phase fraction measurements, were then used to determine the activation energy parameters for the MAT\_244 material model in LS-DYNA by means of optimization of predicted results to match the experimental observations. Optimization was conducted using LS-OPT, a general purpose optimizing tool that directly interfaces with the LS-DYNA solver to compute solutions to the defined constraints and objectives. Generally, for any optimization problem, an objective function must first be defined that either needs to be minimized or maximized. Design variables and constraints must then be identified to specify relevant parameters and determine the scope of the problem. In the current research, the objective function was defined by the difference (or error) between the predicted results and the experimental results. LS-OPT was utilized to minimize the difference between the predicted and measured results, by iteratively varying the activation energies of the material model (and afterwards, the deformation scale factors). The activation energy values that resulted in the lowest error between the predicted and measured results were then determined to be the most optimal values for PHS 1800. Specifically, a metamodel-based optimization algorithm was employed to determine the optimal activation energies. For metamodel-based optimization, a simplified mathematical model (referred to as the metamodel) of the finite element model is generated based on a few initial results of the finite element model. The metamodel approximates the behaviour of the more complex finite element model, and roughly captures the relationship between the design variables and the result. By eliminating the necessity of iteratively computing the more complex and computationally intensive finite element model, the optimization problem

can be solved more rapidly. A successive response surface method optimization algorithm is employed to identify the optimal activation energy values. The optimization process begins by forming an initial model of the problem from randomly determined, and widely distributed sampling points of the parameters of interest. As the optimization scheme iterates, the meta-model better correlates the effect of the input variables to the objective function. After exploring the entire design space (defined by the constraints), the domain of the most optimal solution gradually reduces until a final solution is identified after a convergence is achieved.

For this research, the objective was to minimize the total error, defined as the squared residual between the predicted phase fractions and the measured phase fractions, for all cooling rates. The measured phase fractions were taken from the results presented in Table 9. This follows a similar strategy utilized by George *et al.* [79] for tailored cooling experiments with PHS 1500. The objective function based on phase fractions after quenching is shown in Equation (27).

$$f = \text{total error} = \text{error}_{5^{\circ}\text{C/s}} + \text{error}_{10^{\circ}\text{C/s}} + \text{error}_{50^{\circ}\text{C/s}} \quad (27)$$

The individual error term at each cooling rate is the summation of the difference in predicted and measured phase fractions and is shown in Equation (28).

$$\begin{aligned} \text{error}_i = & (\text{predicted} - \text{experiment})^2_{\text{ferrite}} \\ & + (\text{predicted} - \text{experiment})^2_{\text{pearlite}} \\ & + (\text{predicted} - \text{experiment})^2_{\text{bainite}} \\ & + (\text{predicted} - \text{experiment})^2_{\text{martensite}} \end{aligned} \quad (28)$$

Additionally, a second optimization study is conducted based on the final hardness of the specimen rather than phase fractions. This is proposed as an alternative strategy to eliminate the need for costly and time consuming phase fraction measurements. The objective function remains the same as Equation (27), however the individual error terms at each cooling rate function are modified to reference microhardness instead. The experimental microhardness values used for this optimization study were taken from Figure 69. The error term for predicted and measured Vicker's microhardness is shown in Equation (29).

$$error_i = (\text{predicted HV} - \text{experiment HV})^2 \quad (29)$$

A total of three finite element models were interfaced to LS-OPT to perform the optimization, with each model applying a different temperature versus time profile, to simulate the three different cooling rate scenarios. The design variables were the three activation energies for ferrite, pearlite, and bainite, and variables were constrained to be positive values.

## 5.2. Finite Element Model to Determine Deformation Scale Factors

Building upon the previous section, a 2D single element simulation was also created for the phase transformation experiments involving induced deformation beginning at 800°C. Similar to before, the bottom left-side node was fixed to fully constrain the element, and the experimentally recorded temperature history was applied to all nodes. To apply the deformation, the right-side nodes were prescribed a displacement in the positive x direction up until the desired strain amounts of 10% or 20% true strain, at the experimental strain rate of 0.1s<sup>-1</sup>. This displacement was prescribed starting at 800°C, in line with the experiment. The finite element model for the induced-deformation phase transformation experiments is shown in Figure 87.

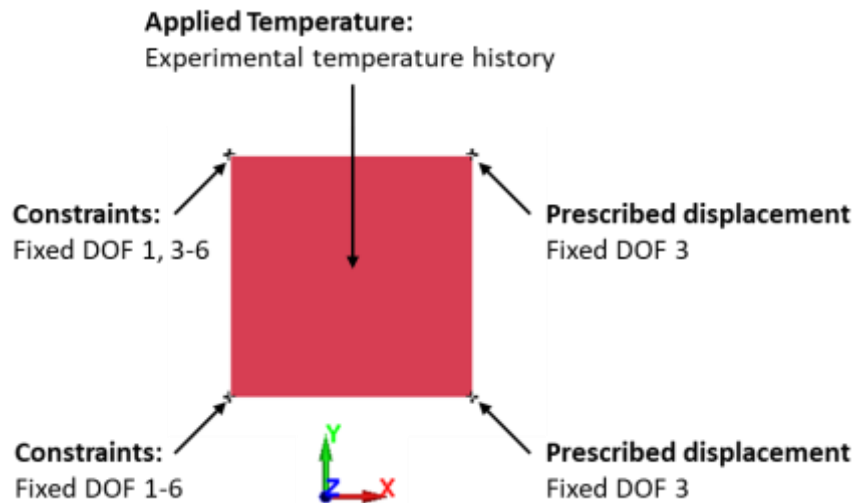


Figure 87: Single element model of the induced-deformation phase transformation experiments

Similar to the zero-deformation simulation, the MAT\_244 material model was used as the material card for this simulation, with updated chemical compositions of PHS 1800 from Table 1. The use of the room



temperature elastic modulus is a source of error, however elastic strains are insignificant compared to the large applied plastic strain. The default MAT\_244 deformation scale factor values are unity, meaning the effects of deformation on phase change are neglected unless otherwise defined. The objective of this study is to define the deformation scale factors for PHS 1800.

Optimization using LS-OPT to determine the deformation scale factors followed a similar strategy to what was outlined in the previous section for activation energy identification. Procedurally, the activation energy was determined first based on the results of the zero-deformation experiments. The new activation energy parameters were then utilized to determine the deformation scale factors based on the results of the induced-deformation experiments. In order to account for the different experimental results from all three deformation conditions, the error equation was expanded to sum the error all three deformation conditions at each cooling rate. This is shown in Equation (30), where a summation symbol is used to shorten the equation, where  $n = 0\%$  strain,  $10\%$  strain, and  $20\%$  strain.

$$\begin{aligned}
 error_i = & \sum_{n=1}^3 [(predicted - experiment)^2_{ferrite} \\
 & + (predicted - experiment)^2_{pearlite} \\
 & + (predicted - experiment)^2_{bainite} \\
 & + (predicted - experiment)^2_{martensite}]_n
 \end{aligned} \tag{30}$$

For the optimization to measured microhardness, an identical modification to the error term at each cooling rate condition is made and shown in Equation (31).

$$\begin{aligned}
 error_i = & (predicted HV - experiment HV)^2_{0\% strain} \\
 & + (predicted HV - experiment HV)^2_{10\% strain} \\
 & + (predicted HV - experiment HV)^2_{20\% strain}
 \end{aligned} \tag{31}$$

A total of nine finite element models were interfaced to LS-OPT to perform the optimization, with each model applying a different temperature versus time profile and a different deformation boundary condition, to simulate the three different deformation conditions at three cooling rate scenarios.

## 5.3. Activation Energy Calibration Results

### 5.3.1. Calibration to Phase Area Fraction Measurements

Table 12 shows the default and optimized activation energy values (in the form required by MAT\_244 in LS-DYNA, represented as the activation energy normalized by the universal gas constant of 8.314 J/mol K), obtained by optimizing the activation energies to the measured phase area fractions. The activation energy values were determined after 305 iterations of sampling values, updating the metamodel, and sampling new values within the design space. A visualization of the sampled values for the activation energy parameter of each phase is shown in Figure 88. From the subplots, it is evident that there are strong local minima for the ferrite and bainite activation energies, whereas the error is less sensitive to the pearlite activation energy.

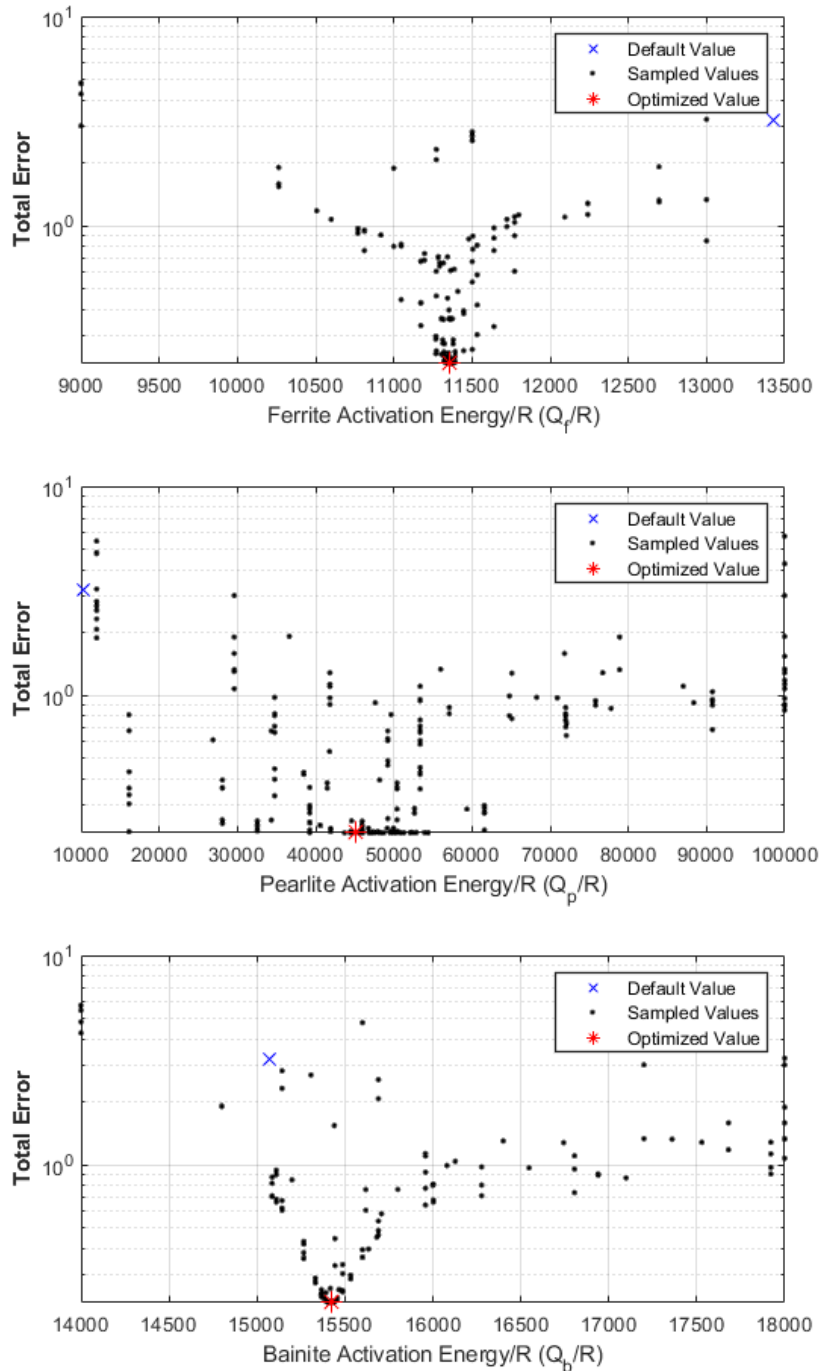


Figure 88: Sampled values of MAT\_244 activation energies during the optimization of said parameters when optimized to experimental phase area fractions

Both the optimized bainite and ferrite activation energies were increased slightly relative to the default values (originally intended for 22MnB5 or PHS 1500 materials), which resulted in a slight decrease in the rate of phase formation. For pearlite, the activation energy was increased significantly, which essentially blocked the formation of pearlite in the simulation. The extremely high pearlite activation energy

corresponds to the lack of pearlite observed in the physical specimens. The overall effect of these optimized activation energy values resulted in greater martensite fractions to compensate for the overall reduction in ferrite and bainite formation, and negligible pearlite formation.

*Table 12: Default and optimized activation energies (normalized by the universal gas constant) for MAT\_244 for the diffusion reactions of ferrite, pearlite, and bainite after calibration to measured phase fractions*

Activation Energy/Universal Gas Constant	Default Value (K) [75]	<b>Optimized Value – Calibrated to Measured Phase Fractions (K)</b>
$Q_{\text{ferrite}}/R$ (QR2)	10,324	<b>11,365.3</b>
$Q_{\text{pearlite}}/R$ (QR3)	13,432	<b>45,063.2</b>
$Q_{\text{bainite}}/R$ (QR4)	15,068	<b>15,421.5</b>

Figure 89 summarizes the measured and predicted phase fractions of PHS 1800 using the default and optimized activation energies (optimized to measured phase fractions). The predictions using the default activation energies (within LS-DYNA) at the lower cooling rates of 5°C/s, and 10°C/s, significantly underpredict the amount of martensite phase compared to the experimental results. This likely occurs due to the low ferrite activation energy value, which consequently results in much greater amount of predicted ferrite when compared to the experimental results. The phase predictions using the optimized activation energies result in a more realistic distribution of martensite and ferrite phases for both lower cooling rate conditions. At 5°C/s, the predicted amount of ferrite and bainite phases are still notably different from the experimental measurements, however the martensite amount is comparable. There is a maximum difference (difference between the experimental value and optimized FEA prediction) of 19% for the ferrite prediction, while only a 7% difference for the martensite prediction. For the 10°C/s condition, the experimental values and optimized predictions of all phases are nearly identical, with a maximum difference of less than 4% between all predicted phases. At 50°C/s, which is well beyond the critical cooling rate, predictions using default or optimized activation energies match the experimental observations of a fully martensitic microstructure.

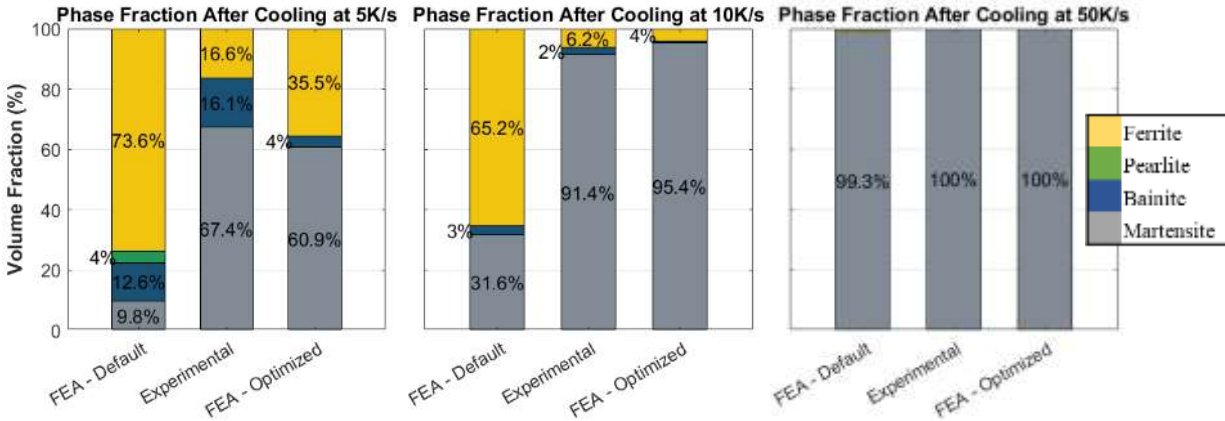


Figure 89: Comparison of measured and FEA predicted phase fractions of PHS 1800 using default and activation energies optimized to measured phase fractions (zero deformation)

Figure 90 shows a comparison of the measured and predicted final microhardness of the specimen after quenching at various cooling rates. Similar to previous result, the FEA predictions are made with the default and optimized activation energies (optimized to measured phase fractions). It is clear that when using the default parameters, the finite element model significantly underpredicts microhardness when compared to the measured results for both 5°C/s and 10°C/s conditions. This lower predicted microhardness is expected due to the predicted phase fractions, in which the soft ferrite phase was overpredicted for both subcritical cooling rate conditions. For the 50°C/s condition, a fully martensitic microstructure is predicted and leads to a high microhardness prediction that is nearly identical to the experimental value. The optimized results show that microhardness predictions align more closely with the experimental results for the 5°C/s and 10°C/s conditions. At 5°C/s, the optimized prediction is approximately 5% lower than the measured microhardness, however, is still comparable given the relatively high standard deviation of the measured results. For the 10°C/s and 50°C/s conditions, the optimized activation energies are capable of predicting microhardness that nearly matches the experimental measurements, resulting in 0% and 1% error respectively. Cumulatively, the microhardness predictions using the optimized activation energies via calibration to phase area fraction measurements result in an average of 2% error for all three cooling rate conditions with no induced deformation.

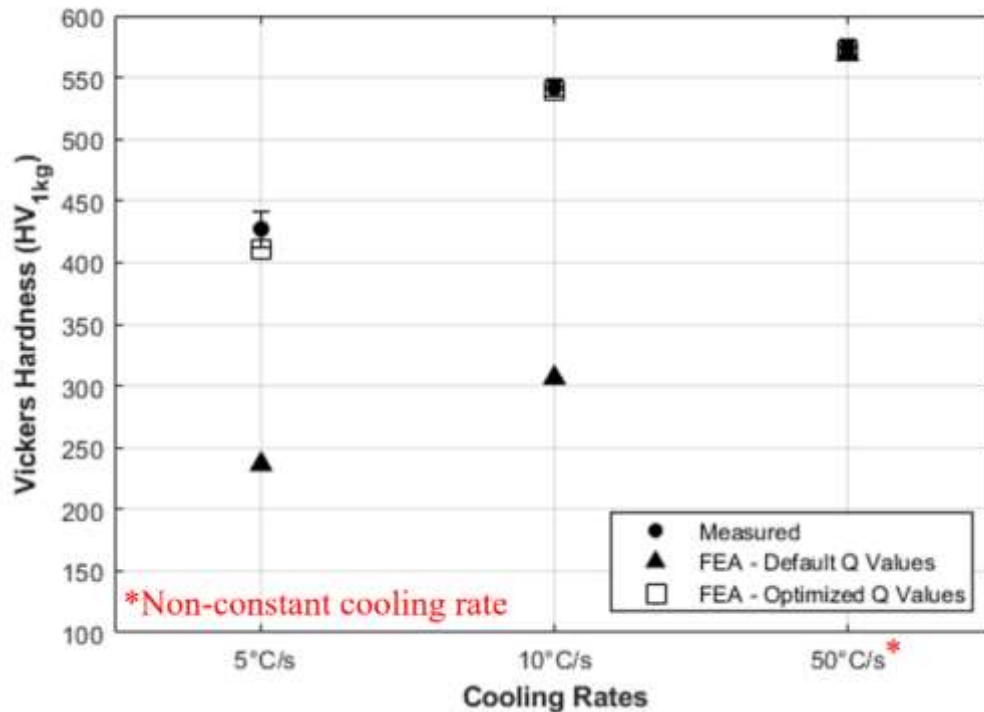


Figure 90: Comparison of measured and FEA predicted microhardness values of PHS 1800 using default and activation energies optimized to measured phase fractions

It should be noted that the 50°C/s cooling rate condition corresponds to the target cooling rate; however, the measured cooling rate of 50°C/s was not achieved after the specimen was cooled below 400°C. As discussed in Section 3.7.1 for Figure 68, the maximum sustained cooling rate after the onset of martensite transformation was only approximately 15°C/s. However, this discrepancy between the target and actual cooling rate is captured by the finite element model because the experimental temperature history was directly prescribed to the finite element model.

Table 13 summarizes the optimized activation energy deformation scale factors at the two strain levels, obtained by the optimizing the deformation scale factor parameter to the phase fraction measurements at each deformation level. For the MAT\_244 material model, ferrite and pearlite have separate activation energies but share the same deformation scale factor [75]. However, concerns regarding pearlite formation can be disregarded, due to extremely high pearlite activation energy calculated in the previous optimization step. For ferrite, the deformation scale factor decreases slightly with increasing strain. This decreased scale factor is applied to the activation energy, and effectively promotes a greater rate of ferrite formation. For

bainite, the deformation scale factor decreases initially at 10% strain, but increases significantly beyond unity at 20% strain. This result indicates the need for decreased bainite formation at 20% strain in order for the finite element model predictions to better match the experimental results.

*Table 13: Optimized deformation scale factors for PHS 1800 for MAT\_244, determined by optimizing to phase fraction measurements*

<b>Parameters calibrated to phase fraction measurements</b>			
<b>True Plastic Strain</b>	0%	10%	20%
<b>Ferrite and Pearlite Deformation Scale Factor (<math>K_{f+p}</math>)</b>	1	0.9852	0.9762
<b>Bainite Deformation Scale Factor (<math>K_b</math>)</b>	1	0.9587	1.1836

A comparison of the measured and predicted final phase distribution for the specimens subjected to constant cooling and induced deformation is shown in Figure 91. The zero-deformation condition results were already presented in Figure 89 and are excluded from this figure. For the 5°C/s condition, the FEA underpredicts the martensite in comparison to the experimental observation for both strain conditions. Conversely for the 10°C/s condition, the amount of martensite phases is overpredicted compared to the measurements for both strain conditions. For both the 5°C/s and 10°C/s condition, the amount of bainite is consistently underpredicted, with no bainite phase formation predicted at 20% strain. The lack of bainite formation (despite ferrite and martensite formation) at 20% strain are unrealistic, suggesting the derived material parameters or the Akerstrom model is not capturing the intrinsic phase change behaviour of PHS 1800. For the 50°C/s cooling rate condition, the effect of the deformation scale factors have negligible effect on the final phases, resulting in a fully (100%) martensitic microstructure which matches the experimental observations. For the 5°C/s condition, the ferrite phase fractions are overpredicted by 15% and 20% for the 10% strain and 20% strain conditions, respectively. For the 10°C/s condition, the ferrite phases are underpredicted by 11% for both strain conditions when compared to the experimental results.

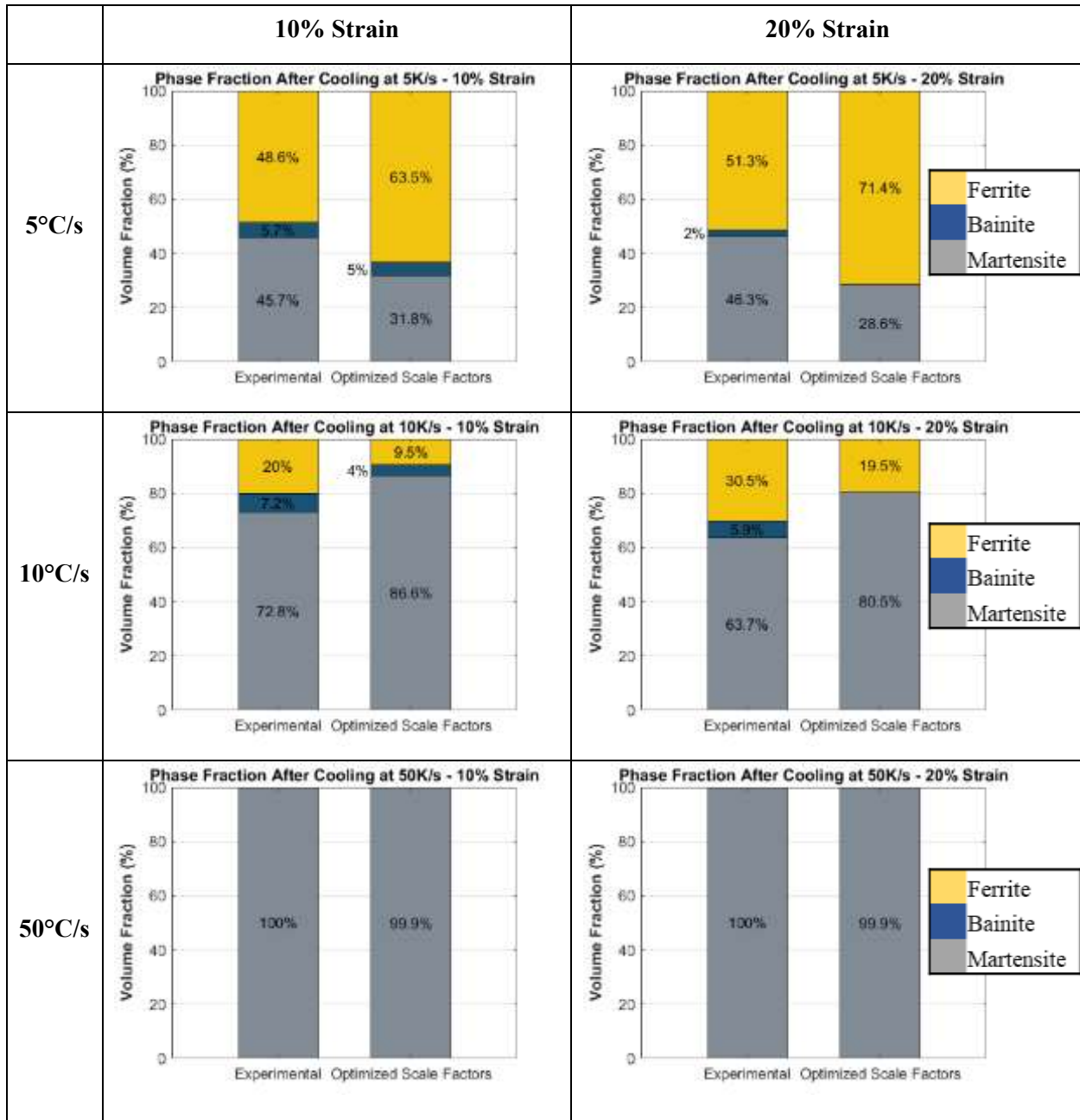


Figure 91: Comparison of measured and FEA predicted phase fractions of PHS 1800 for the quenched and simultaneously deformed specimens, FEA parameters calibrated to phase fractions

In addition to the phase fractions, the optimized microhardness predictions are also compared to the experimental values. Figure 92 shows a comparison of the measured and predicted final Vickers microhardness values for the simultaneously quenched and deformed specimens. As already noted in Figure 90, for the no induced strain condition, the predicted hardness is quite similar to the experimental observations, with an exception at the 5°C/s cooling rate condition. At the 10% strain and all cooling rate



conditions, the predicted results begin to deviate from the measurements, however the predicted microhardness values are still within 1 standard deviation of the measurements (shown by the error bars). At 20% strain, the predicted results show increased error relative to the measured microhardness values for all cooling rate conditions. At 10°C/s, the predicted hardness is consistently greater than the measured values for both strain conditions. This higher hardness is in line expectations set by with the phase fraction results, where the amount of martensite was overpredicted. Similarly for the 5°C/s condition, the predicted hardness is consistently 10-30 HV lower than the measured values at all strain conditions, due to the greater amount of predicted ferrite phases. For the 50°C/s cooling rate condition, the predicted microhardness is constant for all strain rate conditions and does not vary with increasing strain, contrary to the experimental results. The disparity in the hardness predictions at the 50°C/s cooling rate condition shows the Akerstrom model is incapable of accounting for the change in final hardness of a fully martensitic microstructure when PHS 1800 is strained in the austenite state. The maximum difference is observed at 10°C/s and 20% strain, where the predicted hardness is 14% greater than the measured value. For the 5°C/s condition, the FEA hardness prediction is consistently lower than the measurements for all strain conditions, with maximum of 7% error.

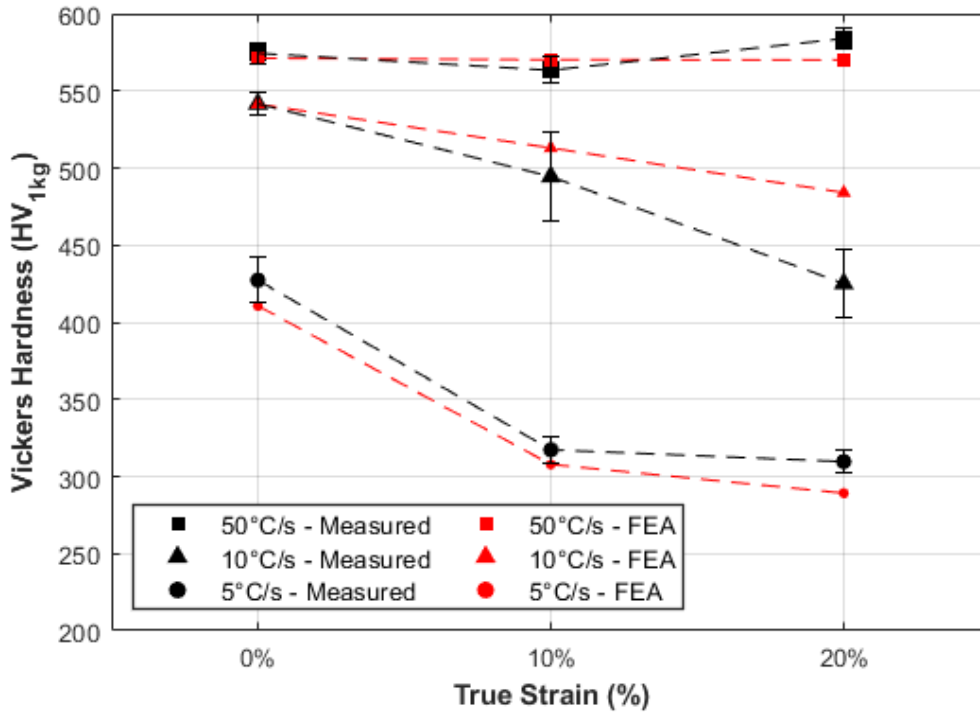


Figure 92: Comparison of measured and FEA predicted microhardness values of PHS 1800 for the quenched and simultaneously deformed specimens, FEA parameters calibrated to phase fractions

In general, optimizing the activation energies and deformation scale factor parameters to the experimental phase area fractions provided acceptable results that match the overall trend of the experimental observations. When comparing the phase fraction predictions to the experimental results, a clear but inconsistent discrepancy can be observed at all sub-critical cooling rates. Notably, the amount of final ferrite phases is overpredicted for all strain conditions for the specimen cooled at 5°C/s. In contrast, the ferrite phase fraction is underpredicted at all strain conditions when the specimen is cooled at 10°C/s. This disparity in the phase fraction predictions consequently leads to a difference in the microhardness predictions for both sub-critical cooling rates with induced strains. However, at the zero-deformation condition, all hardness predictions for the 5°C/s, 10°C/s, and 50°C/s cooling rate conditions are well correlated to the measured results.

### 5.3.2. Calibration to Microhardness Measurements

As an alternative to the prior optimization approach of correlating to phase area fraction, another set of activation energies were generated by optimizing the activation energy and deformation scale factor

parameters to the measured microhardness values. The purpose of this alternative approach is to investigate if calibrating material parameters to hardness results only is capable of achieving accurate phase change predictions (final phase fractions, and hardness), without the need for tedious phase area fraction measurements. As with the previous results, the LS-DYNA MAT\_244 press-hardenable steel material card was used to simulate the phase transformation of the specimen.

Table 14 shows the optimized activation energy values (in the form required by MAT\_244 in LS-DYNA, represented as the activation energy normalized by the universal gas constant of 8.314 J/mol K), when optimized to the final microhardness using Equations (27) and (29). In comparison to the default values (intended for 22MnB5 or PHS 1500 materials), the ferrite activation energy increases slightly, the pearlite activation energy increases significantly, and the bainite activation remains nearly unchanged.

*Table 14: Default and optimized activation energies of PHS 1800 (divided by the universal gas constant) for MAT\_244 calibration to measured Vickers microhardness*

Activation Energy/Universal Gas Constant	Default Value (K) [75]	<b>Optimized Value – Calibrated to Measured Hardness (K)</b>
$Q_{\text{ferrite}}/R$ (QR2)	10,324	<b>11,560.3</b>
$Q_{\text{pearlite}}/R$ (QR3)	13,432	<b>98,230.9</b>
$Q_{\text{bainite}}/R$ (QR4)	15,068	<b>15,072.4</b>

Figure 93 shows the comparison between measured and FEA predicted phase fractions at each cooling rate condition. Because the optimization of the activation energies was based on final microhardness only, the phase predictions were expected to be somewhat arbitrary. However, for all cooling rate conditions, the optimized results are actually quite similar to the measured results. In fact, the predicted phase fractions when optimized to microhardness were actually closer to the experimental values than the predictions optimized to phase fractions presented in Figure 89. For both the 5°C/s and 10°C/s condition, a maximum difference (between the optimized phase prediction and experimental value) of less than 8% is observed for

all phases. This high accuracy was somewhat surprising, and is due to the balancing of the various phases to match the final microhardness value.

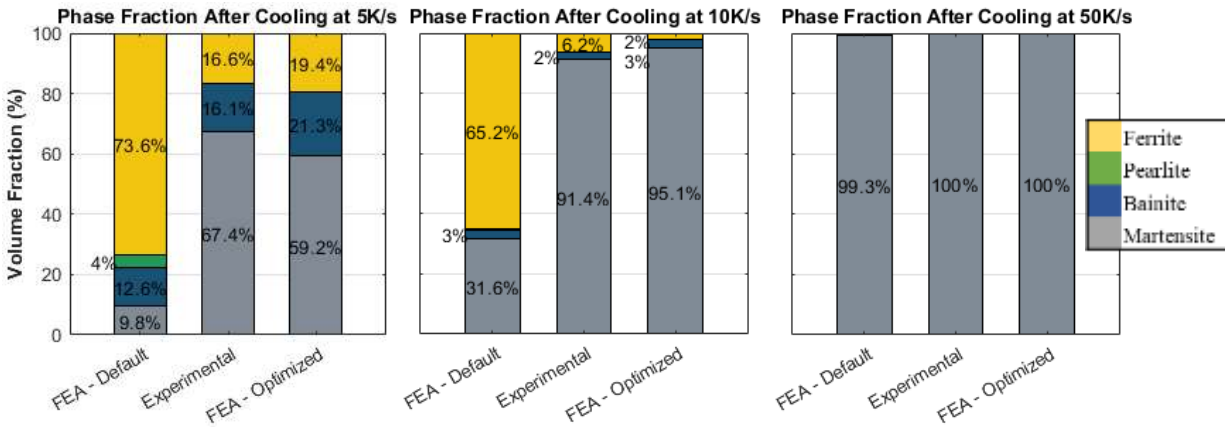


Figure 93: Comparison of measured and FEA predicted phase fractions of PHS 1800 using default and activation energies optimized to measured Vickers microhardness

Figure 94 shows the measured and predicted Vickers microhardness of PHS 1800 after quenching at various cooling rates. The mean measured Vickers hardness results are shown by the circular dots, with error bars showing +/- 1 standard deviation of the measured values. The default predicted (FEA) hardness results were obtained using default activation energy values and are shown by the triangle symbols. The optimized FEA results were obtained with the activation energy values optimized to the experimental microhardness values and are shown by the square symbols. The microhardness predicted using the optimized activation energy values are in very good agreement with the experimental results at all tested cooling rates. There is less than 1% error present at all three cooling rates. This outcome is expected, as the purpose of this optimization strategy was to match the experimental hardness values.

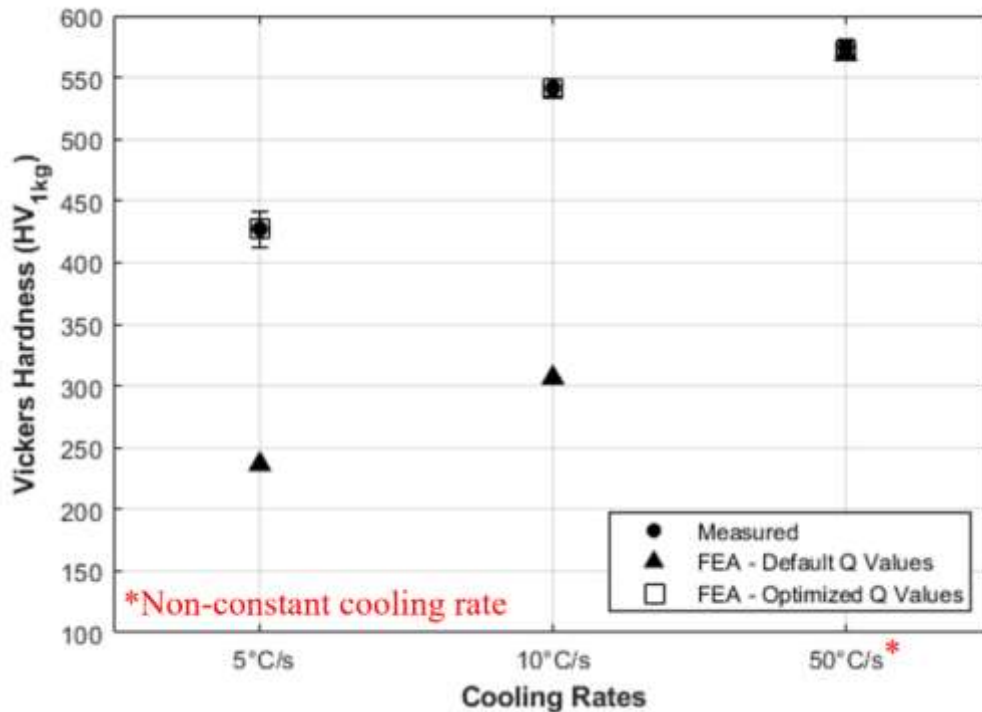


Figure 94: Measured and predicted Vickers microhardness values of PHS 1800 after quenching at various cooling rates, using activation energies optimized to microhardness

Table 15 summarizes the deformation scale factors at increased strains, obtained by optimizing to experimental microhardness values at each strain condition. The pearlite deformation effect was not considered because the extremely high optimized pearlite activation energy prohibits pearlite formation in the simulation. For ferrite, the calculated deformation scale factor remains constant, indicating no change in the rate of ferrite formation with increased strain. For bainite, the deformation scale factor decreases approximately 4% at both strain levels, which results in increased bainite formation with increasing strains. These deformation scale factor values would result in an increase in bainite phases and, as a result, a likely decrease in ferrite phases with increasing strain.

Table 15: PHS 1800 deformation scale factors obtained from optimization to hardness measurements

<b>Parameters calibrated to hardness measurements</b>			
<b>True Plastic Strain</b>	0%	10%	20%
<b>Ferrite and Pearlite Deformation Scale Factor (<math>K_{f+p}</math>)</b>	1	1	1
<b>Bainite Deformation Scale Factor (<math>K_b</math>)</b>	1	0.9685	0.9562

A comparison of the measured and predicted final phase fractions at various cooling rates and induced deformation conditions is shown in Figure 95. The zero-deformation condition results were presented in Figure 93 and are excluded from this figure. At both the 5°C/s and 10°C/s cooling rate conditions, the predicted bainite phases are significantly overrepresented when compared to the experimental measurements. At 5°C/s, the increased formation of bainite almost completely eliminates martensite from the final predicted microstructure. At 10°C/s, the increased bainite formation results in significantly reduced ferrite quantity. The results at 5°C/s and 10°C/s showcase the downside of optimizing the phase change parameters to hardness, shown by the arbitrary nature of the phase fraction predictions in order to achieve more accurate final hardness values. For the 5°C/s condition, bainite phases are significantly overpredicted, leading to a maximum difference of 56% compared to the experimental results at both strain conditions. Similarly for the 10°C/s condition, a 41% difference in the final bainite phase fraction exists between the prediction versus the experimental results. Again at 50°C/s, the substantially greater cooling rate outweighs any effect of the derived deformation scale factors, and results in a fully martensitic microstructure with no difference between the prediction compared to the measurement.

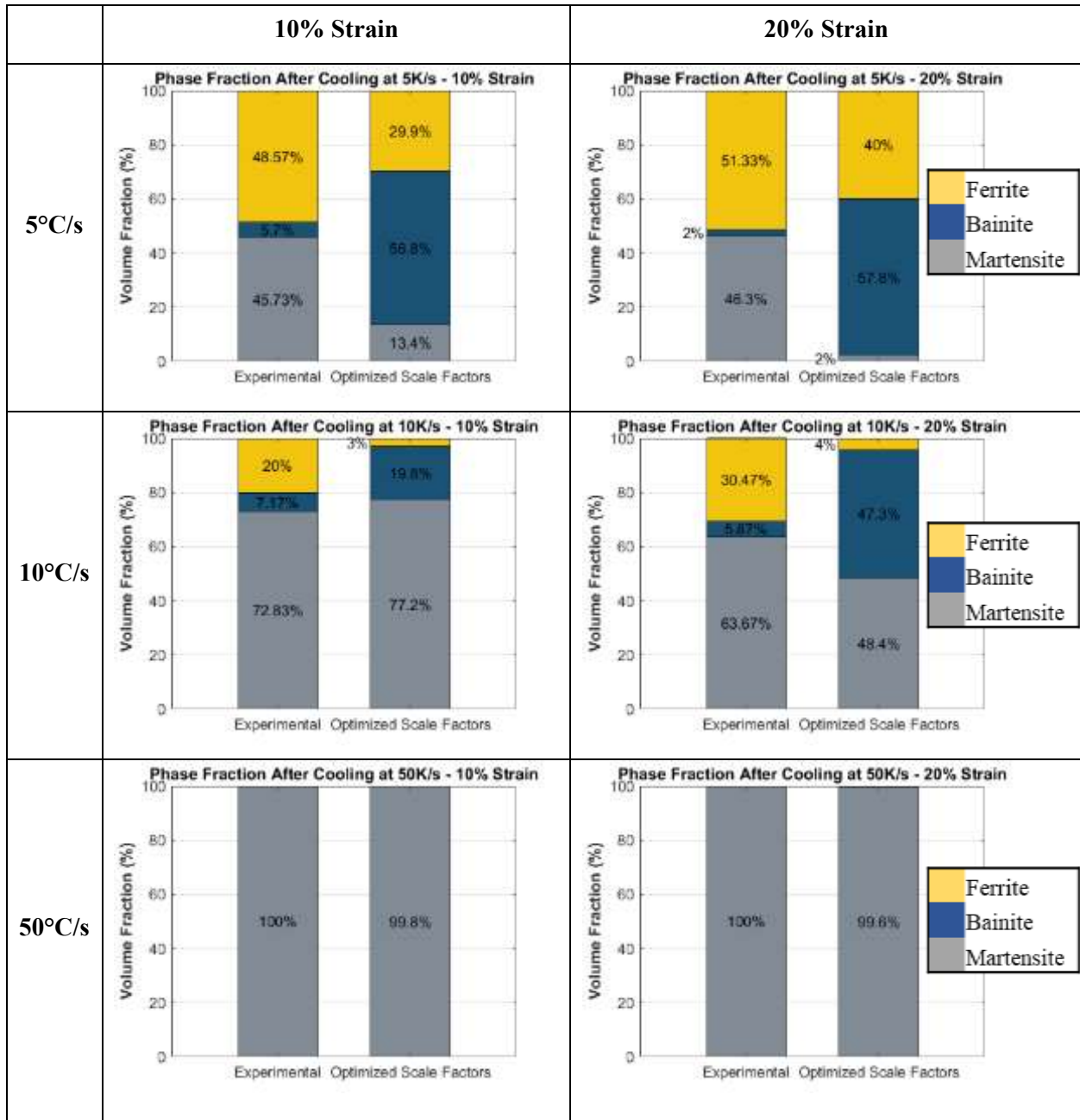


Figure 95: Comparison of measured and predicted phase fractions of PHS 1800 for quenched and simultaneous deformation experiments, with FEA parameters calibrated to microhardness

Figure 96 shows the measured and predicted Vickers hardness of PHS 1800 after quenching, with increasing amounts of deformation applied at 800°C. Comparing the FEA prediction to the experimental results, it can be seen that the general trend of change (or lack thereof) in hardness with increasing deformation is captured for all cooling rates. For the 50°C/s results, the predicted microhardness values are nearly identical to the measured values, however no change in hardness is predicted when specimens are

deformed up to 20% strain, contrary to the experimental results. For the 10°C/s cooling rate condition, the experimentally observed decrease in hardness with increasing strain (deformation) is predicted by the calibrated model. Again, the actual predicted hardness values are extremely similar to the measured values and are within 1 standard deviation of the measurements. For the 5°C/s cooling rate condition, the predicted results differ from the experimental observations at greater applied strains. At 5°C/s, the measured hardness values plateau at around 300-320 HV, however the predicted hardness continues to decrease further with increasing strain. This continued hardness decrease is most likely due to the deformation scale factor promoting greater bainite formation, resulting in less martensite than in reality, therefore decreasing the overall hardness of the final predicted microstructure. The maximum difference exists at the 5°C/s condition at 20% strain, where the predicted microhardness value is 14% lower than the measurement value. The predictions for all other conditions result in less than 3% error when compared to the measured hardness values.

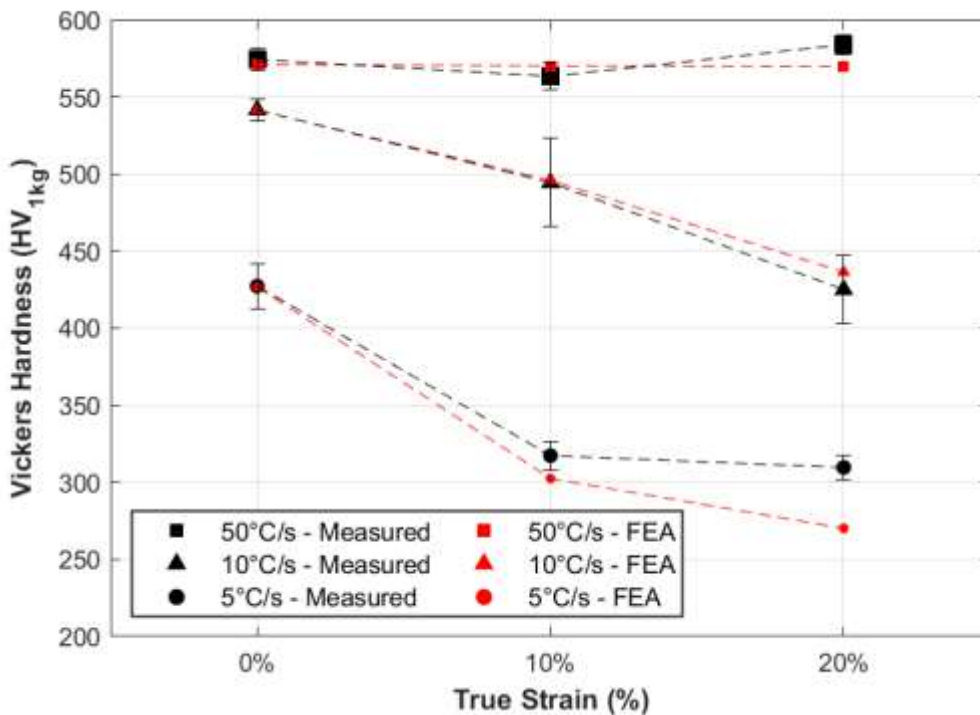


Figure 96: Measured and predicted Vickers hardness of PHS 1800 after quenching at various cooling rates combined with non-isothermal deformation starting at 800°C



## 5.4. Summary of Activation Energy Calibration results

Two viable approaches to calibrating the activation energy parameters have been presented and explored. When calibrating the material parameters to measured phase fractions, a consistent discrepancy is observed between the predicted and measured results at all sub-critical cooling rates. Although, the effects of decreasing cooling rate and increasing applied strains are generally captured by an increase in predicted ferrite phases, the discrepancy in the phase fraction predictions leads to errors in the final microhardness predictions. When calibrating the activation energies to final microhardness, a more accurate microhardness prediction is achieved. However, as seen in Figure 95, unrealistic phase fractions were predicted in order to arrive at the more accurate microhardness values. In general, both sets of calibrated results may provide reasonable predictions and insights to sub-critical cooling simulations, however it should be noted that inaccuracies in the hardness predictions will occur when using material parameters calibrated to phase fractions, and vice versa. In general, it seems that the present PHS material model (MAT\_244) in LS-DYNA would benefit from further development to provide more consistent and accurate predictions for simulations involving sub-critical cooling of PHS 1800. For scenarios in which the cooling rate significantly exceeds the critical cooling rate, both approaches to determining the material parameter would result in accurate predictions.

## 6. Discussion

For elevated temperature tensile testing, an experimental technique was successfully developed to enable DIC image capture and analysis of the surface deformations of Al-Si coated PHS 1500 and PHS 1800. The surface alloying process allows for DIC by preventing the coating from melting and destroying the speckle pattern when heated, and by darkening the coating to act as a naturally ductile and temperature resistant basecoat for white speckles. The main driver behind the time at temperature (7 minutes and 10 minutes at 700°C for PHS 1500 and PHS 1800 respectively) was to sufficiently darken the coating. If a paint was applied to create the basecoat for the speckle pattern, it is possible that a lower heat treatment time is required to develop the coating. Less time at temperature may be desirable to reduce any unwanted annealing effects on the material prior to testing, however the results presented show that the surface alloying treatment has negligible effects on the mechanical response of the material prior to necking. The surface alloying process can henceforth be applied to Al-Si coated specimens for other high temperature applications for which DIC analysis is not possible otherwise. Other researchers (such as He [96]) have adopted this approach in formability testing of PHS materials and future use in large-scale component testing is envisioned. The primary benefit of using DIC analysis for the current work is that it enables full field strain measurements, which is essential for the area reduction method (ARM) to process test data. By using ARM, only results at the centre of the specimen, where temperature is precisely controlled, are used to determine the material flow curve. The ARM overcomes the challenges of measuring strain of resistively heated specimens, where temperature variation along the length of the specimens leads to non-uniform deformation in the gauge area of the specimen. To validate the measurement (DIC and ARM) techniques used in the present study, the PHS 1500 flow curves obtained in this research was compared to results from Merklein and Lechler [42], Abspoel *et al.* [43], and Li *et al.* [45] and were found to be in good agreement at most test conditions.

At elevated temperatures, after austenitization, PHS 1800 flow curves demonstrated approximately 20% greater flow stresses than PHS 1500 for all test conditions. The increased strength be an important

consideration for manufacturers when switching to PHS 1800, because greater press tonnages may be required to form components intended to be made from PHS 1500. PHS 1800 was also observed to have lower necking strains, which indicates decreased formability under uniaxial tension loading. Current hot-stamped (PHS 1500) designs that experience high uniaxial tension strains during forming may need to be re-designed to reduce the likelihood of necking or tearing when switching to PHS 1800. The strain rate test conditions selected in this work were intended to capture the strain rates experienced during an industrial high speed hot stamping operation. If much higher (or lower) deformation speeds are expected, then additional flow curves at the corresponding strain rates should be obtained to capture more relevant material behaviour. The Gleeble and DIC system utilized in this work was suitable for strain rates as high as  $1 \text{ s}^{-1}$ , however higher strain rate testing was not easily achieved due to the long acceleration time of the crosshead, and image acquisition rate of the current cameras. Higher acquisition rates could be achieved by using higher rate cameras, however the tight spacing of the Gleeble made it difficult to implement larger cameras for DIC image capture. Lower strain rate results could have also been studied; however, lower strain rates are of less relevance in industrial hot stamping operations due to the need to rapidly form the part prior to martensite formation.

For PHS 1800, a modified Norton-Hoff equation was fit to the experimental flow curves using a second-order polynomial equation to describe the variation in the strain hardening coefficient and strain rate coefficient with respect to temperature, building upon the work by Merklein and Lechler [42] who introduced this equation for PHS materials. An excellent fit was achieved in the intermediate temperature range of 600-800°C over which the majority of forming (deformation) is intended to take place in a typical hot stamping process, making the fit results quite relevant for hot stamping simulations. A lower quality fit was observed at 900°C, indicating that the Norton-Hoff model could still be improved for PHS materials to better capture the change in strain hardening behaviour with respect to temperature. Although the Norton-Hoff equation was accurately fit to the measured constitutive data at 500°C, it is possible that phase changes could have occurred prior to testing due to the time required to quench the specimen to temperature. An

alternative approach would be to utilize a physically-based constitutive model that accounts for the effects of phase fractions or phase change on the flow stress response of the material. However, such a model would likely introduce complexities that would require significantly more testing and measurements.

To evaluate the fit flow curves for finite element analysis, a finite element model of the hot tensile tests conducted in this present work was created. In general, a good agreement between the FEA predictions and experimental results were achieved, seen by less than 12% error in the flow stress response at any given strain. The benefit of simulating the hot tensile test rather than a more complex hot-stamping process is that there is no need to define contact or heat transfer parameters, which would make it difficult to decouple sources of error in the predictions. The tensile test FE model offered a good “sanity check” for the fit flow curves and basic model parameters such as the prescribed mechanical and temperature boundary conditions. Future work should involve implementing the constitutive results from the current work to a finite element model of an industrial hot stamping operation to better understand if the constitutive results are capable of providing accurate forming predictions.

The phase change experiments carried out in this work quantified the final phase fractions and microhardness of PHS 1800 for three cooling rate and deformation conditions. The results show that if the cooling rate is high enough, then deformation prior to phase change has no effect on the final result. When designing a hot stamping process to produce a fully martensitic structure, it is therefore recommended to maximize the cooling rate. The experiments also confirmed that it is possible to achieve a complex phase final component with varying fractions of ferrite, bainite, and martensite at lower cooling rates. Deformation was observed to affect phase change and hardness results, and the effects of deformation effects and cooling rate were coupled. The aforementioned results indicate that PHS 1800 may be receptive to tailored quenching applications, however, the cooling rate and amount of deformation must be carefully considered to achieve the desired properties.

The experimental phase change results were successfully used to calibrate the phase change parameters of the Åkerström and Oldenburg [66] model in LS-DYNA. In general, the calibrated model was capable of predicting the overall trends in measured phase fractions and hardness for the range of cooling rates and

deformation considered. Relatively high errors were observed for phase fraction predictions at low cooling rates; however, microhardness predictions were typically accurate to within 3% error. The calibrated activation energies presented in the current work provide a good baseline for PHS 1800 modelling and predictions but should be further validated for high deformation and low cooling rate scenarios. The prediction errors could be due to poor calibration of the material parameters, or due to measurement error of phase fractions. Alternatively, the poor predictions may suggest that the Åkerström model is not well suited for deformation induced effects, which is only represented by a scale factor (that is a function of deformation strain) that affects activation energy. Perhaps induced deformation prior to phase change also affects other model parameters (Equation (13)) such as the grain size factor, or the deformation scale factor needs to be a function of temperature and/or cooling rate. Furthermore, it may be possible to improve the accuracy of the calibrated model by simply collecting and correlating to more data points, specifically at more intermediate cooling rates and deformation conditions.

The PHS 1800 studied in the present work is seen as a stronger alternative to conventional PHS 1500. The higher strength after quenching could contribute to overall vehicle weight savings by allowing for structural components to be made of thinner (lighter) blanks. The current work demonstrated several testing methodologies to characterize the constitutive and phase change behaviour of Al-Si coated PHS 1800 materials during hot stamping, which are suitable for other applications, such as formability testing or tailoring processes. The finite element model parameters derived from the experimental results, and the strategies utilized to obtain said parameters, generally enable accurate predictions of both the mechanical and phase change behaviours of the material. Future work should include testing for an expanded range of test conditions (higher strain rates, intermediate cooling rates, greater deformation amounts prior to quenching, etc.) to better understand the behaviour of PHS 1800 for more specific applications.

## 7. Conclusion

The current research has served to identify the constitutive flow stress behaviour of an aluminum-silicon (Al-Si) coated 1,800 MPa press hardenable steel (PHS 1800) at elevated temperature (500 – 900°C) and strain rate (0.01 – 1s<sup>-1</sup>) conditions relevant to the hot stamping process. Experiments were also performed on a commonly available and extensively studied grade of 22MnB5 (or PHS 1500) to validate the test method and enable comparisons between the two grades of PHS. Additionally, the current research also conducted constant cooling rate experiments with induced deformation to evaluate the effects of such conditions on the final phase fractions and hardness values of PHS 1800. From this research, the following conclusions are drawn.

### 7.1. Constitutive Testing and Modelling

- The surface alloying thermal heat treatment process successfully prevented the Al-Si coating from melting when heated to 930°C (the austenitization temperature). This surface treatment also changed the coating color and increased coating ductility to enable digital image correlation (DIC) analysis of specimens, facilitating strain measurements without physical gauges. Surface alloying was determined to not affect the constitutive behaviour of PHS 1500 and PHS 1800 prior to necking, however treated specimens were observed to be more ductile after the onset of necking and up to fracture.
- DIC measurements and the area reduction method (ARM) were determined to be a valid technique for measuring the constitutive behaviour of PHS at elevated temperatures. The challenge posed by non-uniform deformation (due to temperature non-uniformity) of a resistively heated specimen was addressed by only analyzing the centre of the specimen, where the temperature was precisely controlled.
- After quenching to a fully martensitic microstructure, PHS 1800 exhibits a yield strength of approximately 1,400 MPa, and an ultimate tensile strength of approximately 2,000 MPa. Compared

to PHS 1500, PHS 1800 exhibits approximately 20% higher yield strength, 25% higher ultimate tensile strength, but 8% lower total elongation.

- At elevated temperatures, following austenitization, PHS 1800 exhibited approximately 20% higher flow stresses than PHS 1500 at the same test conditions. PHS 1800 also exhibited lower plastic strains prior to necking compared to PHS 1500 for most conditions tested. The flow curves of both studied materials displayed similar strain and temperature sensitivities, in which decreased temperatures and increased strain rates resulted in an increased flow stress response.
- The modified Norton-Hoff constitutive equation, with second-order polynomial strain rate and strain hardening equations, was accurately fit to all PHS 1800 flow curves (R-squared value of 0.971) and enabled a finite element model to predict load versus displacement with less than 12% error.

## **7.2. Phase Transformation Experiments and Modelling**

- Quenching PHS 1800 at 50°C/s resulted in a fully martensitic microstructure with a hardness of 580HV. Lower cooling rates produced complex phase (ferrite, bainite and martensite) microstructures with hardness levels less than 450HV.
- Induced deformation prior to quenching was observed to significantly increase ferrite formation and reduce microhardness at lower (5°C/s and 10°C/s) cooling rates. Microhardness was observed to decrease by up to 26% due to deformation prior to quenching. However, at high cooling rates of 50°C/s, induced deformation had no effect on the final phase fractions (fully martensitic) or hardness of PHS 1800.
- The austenite decomposition model (MAT\_244) in LS-DYNA, calibrated for PHS 1800 using experimental phase fraction and microhardness measurements, predicted microhardness with less than 14% error. When the model parameters were calibrated to phase fraction measurements only, the model predicted up to 20% difference in the final phase fraction distribution.

## 8. Recommendations

1. It is recommended to further explore the effects and applications of the surface alloying heat treatment procedure prior to hot stamping. A more detailed study on the changes in the base material and the coating microstructure may provide valuable insights to the potential effects of surface alloying heat treatment process on the constitutive behaviour of the material during hot stamping. Additionally, it is possible that the surface alloying process may significantly change the performance of the coating (beneficially or detrimentally), in terms formability or resistance to damage or wear.
2. Regarding digital image correlation, alternative methods to generate the required DIC pattern should also be explored in further detail in future studies. This may simply involve using newly developed high temperature paints/coatings (that are sufficiently durable and ductile) that were not yet available when the current research was conducted. The development of a simpler and more convenient speckling procedure would eliminate the need for the surface alloying heat treatment step, which contributes uncertainty to the flow curve results (in the form of potential unknown effects).
3. Additional research should be conducted to develop novel tensile specimen geometries that further reduce (or ideally eliminate) the temperature variation along the gauge region of a resistively heated specimen. This research would not only be directly applicable to hot stamping formability research, but also to other fields of study involving high temperature material characterization and Gleeble-related studies.
4. In terms of constitutive equations and fitting, it is recommended to explore or develop a better suited constitutive model that can more accurately capture the changing strain hardening behaviour of the PHS materials at various temperatures. This could involve deriving a physically-based model that better captures the intrinsic nature of deformation, thermal effects and phase change of boron steels. This may possibly involve the complexities of capturing the change in microstructure



(austenite decomposition) with respect to temperature, strain rate, time, cooling rate, and strain during the tensile test. Alternatively, a broader review of constitutive equations from related fields of study involving phase change, strain rate sensitivity, and thermal sensitivity may reveal a more relevant constitutive model for PHS materials.

5. For the phase change experiments involving PHS 1800, more tests should be conducted at intermediate cooling rates to better understand the behaviour of the material within the vicinity of the critical cooling rate. Additional cooling rates between 10°C/s and 50°C/s should be explored, which could be directly relevant to tailored quenched components. Additionally, deformation experiments should also be conducted at these intermediate cooling rates, to understand the effect of applied strain on increased ferrite and bainite formation. In regard to the constant cooling experiments with applied deformation, more deformation conditions at finer increments and up to greater strains should be conducted to improve the resolution of the results and expand the understanding of deformation effects up to necking strains. A better understanding of the effects of deformation on phase change may be extremely relevant to manufacturability predictions and to the design of processes to produce tailored components. In terms of experimental procedures, a better cooling system and/or greater cooling air pressures should be utilized, to enable greater cooling rates and allow for maintaining constant cooling rates at lower temperatures.
6. For the determination and calibration of activation energies (and deformation scale factors), alternative optimization algorithms should be studied to evaluate the accuracy or speed (computation time) of material parameter identification. Additionally, a more comprehensive error term that combines both the phase fraction error and the hardness error into a single objective function should be explored.

## References

- [1] “U.S. DOT and EPA Put Safety and American Families First with Final Rule on Fuel Economy Standards,” 2020. <https://www.nhtsa.gov/press-releases/us-dot-and-epa-put-safety-and-american-families-first-final-rule-fuel-economy> (accessed Jul. 20, 2021).
- [2] IEA, “Global EV Outlook 2021 - Accelerating ambitions despite the pandemic,” *Glob. EV Outlook 2021*, 2021.
- [3] K. Chang, P. M. S. Choi, and S. H. Huang, “How are new-energy vehicle sales affected by government support? U.S. geospatial evidence,” *Econ. Ann.*, vol. 160, no. 7–8, pp. 14–23, 2016, doi: 10.21003/ea.V160-03.
- [4] “PURCHASING WITH SAFETY IN MIND What to look for when buying a vehicle,” 2017. [Online]. Available: [www.nhtsa.gov](http://www.nhtsa.gov).
- [5] M. Van Ratingen *et al.*, “The European New Car Assessment Programme: A historical review,” 2016, doi: 10.1016/j.cjtee.2015.11.016.
- [6] U.S. Department of Energy, “2010 annual progress report Lightweighting Material,” 2010.
- [7] M. Mikolaiczik, “2021 Mustang Mach-E.” presented at GDIS, 2021, [Online]. Available: <https://www.steel.org/steel-markets/automotive/gdis/2021-gdis-presentations/>.
- [8] J. Sulik and J. Geeraerts, “2019 Chevrolet Silverado Structure Review.” presented at GDIS, 2018, [Online]. Available: <https://www.steel.org/steel-markets/automotive/gdis/2018-gdis-presentations/>.
- [9] T. Taylor and A. Clough, “Critical review of automotive hot-stamped sheet steel from an industrial perspective,” *Mater. Sci. Technol. (United Kingdom)*, vol. 34, no. 7, pp. 809–861, 2018, doi: 10.1080/02670836.2018.1425239.
- [10] D. Reed and P. Belanger, “Hot Stamped Steel One-Piece Door Ring in the All-New 2019 Ram 1500.” presented at GDIS, 2018, [Online]. Available: <https://www.steel.org/steel-markets/automotive/gdis/2018-gdis-presentations/>.
- [11] J. McCormick, “2021 Cadillac Escalade Structure Review.” presented at GDIS, 2021, [Online].

Available: <https://www.steel.org/steel-markets/automotive/gdis/2021-gdis-presentations/>.

- [12] A. Bagley, “The All-New Jeep Wrangler.” presented at GDIS, 2019.
- [13] J. Lucas, “2021 Acura TLX.” presented at GDIS, 2021, [Online]. Available: <https://www.steel.org/steel-markets/automotive/gdis/2021-gdis-presentations/>.
- [14] H. Karbasian and A. E. Tekkaya, “A review on hot stamping,” *J. Mater. Process. Technol.*, vol. 210, no. 15, pp. 2103–2118, 2010, doi: 10.1016/j.jmatprotec.2010.07.019.
- [15] M. Ferstl and V. Clua, “Applying New Blow-Forming Processes To Obtain New Structural Components for Automotive Industry : a-,” no. July, pp. 6–8, 2011.
- [16] K. Mori *et al.*, “Hot stamping of ultra-high strength steel parts,” *CIRP Ann. - Manuf. Technol.*, vol. 66, no. 2, pp. 755–777, 2017, doi: 10.1016/j.cirp.2017.05.007.
- [17] H. Järvinen, M. Honkanen, M. Järvenpää, and P. Peura, “Effect of paint baking treatment on the properties of press hardened boron steels,” *J. Mater. Process. Technol.*, vol. 252, no. September 2017, pp. 90–104, 2018, doi: 10.1016/j.jmatprotec.2017.08.027.
- [18] C. M. Cotell, J. A. Sprague, and F. A. Smidt Jr., Eds., “Surface Engineering.” ASM International, Jan. 01, 1994, doi: 10.31399/asm.hb.v05.9781627081702.
- [19] I. Yakubtsov and R. Sohmshtetty, “Evolution of Al-Si Coating Microstructure during Heat-Treatment of Usibor® 1500,” *IOP Conf. Ser. Mater. Sci. Eng.*, vol. 418, no. 1, 2018, doi: 10.1088/1757-899X/418/1/012015.
- [20] C. M. Klassen and K. J. Daun, “Investigating coating liquefaction and solidification of furnace-heated Al-Si coated 22MnB5 steel using laser reflectance,” *Surf. Coatings Technol.*, vol. 393, no. April, p. 125795, 2020, doi: 10.1016/j.surfcoat.2020.125795.
- [21] C. W. Lee, D. W. Fan, I. R. Sohn, S. J. Lee, and B. C. De Cooman, “Liquid-metal-induced embrittlement of Zn-coated hot stamping steel,” *Metall. Mater. Trans. A Phys. Metall. Mater. Sci.*, vol. 43, no. 13, pp. 5122–5127, 2012, doi: 10.1007/s11661-012-1316-0.
- [22] J. Kondratiuk, P. Kuhn, E. Labrenz, and C. Bischoff, “Zinc coatings for hot sheet metal forming: Comparison of phase evolution and microstructure during heat treatment,” *Surf. Coatings Technol.*,

- vol. 205, no. 17–18, pp. 4141–4153, 2011, doi: 10.1016/j.surfcoat.2011.03.002.
- [23] T. Kurz, P. Larour, J. Lackner, T. Steck, and G. Jesner, “Press-hardening of zinc coated steel - Characterization of a new material for a new process,” *IOP Conf. Ser. Mater. Sci. Eng.*, vol. 159, no. 1, 2016, doi: 10.1088/1757-899X/159/1/012025.
- [24] Q. Lu, S. Tedesco, M. Shi, J. Coryell, and J. Wang, “New Generation Oxidation Resistance (Coating Free) Press Hardening Steel.” presented at GDIS, 2021, [Online]. Available: <https://www.steel.org/steel-markets/automotive/gdis/2021-gdis-presentations/>.
- [25] M. Kang and C. Kim, “Laser welding for hot-stamped tailor-welded blanks with high-strength steel/high-energy absorption steel,” *J. Laser Appl.*, vol. 26, no. 3, p. 032007, 2014, doi: 10.2351/1.4881279.
- [26] P. Samadian, C. Butcher, and M. J. Worswick, “Microstructures and Flow Behavior of Ductibor® 500-AS Steel for a Range of As-Quenched Conditions,” *J. Mater. Eng. Perform.*, vol. 29, no. 11, pp. 7153–7169, 2020, doi: 10.1007/s11665-020-05205-x.
- [27] D. D. Múnera, A. Pic, D. Abou-Khalil, F. Shmit, and F. Pinard, “Innovative press hardened steel based laser welded blanks solutions for weight savings and crash safety improvements,” *SAE Int. J. Mater. Manuf.*, vol. 1, no. 1, pp. 472–479, 2009, doi: 10.4271/2008-01-1076.
- [28] P. Samadian, A. Abedini, C. Butcher, and M. J. Worswick, “Microstructure-Based Modelling of Flow and Fracture Behavior of Tailored Microstructures of Ductibor® 1000-AS Steel,” *Metals (Basel)*, vol. 12, no. 10, 2022, doi: 10.3390/met12101770.
- [29] S.-H. Lee *et al.*, “Development of a 1000 MPa Hot Stamped Crush Tip,” 2022.
- [30] S. Kalpakjian and S. R. Schmid, *Manufacturing Processes for Engineering Materials*, 5th Editio. Singapore: Pearson Education, 2008.
- [31] W. F. Hosford and R. M. Caddell, *Metal forming: Mechanics and metallurgy*. 2011.
- [32] H. Li, L. He, G. Zhao, and L. Zhang, “Constitutive relationships of hot stamping boron steel B1500HS based on the modified Arrhenius and Johnson-Cook model,” *Mater. Sci. Eng. A*, vol. 580, pp. 330–348, 2013, doi: 10.1016/j.msea.2013.05.023.

- [33] W. Volk *et al.*, “Models and modelling for process limits in metal forming,” *CIRP Ann.*, vol. 68, no. 2, pp. 775–798, 2019, doi: 10.1016/j.cirp.2019.05.007.
- [34] N. Li *et al.*, “Experimental investigation of boron steel at hot stamping conditions,” *J. Mater. Process. Technol.*, vol. 228, pp. 2–10, 2016, doi: 10.1016/j.jmatprotec.2015.09.043.
- [35] P. F. Bariani, S. Bruschi, A. Ghiotti, and A. Turetta, “Testing formability in the hot stamping of HSS,” *CIRP Ann. - Manuf. Technol.*, vol. 57, no. 1, pp. 265–268, 2008, doi: 10.1016/j.cirp.2008.03.049.
- [36] A. L. P. H. B. Hochholdinger H. Grass, “Determination of flow curve by stack compression test and inverse analysis for the simulation of hot forming,” *7 th Eur. Ls-DYNA conference*, no. March 2015, 2009.
- [37] A. Ghiotti, S. Bruschi, and F. Borsetto, “Tribological characteristics of high strength steel sheets under hot stamping conditions,” *J. Mater. Process. Technol.*, vol. 211, no. 11, pp. 1694–1700, 2011, doi: 10.1016/j.jmatprotec.2011.05.009.
- [38] M. Nikravesh, M. Naderi, G. H. Akbari, and W. Bleck, “Phase transformations in a simulated hot stamping process of the boron bearing steel,” *Mater. Des.*, vol. 84, pp. 18–24, 2015, doi: 10.1016/j.matdes.2015.06.108.
- [39] D. W. Walsh, M. J. Cieslak, and W. F. Savage, “Temperature Measurements in Resistance-Heated Specimens: Longitudinal Gradients,” *Weld. J. (Miami, Fla)*, vol. 65, no. 7, pp. 184–192, 1986.
- [40] M. Eriksson, M. Oldenburg, M. C. Somani, and L. P. Karjalainen, “Testing and evaluation of material data for analysis of forming and hardening of boron steel components,” *Model. Simul. Mater. Sci. Eng.*, vol. 10, no. 3, pp. 277–294, 2002, doi: 10.1088/0965-0393/10/3/303.
- [41] A. Turetta, S. Bruschi, and A. Ghiotti, “Investigation of 22MnB5 formability in hot stamping operations,” *J. Mater. Process. Technol.*, vol. 177, no. 1–3, pp. 396–400, 2006, doi: 10.1016/j.jmatprotec.2006.04.041.
- [42] M. Merklein and J. Lechler, “Determination of material and process characteristics for hot stamping processes of quenchenable ultra high strength steels with respect to a fe-based process design,” *SAE*

- Int. J. Mater. Manuf.*, vol. 1, no. 1, pp. 411–426, 2009, doi: 10.4271/2008-01-0853.
- [43] M. Abspoel, B. M. Neelis, and P. Van Liempt, “Constitutive behaviour under hot stamping conditions,” *J. Mater. Process. Technol.*, vol. 228, pp. 34–42, 2016, doi: 10.1016/j.jmatprotec.2015.05.007.
- [44] M. Ganapathy, N. Li, J. Lin, M. Abspoel, and D. Bhattacharjee, “A Novel Grip Design for High-Accuracy Thermo-Mechanical Tensile Testing of Boron Steel under Hot Stamping Conditions,” *Exp. Mech.*, vol. 58, no. 2, pp. 243–258, 2018, doi: 10.1007/s11340-017-0333-8.
- [45] Y. Li, S. Li, Y. Chen, and G. Han, “Constitutive parameters identification based on DIC assisted thermo-mechanical tensile test for hot stamping of boron steel,” *J. Mater. Process. Technol.*, vol. 271, no. March, pp. 429–443, 2019, doi: 10.1016/j.jmatprotec.2019.04.020.
- [46] Dynamic Systems Inc., “GLEEBLE SYSTEMS COMPARISON CHART.” <https://www.leeble.com/products/leeble-systems/comparison-chart.html> (accessed Jun. 14, 2021).
- [47] M. Naderi, L. Durrenberger, A. Molinari, and W. Bleck, “Constitutive relationships for 22MnB5 boron steel deformed isothermally at high temperatures,” *Mater. Sci. Eng. A*, vol. 478, no. 1–2, pp. 130–139, 2008, doi: 10.1016/j.msea.2007.05.094.
- [48] R. Bigger *et al.*, “A Good Practices Guide for Digital Image Correlation,” *Int. Digit. Image Correl. Soc.*, p. 94, 2018, [Online]. Available: <http://idics.org/guide/>.
- [49] M. Sutton, J.-J. Orteu, and H. Schreier, *Image Correlation for Shape, Motion and Deformation Measurements. Basic Concepts, Theory and Applications*. 2009.
- [50] S. Bruschi *et al.*, “Testing and modelling of material behaviour and formability in sheet metal forming,” *CIRP Ann. - Manuf. Technol.*, vol. 63, no. 2, pp. 727–749, 2014, doi: 10.1016/j.cirp.2014.05.005.
- [51] B. M. B. Grant, H. J. Stone, P. J. Withers, and M. Preuss, “High-temperature strain field measurement using digital image correlation,” *J. Strain Anal. Eng. Des.*, vol. 44, no. 4, pp. 263–271, 2009, doi: 10.1243/03093247JSA478.

- [52] S. Yoneyama, “Basic principle of digital image correlation for in-plane displacement and strain measurement,” *Adv. Compos. Mater.*, vol. 25, no. 2, pp. 105–123, 2016, doi: 10.1080/09243046.2015.1129681.
- [53] X. Chen, N. Xu, L. Yang, and D. Xiang, “High temperature displacement and strain measurement using a monochromatic light illuminated stereo digital image correlation system,” *Meas. Sci. Technol.*, vol. 23, no. 12, 2012, doi: 10.1088/0957-0233/23/12/125603.
- [54] Correlated Solutions Inc., *Vic-3D 8 Testing Guide*. .
- [55] Correlated Solutions, *VIC-3D Software Manual*, Version 8. .
- [56] Correlated Solutions, “Application Note AN -1701 Speckle Pattern Fundamentals,” *Speckle Pattern Fundam.*, 2017, [Online]. Available: <http://www.correlatedsolutions.com/support/index.php?/Knowledgebase/Article/GetAttachment/80/14750>.
- [57] B. Pan, D. Wu, Z. Wang, and Y. Xia, “High-temperature digital image correlation method for full-field deformation measurement at 1200 °C,” *Meas. Sci. Technol.*, vol. 22, no. 1, 2011, doi: 10.1088/0957-0233/22/1/015701.
- [58] R. B. Berke and J. Lambros, “Ultraviolet digital image correlation (UV-DIC) for high temperature applications,” *Rev. Sci. Instrum.*, vol. 85, no. 4, 2014, doi: 10.1063/1.4871991.
- [59] W. Wang, C. Xu, H. Jin, S. Meng, Y. Zhang, and W. Xie, “Measurement of high temperature full-field strain up to 2000 °c using digital image correlation,” *Meas. Sci. Technol.*, vol. 28, no. 3, 2017, doi: 10.1088/1361-6501/aa56d1.
- [60] M. D. Novak and F. W. Zok, “High-temperature materials testing with full-field strain measurement: Experimental design and practice,” *Rev. Sci. Instrum.*, vol. 82, no. 11, 2011, doi: 10.1063/1.3657835.
- [61] Rust-Oleum Corporation, “PTX-03 PAINTER ’ S TOUCH ® ULTRA COVER 2X PRIMER SPRAYS TECHNICAL DATA.”
- [62] Sharpie, “Sharpie Industrial Permanent Marker, Fine Point.”

- [https://www.sharpie.com/markers/professional-markers/sharpie-industrial-permanent-markers-fine-point/SAP\\_13763PP.html](https://www.sharpie.com/markers/professional-markers/sharpie-industrial-permanent-markers-fine-point/SAP_13763PP.html) (accessed Aug. 06, 2021).
- [63] D. Lorenz and K. Roll, “Modelling and Analysis of Integrated Hotforming and Quenching Processes,” *Adv. Mater. Res.*, vol. 6–8, pp. 787–794, 2005, doi: 10.4028/www.scientific.net/amr.6-8.787.
- [64] P. Hein, “A Global Approach of the Finite Element Simulation of Hot Stamping,” *Adv. Mater. Res.*, vol. 6–8, pp. 763–770, 2005, doi: 10.4028/www.scientific.net/amr.6-8.763.
- [65] M. Oldenburg, P. Åkerström, G. Bergman, and P. Salomonsson, “Microstructure evolution and mechanical response in the hot stamping process,” *6th Eur. LS-DYNA Users’ Conf.*, pp. 135–144, 2007.
- [66] P. Åkerström and M. Oldenburg, “Austenite decomposition during press hardening of a boron steel- Computer simulation and test,” *J. Mater. Process. Technol.*, vol. 174, no. 1–3, pp. 399–406, 2006, doi: 10.1016/j.jmatprotec.2006.02.013.
- [67] Z. Marciniak, J. L. Duncan, and S. J. Hu, *Mechanics of Sheet Metal Forming*. Butterworth-Heinemann, 2002.
- [68] S. Hertelé, W. De Waele, and R. Denys, “A generic stress-strain model for metallic materials with two-stage strain hardening behaviour,” *Int. J. Non. Linear. Mech.*, vol. 46, no. 3, pp. 519–531, 2011, doi: 10.1016/j.ijnonlinmec.2010.12.004.
- [69] D. C. Ludwigson, “Modified stress-strain relation for FCC metals and alloys,” *Metall. Trans.*, vol. 2, no. 10, pp. 2825–2828, 1971, doi: 10.1007/BF02813258.
- [70] H. Li, X. Wu, and G. Li, “Prediction of forming limit diagrams for 22MnB5 in hot stamping process,” *J. Mater. Eng. Perform.*, vol. 22, no. 8, pp. 2131–2140, 2013, doi: 10.1007/s11665-013-0491-5.
- [71] P. Åkerström, “Modelling and Simulation of Hot Stamping,” p. 130, 2006.
- [72] A. Bardelcik, M. J. Worswick, and M. A. Wells, “The influence of martensite, bainite and ferrite on the as-quenched constitutive response of simultaneously quenched and deformed boron steel -



- Experiments and model,” *Mater. Des.*, vol. 55, pp. 509–525, 2014, doi: 10.1016/j.matdes.2013.10.014.
- [73] R. E. Koistinen, D. P. ; Marburger, “A general equation prescribing the extend of the austenite-martensite transformation in pure iron-carbon alloys and plain carbon steels,” pp. 59–60.
- [74] J. S. Kirkaldy and D. Venugopalan, “PREDICTION OF MICROSTRUCTURE AND HARDENABILITY IN LOW ALLOY STEELS.,” 1984.
- [75] Livermore Software Technology Corporation (LSTC), *LS-DYNA KEYWORD USER’S MANUAL VOLUME II Material Models*, LS-DYNA R1., no. February. Livermore, CA, USA, 2017.
- [76] R. W. K. Honeycombe, *Steels: microstructure and properties*. London: Edward Arnold, 1981.
- [77] A. Barcellona and D. Palmeri, “Effect of plastic hot deformation on the hardness and continuous cooling transformations of 22MnB5 microalloyed boron steel,” *Metall. Mater. Trans. A Phys. Metall. Mater. Sci.*, vol. 40, no. 5, pp. 1160–1174, 2009, doi: 10.1007/s11661-009-9790-8.
- [78] P. Hippchen, A. Lipp, H. Grass, P. Craighero, M. Fleischer, and M. Merklein, “Modelling kinetics of phase transformation for the indirect hot stamping process to focus on car body parts with tailored properties,” *J. Mater. Process. Technol.*, vol. 228, pp. 59–67, 2016, doi: 10.1016/j.jmatprotec.2015.01.003.
- [79] R. George, A. Bardelcik, and M. Worswick, “Improving the Prediction of the Bainite and Ferrite Phase Transformation During Hot Stamping Simulations Using LS-DYNA,” in *4th International Conference on Hot Sheet Metal Forming of High-Performance Steel CHS2*, 2013, pp. 67–74.
- [80] K. Omer, R. George, A. Bardelcik, M. Worswick, S. Malcolm, and D. Detwiler, “Development of a hot stamped channel section with axially tailored properties – experiments and models,” *Int. J. Mater. Form.*, vol. 11, no. 1, pp. 149–164, 2018, doi: 10.1007/s12289-017-1338-7.
- [81] C. Bourque, “An Investigation into the Austenite Decomposition Behaviour and Post-Forming Tempering Response of Two 1800 MPa Grades of Press Hardening Steels by,” University of Guelph, 2019.
- [82] T. Taylor and J. McCulloch, “Effect of Part/Die Boundary Conditions on Microstructural Evolution

- during Hot Stamping 2000 MPa Class Boron Steel,” *Steel Res. Int.*, vol. 89, no. 6, pp. 1–10, 2018, doi: 10.1002/srin.201700495.
- [83] Correlated Solutions Inc., “Vic-3D 8.” Irmo, SC, USA, 2020, [Online]. Available: <https://www.correlatedsolutions.com/vic-3d/>.
- [84] Z. X. Gui, W. K. Liang, and Y. S. Zhang, “Formability of aluminum-silicon coated boron steel in hot stamping process,” *Trans. Nonferrous Met. Soc. China (English Ed.)*, vol. 24, no. 6, pp. 1750–1757, 2014, doi: 10.1016/S1003-6326(14)63249-0.
- [85] AMERICAN SOCIETY FOR TESTING AND MATERIALS (ASTM), *ASTM E8/E8M - Standard test methods for tension testing of metallic materials*. 2021.
- [86] J. M. R. S. Appuhamy, T. Kaita, M. Ohga, and K. Fujii, “Prediction of residual strength of corroded tensile steel plates,” *Int. J. Steel Struct.*, vol. 11, no. 1, pp. 65–79, 2011, doi: 10.1007/S13296-011-1006-6.
- [87] A. Zhumagulov, “Crashworthiness and Material Characterization of Multi-Cellular AA6063 Extrusions,” University of Waterloo, 2017.
- [88] R. G. Budynas and J. K. Nisbett, *Shigley’s Mechanical Engineering Design*, 10th ed. McGraw-Hill Education, 2014.
- [89] K. Omer, C. Butcher, and M. Worswick, “Characterization and application of a constitutive model for two 7000-series aluminum alloys subjected to hot forming,” *Int. J. Mech. Sci.*, vol. 165, no. November 2018, p. 105218, 2020, doi: 10.1016/j.ijmecsci.2019.105218.
- [90] The MathWorks Inc., “MATLAB R2019b.” Natick, MA, USA, 2019, [Online]. Available: <https://www.mathworks.com/products/matlab.html>.
- [91] The MathWorks Inc., “MATLAB Documentation,” 2021. [https://www.mathworks.com/help/matlab/index.html?s\\_tid=hc\\_panel](https://www.mathworks.com/help/matlab/index.html?s_tid=hc_panel) (accessed Nov. 24, 2021).
- [92] A. Bardelcik, C. P. Salisbury, S. Winkler, M. A. Wells, and M. J. Worswick, “Effect of cooling rate on the high strain rate properties of boron steel,” *Int. J. Impact Eng.*, vol. 37, no. 6, pp. 694–702, 2010, doi: 10.1016/j.ijimpeng.2009.05.009.

- [93] H. Järvinen, M. Isakov, T. Nyysönen, M. Järvenpää, and P. Peura, “The effect of initial microstructure on the final properties of press hardened 22MnB5 steels,” *Mater. Sci. Eng. A*, vol. 676, pp. 109–120, 2016, doi: 10.1016/j.msea.2016.08.096.
- [94] F. Borsetto, A. Ghiotti, and S. Bruschi, “Investigation of the high strength steel Al-Si coating during hot stamping operations,” *Key Eng. Mater.*, vol. 410–411, pp. 289–296, 2009, doi: 10.4028/www.scientific.net/KEM.410-411.289.
- [95] M. J. Holzweissig, J. Lackmann, S. Konrad, M. Schaper, and T. Niendorf, “Influence of Short Austenitization Treatments on the Mechanical Properties of Low-Alloy Steels for Hot Forming Applications,” *Metall. Mater. Trans. A Phys. Metall. Mater. Sci.*, vol. 46, no. 7, pp. 3199–3207, 2015, doi: 10.1007/s11661-015-2907-3.
- [96] R. He, “Characterization of Formability and Friction during Hot Stamping of Al-Si Coated Press Hardened Steel,” 2023.

## Appendix A: Modifications to Gleeble Grips

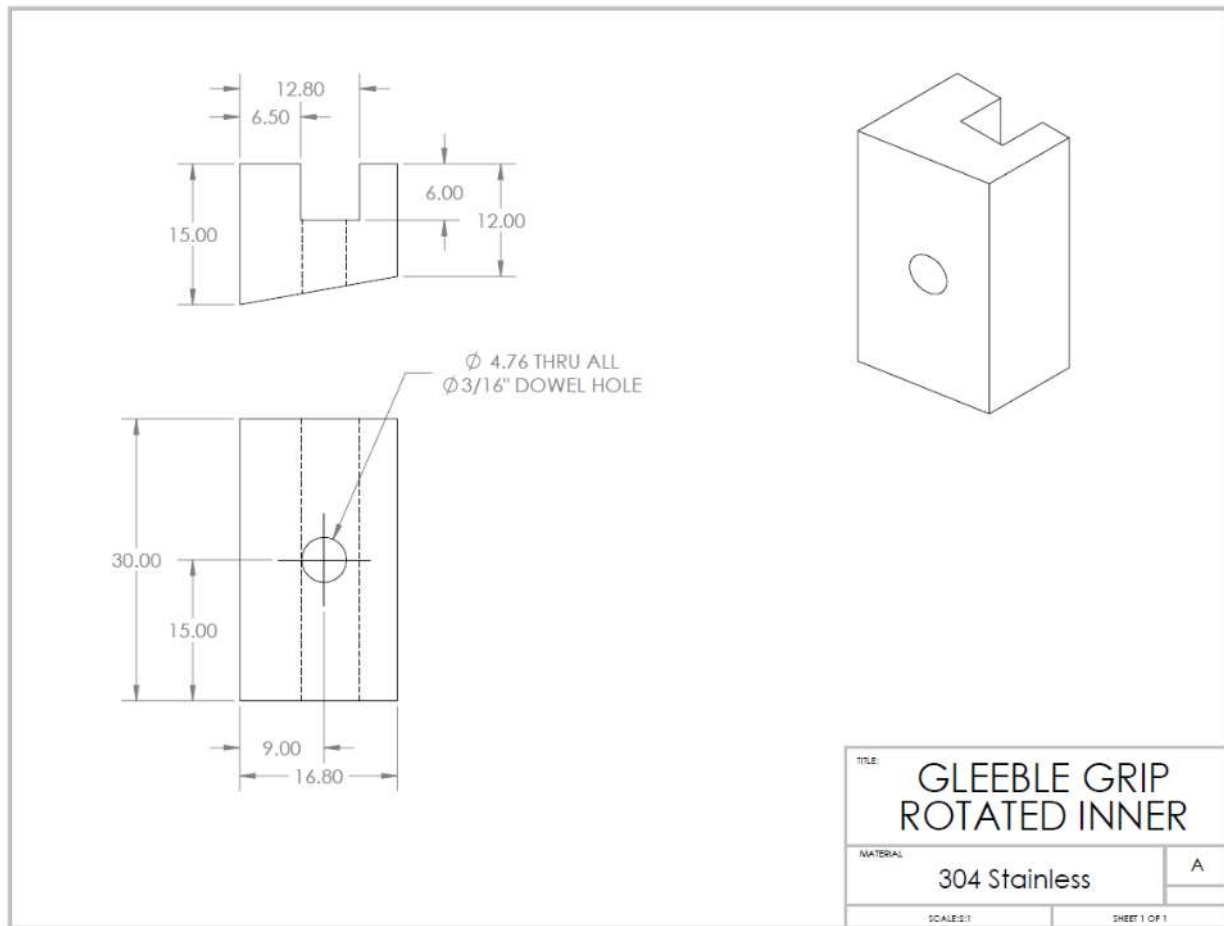


Figure 97: Drawing for the inner set of grips for rotating the orientation of the tensile specimen

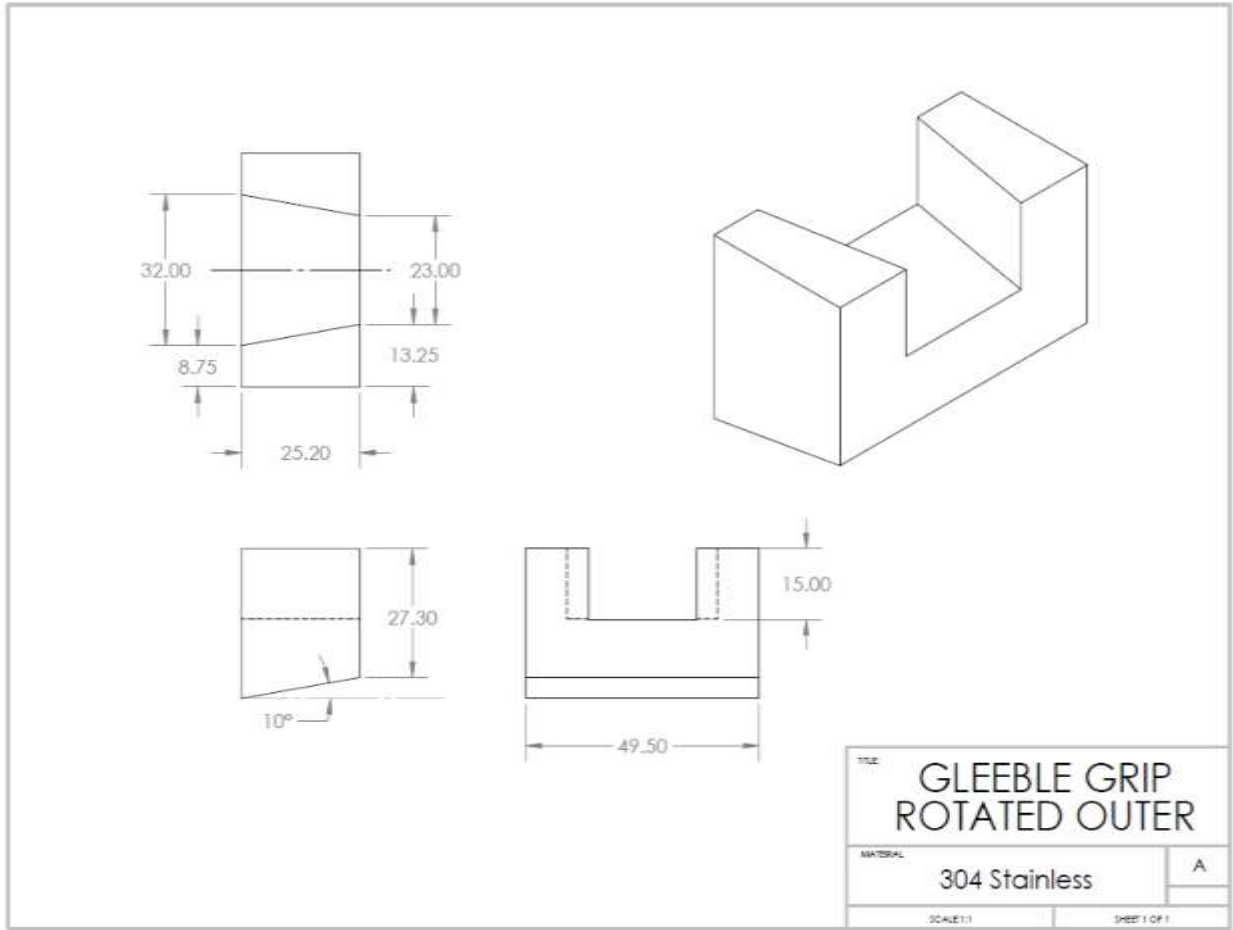


Figure 98: Drawing for the outer set of grips for rotating the orientation of the tensile specimen

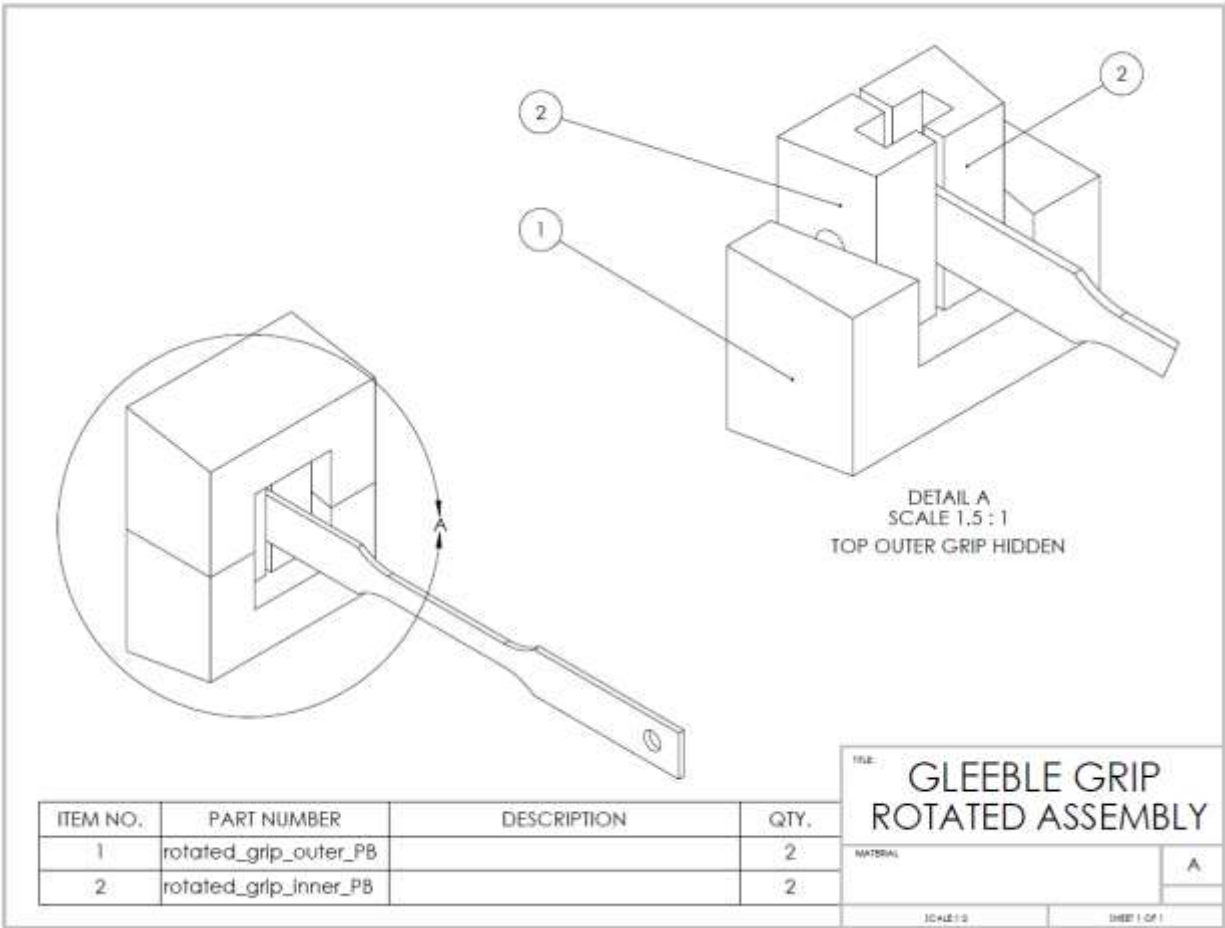


Figure 99: Assembly drawing of the grips for rotating the orientation of the specimen, the required dowel pin is not shown

## Appendix B: Stress-Strain Data Showing Variability in Measurements

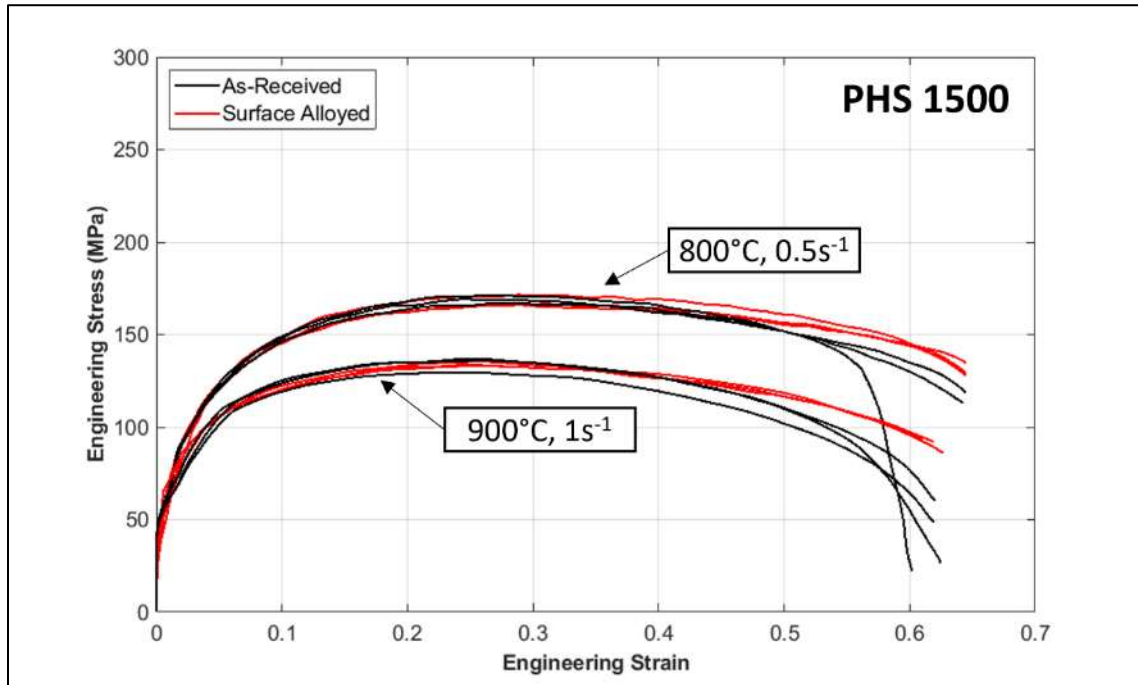


Figure 100: Engineering stress-strain curves of as-received and surface alloyed PHS 1500 from isothermal tensile tests at 800°C and 0.5s<sup>-1</sup>, and at 900°C and 1s<sup>-1</sup>

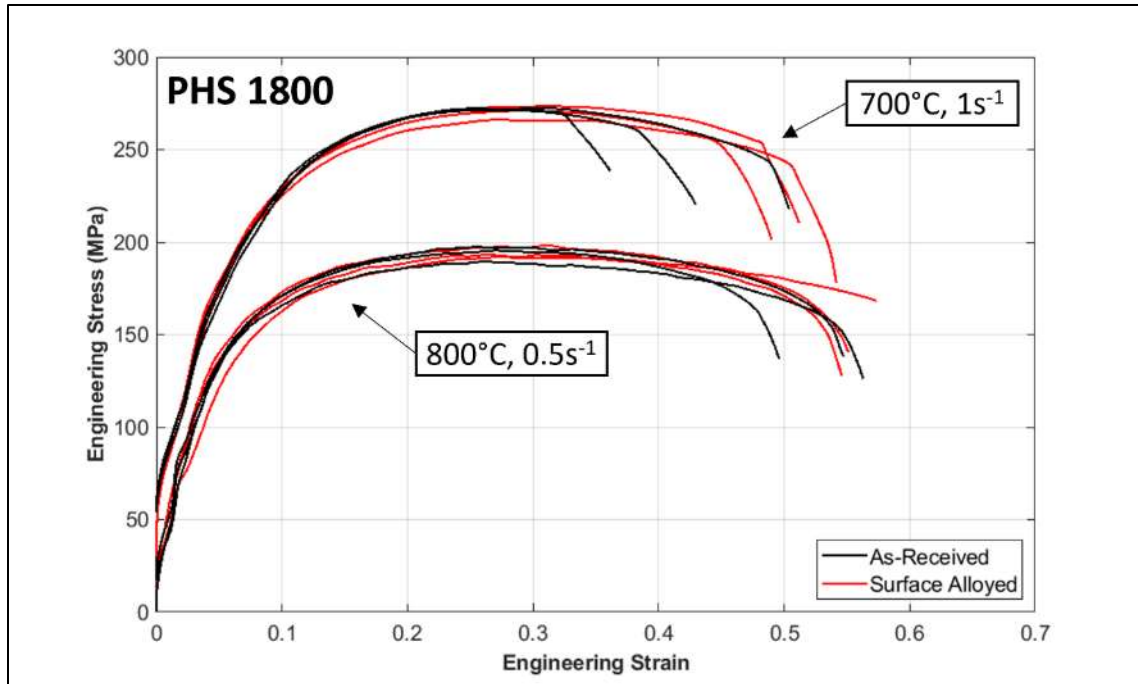


Figure 101: Engineering stress-strain curves of as-received and surface alloyed PHS 1800 from isothermal tensile tests at 700°C and 1s<sup>-1</sup>, and at 800°C and 0.5s<sup>-1</sup>



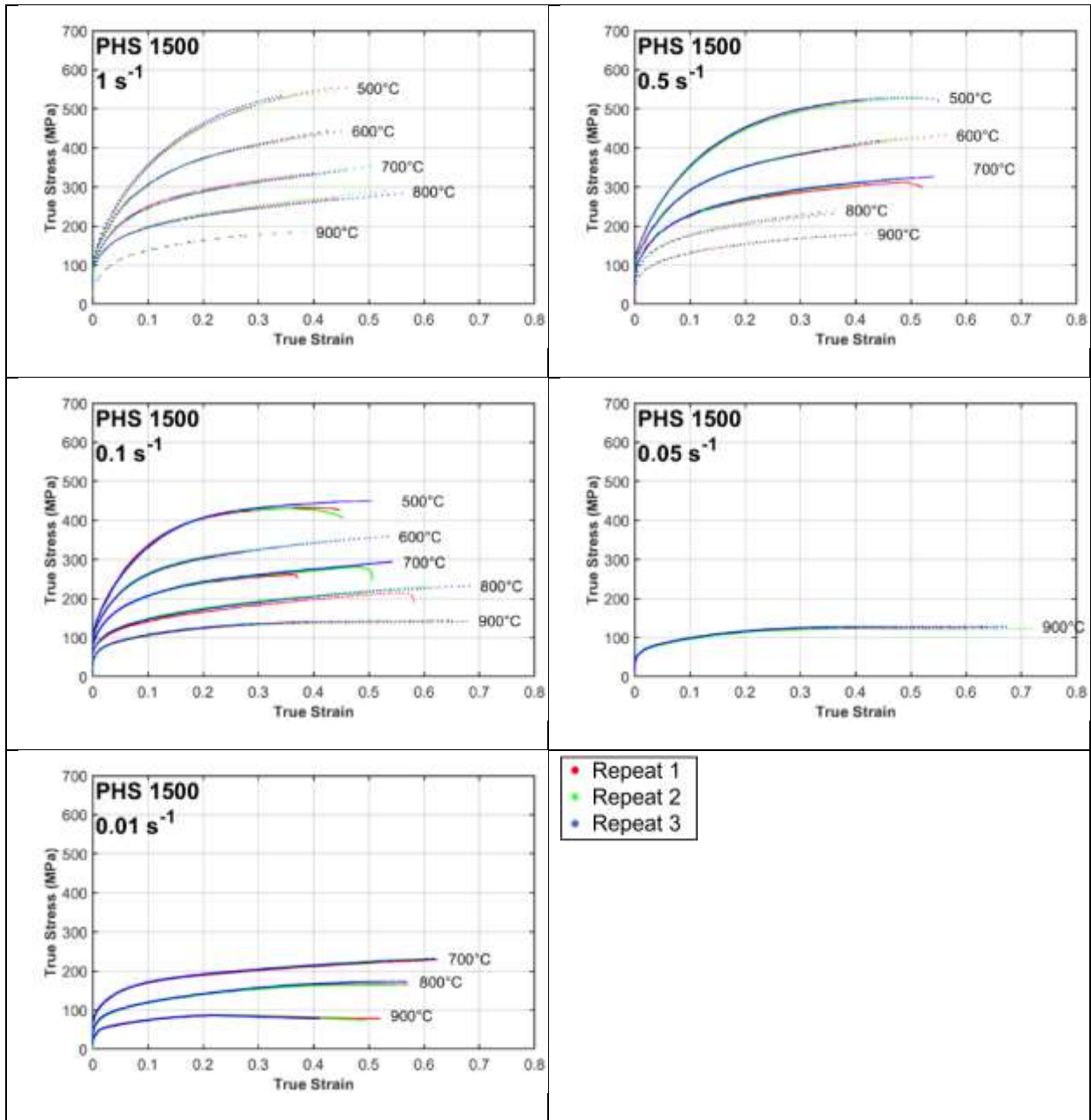


Figure 102: Experimental PHS 1500 flow curves at with all three repeat test results plotted for a range of conditions

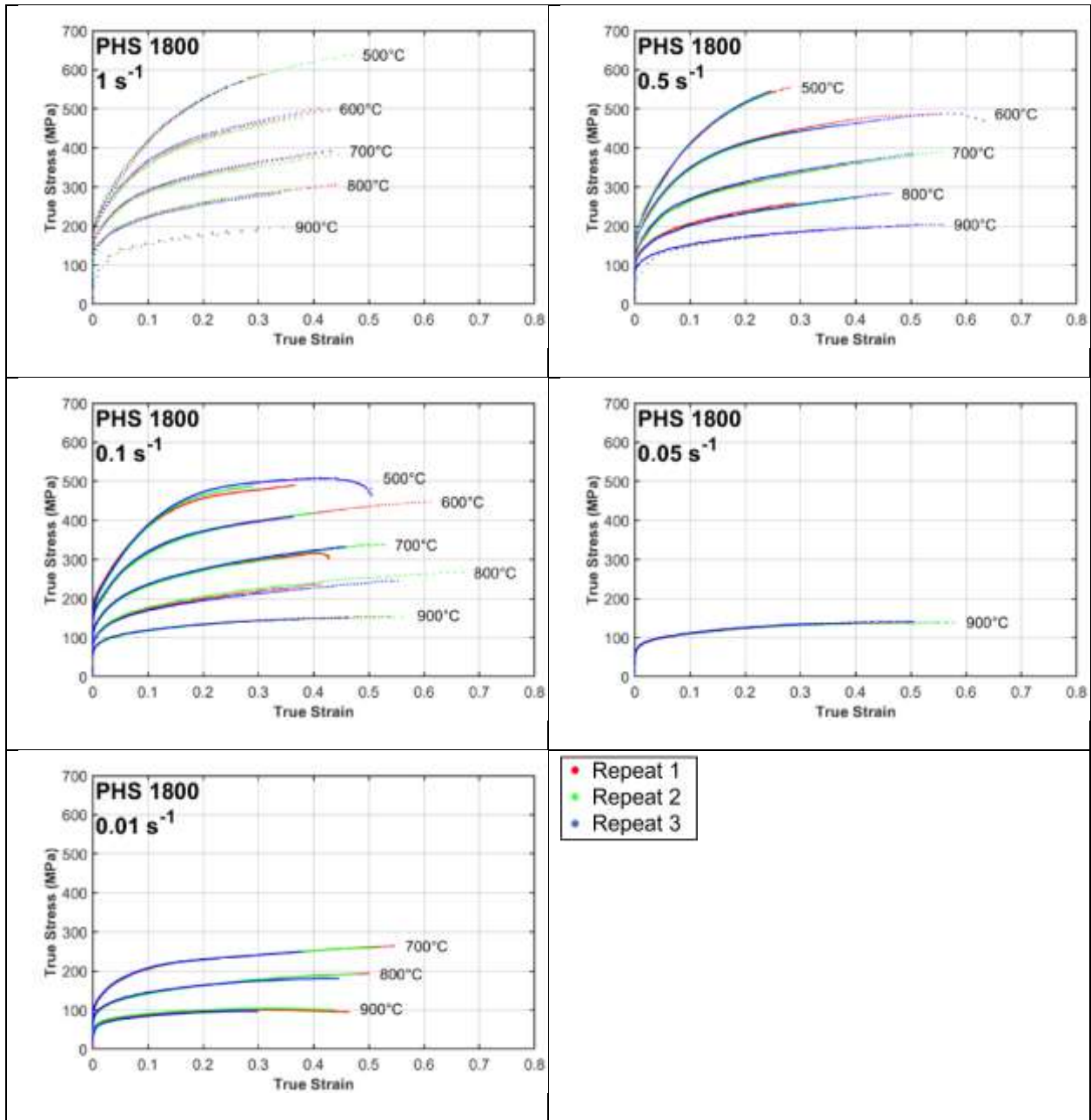


Figure 103: Experimental PHS 1800 flow curves at with all three repeat test results plotted for a range of conditions

## Appendix C: Flow Curve Results in Strain Rate Subplots

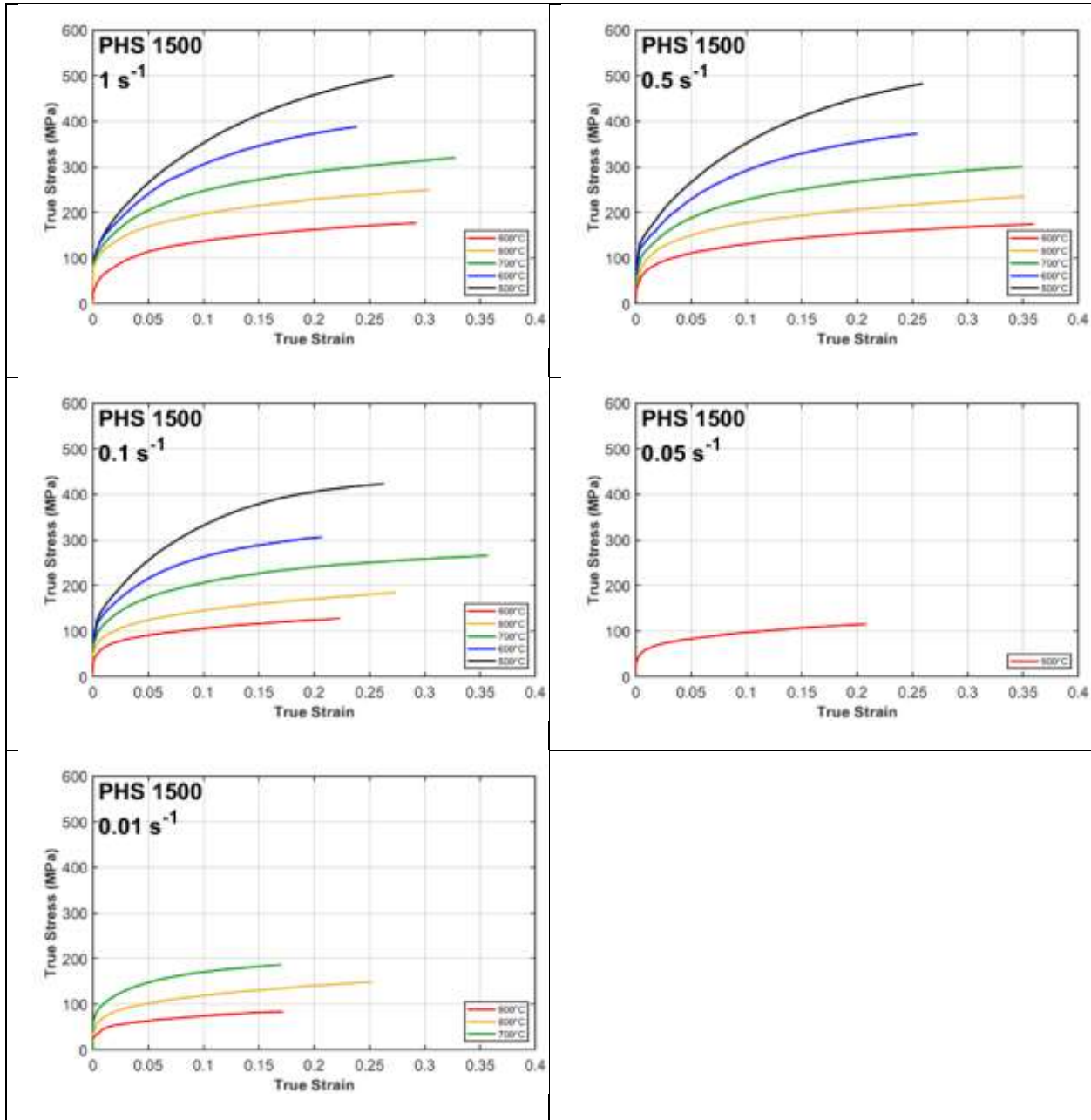


Figure 104: Experimental PHS 1500 flow curves at various temperatures, plotted together with the same strain rate conditions

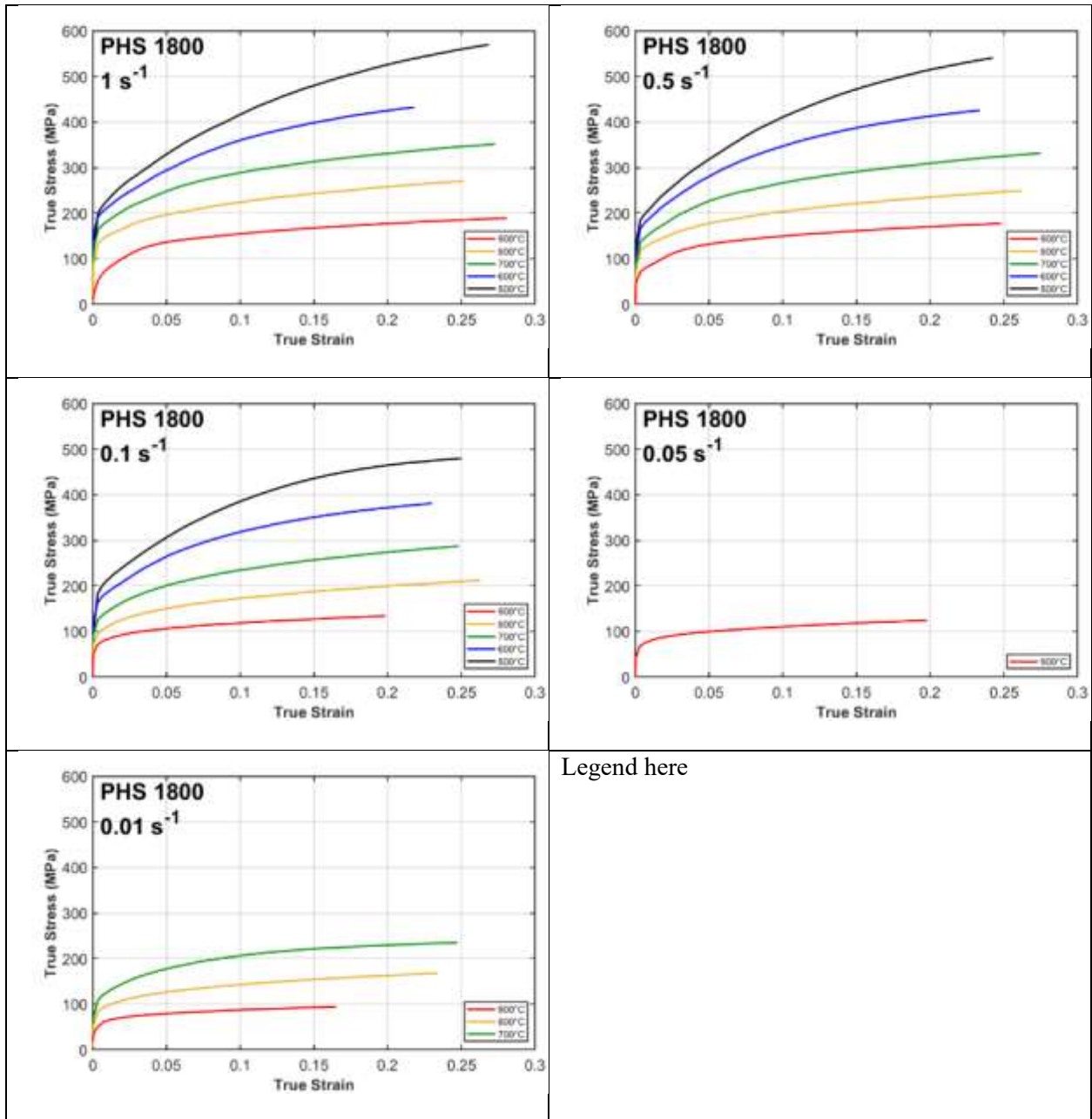


Figure 105: Experimental PHS 1800 flow curves at various temperatures, plotted together with the same strain rate conditions

## Appendix D: Norton-Hoff (Equations (24) - (26)) Fits for PHS 1500

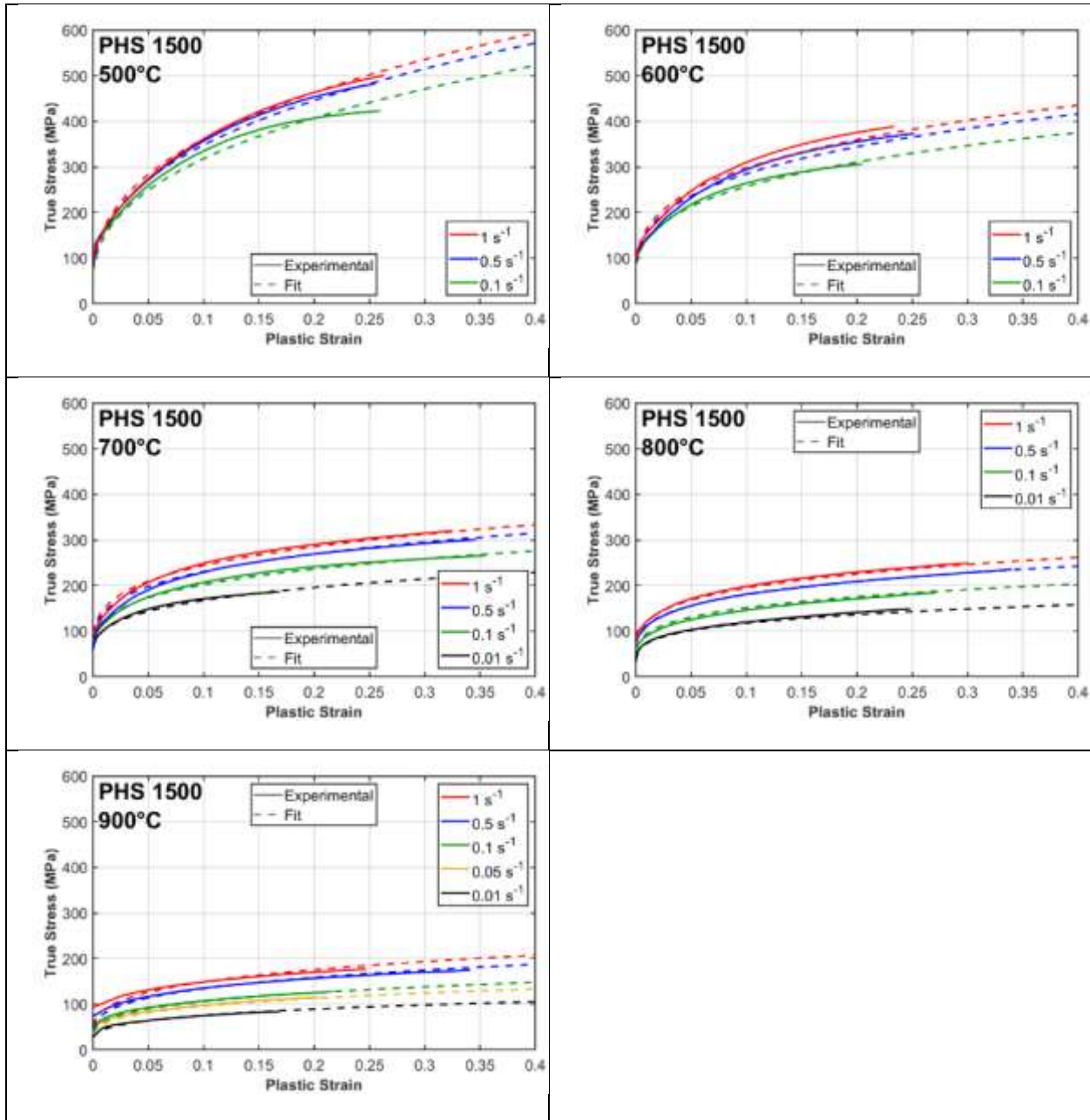


Figure 106: Experimental (solid) and fit (dash) flow curves of PHS 1500 fit to the modified second order polynomial Norton-Hoff equation

Table 16: Coefficients for the Modified Norton-Hoff equation for PHS 1500, obtained by fitting Equations (24)(6), (25) and (26) to the experimental flow curves

<b>A (MPa s<sup>m</sup>)</b>	<b>B (K)</b>	<b>b</b>	<b>n1 (K<sup>-2</sup>)</b>	<b>n2 (K<sup>-1</sup>)</b>	<b>n3</b>	<b>m1 (K<sup>-2</sup>)</b>	<b>m2(K<sup>-2</sup>)</b>	<b>m3</b>
26.146	2651.521	0.00133	1.879e-6	-3.968e-3	2.294	4.602e-7	-6.663e-4	0.296

Table 17: R-Squared of the fit flow curves compared to the experimental PHS 1500 flow curves, using the coefficients from Table 16

Temperature Condition (°C)	Strain Rate Condition (s <sup>-1</sup> )	R-Squared
500°C	0.1	0.976
	0.5	0.994
	1	0.997
600°C	0.1	0.992
	0.5	0.978
	1	0.969
700°C	0.01	0.985
	0.1	0.991
	0.5	0.984
	1	0.989
800°C	0.01	0.970
	0.1	0.973
	0.5	0.999
	1	0.991
900°C	0.01	0.988
	0.05	0.964
	0.1	0.982
	0.5	0.969
	1	0.878

The R-squared of the modified second-order polynomial Norton-Hoff equation fit to all PHS 1500 experimental results was 0.985. In comparison, the R-squared of the exponential Norton-Hoff equation was 0.960.

# Appendix E: LS-DYNA MAT\_244 Material Parameters for Baseline Austenite Decomposition Simulations

\*MAT\_UHS\_STEEL\_(TITLE) (244) (1)

TITLE								
PHS 1800 - SL 2021								
1	MID	RO	E	PR	TUNIT	CRSH	PHASE	HEAT
	1	7.830e-06	2.070e+05	0.3000000	3600.0000	0	0	0
2	LCY1	LCY2	LCY3	LCY4	LCY5	KFER	KPER	B
	-1	-1	-1	-1	-1	1.900e+05	3100.0000	0.0020000
3	C	Co	Mo	Cr	Ni	Mn	Si	V
	0.3200000	0.0	0.1500000	0.3100000	0.3600000	0.5700000	0.5700000	0.0
4	W	Cu	P	Al	As	Ti	CWM	LCTRE
	0.0	0.0100000	0.0120000	0.0500000	0.0	0.0210000	0	0
5	THEXP1	THEXP5	LCTH1	LCTH5	TREF	LAT1	LAT5	TABTH
	2.510e-05	1.110e-05	0	0	293.14999	590.00000	640.00000	0
6	QR2	QR3	QR4	ALPHA	GRAIN	TOFFE	TOFPE	TOFBA
	1.032e+04	1.343e+04	1.507e+04	0.0330000	6.8000002	0.0	0.0	0.0
7	PLMEM2	PLMEM3	PLMEM4	PLMEM5	STRC	STRP	REACT	TEMPER
	0.0	0.0	0.0	0.0	0.0	0.0	0	0

Figure 107: LS-DYNA MAT\_244 material card used for the baseline activation energy simulations. All parameters are default values taken from the LS-DYNA Keyword Manual [75] with the exception of the chemical composition, which was updated to that of the studied PHS 1800